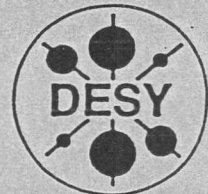


*liegt aus*

DEUTSCHES ELEKTRONEN-SYNCHROTRON

DESY-THESIS-1998-004  
March 1998

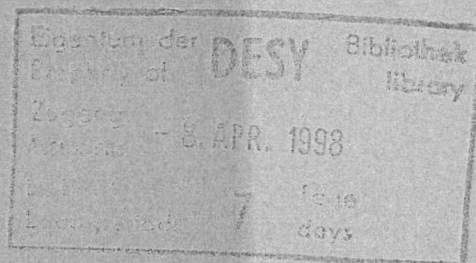


*D, B, C*

Measurement of the Proton Structure Function  $F_2$   
at Low  $Q^2$  and Very Low  $x$   
with the ZEUS Beam Pipe Calorimeter  
at HERA

by

B. Surrow



NOTKESTRASSE 85 - 22607 HAMBURG

**DESY behält sich alle Rechte für den Fall der Schutzrechtserteilung und für die wirtschaftliche Verwertung der in diesem Bericht enthaltenen Informationen vor.**

**DESY reserves all rights for commercial use of information included in this report, especially in case of filing application for or grant of patents.**

**"Die Verantwortung für den Inhalt dieses Berichtes liegt ausschließlich beim Verfasser"**

Measurement  
of the Proton Structure Function  $F_2$   
at Low  $Q^2$  and Very Low  $x$   
with the ZEUS Beam Pipe Calorimeter  
at HERA

DISSERTATION

zur Erlangung des Doktorgrades  
des Fachbereichs Physik  
der Universität Hamburg

vorgelegt von

Bernd Surrow ✓  
aus Schwäbisch Hall

Hamburg  
Januar 1998



Measurement  
of the Proton Structure Function  $F_2$   
at Low  $Q^2$  and Very Low  $x$   
with the ZEUS Beam Pipe Calorimeter  
at HERA

DISSERTATION

zur Erlangung des Doktorgrades  
des Fachbereichs Physik  
der Universität Hamburg

vorgelegt von

Bernd Sorrow  
aus Schwäbisch Hall

Hamburg  
Januar 1998

Gutachter der Dissertation: Prof. Dr. Robert Klanner  
Prof. Dr. Beate Naroska  
Prof. Dr. Karlheinz Meier

Gutachter der Disputation: Prof. Dr. Erich Lohrmann  
Prof. Dr. Albrecht Wagner

Datum der Disputation: 01.04.1998

Dekan des  
Fachbereichs Physik und  
Vorsitzender des  
Promotionsausschusses: Prof. Dr. B. Kramer

## Abstract

Results on measurements of the proton structure function  $F_2$  from the two HERA experiments H1 and ZEUS in 1994 show that perturbative QCD (pQCD) allows to describe the observed rapid rise of  $F_2$  with decreasing  $x$  down to  $Q^2 = 1.5 \text{ GeV}^2$ . Whereas the pQCD region exhibits a strong rise of  $\sigma_{tot}^{\gamma^*p}$  with increasing  $W^2$ , the total cross-section for real photon-proton scattering  $\sigma_{tot}^{\gamma p}$  shows only a modest rise with  $W^2$ .

The proton structure function  $F_2$  and the total virtual photon-proton ( $\gamma^*p$ ) cross-section  $\sigma_{tot}^{\gamma^*p}$  have been measured in inelastic neutral current scattering,  $e^+p \rightarrow e^+X$ , at HERA in the previously unexplored transition region of non-perturbative to perturbative QCD at low  $Q^2$ . To study this kinematic region, a small electromagnetic Beam Pipe Calorimeter (BPC) has been designed, constructed and installed in the ZEUS experiment in 1995. The accuracy of the measurement of  $F_2$  in this kinematic region relies mainly on a precise energy calibration and detector alignment. An energy calibration with a precision of 0.5% and a detector alignment of 0.5 mm have been achieved.

Results on a measurement of  $F_2$  and  $\sigma_{tot}^{\gamma^*p}$  are obtained for  $0.11 \leq Q^2 \leq 0.65 \text{ GeV}^2$  and  $1.7 \cdot 10^{-6} \leq x \leq 6.0 \cdot 10^{-5}$ , corresponding to a range in the  $\gamma^*p$  center-of-mass energy of  $104 \leq W \leq 251 \text{ GeV}$ .

The results on  $F_2$  and  $\sigma_{tot}^{\gamma^*p}$  indicate a smooth transition between the pQCD region and the photoproduction region. A detailed phenomenological analysis as well as a QCD analysis has been carried out to investigate the limitations of a non-perturbative as well as a perturbative QCD description.

## Zusammenfassung

Ergebnisse aus Messungen der Proton-Strukturfunktion  $F_2$  der beiden HERA Experimente H1 und ZEUS aus dem Jahre 1994 zeigen, daß die perturbative QCD (pQCD) in der Lage ist, den beobachteten starken Anstieg von  $F_2$  für kleine Werte von  $x$  bis hinab zu  $Q^2 = 1.5 \text{ GeV}^2$  zu beschreiben. Während im Bereich der pQCD,  $\sigma_{tot}^{\gamma^*p}$  mit steigendem  $W^2$  stark anwächst, steigt der totale Photoproduktionswirkungsquerschnitt  $\sigma_{tot}^{\gamma p}$  nur schwach mit  $W^2$  an.

Die Proton-Strukturfunktion  $F_2$  und der totale virtuelle Photon-Proton ( $\gamma^*p$ ) Wirkungsquerschnitt  $\sigma_{tot}^{\gamma^*p}$  wurden in dem bisher experimentell nicht untersuchten kinematischen Gebiet des Übergangs von nicht-perturbativer zu perturbativer QCD bei kleinen Werten von  $Q^2$  in der Reaktion  $e^+p \rightarrow e^+X$  bei HERA gemessen. Um dieses kinematische Gebiet zu untersuchen, wurde ein kleines elektromagnetisches Strahlrohrkalorimeter (BPC) entworfen, gebaut und im Jahre 1995 in das ZEUS Experiment installiert. Die Genauigkeit der Messung von  $F_2$  in diesem kinematischen Gebiet hängt hauptsächlich von der Energiekalibration und der Detektorpositionierung ab. Eine Energiekalibration mit einer Genauigkeit von 0.5% und eine Detektorpositionierung von 0.5 mm wurden erreicht.

$F_2$  und  $\sigma_{tot}^{\gamma^*p}$  wurden im Bereich  $0.11 \leq Q^2 \leq 0.65 \text{ GeV}^2$  und  $1.7 \cdot 10^{-6} \leq x \leq 6.0 \cdot 10^{-5}$  gemessen. Dies entspricht einem Bereich der  $\gamma^*p$  Schwerpunktsenergie von  $104 \leq W \leq 251 \text{ GeV}$ .

Die Ergebnisse zu  $F_2$  und  $\sigma_{tot}^{\gamma^*p}$  zeigen einen stetigen Übergang zwischen dem Gebiet der pQCD und der Photoproduktion. Eine detaillierte phänomenologische Untersuchung sowie eine QCD Analyse wurden durchgeführt, um die Grenzen einer nicht-perturbativen sowie einer perturbativen QCD Beschreibung zu untersuchen.

To

my dear wife  
Suzanne

and

my precious son  
Carl

# Contents

<b>1</b>	<b>Introduction</b>	<b>1</b>
<b>2</b>	<b>Theoretical background</b>	<b>5</b>
2.1	Historical review of lepton-nucleon scattering . . . . .	5
2.2	Basic elements of lepton-nucleon scattering . . . . .	8
2.2.1	Kinematic variables . . . . .	8
2.2.2	Cross-sections and Structure Functions . . . . .	10
2.2.3	Naive Quark-Parton model . . . . .	14
2.2.4	QCD and evolution equations . . . . .	16
2.3	Low- $x$ -low- $Q^2$ physics . . . . .	22
2.3.1	Introduction . . . . .	22
2.3.2	Vector Dominance Model . . . . .	22
2.3.3	Regge-phenomenology . . . . .	24
2.3.4	Low- $x$ -low- $Q^2$ models . . . . .	26
2.3.5	Motivation to explore the low- $x$ -low- $Q^2$ region . . . . .	29
2.3.6	DIS experiments . . . . .	29
2.4	Reconstruction of kinematic variables at HERA . . . . .	30
<b>3</b>	<b>HERA</b>	<b>37</b>
3.1	The electron-proton collider HERA . . . . .	37
3.2	HERA parameters in the year 1995 . . . . .	39
<b>4</b>	<b>ZEUS - A Detector for HERA</b>	<b>43</b>
4.1	Overview . . . . .	43
4.2	The uranium calorimeter (UCAL) . . . . .	45
4.3	The central-tracking detector (CTD) . . . . .	46
4.4	The luminosity detector (LUMI) . . . . .	47
4.5	The trigger and data acquisition system . . . . .	48
4.6	Event reconstruction and analysis . . . . .	50
<b>5</b>	<b>The Beam Pipe Calorimeter (BPC)</b>	<b>51</b>
5.1	Introduction . . . . .	51
5.2	Basic concepts in calorimetry . . . . .	53
5.3	Requirements . . . . .	62
5.4	Design and construction . . . . .	68
5.4.1	Geometry . . . . .	68
5.4.2	Overview of the calorimeter design . . . . .	70
5.4.3	Details on the design and construction of the BPC . . . . .	75
5.5	Readout . . . . .	88

5.6	Trigger	88
5.7	Monitoring	90
5.8	Survey	92
<b>6</b>	<b>Monte-Carlo simulation</b>	<b>95</b>
6.1	Introduction	95
6.2	Simulation of the BPC within EGS4	95
6.3	Simulation of the ZEUS detector within MOZART	98
6.4	Basic elements of the simulation of $ep$ physics events	98
6.5	MC event generators and samples	101
<b>7</b>	<b>The 95-running conditions</b>	<b>105</b>
7.1	Trigger configuration and implementation	105
7.2	Radiation dose measurements	109
<b>8</b>	<b>BPC Reconstruction and performance</b>	<b>115</b>
8.1	Introduction	115
8.2	DESY II test-beam measurements	115
8.2.1	Introduction	115
8.2.2	Overview of the experimental setup	116
8.2.3	Electronics and Data Acquisition system	118
8.2.4	Data quality	118
8.3	Position reconstruction	120
8.3.1	Introduction	120
8.3.2	Method	120
8.3.3	Detailed studies on position resolution and bias	125
8.3.4	Determination of the absolute BPC position	130
8.3.5	Comments on the position and polar angle reconstruction	135
8.4	Lateral shower behavior	137
8.4.1	Introduction	137
8.4.2	Lateral shower distribution	138
8.4.3	Details on the shower width reconstruction	142
8.5	Energy reconstruction	146
8.5.1	Introduction	146
8.5.2	Method	146
8.5.3	Calibration	149
8.5.4	Energy resolution and linearity	158
8.6	Reconstruction of time	162
<b>9</b>	<b>Efficiencies and systematics</b>	<b>165</b>
9.1	Introduction	165
9.2	Trigger efficiency	165
9.3	Vertex determination and positron beam tilt	167
9.4	Positron identification	171
9.5	Acceptance and MC sample composition	171
9.6	Radiative corrections	174

<b>10</b>	<b>The Data sample</b>	<b>175</b>
10.1	Introduction	175
10.2	Selection cuts	175
10.3	Effect of selection cuts	183
10.4	Background subtraction	184
10.4.1	Non- $e^+p$ background	185
10.4.2	Photoproduction background	186
<b>11</b>	<b>Extraction of <math>F_2</math> and <math>\sigma_{tot}^{\gamma^*p}</math></b>	<b>189</b>
11.1	Introduction	189
11.2	Bin selection	190
11.3	Determination of $F_2$ and $\sigma_{tot}^{\gamma^*p}$	194
11.3.1	Introduction	194
11.3.2	Treatment of the longitudinal structure function $F_L$	196
11.3.3	Unfolding procedure	197
11.4	Comparison of Data and MC	202
11.5	Evaluation of systematic errors	202
11.6	Presentation of final results on $F_2$ and $\sigma_{tot}^{\gamma^*p}$	206
<b>12</b>	<b>Results</b>	<b>213</b>
12.1	Introduction	213
12.2	Dependence of $F_2$ and $\sigma_{tot}^{\gamma^*p}$ on $x$ , $W^2$ and $Q^2$	214
12.3	Phenomenological analysis	223
12.4	QCD analysis at low $Q^2$	229
12.5	Summary	237
<b>13</b>	<b>Summary and conclusions</b>	<b>239</b>
<b>A</b>	<b>Drawings and pictures on the design and construction of the BPC</b>	<b>241</b>
A.1	Beam pipe	241
A.2	Top and side view of the BPC	244
A.3	ZEUS survey coordinate systems	246
A.4	Pictures of various BPC components	247
A.5	BPC readout system	250
A.6	BPC First-Level Trigger	251
A.7	Location of various BPC readout components	252
<b>B</b>	<b>Summary of off-line selection cuts</b>	<b>253</b>
B.1	BPC $F_2$ analysis	253
B.2	BPC kinematic peak events	253
B.3	BPC elastic QED Compton events	254
B.4	BPC elastic $\rho^0$ events	254

## List of Figures

2.1	Lowest order Feynman diagram describing unpolarized $ep$ scattering . . . . .	9
2.2	Interrelationship between the substructure of the proton and $F_2$ . . . . .	18
2.3	Range of validity for various evolution equations in the $Q^2 - x$ plane . . . . .	21
2.4	Kinematic coverage in the $Q^2 - x$ plane of fixed-target and HERA experiments . . . . .	30
2.5	Schematic of the neutral current $ep$ scattering process . . . . .	31
2.6	Isolines of the primary measured variables . . . . .	33
3.1	Bird's eye view of the DESY laboratory . . . . .	37
3.2	The HERA accelerator complex . . . . .	38
3.3	Integrated luminosity delivered by HERA . . . . .	40
3.4	HERA luminosity operation during 24 hours . . . . .	40
4.1	Cross-section of the ZEUS detector along the beam direction . . . . .	44
4.2	Cross-section of the ZEUS detector perpendicular to the beam direction . . . . .	45
4.3	Layout of a FCAL module . . . . .	46
4.4	Layout of a CTD octant . . . . .	47
4.5	Layout of the luminosity monitor . . . . .	48
4.6	Schematic diagram of the ZEUS trigger and data acquisition system . . . . .	49
4.7	ZEUS off-line and Monte Carlo (MC) programs . . . . .	50
5.1	Schematic description of three methods to study the low $Q^2$ region . . . . .	52
5.2	Low $Q^2$ acceptance at ZEUS . . . . .	53
5.3	Graphical representation of an electromagnetic shower within the BPC . . . . .	56
5.4	Longitudinal shower profile within the BPC . . . . .	58
5.5	Radial shower distribution within the BPC . . . . .	59
5.6	Relative error on $y$ . . . . .	63
5.7	Relative error on $Q^2$ . . . . .	64
5.8	Systematic shifts on $y$ and $Q^2$ . . . . .	65
5.9	Location of the BPC within the ZEUS detector . . . . .	68
5.10	Schematic layout of the BPC and the new beam pipe . . . . .	69
5.11	CAD drawing of both BPC modules . . . . .	70
5.12	Closeup view of both BPC modules . . . . .	71
5.13	Photography of single plate of the BPC North module . . . . .	72
5.14	Photography of a BPC WLS and WLS cassette . . . . .	74
5.15	Side and bottom view of the Hamamatsu R5600-03 miniature PMT . . . . .	76
5.16	Photography of the Hamamatsu R5600-03 miniature PMT . . . . .	77
5.17	Measured gain curve for a typical Hamamatsu R5600-03 miniature PMT . . . . .	78
5.18	Photography of an ARMCO magnetic iron block . . . . .	79
5.19	Setup for scanning the BPC scintillator fingers . . . . .	80
5.20	Scan of a scintillator finger . . . . .	81
5.21	Setup for scanning the BPC WLS . . . . .	82
5.22	Deviation from linearity due to a WLS non-uniformity . . . . .	83
5.23	WLS scanning result . . . . .	84
5.24	Interface between scintillator fingers and WLS . . . . .	85
5.25	Schematic drawing of the LED light distribution system . . . . .	86
5.26	Photography during the BPC assembly . . . . .	87
5.27	Photography of assembled BPC North module . . . . .	87
5.28	Location of TLDs and Si-diodes for the BPC radiation monitoring . . . . .	90
5.29	Schematic drawing to illustrate the BPC $^{60}\text{Co}$ scans . . . . .	92
5.30	Side view of the BPC survey setup. . . . .	93
6.1	Implementation of the BPC design within EGS4 . . . . .	97
6.2	Implementation of the BPC design within GEANT . . . . .	99
6.3	QED radiative corrections . . . . .	100
6.4	Magnitude of radiative corrections . . . . .	101
6.5	Formation of the hadronic final state of the $ep$ scattering process . . . . .	102
7.1	BPC FLT energy and timing spectra . . . . .	106
7.2	BPC FLT FADC calibration . . . . .	107
7.3	Use of the BPC in the 1995 trigger configuration . . . . .	108
7.4	Dose profile measured in front of the BPC North module . . . . .	110
7.5	Measured accumulated dose in the front and back of the BPC modules . . . . .	111
7.6	Results from the $^{60}\text{Co}$ -scans of the BPC North module . . . . .	112
7.7	Scan of scintillator fingers from the BPC North module . . . . .	113
7.8	Scan and fit of radiation damaged scintillator finger . . . . .	114
8.1	Schematic drawing of the DESY II test-beam area 21 . . . . .	116
8.2	Trigger and DAQ setup for the DESY II test-beam experiment . . . . .	118
8.3	Pedestal distributions of the BPC test-beam experiment . . . . .	119
8.4	Schematic drawing of the $X$ -scintillator readout . . . . .	121
8.5	Intrinsic position bias for the linear weighting method . . . . .	122
8.6	Intrinsic position bias for the logarithmic weighting method . . . . .	123
8.7	Optimization of the logarithmic weighting parameter $W_0$ . . . . .	126
8.8	Comparison between different reconstruction methods . . . . .	126
8.9	Intrinsic position bias as a function of the impact position . . . . .	127
8.10	Dependence of the position resolution on the impact position . . . . .	129
8.11	BPC position resolution of 5 GeV electrons from the DESY II test-beam experiment . . . . .	129
8.12	Effects of the position reconstruction at the BPC edge . . . . .	130
8.13	Dependence of the position resolution on the electron energy . . . . .	131
8.14	Dependence of the position resolution on the strip width . . . . .	131
8.15	Lowest order Feynman diagrams describing the QED Compton process . . . . .	132
8.16	Schematic layout of the in-situ position calibration of the BPC . . . . .	133
8.17	Result of the in-situ position calibration of the BPC using QED Compton events . . . . .	134
8.18	Transverse energy leakage of 25 GeV electrons at the BPC edge . . . . .	137
8.19	Parameterization of transverse energy leakage . . . . .	138
8.20	Procedure to correct for transverse energy leakage . . . . .	140
8.21	Dependence of transverse energy correction on the electron impact energy . . . . .	141
8.22	Number of X(Y)-strips included in the determination of the shower width . . . . .	142
8.23	Display of a shower within the BPC and its relation to the shower width . . . . .	143

8.24	Shower width correction procedure	144
8.25	Dependence of the shower width correction procedure on the impact energy	145
8.26	Strip energy distribution around the strip with the maximum energy deposition	146
8.27	Energy uniformity across one scintillator finger	147
8.28	Fiducial volume of the BPC (North module)	148
8.29	Attenuation effect in scintillator fingers from the DESY II test-beam experiment	150
8.30	Relative strip-to-strip calibration procedure	151
8.31	Uniformity of $E_{BPC}$ as a function of $X$ and $Y$	152
8.32	Energy uniformity within the fiducial volume in bins of 8 mm	153
8.33	Selection of kinematic peak events in the BPC region	154
8.34	Determination of the BPC energy scale	155
8.35	Comparison between MC and data for $E_X$ , $E_Y$ and $E_{BPC}$ for KP events	156
8.36	Event display of a typical elastic $\rho^0$ event	157
8.37	Validation of the BPC energy scale using elastic $\rho^0$ events	157
8.38	Linearity of the BPC from the DESY II test-beam experiment	159
8.39	Linearity of the BPC from an EGS4 MC-simulation	159
8.40	Deviation from linearity due to radiation damage	160
8.41	Energy resolution of the BPC from the DESY II test-beam experiment	161
8.42	Energy resolution of the BPC from an EGS4 MC-simulation	161
8.43	Energy resolution of the BPC at the edge	162
8.44	BPC timing distribution	163
9.1	BPC FLT trigger efficiency as a function of run number	165
9.2	BPC FLT trigger efficiency as a function of energy	166
9.3	Comparison of the $Z$ vertex distribution between data and MC	167
9.4	Mean $X$ and $Y$ vertex positions as a function of run number	168
9.5	$X$ and $Y$ position distribution in the LUMIG detector	169
9.6	Efficiency of the positron shower width cut	170
9.7	Fraction of events with $\eta_{MAX} < 1.5$ as a function of $Q^2$ in data	171
9.8	Fraction of events which pass the cut on $\delta = E - P_Z$	172
9.9	Radiative corrections as a function of $y$	173
9.10	Positron and photon scattering angles in FSR and ISR events	174
10.1	BPC timing distribution	177
10.2	BPC fiducial volume cut	178
10.3	Effect of selection cuts	182
10.4	Effect of selection cuts on the $\delta$ and $E_{BPC}$ distributions	183
10.5	Events rejected by various off-line selection cuts	184
10.6	Positron and proton gas events passing off-line selection cuts	185
10.7	Luminosity weighted current ratios for positron-pilot and proton-pilot bunches	186
10.8	$Q^2 - x$ distribution of photoproduction background events	187
10.9	$\delta$ distribution	188
11.1	Resolution of $y$ and $Q^2$	190
11.2	Selected $y-Q^2$ bins	191
11.3	$Q^2$ resolution	192
11.4	$y$ resolution	192
11.5	Migration of $y$ and $Q^2$	193
11.6	Bin quality factors for each $y-Q^2$ bin	194

11.7	Measurement of $R$ at various fixed target experiments	197
11.8	Iterative unfolding of $F_2$	199
11.9	Comparison between different unfolding methods	200
11.10	Comparison of various variables between data and MC	201
11.11	Percent deviation of data and MC distributions	202
11.12	Individual systematic errors as a function of $y$	207
11.13	Individual systematic errors for each $y-Q^2$ bin	208
11.14	$F_2(x, Q^2)$ as a function of $x$ for different $Q^2$ values	210
11.15	$\sigma_{tot}^{\gamma^*p}$ as a function of $W^2$ for different $Q^2$ values	211
12.1	Kinematic coverage in the $Q^2 - x$ plane of fixed-target and HERA experiments	214
12.2	Bjorken plot of $Q^2 \sigma_{tot}^{\gamma^*p}$ as a function of $Q^2$	218
12.3	$F_2$ as a function of $x$	219
12.4	$\sigma_{tot}^{\gamma^*p}$ as a function of $W^2$	220
12.5	$F_2$ as a function of $Q^2$	221
12.6	$\sigma_{tot}^{\gamma^*p}$ as a function of $Q^2$	222
12.7	Extrapolation to the total photoproduction cross-section	224
12.8	$\sigma_T + \epsilon \sigma_L$ and $R_{GVDM}$ as a function of $Q^2$	226
12.9	Comparison of a Regge-fit and a QCD fit to $F_2$	228
12.10	$\lambda_{eff}$ as a function of $Q^2$	229
12.11	$\chi^2$ per degree of freedom of QCD fits at low $Q^2$	232
12.12	Exponents of the gluon and sea quark distribution as a function of $Q_0^2$	233
12.13	Gluon distribution at low $Q^2$	234
12.14	$F_2$ as a function of $Q^2$ for different values of $x$	235
12.15	Comparison of $F_2$ and $F_2^c$ in LO and NLO QCD evolution	236
A.1	Top and side view of the beam pipe	241
A.2	Front view of the beam pipe exit window	242
A.3	Top view of the ZEUS interaction region	243
A.4	CAD drawing of the BPC ( $X - Y$ view)	244
A.5	CAD drawing of the BPC ( $Y - Z$ view)	245
A.6	ZEUS survey coordinate systems	246
A.7	Side view of the BPC North calorimeter stack	247
A.8	Stacking of individual tungsten-scintillator layers	248
A.9	Completed stack of individual tungsten-scintillator layers	248
A.10	View of the assembled BPC North module	249
A.11	View of the assembled BPC North module	249
A.12	Schematic diagram of the BPC trigger and readout system	250
A.13	Schematic diagram of the BPC FLT	251
A.14	Location of various BPC readout components	252

## List of Tables

3.1	HERA parameters . . . . .	39
5.1	Electromagnetic shower quantities based on the approximation B by Rossi . . . . .	58
5.2	BPC performance specifications . . . . .	75
5.3	Results of magnetic field measurements . . . . .	76
5.4	Survey results of the BPC North and South modules in 1995 . . . . .	93
8.1	Parameterization of lateral shower profiles . . . . .	140
8.2	$\chi^2/ndf$ values for $E_X$ and $E_Y$ for all four calibration periods . . . . .	155
11.1	Summary of bin quantities . . . . .	190
11.2	Results on the measurement of $F_2$ and $\sigma_{tot}^{\gamma^*p}$ . . . . .	209
12.1	Extrapolation to the total photoproduction cross-section . . . . .	225
B.1	Off-line selection cuts for the BPC $F_2$ sample . . . . .	253
B.2	Off-line selection cuts for the kinematic peak event sample . . . . .	253
B.3	Off-line selection cuts for the elastic QED Compton event sample . . . . .	254
B.4	Off-line selection cuts for the elastic $\rho^0$ event sample . . . . .	254

## Chapter 1

### Introduction

Our current physical understanding of the world around us is summarized in the *Standard Model*. It consists of three key elements:

- matter consists of the fermions *leptons* and *quarks*,
- the forces acting between them are mediated by *gauge fields* via *gauge bosons* and
- the masses of leptons, quarks and gauge bosons are generated by the *Higgs-mechanism*.

The Standard Model is the synthesis of enormous experimental and theoretical efforts since the beginning of this century. Many of its predictions have been experimentally confirmed with great success. Nevertheless, there are several open questions which are still lacking an experimental verification such as the existence of the Higgs-boson which is postulated by the Higgs-mechanism. The Standard Model does not provide answers to some of the most fundamental questions in science. Why are there exactly three families of leptons and quarks in nature as it was experimentally concluded from very early results at the LEP collider at CERN? Are leptons and quarks really fundamental particles or is there a substructure of leptons and quarks? Is there a deeper symmetry between fermions and bosons in nature, known as supersymmetry? These are only a few of the most challenging questions in the future to be answered by elementary particle physics.

Lepton-nucleon scattering experiments have played an important role in our current understanding of hadronic matter. Early electron-proton scattering experiments at SLAC, followed by a series of fixed-target experiments, established the constituent structure of the proton with the observation of Bjorken scaling and its interpretation within the Quark-Parton model. The later observation of scaling violation contributed to the development of a field theory among quarks and gluons known as Quantum Chromodynamics (QCD) as the theory of strong interaction.

The first electron-proton collider HERA, with its center-of-mass energy of 300 GeV, has allowed to explore the structure of the proton in a new kinematic region compared to previous fixed-target experiments. One of the most interesting and challenging investigations at HERA is to explore the transition region between the domain of non-perturbative and perturbative QCD. The kinematic region of  $Q^2 \geq 1.5 \text{ GeV}^2$  exhibits a strong rise of  $F_2$  with decreasing  $x$  (Bjorken scaling variable) or equivalently of  $\sigma_{tot}^{\gamma^*p}$  with increasing  $W^2$ , the square of the  $\gamma^*p$  center-of-mass energy. Perturbative QCD (pQCD) allows to describe the observed rapid rise of  $F_2$  with decreasing  $x$  down to  $Q^2 = 1.5 \text{ GeV}^2$  as it was concluded from measurements of the proton structure function  $F_2$  at the two HERA experiments H1 and ZEUS in 1994. In the photoproduction region, the total cross-section for real photon-proton scattering  $\sigma_{tot}^{\gamma p}$  shows only

a modest rise with  $W^2$ . This behavior can be well described by models within the framework of non-perturbative QCD such as Regge theory.

In order to study the transition from the photoproduction to the deep-inelastic scattering region, the kinematic coverage of the ZEUS detector was substantially extended in 1995 with the installation of a new Beam Pipe Calorimeter (BPC). The first part of this thesis concerns the design, construction and operation of the BPC, a tungsten-scintillator sampling calorimeter, within the existing ZEUS experiment. The second part focuses on the reconstruction and performance of the BPC. To investigate the transition region, a measurement of the proton structure function  $F_2$  and the total virtual photon-proton ( $\gamma^*p$ ) cross-section  $\sigma_{tot}^{\gamma^*p}$  is presented in the third part of this thesis for momentum transfers between 0.11 and 0.65 GeV<sup>2</sup> from  $e^+p$  scattering at a center-of-mass energy of 300 GeV using the ZEUS detector with the new BPC. This analysis is based on 1.65 pb<sup>-1</sup> of data taken during the 1995 HERA run. The last part of this thesis concerns a detailed discussion on the interpretation of the obtained results on  $F_2$  and  $\sigma_{tot}^{\gamma^*p}$  to gain a deeper insight in this previously unexplored kinematic region. The results on  $F_2$  and  $\sigma_{tot}^{\gamma^*p}$  indicate a smooth transition between the pQCD region and the photoproduction region.

A review of basic theoretical concepts for the description of inelastic lepton-nucleon scattering is presented in chapter one. This includes a discussion on various aspects of the physics related to the transition region such as a brief introduction into the Vector Dominance Model, Regge theory and several models concerning the transition region. These concepts are important for the later discussion on the interpretation of the obtained results. The last section of this chapter focuses on the reconstruction of kinematic variables at HERA whose understanding is necessary for the design of the BPC to be discussed in chapter five.

Chapter three and four will briefly summarize the HERA collider and the ZEUS detector, respectively.

The design and construction of the BPC is the main focus of chapter five starting with a brief discussion on the experimental configuration to achieve a measurement in the transition region followed by a brief overview of basic concepts in calorimetry and a detailed discussion on the requirements of the BPC. Subsequent sections of this chapter will focus on all technical aspects of the BPC such as the actual design and construction, the BPC readout, the BPC trigger, the monitoring system and the survey of the BPC.

Chapter six introduces the Monte Carlo simulation of  $e^+p$  physics events and of the detector performance.

The running conditions of the BPC during the 1995 HERA run are summarized in chapter seven which includes the BPC trigger configuration and implementation into the ZEUS trigger scheme and in particular a detailed discussion on the radiation monitoring of the BPC.

Chapter eight focuses in detail on the second part of this thesis, i.e. on the reconstruction and performance of the BPC including the position and energy reconstruction of the BPC as well as a discussion of the transverse shower behavior.

Various efficiency and systematic aspects which are relevant for the measurement of the proton structure function  $F_2$  are presented in chapter nine.

Chapter ten concerns the data sample for the physics analysis presented in this thesis, i.e. a thorough discussion of all selection criteria followed by a discussion on the background subtraction.

The extraction of the proton structure function  $F_2$  and the total virtual photon-proton cross-section  $\sigma_{tot}^{\gamma^*p}$  is described in chapter eleven, including a detailed discussion on the determination of systematic uncertainties.

Chapter twelve presents an analysis of the obtained results within the transition region by first comparing the results on  $F_2$  and  $\sigma_{tot}^{\gamma^*p}$  to various models. The second and third part of this chapter concerns a phenomenological analysis as well as a QCD analysis to investigate the limitations of a non-perturbative as well as perturbative QCD description.

A summary of this thesis, together with a conclusion drawn from the obtained results, is given in chapter thirteen.

## Chapter 2

### Theoretical background

#### 2.1 Historical review of lepton-nucleon scattering

The experimental investigation of the structure of atoms began at the end of the last century. In 1897 Thomson found in cathode rays a negative charged particle which was later on called the electron [Cl86]. Together with Geiger and Marsden, Rutherford performed an experiment (1909-1911) scattering  $\alpha$ -particles on a thin sheet of gold foil [Cl86]. A small fraction of the incoming  $\alpha$ -particles were scattered through large angles. The interpretation of these results by Rutherford led to the development of an atomic model named after him. According to Rutherford's model, the atom consists of a tiny positively charged nucleus with a radius of less than 30 fm and electrons circulating around the nucleus [Ru11]. This is in contradiction to classical electrodynamics.

The development of quantum mechanics in the 1920's made it possible to understand microscopic phenomena [He44]. The extension of quantum theory including the special theory of relativity led to the formulation of quantum field theory which is the fundamental theoretical basis of today's particle physics.

With the discovery of the neutron by James Chadwick in 1932 [Cl86], it became apparent that the atom consists of protons, neutrons and electrons. Since today, scattering experiments such as the famous scattering experiment by Rutherford are one of the most important experimental techniques to reveal the structure of matter, i.e. the structure of atoms as well as the structure of the nucleus and its constituents. The principle idea of a scattering experiment is to scatter a high energy particle such as a high energy electron on a piece of matter (fixed-target experiment) or on another high energy particle such as a proton (colliding beam experiment). Using the measured angular and energy distribution of the scattered electron, one can infer the structure of the target particle.

The mathematical formulation of the angular distribution for the scattering of  $\alpha$ -particles on a thin sheet of gold foil by Rutherford is based on the assumption of a non-relativistic spinless point-like projectile being scattered on a spin-less point-like heavy target. In 1929, Mott presented a formulation of the angular distribution of relativistic electrons of spin  $\frac{1}{2}$  on a spinless point-like heavy target [Mo29]. The Mott cross-section does not provide a description of the scattering of an electron on a proton since the proton has an anomalous magnetic moment. Furthermore, any possibility for the proton not to be point-like but distributed over a small region in space cannot be described within the framework of Mott's ansatz.

In 1950, Rosenbluth calculated the cross-section for the elastic scattering of a relativistic electron of spin  $\frac{1}{2}$  on a proton of spin  $\frac{1}{2}$  having a finite size and an anomalous magnetic moment [Ro50]. The first experimental evidence for an extended structure of the proton came from an

experiment on elastic electron-proton scattering which was conducted by Hofstadter in the early 1950s at the High Energy Physics Laboratory at Stanford University [Ho53, Ho55, Ho57]. The proton form factor was found to drop sharply with increasing momentum transfer compared to that of a point charge. The radius of the proton was estimated to be  $(0.7 \pm 0.2) \cdot 10^{-13}$  cm. The observation that the proton is not a point-like object verified the prevailing opinion that the proton is a complicated object. The success of this milestone experiment led to the proposal to build SLAC<sup>1</sup>, in order to raise the energy of the electron beam and therefore the available momentum transfer by more than an order of magnitude compared to the first experiments by Hofstadter.

Besides the investigation of matter in scattering experiments, several short-lived hadrons were observed during the 1950s and 1960s in cosmic rays and first accelerator type experiments such as at BNL<sup>2</sup> and at LBL<sup>3</sup>. By 1960, the number of observed hadrons had grown enormously. The need was there to classify the observed hadrons in a scheme similar to the periodic table of elements as introduced by Mendeleev. In 1961, Gell-Mann and Ne'eman proposed independently a classification of observed hadrons known as the *Eightfold Way* based on a SU(3) symmetry with the third component of the isospin  $T_3$  and the hypercharge  $Y$  as the two underlying internal quantum numbers, where  $Y = B + S$  with  $B$  the baryon number and  $S$  the strangeness quantum number [Ge62, Ge64b, Ne61]. The term strangeness was already introduced by Gell-Mann in 1953 to describe hadrons having a rather unusual behavior in their production and decay properties compared to other known hadrons at that time [Ge53]. These particles are produced on a time scale of about  $10^{-23}$  s but decay relatively slowly (about  $10^{-10}$  s). The representation of SU(3) among the observed hadrons leads to baryon and meson octets. Besides a spin  $\frac{1}{2}$  octet, a triangular shaped multiplet (Baryon decuplet) allowed to incorporate ten heavy spin  $\frac{3}{2}$  baryons. At this point, only nine observed heavy spin  $\frac{3}{2}$  baryons found their place in this scheme. The one with a charge  $-1$  and strangeness  $-3$  was missing. Gell-Mann predicted that such a particle should exist in nature. In 1964, this particle,  $\Omega^-$ , was discovered at the Brookhaven Cosmotron [Ba64].

The question which naturally arose from the classification of observed hadrons using SU(3) is why hadrons obey such a symmetry. An understanding of the Eightfold Way was independently given by Gell-Mann and Zweig in 1964, who proposed that hadrons consist of more elementary objects which Gell-Mann named *quarks* [Ge64a, Zw64]. These new objects come in three types known as *flavor* s up (u), down (d) and strange (s) and are spin  $\frac{1}{2}$  particles<sup>4</sup>. Up quarks carry a charge of  $+\frac{2}{3}e$  and down and strange quarks carry a charge of  $-\frac{1}{3}e$  with  $e$  the charge of the proton. This *Quark-Model* contains two dilemmas which needed an explanation. According to the Quark-Model, the  $\Delta^{++}$  resonance consists of three identical u quarks which are spin  $\frac{1}{2}$  particles. This is inconsistent with the Pauli exclusion principle. In 1964, O.W. Greenberg suggested that quarks carry an additional quantum number known as *color* [Gr64]. The composition of hadrons in terms of quarks carrying a certain color is such that all hadrons in nature appear colorless. If hadrons consist of quarks, one should be able to observe free quarks in nature. None of these experiments have given so far an indication for the existence of free quarks in nature. The term to describe the phenomenon of quarks being confined within hadrons is called *quark confinement*.

With the completion of the linear accelerator at SLAC in the late 1960s, a long series of

<sup>1</sup>Stanford Linear Accelerator Center.

<sup>2</sup>Brookhaven National Laboratory.

<sup>3</sup>Lawrence Berkeley Laboratory.

<sup>4</sup>The discovery of three additional quark flavors, known as charm (c), bottom (b) and top (t), contributed enormously to the success of the Quark-Model.

experiments started on deep inelastic electron-proton scattering. These scattering experiments revealed in a much more direct way the assumption that protons have an internal structure [Pa68, Bl69]. In 1964, Drell and Walecka calculated the cross-section for deep-inelastic electron-proton scattering introducing the two structure functions  $W_1$  and  $W_2$  to describe the structure of the proton [Dr64]. The deep-inelastic structure functions  $W_1$  and  $W_2$  were found to hardly vary with the momentum transfer between the incoming electron and the target proton and only depend on the Bjorken scaling variable  $x$ . This result implies that the scattering had to take place from point-like charge centers. This phenomenon is known as scaling. Using current-algebra, Bjorken predicted that a scaling behavior of the deep-inelastic structure functions  $W_1$  and  $W_2$  follows from the scattering of electrons on free point-like objects within a nucleon [Bj67, Bj69a]. Feynman introduced in his parton model a picture to understand the data at SLAC [Fe69]. It assumes the proton to consist of point-like constituents known as partons. The scattering of electrons on protons takes place through the scattering of electrons on partons. The most obvious candidates for the point-like objects within a nucleon were the quarks. This identification had been suggested in 1969 by Bjorken and Paschos [Bj69b].

The gauge theory *Quantum Chromodynamics* (QCD) provides a comprehensive theory of quarks and the gluon field quanta and therefore of strong interactions in general [Fr73, Gr73, We73]. QCD as a non-Abelian gauge theory contains the concept of asymptotic freedom which allowed to understand the quasi-free behavior of partons within nucleons when short distances are being probed. At large distances, the interaction becomes stronger due to the possibility of interactions among gluons themselves characterizing QCD as a non-Abelian gauge theory. This provides a framework to understand the phenomenon of quark confinement. QCD predicts that the scaling behavior of the deep-inelastic structure functions  $W_1$  and  $W_2$  is logarithmically broken. It was a great triumph when the violation of scaling was experimentally observed, e.g. at FNAL<sup>5</sup> in 1974 using a beam of muons incident on a stationary iron target [Fo74].

Since the pioneering deep-inelastic electron-proton scattering experiments at SLAC, several fixed-target experiments have been carried out up until today at SLAC, FNAL and CERN<sup>6</sup> using lepton beams of electrons, muons and neutrinos with higher energies to cover an increasing kinematic region. The square of the center-of-mass energy in a fixed-target experiment is proportional to the lepton beam energy and therefore fixed-target experiments are limited to moderate values in the momentum transfer and the Bjorken scaling variable. In a collider experiment, significantly larger values in the center-of-mass energy are possible since the square of the center-of-mass energy is directly proportional to the product of both beam energies. The electron-proton collider HERA<sup>7</sup> at DESY<sup>8</sup> allows to extend the kinematic coverage towards very large values in the momentum transfer and towards very low values in the Bjorken scaling variable  $x$  by orders of magnitude compared to fixed-target experiments. HERA therefore provides a unique opportunity to study the structure of the proton in a completely new unexplored kinematical region such as the region of very small  $x$  values [Ai96, De96a].

<sup>5</sup>Fermi National Accelerator Laboratory.

<sup>6</sup>Conseil Européen pour la Recherche Nucléaire.

<sup>7</sup>Hadron-Elektron-Ring-Anlage.

<sup>8</sup>Deutsches Elektronen-Synchrotron.

## 2.2 Basic elements of lepton-nucleon scattering

### 2.2.1 Kinematic variables

Throughout the following discussion, the natural system of units is used, i.e.  $\hbar = 1$  and  $c = 1$ . The scattering of unpolarized electrons (positrons) on unpolarized protons, as shown to first order perturbation theory in Figure 2.1, is described through the exchange of a Standard Model electroweak gauge boson:

$$e(k) + P(p) \rightarrow l(k') + X(p') \quad (2.1)$$

with the electron (positron) and proton in the initial state denoted by the four vectors  $k = (E_e; \vec{k}_e)$  and  $p = (E_p; \vec{P})$ , respectively. The final state consists of the scattered lepton  $k' = (E'_l; \vec{k}'_l)$  and the hadronic final state system  $p' = (E_X; \vec{p}'_X)$ .

Depending on the type of the exchanged electroweak gauge boson, one distinguishes two classes of events:

- Neutral Current (NC) (electroweak gauge boson: virtual photon  $\gamma^*$  or  $Z^0$  boson) and
- Charged Current (CC) (electroweak gauge boson:  $W^\pm$  boson) events.

Both event classes can be distinguished by the final state lepton. In the case of NC events an electron (positron) is found in the final state ( $l = e$ ) whereas in the case of CC events the final state system consists of a neutrino (antineutrino) which escapes detection ( $l = \nu_e$ ).

The HERA collider experiments ZEUS and H1 are able to directly measure the energy and direction of both the scattered lepton (in case of NC events only) and the hadronic final state system. Two independent variables are sufficient in defining the unpolarized inelastic  $ep$  event kinematics at fixed beam energies, e.g. in the case of a NC event the energy  $E'_e$  and polar angle  $\theta'_e$  of the scattered electron (positron).

The following variables provide a relativistic-invariant formulation of the unpolarized inelastic  $ep$  event kinematics:

$$s = (k + p)^2 \simeq 4E_e E_p \quad (2.2)$$

$$t = (p - p')^2 \quad (2.3)$$

$$u = (k' - p)^2 \quad (2.4)$$

$$Q^2 = -(k - k')^2 = -(p - p')^2 = -t = -q^2 \quad (2.5)$$

$$x = \frac{Q^2}{2(p \cdot q)} = -\frac{t}{u+s} \quad 0 \leq x \leq 1 \quad (2.6)$$

$$y = \frac{p \cdot q}{p \cdot k} = \frac{u+s}{s} \quad 0 \leq y \leq 1 \quad (2.7)$$

$$W^2 = (p + q)^2 = (p')^2 = m_p^2 + \frac{Q^2}{x}(1-x) = s + t + u \quad (2.8)$$

$$\nu = \frac{p \cdot q}{m_p} \quad (2.9)$$

The electron and proton masses have been neglected in the evaluation of  $s$ .

$Q^2$  is the negative square of the momentum transfer  $q$  and denotes the virtuality of the exchanged gauge boson. The momentum transfer  $q$  determines the size of the wavelength of the

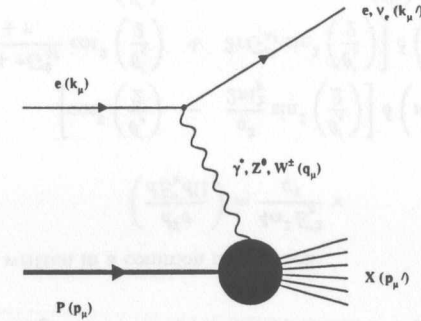


Figure 2.1: Feynman diagram describing unpolarized  $ep$  scattering to lowest order perturbation theory.

virtual boson and therefore the object size  $\Delta$  which can be resolved in the scattering process. To resolve objects of size  $\Delta$  requires the wavelength of the virtual boson  $\lambda$  to be smaller than  $\Delta$ . The wavelength  $\lambda$  of the virtual boson can be written employing the uncertainty principle by Heisenberg as follows:

$$\lambda = \frac{1}{|q|} = \frac{1}{\sqrt{\nu^2 + Q^2}} \approx \frac{2m_p x}{Q^2} \quad (2.10)$$

Better resolution requires smaller wavelengths of the virtual boson and therefore larger momentum transfers. The maximum possible value for  $Q^2$  is given by  $Q_{max}^2 \simeq s$ .

$W^2$  is the square of the invariant mass of the hadronic final state system  $X$ .  $W$  can also be interpreted as the center-of-mass energy of the gauge boson proton system. Small values of  $x$  correspond to large values of the invariant mass  $W$ .

$s$  is the square of the center-of-mass energy of the electron-proton system. With  $E_e = 27.5$  GeV and  $E_p = 820$  GeV, one obtains a center-of-mass energy at HERA of 300 GeV. This is equivalent to a fixed-target experiment with an incident electron beam energy of 48 TeV, since in the fixed-target case  $\sqrt{s} = \sqrt{2m_p E_e}$ .

$x$  is the Bjorken scaling variable and is interpreted in the Quark-Parton Model as the fraction of the proton momentum carried by the struck parton. The limits on  $x$  follow from the fact that the square of the invariant mass  $W^2$  has to be larger or equal to the square of the mass of the proton  $m_p^2$ , i.e.  $W^2 = m_p^2 + (Q^2/x)(1-x) \geq m_p^2$  where  $x = 1$  corresponds to the elastic case for which  $W = m_p$ . In the proton rest frame,  $\nu$  is the energy of the exchanged gauge boson

$$\nu = \frac{p \cdot q}{m_p} = \frac{m_p(E_e - E'_e)}{m_p} = (E_e - E'_e) \quad (2.11)$$

The maximum energy transfer  $\nu_{max}$  is given by  $\nu_{max} = s/(2m_p)$  which amounts to 48 TeV in case of HERA.

$y$  is the fraction of the incoming electron energy carried by the exchanged gauge boson also known as inelasticity in the rest frame of the proton.  $y$  can be also written as  $y = \nu/\nu_{max}$  which yields the limits on  $y$  as given above.

$t$  denotes the momentum transfer at the hadronic vertex. The relativistic invariant variables  $x$ ,  $y$ ,  $Q^2$  and  $s$  are connected through the following relation:

$$Q^2 \simeq s \cdot x \cdot y \quad (2.12)$$

where the electron and proton masses have been ignored. This relation shows that for fixed  $x$  and  $y$ , HERA allows to reach much larger values in  $Q^2$  as well as much lower values in  $x$  keeping  $y$  and  $Q^2$  fixed due to the larger center-of-mass energy  $\sqrt{s}$  compared to fixed-target experiments.

## 2.2.2 Cross-sections and Structure Functions

Long before the formulation of the Quark-Parton model, a formalism was developed to quantitatively describe the structure of a target being probed by a point-like energetic particle. This formulation emerged from the famous Rutherford experiment. The concept of structure functions is one of the main tools to explore the structure of the nucleus in general [Ha84].

In the following, a detailed discussion is presented on the derivation of the inelastic electron-proton cross-section which is the fundamental basis of the HERA structure function measurements.

Figure 2.1 shows the Feynman diagram describing inelastic electron-proton scattering to lowest order perturbation theory. The following discussion will be restricted to the case of NC scattering through a virtual photon as the exchanged gauge boson to lowest order perturbation theory. At low momentum transfers  $Q^2$ , the proton is excited to higher mass states such as the  $\Delta$ -state. For these events, the invariant mass  $W$  is given by  $W \simeq M_\Delta$ . For larger values in  $Q^2$ , the proton breaks up in several hadrons which leads to a smooth distribution in the invariant mass  $W$ .

The four vectors of the electron in the initial and final states are given as follows:  $k = (E_e; \vec{k}_e)$  and  $k' = (E'_e; \vec{k}'_e)$ . Employing Feynman rules to evaluate the Feynman graph in Figure 2.1 to first order perturbation theory considering the photon propagator only, one obtains the following expression for the amplitude  $\mathcal{M}_n$  which describes the scattering of an electron of four momentum  $k$  and polarization  $s$  and a proton of momentum  $p$  and polarization  $\sigma$  into a scattered electron of four momentum  $k'$  and polarization  $s'$  and some unknown hadronic final state  $|n\rangle$ :

$$\mathcal{M}_n = 4\pi\alpha[\bar{u}(k', s')\gamma_\mu u(k, s)] \left(\frac{1}{q^2}\right) [\langle n|J^\mu(0)|p, \sigma\rangle] \quad (2.13)$$

The exchange of the heavy gauge bosons  $Z^0$  and  $W^\pm$  with  $m_{Z^0} = 91.2\text{ GeV}$  and  $m_{W^\pm} = 80.2\text{ GeV}$  respectively, is kinematically suppressed by a term  $Q^4/(Q^2 + M_{Z^0, W^\pm}^2)$  [In87]. The  $\gamma^* - Z^0$  interference term is suppressed by a factor  $Q^2/(Q^2 + M_{Z^0}^2)$  [In87]. At low  $Q^2$ , the single  $\gamma^*$  propagator term is therefore the dominant contribution.

Unlike the electromagnetic current  $\bar{u}(k', s')\gamma_\mu u(k, s)$  which is known from QED, the proton current  $J^\mu(0)$  cannot be calculated at present<sup>9</sup>. The cross-section is determined as follows ignoring the mass of the electron:

$$d\sigma_n = \frac{1}{4\sqrt{(k \cdot p)^2}} \left(\frac{d^3\vec{k}'_e}{(2\pi)^3 2E'_e}\right) \prod_{i=1}^n \left(\frac{d^3\vec{p}'_i}{(2\pi)^3 2E'_i}\right) \times \langle |\mathcal{M}_n|^2 \rangle \cdot (2\pi)^4 \cdot \delta^4(k + p - k' - p') \quad (2.14)$$

where  $p' = \sum_{i=1}^n p'_i$ . Only the inclusive case is being considered, i.e. only the case for which the outgoing electron is measured in contrast to the semi-inclusive scenario in which one hadron is identified and the exclusive case in which all outgoing hadrons are identified. Summing over all

<sup>9</sup>Several attempts in the framework of lattice QCD are undertaken to constrain the proton current [Be97, Gr96].

possible hadronic final states and taking into account that  $d^3\vec{k}'_e = |\vec{k}'_e|^2 d|\vec{k}'_e| d\Omega$  and  $|\vec{k}'_e| = E'_e$ , one obtains:

$$\left(\frac{d^2\sigma}{dE'_e d\Omega}\right) = \frac{\alpha^2 E'_e}{q^4 E_e} L_{\mu\nu} W^{\mu\nu} \quad (2.15)$$

The double differential cross-section is characteristic for the inelastic case in contrast to elastic electron-proton scattering since the invariant mass  $W$  is no longer constrained by  $W = m_p$ . The leptonic tensor  $L_{\mu\nu}$  is given by:

$$L_{\mu\nu} = \frac{1}{2} \text{Tr}(k' \gamma_\mu k \gamma_\nu) = 2(k'_\mu k_\nu + k_\mu k'_\nu + \frac{q^2}{2} g_{\mu\nu}) \quad (2.16)$$

The hadronic tensor  $W^{\mu\nu}$  cannot be calculated from first principles as the leptonic tensor.  $W^{\mu\nu}$  is a second-rank tensor and only depends on the two four-vectors  $p$  and  $q$ . The most general form out of  $p$  and  $q$  is given as follows:

$$W^{\mu\nu} = -W_1 g^{\mu\nu} + \frac{W_2}{m_p^2} p^\mu p^\nu + \frac{W_4}{m_p^2} q^\mu q^\nu + \frac{W_5}{m_p^2} (p^\mu q^\nu + q^\mu p^\nu) \quad (2.17)$$

The scalars  $W_i$  depend on  $q^2$  and  $p \cdot q$ . The expression for  $W^{\mu\nu}$  can be significantly simplified by using current conservation, i.e.  $\partial_\mu J^\mu = 0$  which yields  $q_\mu W^{\mu\nu} = q_\nu W^{\mu\nu} = 0$ .  $W^{\mu\nu}$  can then be written in terms of only two scalar functions  $W_1$  and  $W_2$ :

$$W^{\mu\nu} = \left(-g^{\mu\nu} + \frac{q^\mu q^\nu}{q^2}\right) W_1 + \left(p^\mu - q^\mu \frac{p \cdot q}{q^2}\right) \left(p^\nu - q^\nu \frac{p \cdot q}{q^2}\right) \frac{W_2}{m_p^2} \quad (2.18)$$

With  $L_{\mu\nu}$  and  $W^{\mu\nu}$ , the double-differential cross-section in equation 2.15 can then be written as follows:

$$\left(\frac{d^2\sigma}{dE'_e d\Omega}\right) = \frac{4\alpha^2 E_e'^2}{q^4} \left[ W_2(\nu, q^2) \cos^2\left(\frac{\theta}{2}\right) + 2W_1(\nu, q^2) \sin^2\left(\frac{\theta}{2}\right) \right] \quad (2.19)$$

with  $\nu = (p \cdot q)/m_p$ . Electron-proton scattering can be formulated for three distinct cases [Ha84]:

- elastic  $ep$  scattering assuming the proton to be a Dirac particle (Equation 2.20),
- elastic  $ep$  scattering taking into account the anomalous electric and magnetic moment of the proton (Rosenbluth-formula) (Equation 2.21) and
- inelastic  $ep$  scattering in terms of the structure functions  $W_1(\nu, q^2)$  and  $W_2(\nu, q^2)$  (Equation 2.22)

All three cases can be written in a common description:

$$\left(\frac{d^2\sigma}{dE'_e d\Omega}\right) = \frac{4\alpha^2 E_e'^2}{q^4} \times$$

$$\left[ \cos^2\left(\frac{\theta'_e}{2}\right) - \frac{q^2}{2m_p^2} \sin^2\left(\frac{\theta'_e}{2}\right) \right] \delta\left(\nu + \frac{q^2}{2m_p}\right) \quad (2.20)$$

$$\left[ \frac{G_E^2 + \tau G_M^2}{1 + \tau} \cos^2\left(\frac{\theta'_e}{2}\right) + 2\tau G_M^2 \sin^2\left(\frac{\theta'_e}{2}\right) \right] \delta\left(\nu + \frac{q^2}{2m_p}\right) \quad (2.21)$$

$$\left[ W_2(\nu, q^2) \cos^2\left(\frac{\theta'_e}{2}\right) + 2W_1(\nu, q^2) \sin^2\left(\frac{\theta'_e}{2}\right) \right] \quad (2.22)$$

At small values of  $x$ , i.e. in the kinematic region of HERA, one obtains:

$$\sigma_{tot}^{\gamma^*p} \approx \frac{4\pi^2\alpha}{Q^2} F_2(x, Q^2) \quad (2.38)$$

The expressions for  $\sigma_T$  and  $\sigma_L$  in terms of  $F_1$  and  $F_2$  can be used to express the double-differential cross-section in terms of the total cross-sections  $\sigma_T$  and  $\sigma_L$ :

$$\frac{d^2\sigma}{dydQ^2} = \Gamma \cdot (\sigma_T + \epsilon\sigma_L) = \Gamma \cdot (\sigma_{tot}^{\gamma^*p})_{eff} \quad (2.39)$$

where  $(\sigma_{tot}^{\gamma^*p})_{eff} = \sigma_T + \epsilon\sigma_L$  is called the effective  $\gamma^*p$  cross-section. The photon polarization  $\epsilon$  and the photon flux factor  $\Gamma$  are given by:

$$\epsilon = 2(1-y)/(1+(1-y)^2) \quad (2.40)$$

$$\Gamma = \alpha(1+(1-y)^2)/(2\pi Q^2 y) \quad (2.41)$$

The ratio  $R$  of the longitudinal and transverse cross-section  $R = \sigma_L/\sigma_T = F_L/2xF_1$  can be used to re-write the above expression in the following form:

$$\frac{d^2\sigma}{dydQ^2} = \Gamma \cdot \sigma_T(1 + \epsilon R) \quad (2.42)$$

The proton structure function  $F_2$  is extracted from the differential cross-section  $d^2\sigma/dydQ^2$  over a certain bin size  $(\Delta y, \Delta Q^2)$ . It requires to know  $F_L$  or equivalently the value of  $R$ . The contribution of  $F_L$  to the differential  $ep$  cross-section increases for  $y \rightarrow 1$ . A measurement of  $F_L$  can be achieved by measuring  $d^2\sigma/dxdQ^2$  for fixed values of  $x$  and  $Q^2$  at different values of  $\epsilon$  and therefore for different values of  $y$ . This means, one has to perform a measurement of  $d^2\sigma/dxdQ^2$  at different center-of-mass energies  $\sqrt{s}$  by varying, in case of HERA, the energies of either the electron or the proton beam. An overview of the status of the  $F_L$  measurement at HERA can be found in [Ba95b].

### 2.2.3 Naive Quark-Parton model

As soon as the momentum transfer in an inelastic  $ep$  reaction gets larger, the wavelength with which the proton is going to be examined gets smaller and therefore smaller structures can be resolved (Section 2.2.1). Under the assumption that the proton consists of free point-like objects, one would expect that for large momentum transfers  $Q^2$  the structure functions  $W_1$  and  $W_2$  in equation 2.19 would turn simply into the following form:

$$2W_1^i(\nu, Q^2) = \frac{Q^2}{2m_i^2} \delta\left(\nu - \frac{Q^2}{2m_i}\right) \quad (2.43)$$

$$W_2^i(\nu, Q^2) = \delta\left(\nu - \frac{Q^2}{2m_i}\right) \quad (2.44)$$

which follows from equations 2.20 and 2.22.  $m_i$  is the mass of one of the point-like objects within the proton. One obtains the case for the scattering of an electron on a Dirac particle (Equation 2.20). The structure functions no longer depend on two independent variables, but simply on the scaling variable  $x = Q^2/(2m_p\nu)$  alone. Therefore, if  $Q^2$  gets large, one finds:

$$\begin{aligned} F_1(x, Q^2) &\rightarrow F_1(x) \\ F_2(x, Q^2) &\rightarrow F_2(x) \end{aligned}$$

This is in short the main ingredient of Bjorken scaling of structure functions. This behavior of structure functions in the limit  $Q^2 \rightarrow \infty$ ,  $\nu \rightarrow \infty$  with  $x = Q^2/(2m_p\nu)$  fixed (Bjorken limit) was deduced by Bjorken in 1968 by means of current algebra.

The scaling behavior of structure functions was observed at SLAC just after Bjorken announced his results.

Based on these results, Feynman developed a model (Parton Model) assuming the proton to consist of free point-like constituents called partons. The application of the parton model to evaluate various processes such as inelastic  $ep$  scattering relies on two basic assumptions. In the infinite momentum frame of the proton, one can neglect the masses and transverse momenta of the partons. The momenta of the partons are then given by,  $p_i = \xi_i p$ .  $p$  is the momentum of the proton,  $p_i$  is the momentum of parton  $i$  and  $\xi_i$  is the respective momentum fraction ( $0 \leq \xi_i \leq 1$ ). The parton density of parton  $i$  in the proton is described by means of a parton distribution function  $f_i(\xi_i)$ , where  $f_i(\xi_i)d\xi_i$  denotes the number of partons  $i$  having a momentum fraction between  $\xi_i$  and  $\xi_i + d\xi_i$ . The second assumption concerns the relation between the measurable  $ep$  cross-section and the detailed interaction mechanism, i.e. the electron-parton interaction. The  $ep$  cross-section is written as the incoherent sum of the elastic electron-parton cross-sections weighted by the parton distribution functions  $f_i(\xi_i)$ .

These assumptions can be justified by the following parton model argument [St95]. At a given time, the hadron of momentum  $p$  under consideration consists of a group of virtual partons  $i$  having a momentum  $\xi_i p$ . Let the lifetime of this virtual state in the rest frame of the hadron be  $\tau$ . This lifetime is significantly larger in the center-of-mass system since the hadron undergoes a Lorentz contraction and a time dilation. In the limit of infinite center-of-mass energy, the lifetime of the virtual state will be much larger compared to the collision time, i.e. the time it takes the electron to cross the hadron. The probability to find an additional parton to take as well part in the hard scattering among the incoming electron is suppressed by the geometrical factor  $1/(\pi R^2 Q^2)$  with  $R$  being the radius of the hadron. The parton configuration which the electron sees during the collision is effectively frozen. After the collision, the fragmentation and hadronization takes place among the debris of the hadrons (Section 6.4). This occurs too late to influence the hard scattering process. This provides a qualitative picture to formulate the  $ep$  cross-section as the incoherent elastic scattering of a virtual photon off the partons  $i$  which are characterized by the probability density function  $f_i(\xi_i)$ .

The variable  $\xi_i$  is identical under the above assumptions to the Bjorken scaling variable  $x$ . The momenta  $p'_i$  of the struck parton is given by:  $p'_i = \xi_i p + q$ . Taking the square on both sides and ignoring the parton masses and transverse momenta, one obtains  $\xi_i = Q^2/(2p \cdot q)$  which is identical to the definition of  $x$ , i.e. in the parton model  $\xi_i = x$ . The Bjorken scaling behavior was introduced through the assumption of free point-like objects within the proton. This picture is identical to the parton model and demonstrates that Bjorken scaling follows from the parton model.

The  $ep$  cross-section is given by summing over all contributions of the electron-parton cross-sections which follow from equation 2.22 using the above structure functions  $W_1^i$  and  $W_2^i$  weighted by  $f_i(\xi_i)$ . By comparing the so-obtained expression with the  $ep$  cross-section in equation 2.19, one can write the structure functions  $W_1$  and  $W_2$  as follows:

$$W_1 = \sum_i \int_0^1 \left(\frac{e_i^2}{2m_p}\right) \delta(x - \xi_i) f_i(\xi_i) d\xi_i = \frac{1}{2m_p} \sum_i e_i^2 f_i(x) \quad (2.45)$$

$$W_2 = \sum_i \int_0^1 \left(\frac{-2x^2 m_p}{q^2}\right) e_i^2 \delta(x - \xi_i) f_i(\xi_i) d\xi_i = -\frac{2m_p x^2}{q^2} \sum_i e_i^2 f_i(x) \quad (2.46)$$

where  $\tau = -q^2/(4m_p^2)$ . The electric and magnetic form factors  $G_E^2$  and  $G_M^2$  describe the structure of the proton and therefore the deviation from the assumption that the proton is a Dirac particle. The scalar functions  $W_1$  and  $W_2$  provide a description of the proton structure in the case of inelastic  $ep$  scattering.

The double-differential cross-section is usually expressed in terms of two of the relativistic invariant quantities  $x$ ,  $y$  and  $Q^2$ . Instead of using the structure functions  $W_1$  and  $W_2$ , the structure functions  $F_1$  and  $F_2$  are used which are defined as follows:

$$F_1 = m_p W_1 \quad (2.23)$$

$$F_2 = \nu W_2 \quad (2.24)$$

One obtains the following expression for the Born cross-section in terms of  $y$  and  $Q^2$ :

$$\left(\frac{d^2\sigma}{dydQ^2}\right)_{\text{Born}} = \frac{2\pi\alpha^2 Y_+}{yQ^4} \left(F_2 - \frac{y^2}{Y_+} F_L\right) \quad (2.25)$$

with  $Y_+ = 1 + (1-y)^2$  and  $F_L = F_2 - 2xF_1$  known as the longitudinal structure function whose contribution to the double-differential cross-section starts to become more significant at large values of  $y$ . It can be neglected at very small  $y$  values.

The double-differential cross-section and therefore the event rate increases for  $Q^2 \rightarrow 0$  and  $y \rightarrow 0$ . The kinematic variable  $y$  for very small values of the electron scattering angle with respect to the incoming electron is given by:  $y \approx 1 - E'_e/E_e$  with  $E_e$ , the electron beam energy and  $E'_e$ , the energy of the scattered electron (Section 2.4). The limit  $y \rightarrow 0$  is therefore equivalent to  $E'_e \rightarrow E_e$ . The measured energy distribution of the scattered electron at low  $Q^2$  is expected to exhibit a characteristic peak at the electron beam energy  $E_e$ . This peak is called *kinematic peak* (KP).

Higher order QED corrections lead to additional contributions to the Born cross-section and result in a measured double differential cross-section which is different from the Born cross-section (Section 6.4):

$$\left(\frac{d^2\sigma}{dydQ^2}\right)_{\text{meas}} = \left(\frac{d^2\sigma}{dydQ^2}\right)_{\text{Born}} \cdot [1 + \delta_r(y, Q^2)] \quad (2.26)$$

where  $\delta_r(y, Q^2)$  is the QED radiative correction factor to the Born cross-section. These radiative corrections have to be taken into account in the extraction of the proton structure function  $F_2$  since  $F_2$  is defined with respect to the Born cross-section (Section 11.3.1).

Besides the above expression for the differential  $ep$  cross-section in terms of the structure functions  $F_1$  and  $F_2$ , one can interpret the  $ep$  cross-section as the product of a flux of virtual photons and the total cross-section  $\sigma_{\text{tot}}^{\gamma^*p}$  for the scattering of virtual photons on protons [Dr64, Ha63, Gi72]. This separation is only valid if the lifetime of the virtual photon is large compared to the interaction time [Io69]. This leads to the following requirement on the applicability of this picture:

$$x \ll \frac{\sqrt{1 + \frac{4m_p^2 x^2}{Q^2}}}{2r_p m_p} \quad (2.27)$$

where  $r_p \approx 5\text{GeV}^{-1}$  is the radius of the proton. The cross-section for photons on protons is defined as:

$$\sigma_{\lambda}^{\text{tot}} = \frac{4\pi^2\alpha}{K} \epsilon_{\lambda}^{\mu} \epsilon_{\lambda}^{\nu} W_{\mu\nu} \quad (2.28)$$

where  $K$  is the flux factor and  $\epsilon_{\lambda}^{\mu}$  the polarization vector.  $\lambda$  denotes the helicity state of the photon. In case of real photons,  $K = \nu$  and  $\lambda = \pm 1$  (transverse polarized). To obtain an expression for  $\sigma_{\text{tot}}^{\gamma^*p}$ , one requires to know  $K$  and  $\epsilon_{\lambda}^{\mu}$  for the case of virtual photons. In analogy to the case of massive spin 1 particles, one uses the following expressions:

$$\epsilon_{\pm 1}^{\mu} = \pm \frac{1}{\sqrt{2}}(0; 1, \pm i, 0) \quad \epsilon_0^{\mu} = \pm \frac{1}{\sqrt{Q^2}}(\sqrt{\nu^2 + Q^2}; 0, 0, \nu) \quad (2.29)$$

The flux factor  $K$  for the cross-section of virtual photons is not uniquely defined. Two flux conventions are commonly used which both require that the flux in case of virtual photons approaches the one for real photons in the limit  $Q^2 \rightarrow 0$ , i.e.  $K \rightarrow \nu$ . Gilman chooses  $K$  to be  $K_{\text{Gilman}} = \sqrt{\nu^2 + Q^2}$  [Gi72]. The most popular choice of  $K$  is based on a convention by Hand [Ha63]. It requires the invariant mass of a real and virtual photon respectively, scattered on a proton to be the same, i.e.  $K$  is the energy of a real photon needed to create an equivalent invariant mass for a virtual photon on a proton. One obtains the following expressions for  $W^2$  for real and virtual photons:

$$W^2 = m_p^2 + 2m_p K \quad (2.30)$$

$$W^2 = -Q^2 + m_p^2 + 2m_p \nu \quad (2.31)$$

This yields the following expression for  $K$  based on Hand's convention:

$$K_{\text{Hand}} = \nu - \frac{Q^2}{2m_p} \quad (2.32)$$

With this expression for  $K_{\text{Hand}}$ , the above expressions for the polarization vectors  $\epsilon_{\lambda}^{\mu}$  and equation 2.18, one obtains the following total cross-sections for polarized photons:

$$\sigma_T \equiv \frac{1}{2}(\sigma_+^{\text{tot}} + \sigma_-^{\text{tot}}) = \frac{4\pi^2\alpha}{K} W_1(\nu, q^2) \quad (2.33)$$

$$\sigma_L \equiv \sigma_0^{\text{tot}} = \frac{4\pi^2\alpha}{K} \left[ \left(1 + \frac{\nu^2}{Q^2}\right) W_2(\nu, q^2) - W_1(\nu, q^2) \right] \quad (2.34)$$

The term  $\nu^2/Q^2$  is in case of HERA significantly larger than one. Using the conventional choice of the structure functions  $F_1$  and  $F_2$ , one can express the above two equations in the following form:

$$\sigma_T = \frac{4\pi^2\alpha}{m_p K} F_1 \quad (2.35)$$

$$\sigma_L = \frac{4\pi^2\alpha}{m_p K} \left( \frac{F_2}{2x} - F_1 \right) = \frac{4\pi^2\alpha}{m_p K} \frac{F_L}{2x} \quad (2.36)$$

The last equation motivates to call  $F_L$  the longitudinal structure function.  $F_L$  is bound to be in the range of  $0 \leq F_L \leq F_2$  which follows from the requirement of  $\sigma_T \geq 0$  and  $\sigma_L \geq 0$ . The total virtual-photon proton cross-section is given as follows:

$$\begin{aligned} \sigma_{\text{tot}}^{\gamma^*p} &\equiv \sigma_T + \sigma_L \\ &= \frac{4\pi^2\alpha}{Q^2(1-x)} \frac{Q^2 + 4m_p^2 x^2}{Q^2} \cdot F_2(x, Q^2) \end{aligned} \quad (2.37)$$

and therefore:

$$F_1(x) = \frac{1}{2} \sum_i e_i^2 f_i(x) \quad (2.47)$$

$$F_2(x) = x \sum_i e_i^2 f_i(x) \quad (2.48)$$

where  $e_i$  is the charge of parton  $i$  in units of the proton charge  $e$ . This result reproduces the Bjorken scaling behavior due to the assumption of free point-like constituents within the proton.

$F_1(x)$  and  $F_2(x)$  are related through the Callan-Gross relation [Ca69]:

$$F_2(x) = 2xF_1(x) \quad (2.49)$$

This is a consequence of the parton model ansatz and the treatment of partons as spin  $\frac{1}{2}$  particles. This relation implies that the longitudinal structure function  $F_L$  as well as the longitudinal cross-section  $\sigma_L$  vanish. The Callan-Gross relation has been confirmed as well at SLAC in a restricted kinematic region.

The success of the parton model in explaining the observed scaling phenomenon as well as the confirmation of the Callan-Gross relation led to the identification of the partons with the quarks in Gell-Mann's additive quark model, thus the term Quark-Parton Model (QPM).

If the proton only consisted of charged quarks, the sum of the respective integrated distribution functions  $f_i(x)$  should be equal to unity, i.e.:

$$\int_0^1 dx x \sum_i f_i(x) = 1 \quad (2.50)$$

This sum-rule turned out to be not fulfilled and the experimentally obtained value was approximately given by 0.5 which led to the conclusion that about half of all partons within the proton must be neutral [Ab83]. These partons are the gluons which were directly observed through three-jet events at PETRA in 1979 [Wu84].

Although the QPM was very successful in explaining some of the early  $ep$  results, it does not provide an answer to the problem of quark confinement. The formulation of Quantum Chromodynamics (QCD) as the field theory of strong interaction allows to incorporate the two rather contradicting phenomena of scaling and confinement.

### 2.2.4 QCD and evolution equations

The theory which describes the interaction among quarks was developed at the beginning of the 1970s and is called Quantum Chromodynamics (QCD). It is a local non-Abelian gauge theory based on a  $SU(3)$  gauge group. The gauge bosons are called gluons. The choice of a  $SU(3)$  gauge group in the end goes back to O.W.Greenberg who postulated that quarks carry an additional quantum number known as color with three degrees of freedom known as 'red' (r), 'green' (g) and 'blue' (b) [Gr64]. Three colored quarks of each quark flavor form a triplet whereas eight gluons form an octet<sup>10</sup>. QCD is conceptually very similar to the theory of electromagnetic interaction (QED), since both are based on Yang-Mills fields. However, QED is based on a

<sup>10</sup>The gauge group  $U(3)$  would imply nine gluons. However, experimental results favor the existence of eight gluons which form a *color octet* and exclude a *color singlet* state.

$U(1)$  gauge group whereas QCD is based on a  $SU(3)$  gauge group. This leads to the Abelian structure in case of QED and the non-Abelian structure in case of QCD which implies that gluons can interact among themselves since they are carrier of color charges<sup>11</sup>. This leads to the possibility of having three-gluon as well as four-gluon vertices which is in striking contrast to QED.

The non-Abelian character of QCD through the self-coupling of gluons leads to a fundamental difference in the coupling constant of QCD compared to QED. In QED, the effective charge increases at very small distances whereas in QCD, the color coupling decreases at short distances. Therefore, at sufficiently high energies the quarks inside the proton can be regarded as quasi-free, a behavior which is known as *asymptotic freedom*. Asymptotic freedom within QCD follows quantitatively from the renormalization procedure.

One finds the following expression in leading order for the strong coupling constant  $\alpha_s(Q^2)$ :

$$\alpha_s(Q^2) = \frac{4\pi}{(11 - 2n_f/3) \ln(\frac{Q^2}{\Lambda^2})} \quad (2.51)$$

where  $n_f$  is the number of quark flavors. The free scale parameter,  $\Lambda$ , follows e.g. from a measurement of  $\alpha_s(Q^2)$  which requires a well-defined description of  $\alpha_s(Q^2)$  to obtain a unique value for  $\Lambda$ . At higher orders in perturbation theory,  $\alpha_s(Q^2)$  depends on the renormalization procedure used.  $\Lambda$  has been measured to be 100–300 MeV [Ba96b]. This sets the scale at which the coupling constant  $\alpha_s(Q^2)$  becomes large. For large values of  $Q^2$ ,  $\alpha_s$  decreases logarithmically and perturbative calculations can be performed. This property is called asymptotic freedom. At small values of  $Q^2$  where  $\alpha_s$  gets large, perturbative calculations can no longer be trusted and one enters the region of non-perturbative QCD. This will be discussed in detail in section 2.3.

In summary, asymptotic freedom leads to the observed behavior that at short distances the coupling becomes smaller and the theory appears as a free theory which leads to the observed Bjorken scaling. At large distances the coupling constant becomes larger and quarks are confined due to the strength of the coupling

One of the main successes of QCD is to provide a field theoretical framework which allows an explanation of the two rather contradicting ideas of asymptotic freedom and confinement.

QCD, as discussed so far, modifies the conclusions drawn from the naive Quark-Parton model. The naive Quark-Parton model appears only in the asymptotic limit  $Q^2 \rightarrow \infty$  within the framework of QCD. The modifications to the naive Quark-Parton model result from the dynamics among the quarks via the gluon as the mediating gauge boson. Gluon radiation leads to transverse momentum of the quarks and therefore to the possibility to couple to the longitudinally polarized virtual photon which is probing the proton. Therefore, the longitudinal structure function  $F_L$  will no longer vanish and the Callan-Gross relation is no longer valid.

Figure 2.2 gives a picture of the interrelationship between the substructure of the proton and the functional form expected for  $F_2$ . Gluon radiation leads to a violation of scaling of the structure functions which show a logarithmic dependence on  $Q^2$ . Gluon radiation populates the inside of the proton with an increasing number of gluons as  $Q^2$  increases. These in turn can split into  $q\bar{q}$  pairs which themselves can radiate gluons. The momentum fraction  $x$  of the radiated gluons decreases with each step. Therefore, the proton consists not only of three valence quarks but due to the QCD dynamics also of so-called *sea quarks*. Gluons and sea quarks populate the low  $x$  region. With increasing  $Q^2$ , the resolution increases and therefore the probability that the virtual photon couples to one of the sea quarks. At large values of  $x$ ,

<sup>11</sup>Gluons carry always a combination of a 'color' and an 'anti-color'.

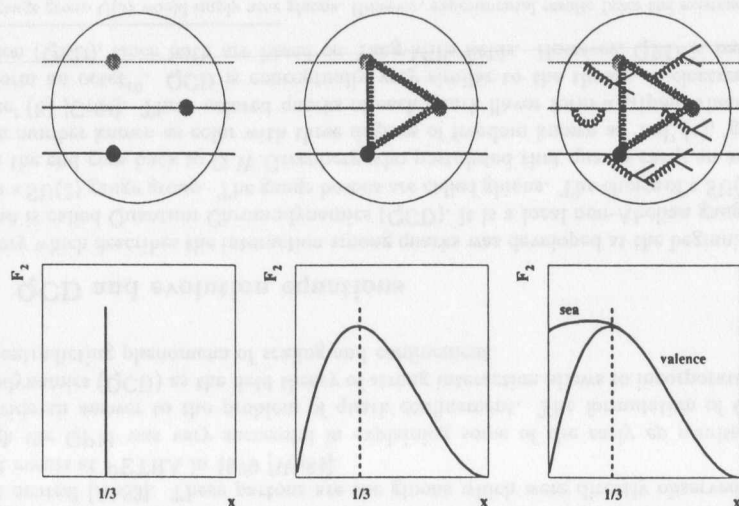


Figure 2.2: Interrelationship between the substructure of the proton and the functional form expected for  $F_2$ : Three valence quarks (left), three bound valence quarks (middle) and valence quarks plus QCD dynamics (right).

where valence quarks dominate the content of  $F_2$ , the quark density is small. At small  $x$ , the quark density is large. Therefore,  $F_2$  is expected to decrease with  $Q^2$  at large values of  $x$ , and increase with  $Q^2$  at small values of  $x$ . For fixed values of  $Q^2$ ,  $F_2$  is expected to increase with smaller  $x$  values due to the significant increase of the quark density. This behavior of  $F_2$ , i.e. the  $F_2$  scaling violation and the rapid rise of  $F_2$  at small  $x$ , has indeed been verified at HERA. The calculation of the inclusive  $ep$  cross-section requires the knowledge of the cross-section for the interaction between the virtual photon and a quark of momentum fraction  $x$  inside the proton as well as the knowledge of the momentum distribution which defines the probability to find a particular quark having a momentum fraction between  $x$  and  $x + dx$ . This approach emerges from the Quark-parton model. The first short distance process can be calculated using perturbative calculations whereas the second long-range process is not calculable within the framework of perturbative QCD (pQCD). This is the physical concept of the QCD factorization theorem. Factorization introduces an additional scale, the factorization scale  $\mu_F$ , to denote the separation into short and long range interactions. By employing the QCD factorization theorem, the structure functions  $F_1$  and  $F_2$  can be expressed in the following form [St95]:

$$F_1^{\gamma^*p} = \sum_{j,f,g} \int_x^1 \frac{dz}{z} C_1^{\gamma^*i} \left( \frac{x}{z}; \frac{Q^2}{\mu_R^2}, \frac{\mu_F^2}{\mu_R^2}; \alpha_S(\mu_R^2) \right) f_{i/p}(z; \mu_F; \mu_R^2) + \mathcal{O}\left(\frac{\Lambda^2}{Q^2}\right) \quad (2.52)$$

$$F_2^{\gamma^*p} = \sum_{j,f,g} \int_x^1 dz C_2^{\gamma^*i} \left( \frac{x}{z}; \frac{Q^2}{\mu_R^2}, \frac{\mu_F^2}{\mu_R^2}; \alpha_S(\mu_R^2) \right) f_{i/p}(z; \mu_F; \mu_R^2) + \mathcal{O}\left(\frac{\Lambda^2}{Q^2}\right) \quad (2.53)$$

where the so called higher twist terms  $\mathcal{O}\left(\frac{\Lambda^2}{Q^2}\right)$  which arise from parton-parton interactions have been neglected. The above expressions therefore consider only the leading twist case which is the

dominant contribution at high  $Q^2$ . The process dependent coefficient functions  $C_j^{\gamma^*i}$  ( $j = 1, 2$ ) denote the short range interactions and are calculable using perturbative QCD (pQCD).  $f_{i/p}$  are the universal, process independent parton distribution functions of the hadron under consideration.  $\mu_F$  denotes the factorization scale, whereas  $\mu_R$  is the renormalization scale. Using these expressions for  $F_1$  and  $F_2$ , one can determine the inclusive  $ep$  cross-section. There exist several renormalization schemes in order to compute  $F_1$  and  $F_2$ . In the DIS scheme, the structure function  $F_2(x, Q^2)$  is simply given by:

$$F_2(x, Q^2) = x \sum_i e_i^2 f_{i/p}(x, Q^2) \quad (2.54)$$

The parton distribution functions  $f_{i/p}(x, Q^2)$  cannot be calculated within the framework of pQCD and have to be determined experimentally. However, knowing  $f_{i/p}(x, Q_0^2)$  at a particular value  $Q_0^2$  within the range of applicability of pQCD, allows the determination of  $f_{i/p}(x, Q^2)$  and therefore  $F_2$  at any other value of  $Q^2$ . This increases the predictive power of pQCD enormously. This procedure is called the evolution of structure functions.

The evolution in  $Q^2$  follows from a set of integro-differential equations known as the DGLAP equations [Al77, Gr72]. Both  $F_1$  and  $F_2$  are measurable quantities and therefore cannot depend on the choice of the factorization scale  $\mu_F$ . Therefore, requiring that  $\mu_F^2 (dF_i(x, Q^2)/d\mu_F^2) = 0$  ( $i = 1, 2$ ), one obtains the DGLAP equations.

The DGLAP equations can be written in its most general form as follows:

$$\frac{df_i(x, Q^2)}{d \ln Q^2} = \frac{\alpha_s(Q^2)}{2\pi} \sum_{j=-n_f}^{n_f} \int_x^1 \frac{dz}{z} P_{ij} \left( \frac{x}{z} \right) f_j(z, Q^2) \quad (2.55)$$

$f_j(x, Q^2)$  are the parton density distributions and  $P_{ij}(x/z)$  are the QCD splitting functions. The splitting functions can be interpreted as the probability for finding a parton of type  $i$  with momentum fraction  $x$  which originated from a parton  $j$  having a momentum fraction  $z$ .  $n_f$  is the number of flavors.  $f_{j>0}$  are the quark distribution functions  $q_j(x, Q^2)$ ,  $f_{j<0}$  are the anti-quark distribution functions  $\bar{q}_j(x, Q^2)$  and  $f_{j=0}$  is the gluon distribution function  $g(x, Q^2)$ . The above equation represents a set of  $2n_f + 1$  coupled integro-differential equations. These equations can be simplified for the evolution of flavor singlet and flavor non-singlet quark distributions. The singlet distribution is given by:  $\Sigma(x, Q^2) = \sum_{i=1}^{n_f} [q_i(x, Q^2) + \bar{q}_i(x, Q^2)]$  which gives rise to the following evolution equations:

$$\frac{d\Sigma(x, Q^2)}{d \ln Q^2} = \frac{\alpha_s(Q^2)}{2\pi} \int_x^1 \frac{dz}{z} \left[ P_{qq} \left( \frac{x}{z} \right) \Sigma(z, Q^2) + P_{gg} \left( \frac{x}{z} \right) g(z, Q^2) \right] \quad (2.56)$$

$$\frac{dg(x, Q^2)}{d \ln Q^2} = \frac{\alpha_s(Q^2)}{2\pi} \int_x^1 \frac{dz}{z} \left[ P_{gq} \left( \frac{x}{z} \right) \Sigma(z, Q^2) + P_{gg} \left( \frac{x}{z} \right) g(z, Q^2) \right] \quad (2.57)$$

$$(2.58)$$

The non-singlet distributions,  $q_i^-(x, Q^2) = q_i(x, Q^2) - \bar{q}_i(x, Q^2)$  and  $q_i^+(x, Q^2) = q_i(x, Q^2) + \bar{q}_i(x, Q^2) - (1/n_f)\Sigma(x, Q^2)$  evolve as follows, independently of the gluon distribution:

$$\frac{dq_i^\pm(x, Q^2)}{d \ln Q^2} = \frac{\alpha_s(Q^2)}{2\pi} \int_x^1 \frac{dz}{z} \left[ P_\pm \left( \frac{x}{z} \right) q_i^\pm(z, Q^2) \right] \quad (2.59)$$

The splitting functions are presently calculated up to next-to-leading order. Expressions for the splitting functions  $P_{ij}$  and  $P_\pm$  in NLO can be found in [Gu80, Fu82].

The quark and gluon distributions are expressed in terms of singlet and non-singlet distributions which are then evolved using the above equations (Section 12.4).

The range of validity for the DGLAP equations is given by:

$$\alpha_s(Q^2) \ln(Q^2) \sim \mathcal{O}(1) \quad \alpha_s(Q^2) \ln \frac{1}{x} \ll 1 \quad (2.60)$$

The  $Q^2$  dependence of the proton structure function  $F_2$  can be written in the following form:

$$\frac{dF_2(x, Q^2)}{d \ln Q^2} = \frac{\alpha_s(Q^2)}{2\pi} \left[ \int_x^1 \frac{dz}{z} \frac{x}{z} P_{qq}(x/z) F_2(z, Q^2) + 2 \sum_q e_q^2 \int_x^1 \frac{dz}{z} \frac{x}{z} P_{qg}(x/z) z g(z, Q^2) \right] \quad (2.61)$$

The Prytz LO method [Pr93] allows to extract the gluon density directly from a measurement of  $F_2$  which follows from the last equation by ignoring the contributions of quarks since the gluon density is expected to be the dominant contribution at low  $x$ :

$$\frac{dF_2(x, Q^2)}{d \ln Q^2} \approx \frac{5\alpha_s(Q^2)}{9\pi} \frac{2}{3} x g(2x, Q^2) \quad (2.62)$$

In the derivation of the DGLAP equations, only terms of the form  $\alpha_s^n \cdot (\ln Q^2)^n$  are kept and summed to all orders which give the dominant contribution at large  $x$  and large  $Q^2$ . This approximation is known as the *leading logarithmic approximation (LLA)*. At small values of  $x$ , terms containing  $\ln \frac{1}{x}$  are no longer negligible. The Double Logarithmic Approximation (DLA) provides for moderate values in  $x$ , i.e. for  $\alpha_s(Q^2) \ln Q^2 \ll 1$ ,  $\alpha_s(Q^2) \ln \frac{1}{x} \ll 1$  and  $\alpha_s(Q^2) \ln Q^2 \ln \frac{1}{x} \sim \mathcal{O}(1)$ , a scheme to include leading terms  $\ln \frac{1}{x}$  accompanied by leading terms  $\ln Q^2$ .

Within the DLA approximation, one can determine the small  $x$  behavior of the gluon distribution function:

$$xg(x, Q^2) \sim \exp \sqrt{\left[ \frac{48}{11 - \frac{2}{3}n_f} \ln \left( \frac{\ln \frac{Q^2}{\Lambda^2}}{\ln \frac{Q_0^2}{\Lambda^2}} \right) \ln \frac{1}{x} \right]} \quad (2.63)$$

where  $Q_0^2$  is the starting scale for the evolution in  $Q^2$ . This behavior is numerically compatible with a power-like behavior of  $x^{-0.4}$  [Le97].

The DGLAP evolution equations allow only to determine the  $Q^2$  dependence of the parton densities but not their  $x$  dependence. The BFKL evolution equation provides an evolution in  $x$  for fixed values of  $Q^2$  [Ba78]. Whereas in the DLA approximation only leading terms  $\ln \frac{1}{x}$  which are accompanied by leading terms  $\ln Q^2$  are summed, the BFKL evolution scheme provides a way to sum up all leading terms  $\ln \frac{1}{x}$ . With  $xg(x, Q^2) = \int_0^{Q^2} (dk_T^2/k_T^2) f_g(x, k_T^2)$ , the BFKL equation is given as follows [As94a]:

$$-x \frac{\partial f_g(x, k_T^2)}{\partial x} = 3 \frac{\alpha_s}{\pi} k_T^2 \int_0^\infty \frac{dk_T'^2}{k_T'^2} \left[ \frac{f_g(x, k_T'^2) - f_g(x, k_T^2)}{|k_T'^2 - k_T^2|} + \frac{f_g(x, k_T^2)}{\sqrt{4k_T'^4 + k_T^4}} \right] \equiv K \otimes f_g \quad (2.64)$$

where  $K$  is the BFKL kernel. The BFKL equation only refers to the gluon distribution. It provides an evolution in  $x$  at fixed  $Q^2$  with a certain starting distribution at  $x_0$ . The solution of the BFKL equation is dominated by the largest eigenvalue  $\lambda$  of the kernel  $K$ . This leads to a characteristic  $Q^2$  and  $x$  dependence for  $F_2(x, Q^2)$  [As94b]:

$$F_2(x, Q^2) \sim (Q^2)^{1/2} x^{-\lambda} \quad \lambda = \frac{3\alpha_s}{\pi} 4 \ln 2 \quad (2.65)$$

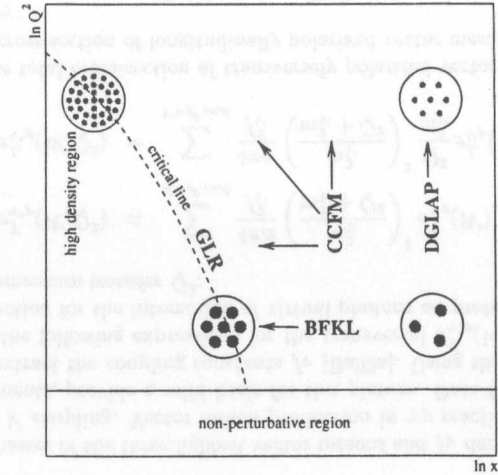


Figure 2.3: Range of validity for various evolution equations. Increasing  $Q^2$  leads to a better spatial resolution (DGLAP). Smaller values in  $x$  yield an increase in the parton density (BFKL). The region of high parton density is the region where saturation effects are expected to diminish the rise of  $F_2$  with decreasing  $x$ .

The range of applicability is as follows:

$$\alpha_s \ln(Q^2) \ll 1 \quad \alpha_s \ln \frac{1}{x} = \mathcal{O}(1) \quad (2.66)$$

The BFKL power law behavior leads to a violation of unitarity in the limit  $x \rightarrow 0$ . The rise of  $F_2$  through the rise of the gluon distribution at small values of  $x$  and therefore in  $\sigma_{tot}^{\gamma^*p}$  is limited by the Froissart bound [Fr61]:

$$\sigma_{tot}^{\gamma^*p} \leq \frac{\pi}{m_\pi^2} (\ln \frac{s}{s_0})^2 \quad (2.67)$$

where  $m_\pi$  is the mass of the pion and  $s_0$  is an unknown scale factor.

It is therefore expected that the rise of  $F_2$  and  $\sigma_{tot}^{\gamma^*p}$  with decreasing  $x$  is limited. At small values in  $x$ , the density of quarks and gluons increases drastically and quarks and gluons start to overlap. Two competitive processes, the annihilation and recombination of gluons, at high parton densities will eventually limit the increase in the number of quarks and gluons. Recombination effects become important at  $xg(x, Q^2) \sim r_p^2/r_g^2$  where  $r_p \sim 1 \text{ fm} \sim 5 \text{ GeV}^{-1}$  and  $r_g \sim 2/Q$ . This yields  $xg(x, Q^2) \simeq 6Q^2$  which is well outside the scope of HERA and could be only reached at much smaller values in  $x$  [Le97]. However, in the *hot spot* picture the size of  $r_p$  can be significantly smaller if one assumes that saturation effects start to occur in a small localized region (hot spot) within the proton [Mu90]. So far, no evidence has been seen at HERA for this effect.

Recombination effects can be included in the BFKL equation through non-linear terms which lead to the GLR equation [Gr81]:

$$-x \frac{\partial f_g(x, k_T^2)}{\partial x} = K \otimes f_g - \frac{81\alpha_s^2(k_T^2)}{16R^2 k_T^2} [xg(x, k_T^2)]^2 \quad (2.68)$$

The inclusive measurement of  $F_2$  at HERA has shown that the evolution of structure functions through the DGLAP evolution equations are in good agreement with experimental results. Up until now it has not been possible to discriminate between the DGLAP evolution and the BFKL equation (Section 12.2). It has been suggested that differences in the DGLAP and the BFKL evolution equations could show up in exclusive measurements such as in high  $p_t$  forward jets [Mu90] and in the forward energy flow [Kw94].

Attempts have been made to achieve a unified BFKL/DGLAP description [Kw97]. Evolution equations which allow an evolution in  $Q^2$  as well as in  $x$  to provide a prescription for the parton distribution functions in both  $x$  and  $Q^2$  are considered in the framework of the CCFM evolution equations [Ca90]. The domain of the various evolution equations is illustrated in Figure 2.3.

## 2.3 Low- $x$ -low- $Q^2$ physics

### 2.3.1 Introduction

Approaching from the region of perturbative QCD the region of non-perturbative QCD, i.e.  $Q^2 \rightarrow 0$  results in several constraints on the structure functions  $F_1$  and  $F_2$  which every parameterization has to fulfill in order to connect these two regions [Ba96a].

The hadronic tensor  $W_{\mu\nu}$  can be written in the following form using the definition for  $F_1$  and  $F_2$ :

$$W_{\mu\nu} = -\frac{F_1}{m_p} g_{\mu\nu} + \frac{F_2}{m_p} \frac{p^\mu p^\nu}{m_p(p \cdot q)} + \left[ \frac{F_1}{m_p} + \frac{F_2 p \cdot q}{m_p} \right] \frac{q^\mu q^\nu}{q^2} - \frac{F_2 q^\mu p^\nu + p^\mu q^\nu}{m_p q^2} \quad (2.69)$$

For  $Q^2 \rightarrow 0$ ,  $W_{\mu\nu}$  exhibits two singularities which have to be absorbed within  $F_1$  and  $F_2$  which therefore yield tight constraints on the behavior of  $F_1$  and  $F_2$  approaching the photoproduction limit. One imposes the following constraints:

$$F_2 = \mathcal{O}(Q^2) \quad F_1 - F_2 \frac{1}{2x} = \mathcal{O}(Q^2) \quad (2.70)$$

where  $(p \cdot q) = -q^2/2x$ . The proton structure function  $F_2$  has to vanish linearly in  $Q^2$  whereas the longitudinal structure function  $F_L = F_2 - 2xF_1$  has to vanish like  $Q^4$  for  $Q^2 \rightarrow 0$ . The latter condition is equivalent to the fact that  $\sigma_L \rightarrow 0$  for  $Q^2 \rightarrow 0$  since real photons are only transversally polarized. Therefore,  $\sigma_T \rightarrow \sigma_{tot}^{\gamma p}$  for  $Q^2 \rightarrow 0$ . Using the definition for  $\sigma_{tot}^{\gamma p}$  one finds:

$$\sigma_{tot}^{\gamma p} = \lim_{Q^2 \rightarrow 0} \left[ \frac{4\pi^2\alpha}{Q^2} F_2(x, Q^2) \right] \quad (2.71)$$

For  $Q^2 \rightarrow 0$ , pQCD can no longer be used and other, non-perturbative, concepts have to be considered. The following two sections provide a brief overview of two well-known non-perturbative concepts, the *Vector Dominance Model (VDM)* [Sa60] and *Regge theory* [Co70]. Both concepts are used in a variety of *phenomenological models* to provide a description of the transition region from the photoproduction to the deep-inelastic scattering region, i.e. from non-perturbative to perturbative QCD (Chapter 12).

### 2.3.2 Vector Dominance Model

It is a well-known experimental fact that photon-proton type interactions exhibit clear similarities compared to pure hadron-hadron type interactions. Such a behavior can be understood

through the assumption that the photon has a dual nature in the sense that it appears as a superposition of a bare photon as well as a hadronic component:

$$|\gamma\rangle = |\gamma\rangle_{bare} + |\gamma\rangle_{hadronic} \quad (2.72)$$

The uncertainty principle allows the bare photon to fluctuate into a  $q\bar{q}$  pair with the same quantum numbers as the bare photon, i.e.  $J^{PC} = 1^{--}$  and  $Q = B = S = 0$  which are the quantum numbers of the three lightest vector mesons:  $\rho^0$ ,  $\omega$  and  $\phi$ . If the fluctuation time  $\tau_f$  into a  $q\bar{q}$  pair is large compared to the interaction time, a photon-proton interaction is expected to show the characteristics of a hadronic-type interaction. The fluctuation time can be estimated on the basis of the uncertainty principle [Le97]. The energy difference between the  $q\bar{q}$  pairs, i.e. vector mesons of mass  $m_V$  having the same momentum  $\nu$  as the real bare photon and the energy  $\nu$  of the real bare photon itself is given by:  $\Delta E = (m_V^2 + \nu^2)^{1/2} - \nu$ . Using  $\tau_f \sim 1/\Delta E$  one obtains for high energy photons, i.e.  $\nu \gg m_V$  in case of  $Q^2 = 0$ :

$$\tau_f(Q^2 = 0) \approx \frac{2\nu}{m_V^2} \quad (2.73)$$

For  $Q^2 \neq 0$ , one receives:

$$\tau_f(Q^2 \neq 0) \approx \frac{2\nu}{m_V^2 + Q^2} \quad (2.74)$$

At low values of  $x$  one finds that  $\tau_f(Q^2 \neq 0) \approx 1/(2m_p x)$  [Ab95], i.e. at small values of  $x$  a photon even of very high virtuality  $Q^2$ , is able to fluctuate into a  $q\bar{q}$  pair and interact as such with the incoming proton.

The quantitative realization of this picture goes back to Sakurai [Sa60]. The vector dominance model (VDM) rests on the assumption that a photon-hadron reaction proceeds via the interaction of the hadronic photon component  $|\gamma\rangle_{hadronic}$  with the hadron only. The hadronic component within the VDM ansatz is given as the sum over the three lightest vector mesons:

$$|\gamma\rangle_{hadronic} \propto \sum_{V=\rho^0, \omega, \phi} \frac{1}{f_V} \left( \frac{m_V^2}{m_V^2 + Q^2} \right) |V\rangle \quad (2.75)$$

where  $m_V$  are the masses of the three lightest vector mesons and  $f_V$  denotes the corresponding strength of the  $\gamma - V$  coupling. Vector meson production in  $\gamma p$  reactions, as well as in  $e^+e^-$  annihilation experiments, provide a solid basis for this picture. Data from these experiments have been used to extract the coupling constants  $f_V$  [Ba92a]. Using this ansatz for  $|\gamma\rangle_{hadronic}$ , one can determine the following expressions for the transversal  $\sigma_{\gamma^* p}^T(W, Q^2)$  and longitudinal  $\sigma_{\gamma^* p}^L(W, Q^2)$  cross-section for the interaction of virtual photons on protons at a center-of-mass energy  $W$  and a momentum transfer  $Q^2$ :

$$\sigma_{\gamma^* p}^T(W, Q^2) = \sum_{V=\rho^0, \omega, \phi} \frac{4\pi\alpha}{f_V^2} \left( \frac{m_V^2}{m_V^2 + Q^2} \right)^2 \sigma_{Vp}^T(W) \quad (2.76)$$

$$\sigma_{\gamma^* p}^L(W, Q^2) = \sum_{V=\rho^0, \omega, \phi} \frac{4\pi\alpha}{f_V^2} \left( \frac{m_V^2}{m_V^2 + Q^2} \right)^2 \frac{Q^2}{m_V^2} \sigma_{Vp}^L(W) \quad (2.77)$$

where  $\sigma_{Vp}^T(W)$  is the total cross-section of transversely polarized vector mesons on protons at  $Q^2 = 0$ . The total cross-section of longitudinally polarized vector mesons  $\sigma_{Vp}^L(W)$  on protons at  $Q^2 = 0$  is given by:

$$\sigma_{Vp}^L(W) = \xi_V \cdot \sigma_{Vp}^T(W) \quad (2.78)$$

The factor  $\xi_V$  is introduced to account for the fact that the total transverse cross-section  $\sigma_{Vp}^T(W)$  need not be the same as the total longitudinal cross-section  $\sigma_{Vp}^L(W)$ .  $\xi_V$  is expected to be within  $0 \leq \xi_V \leq 1$  [Ba92a].

The ratio  $R$  of the total longitudinal to the total transversal  $\gamma^*p$  cross-section is given as follows:

$$R = \frac{\sigma_{\gamma^*p}^L(W, Q^2)}{\sigma_{\gamma^*p}^T(W, Q^2)} = \xi_V \frac{Q^2}{m_V^2} \quad (2.79)$$

Using the above expressions for  $\sigma_{\gamma^*p}^T(W, Q^2)$  and  $\sigma_{\gamma^*p}^L(W, Q^2)$ , one obtains a VDM representation of the proton structure function  $F_2$  (Equation 2.37).

The VDM approach, including only the three lightest vector mesons, is not able to account for various constraints coming from inelastic  $ep$  scattering. In an extension of the VDM approach, all higher mass states are included which is known as the generalized vector dominance model (GVDM) [Sa72]. The total transverse cross-section  $\sigma_{\gamma^*p}^T(W^2, Q^2)$  and the total longitudinal cross-section  $\sigma_{\gamma^*p}^L(W^2, Q^2)$  are written in the following form:

$$\sigma_{\gamma^*p}^T(W^2, Q^2) = \int_{m_0^2} dm^2 \frac{\rho_T(W^2, m^2) m^4}{(m^2 + Q^2)^2} \quad (2.80)$$

$$\sigma_{\gamma^*p}^L(W^2, Q^2) = \int_{m_0^2} dm^2 \frac{\xi \rho_T(W^2, m^2) m^4 Q^2}{(m^2 + Q^2)^2 m^2} \quad (2.81)$$

taking into account the diagonal approximation of the transverse photon absorption cross-section.  $\rho_T(W^2, m^2)$  is the spectral weight-function. It is proportional to the product of the cross-section describing the annihilation of  $e^+e^-$  pairs into a vector meson state of mass  $m$  and the hadronic cross-section of this state of mass  $m$  and a nucleon:  $\rho_T(W^2, m^2) = (1/4\pi^2\alpha)\sigma_{e^+e^-}(m^2)\sigma_{\text{hadr}}(W^2, m^2)$ . For  $\rho_T(W^2, m^2) = \sum_V 4\pi\alpha/f_V^2 \delta(m^2 - m_V^2) \cdot \sigma_{Vp}^T(W)$ , one obtains the VDM case as given in equations 2.76 and 2.77.

### 2.3.3 Regge-phenomenology

Long before the formulation of QCD as the microscopic theory of strong interactions, Regge theory had been successfully used to describe the phenomenology of hadron dynamics of two-particle scattering processes. Regge theory allows to estimate characteristic features of the behavior of hadronic type interactions in the high energy limit. The region of large values in  $W$  (equivalent to the small  $x$  region) accessible at HERA corresponds to the high energy limit within the Regge approach and motivates why Regge theory is still of significant interest in particular for the transition region. This is as well reflected by various low  $x$ -low  $Q^2$  models (Section 2.3.4) employing Regge theory.

Even before the advent of Regge theory, the one-particle exchange model was developed to provide an attempt in the description of strong interactions of two-particle scattering processes. Within this framework, the exchange of one particle in the  $t$  channel with spin  $j$  ( $j > 1$ ) yields a scattering amplitude which is proportional to  $s^j$ . The total cross-section would therefore rise with  $s$  like  $\sigma_{\text{tot}} \sim s^{2(j-1)}$  which would violate the Froissart bound and therefore unitarity. Regge theory provides a scheme to avoid such difficulties by including multiple particle exchanges in the two-particle scattering process instead of a single particle exchange.

In the following, only the basic steps of the Regge approach are outlined. An introduction into this field can be found in [Co70]. The foundation of Regge theory rests on general properties of the S-matrix, unitarity and analyticity. The scattering amplitude  $\mathcal{A}(s, t)$  of a two-particle

scattering process using a decomposition into partial waves is given as follows:

$$\mathcal{A}(s, t) = \sum_{j=0}^{\infty} (2j+1) a_j(t) P_j(z) \quad (2.82)$$

where  $z = \cos \theta_t = 1 - 2s/(t - 4m_j^2)$ . The partial wave amplitude  $a_j(t)$  of a resonance contribution which corresponds to a particular exchanged particle of mass  $m_j$ , decay width  $\Gamma_j(t)$  and spin  $j$  can be viewed as a propagator like term and is given as follows:

$$a_j(t) = \frac{\Gamma_j(t)}{t - m_j^2} \quad (2.83)$$

All possible exchanged particles line up on a linear trajectory called *Regge trajectory* or *Reggeon* in a plot of the spin  $j$  versus the corresponding mass  $m_j^2$  (Chew-Frautschi plot). Each trajectory can be parameterized by a linear function  $\alpha(t)$ , i.e.  $j = \alpha(m_j^2)$ . The main idea of the Regge approach is to evaluate the scattering amplitude  $\mathcal{A}(s, t)$  taking into account all particles which correspond to a particular trajectory through an analytical continuation of the scattering amplitude into the complex angular momentum plane. The sum over exchanged particles is transformed into an integral by means of the Sommerfeld-Watson transformation:

$$\mathcal{A}(s, t) = \frac{1}{2i} \int_C dj (2j+1) \frac{\Gamma_j(t)}{(t - m_j^2)} \frac{e^{i\pi j} \pm 1}{2} \frac{P_j(z)}{\sin(\pi j)} \quad (2.84)$$

Using the parameterization  $\alpha(t)$  for the Regge trajectory, one can formulate the partial wave amplitude  $a_j(t)$  as  $a_j(t) = (\Gamma_j(t) d\alpha(t)/dt) / (\alpha(t) - j)$ . Choosing a suitable path  $C$  in the complex angular momentum plane, the above integral is simply given by the residue of the poles at  $\alpha(t) = j$  (*Regge poles*) employing Cauchy's theorem:

$$\mathcal{A}(s, t) = -\pi \frac{e^{i\pi\alpha(t)} \pm 1}{2 \sin(\pi\alpha(t))} (2\alpha(t) + 1) \Gamma_{\alpha(t)} \frac{d\alpha(t)}{dt} P_{\alpha(t)}(z) \quad (2.85)$$

Using the asymptotic expression of the Legendre polynomial  $P_{\alpha(t)}(z)$  for  $|t| \ll s$  yields  $P_{\alpha(t)}(z) \approx e^{-i\pi\alpha(t)} \cdot (s/s_0)^{\alpha(t)}$ . In the high energy limit (*Regge limit*),  $s \rightarrow \infty$ , the scattering amplitude is then given as follows:

$$\mathcal{A}(s, t) = \beta(t) \cdot \left(\frac{s}{s_0}\right)^{\alpha(t)} \quad (2.86)$$

Via the optical theorem  $\sigma_{\text{tot}} = \frac{1}{s} \text{Im} \mathcal{A}(s, t=0)$ , one obtains the total cross-section:

$$\sigma_{\text{tot}} \propto s^{\alpha(t=0)-1} \quad (2.87)$$

The region of small values in  $x$  which is equivalent to the high-energy limit ( $s \gg Q^2$ ), is defined to be the Regge limit.

The intercept of the Regge trajectory for  $\rho, \omega, \dots$  exchange is approximately given by  $\alpha(t=0) \approx 0.5$ . The total cross-section is then proportional to  $s^{-0.5}$  and decreases with increasing energy  $s$ . Unitarity is therefore conserved.

Measurements of the total cross-section of hadronic interactions have shown that  $\sigma_{\text{tot}}$  slowly rises towards higher energies ( $W > 10 \text{ GeV}$ ). Such a behavior cannot be generated by any of the known trajectories since  $\alpha(t=0) < 1$ . One therefore postulated the existence of a new trajectory (*Pomeranchuk trajectory*) with the leading Regge pole called *Pomeron* with

$\alpha(t=0) \geq 1$  which yields the observed rise of the total cross-section at high energies. The Pomeron is not an observed particle but simply a mathematical construct which followed from the high energy limit in the Regge approach to account for the observed rise of the total cross-section. It must have the quantum numbers of the vacuum, i.e.  $J^{PC} = 0^{++}$ .

The behavior of the total hadron-hadron and  $\gamma p$  cross-sections show a slow rise with the square of the center-of-mass energy  $W^2$  which can be described by a pomeron trajectory with  $\alpha_p^{(soft)}(t) = 1.08 + 0.25t$  [Do92]. This pomeron is usually referred to as the *soft* or *non-perturbative pomeron*. One therefore expects the cross-section to behave like  $\sigma_{tot}^{\gamma p} \propto (W^2)^{\alpha_p(0)-1} = (W^2)^{0.08}$ .

In contrast to the behavior of the total  $\gamma p$  cross-section, the total  $\gamma^* p$  cross-section shows a steep rise with  $W^2$  for  $Q^2 > 1.5 \text{ GeV}^2$  based on the 1994  $F_2$  results at HERA [De96a, Ai96]. Such a behavior can be taken into account with a pomeron intercept significantly larger than 1.08 which one assumes for the case of the soft pomeron. The intercept gets larger for larger values of  $Q^2$ . Such a behavior at large  $W^2$  or small values in  $x$  is expected since the slope of the proton structure  $F_2$  is found to increase with increasing values in  $Q^2$  due to the smaller wavelength of the virtual photon probing the proton at small  $x$ , i.e. at high parton density. This pomeron is usually referred to as the *hard* or *perturbative pomeron*. In the language of Pomeron exchange, one expects the pomeron behavior to change from being hard into soft when going from large to small values of  $Q^2$ . In summary, the Reggeon, which denotes a particular Regge trajectory, accounts for the decrease of the total cross-section at small energies above the resonance region. This behavior turns around at higher energies and exhibits a rise of the total cross-section which can be taken into account by introducing the Pomeranchuk trajectory.

Introducing the Pomeranchuk trajectory leads to a violation of unitarity at very high energies. Therefore, some mechanism must exist which eventually diminishes the rise of the total cross-section at very high energies (Section 2.2.4, hot spot picture).

So far, it is not understood how the Pomeron can be explained in terms of known Standard model particles. Due to the fact that the Pomeron is expected to be a colorless object, in some models it is considered to be composed of two gluons [Ab96].

### 2.3.4 Low- $x$ -low- $Q^2$ models

The following section provides a brief overview of current models for the low  $x$ -low  $Q^2$  region. A more detailed overview can be found in [Ba96a, Le97].

#### Donnachie, Landshoff - DL

Donnachie and Landshoff showed that Regge theory provides a successful description of all total cross-sections for  $pp$ ,  $p\bar{p}$ ,  $\pi^\pm p$ ,  $K^\pm p$  and  $\gamma p$  scattering [Do92]. They fitted the total cross-sections to the sum of two powers:

$$\sigma_{tot} = X s^\epsilon + Y s^{-\eta} \quad (2.88)$$

where the first term accounts for the Pomeron exchange and the second term for the exchange of a conventional trajectory ( $\rho, \omega, \dots$ ), i.e. a Reggeon. In case of the total  $\gamma p$  cross-section the above parameterization together with  $X = 0.0677 \text{ mb}$ ,  $\epsilon = 0.0808$ ,  $Y = 0.129 \text{ mb}$  and  $\eta = 0.4525$  provides a good description of  $\sigma_{tot}^{\gamma p}$  measured at HERA [De94, Ai95]. A similar analysis has been presented by Cudell et al. [Cu96], who determined the Pomeron intercept to be  $1.096^{+0.012}_{-0.009}$  instead of 1.0808 which was obtained by Donnachie and Landshoff.

This Regge ansatz was extended to virtual photons to investigate the contribution of non-perturbative mechanisms at larger values in  $Q^2$  [Do94]. The proton structure function is

parameterized in terms of valence and sea quarks with a  $x$  dependence like  $x^{0.56}(1-x)^3$  and  $x^{-0.08}(1-x)^5$ , respectively. These contributions are weighted by factors of the form  $Q^2/(Q^2 + m_v^2)$  and  $Q^2/(Q^2 + m_s^2)$  respectively, to ensure that  $F_2$  vanishes like  $Q^2$  in the limit  $Q^2 \rightarrow 0$ . The valence quark term accounts for the Reggeon contribution whereas the sea quark term accounts for the Pomeron contribution. The parameters in the fit are constrained such that for  $Q^2 \rightarrow 0$  one retrieves the value for the  $\sigma_{tot}^{\gamma p}$  measurement.

This ansatz does not provide by construction a description for all values in  $Q^2$  but is rather meant as a way to investigate the range of validity of the simple soft pomeron picture starting from  $Q^2 = 0$  towards  $Q^2 = 10 \text{ GeV}^2$  which is the fitted range in  $Q^2$ . The authors remark that 'If the HERA experiments find results for  $F_2$  significantly larger at small  $x$  than our extrapolations, we claim that this will be a clear signal that they have discovered new physics'. This will be discussed in chapter 12.

#### Capella, Kaidalov, Merino, Tran-Thanh-Van - CKMT

Within the framework of conventional Regge theory, Capella et al. presented a common description of  $\sigma_{tot}^{\gamma p}$  and  $F_2$  for  $0 \leq Q^2 \leq 5 \text{ GeV}^2$  [Ca94]. This description is then used as an initial condition for a pQCD evolution. They use in their Regge theory motivated ansatz one bare pomeron with an intercept  $1 + \Delta(Q^2)$  which interpolates between the effective soft pomeron and the effective hard pomeron. The authors provide the following simple parameterization of  $F_2$  for  $0 \leq Q^2 \leq 5 \text{ GeV}^2$ :

$$F_2(x, Q^2) = Ax^{-\Delta(Q^2)}(1-x)^{n(Q^2)+4} \left( \frac{Q^2}{Q^2+a} \right)^{1+\Delta(Q^2)} + Bx^{1-\alpha_R}(1-x)^{n(Q^2)} \left( \frac{Q^2}{Q^2+b} \right)^{\alpha_R} \quad (2.89)$$

The first term accounts for the Pomeron contribution with the  $Q^2$  dependent intercept given by  $\Delta(Q^2) = \Delta_0(1 + \frac{Q^2}{Q_0^2+d})$ . The second term corresponds to the Reggeon contribution at  $x \rightarrow 0$ . The behavior of  $F_2$  for  $x \rightarrow 1$  is given by the second factor in each term with  $n(Q^2)$  parameterized as  $n(Q^2) = \frac{3}{2}(1 + \frac{Q^2}{Q_0^2+c})$ .

#### Abramowicz, Levin, Levy, Maor - ALLM

The proposed parameterization which is based on a Regge motivated ansatz including pQCD expectations at high  $Q^2$ , allows to parameterize  $F_2$  over the whole phase space in  $Q^2$  and  $x$  at the expense of introducing 23 free parameters to be determined from a fit to experimental data [Ab90, Ab97].  $F_2$  is decomposed in two terms describing the contribution from Reggeon and Pomeron exchange:

$$F_2 = F_2^R + F_2^P \quad (2.90)$$

Each term is represented by

$$F_2^i = \frac{Q^2}{Q^2 + m_0^2} C_i(t) x_i^{a_i(t)} (1-x)^{b_i(t)} \quad (2.91)$$

with  $\frac{1}{x_i} = 1 + \left( \frac{W^2 - m_p^2}{Q^2 + m_i^2} \right)$  and  $t = \ln \left( \frac{\ln \frac{Q^2 + Q_0^2}{\Lambda^2}}{\ln \frac{Q_0^2}{\Lambda^2}} \right)$ .  $C_R, b_R, a_R$  and  $b_P$  are assumed to be of the form  $p(t) = p_1 + (p_1 - p_2)t^{p_3}$  and  $C_P, a_P$  of  $p(t) = p_1 + (p_1 - p_2) \left( \frac{1}{1+t^{p_3}} - 1 \right)$ .

### Schildknecht, Spiesberger, - *ScSp*

A formulation of  $F_2$  in the framework of the generalized vector dominance model is presented by providing explicit expressions for  $\sigma_T$  and  $\sigma_L$  [Sc97a]. Using  $F_2 = \frac{Q^2}{4\pi^2\alpha}(\sigma_T + \sigma_L)$  the following expression for  $F_2$  is obtained:

$$F_2(W^2, Q^2 \gg m_0^2) = \frac{N}{4\pi^2\alpha} \left( \ln \frac{1}{ax} \right) \left[ 1 + \xi \left( \ln \frac{Q^2}{m_0^2} - 1 - \frac{1}{6} \frac{3 \ln^2(\frac{Q^2}{m_0^2}) + \pi^2}{\ln(\frac{1}{ax})} \right) \right] \quad (2.92)$$

where  $N = 1.48$ ,  $m_0^2 = 0.89 \text{ GeV}^2$ ,  $\xi = 0.171$  and  $a = 15.1$ . These parameters were obtained from fits to H1 and ZEUS data in the range of  $Q^2 < 350 \text{ GeV}^2$ .

The authors remark that refinements to their GVDM ansatz following an old idea [Sa72] are necessary such as the treatment of the charm contribution to  $F_2$  and the low energy behavior of photoproduction.

### Badelek, Kwiecinski - *BK*

$F_2$  is represented using the generalized vector dominance model [Ba90]. The three lightest vector mesons are summed explicitly whereas the contribution of all higher mass vector meson states with  $m_V^2 > Q_0^2$  are determined by the structure function  $F_2^{AS}$  in the large  $Q^2$  region and is assumed to be given.  $F_2(x, Q^2)$  is then given as the sum of a vector meson part and a partonic part:

$$\begin{aligned} F_2(x, Q^2) &= F_2^V(x, Q^2) + F_2^{par}(x, Q^2) \\ &= \frac{Q^2}{4\pi} \sum_{V=\rho^0, \omega, \phi} \left( \frac{m_V^4 \sigma_V(W^2)}{\gamma_V^2(Q^2 + m_V^2)^2} \right) + \left( \frac{Q^2}{Q^2 + Q_0^2} \right) F_2^{AS}(\bar{x}, Q^2 + Q_0^2) \end{aligned} \quad (2.93)$$

where  $\bar{x} = (Q^2 + Q_0^2)/(s + Q^2 - m_p^2 + Q_0^2)$ . The value of  $Q_0^2$  is chosen such that  $Q_0^2 > (m_V^2)_{max}$ , where  $(m_V)_{max}$  is the mass of the heaviest vector meson included in the sum of light vector mesons ( $Q_0^2 = 1.2 \text{ GeV}^2$ ). The authors stress that apart from  $Q_0^2$  which is constrained by physical requirements, the proposed representation of  $F_2$  does not contain any free parameters apart from those included in  $F_2^{AS}$ .

### Adel, Barreiro, Ynduráin - *ABY*

A parameterization for  $F_2$  at small  $x$  is presented extending a high  $Q^2$  QCD-inspired ansatz into the low  $Q^2$  region [Ad96a]. The assumption is made that at low values of  $Q^2$   $F_2$  can be written in terms of a soft as well as a hard component. The evolution of  $\alpha_s$  is modified such that it saturates at a finite value when going to low values of  $Q^2$ . The proposed description of  $F_2$  is given as follows:

$$F_2(x, Q^2) = \langle e_q^2 \rangle \left[ B_{ns} \tilde{\alpha}_s(Q^2)^{-(1-\rho_0)} x^{\rho_0} + B_s \tilde{\alpha}_s(Q^2)^{-(1+\lambda_0)} x^{-\lambda_0} + C \frac{Q^2}{Q^2 + \Lambda_{eff}^2} \right] \quad (2.94)$$

### Glück, Reya, Vogt - *GRV*

Purely QCD based  $F_2$  parameterizations such as the global fit analysis performed by MRS and CTEQ start with a certain functional form for the quark and gluon distributions. These are then evolved using the DGLAP evolution equations with a starting scale  $Q_0^2 = 3 - 5 \text{ GeV}^2$ .

In contrast, the approach taken by Glück, Reya and Vogt is very different from those of conventional QCD analyses [G194]. The assumption is made that at a very low starting scale of  $Q_0^2 = 0.34 \text{ GeV}^2$ , the nucleon consists entirely of valence-like quarks and gluons. The parton distributions are then evolved using a next-to-leading order (NLO) DGLAP calculation. The observed rise of  $F_2$  with decreasing  $x$  is generated dynamically which appears very close to the starting scale.  $\alpha_s$  is very large in this region which is subject to some debate. It was shown that including charm quark mass effects provides a more successful prediction rather than massless charm evolutions. The ansatz taken by GRV describes the rapid rise of  $F_2$  with decreasing  $x$  down to  $Q^2 = 1.5 \text{ GeV}^2$  reasonably well based on the  $F_2$  measurements at HERA. The most recent parameterization is denoted by *GRV94*.

### 2.3.5 Motivation to explore the low- $x$ -low- $Q^2$ region

In 1994, the H1 [Ai96] and ZEUS [De96a] collaborations extended the measurement of  $F_2$  down to  $Q^2$  values of  $1.5 \text{ GeV}^2$ . One of the most interesting features of those data is the persistence of the rapid rise of  $F_2$  with decreasing  $x$  to the lowest  $Q^2$ . The perturbative QCD (pQCD) predictions of Glück, Reya and Vogt (GRV) (Section 2.3.4) are in broad agreement with this observation. At fixed  $Q^2$ , the rapid rise of  $F_2$  with decreasing  $x$  is equivalent to a rapid rise of the total virtual-photon proton cross-section,  $\sigma_{tot}^{\gamma^*p}$ , with the  $\gamma^*p$  center-of-mass energy  $W$  ( $W^2 \approx Q^2/x$  in this kinematic regime). In contrast to the  $W$  dependence of  $\sigma_{tot}^{\gamma^*p}$ , the total cross-section for real photon-proton scattering (photoproduction, with  $Q^2 = 0$ ) shows only a modest rise with  $W$ , consistent with the energy behavior of the total  $p\bar{p}$  cross-section. Regge theory (Section 2.3.3) has been used successfully by, e.g., Donnachie and Landshoff (DL) (Section 2.3.4) to describe the energy dependence of the total cross-section for hadron-hadron scattering and real photon-proton scattering. However, their prediction for virtual photon-proton scattering fails to describe the data for  $Q^2 \geq 1.5 \text{ GeV}^2$ . At high  $W$ ,  $\sigma_{tot}^{\gamma^*p}$  can be described by a power law behavior,  $\sigma_{tot}^{\gamma^*p} \propto W^{2\lambda}$ . For  $Q^2 \geq 1.5 \text{ GeV}^2$ , the power  $\lambda$  is between 0.15 and 0.35.

A transition between the domain of non-perturbative QCD ('soft') and perturbative QCD ('hard') is therefore expected. The investigation of this transition region by measuring the proton structure function  $F_2$  and the total virtual-photon proton cross-section  $\sigma_{tot}^{\gamma^*p}$  respectively, is the main motivation of this thesis as briefly outlined in the introduction.

### 2.3.6 DIS experiments

Figure 2.4 shows the kinematic coverage in the  $Q^2 - x$  plane for fixed-target experiments (NMC, BCDMS, E665, SLAC, CCFR) and the range covered by the HERA experiments H1 and ZEUS in 1993 and 1994.

Fixed-target experiments in various laboratories (SLAC, FNAL and CERN) were carried out with a variety of lepton beams ( $e, \mu$ , and  $\nu$ ) on a stationary target.

The SLAC experiments concentrated on structure function measurements using an electron beam of 2.65 GeV to 20 GeV on a hydrogen and deuterium target.

Using a muon beam of 100, 120, 200 and 280 GeV on a hydrogen target, the BCDMS (Bologna, CERN, Dubna, Munich, Saclay) collaboration investigated the region of  $0.06 < x < 0.8$  and  $7.0 < Q^2 < 260 \text{ GeV}^2$ . The NMC (New Muon Collaboration) experiment at CERN explored the scattering of muons of 90 GeV to 280 GeV on a liquid hydrogen target. The kinematic range covered amounts to  $0.006 < x < 0.6$  and  $0.5 < Q^2 < 55 \text{ GeV}^2$ .

The E665 collaboration at FNAL took data using 400 to 500 GeV muons using liquid hydrogen and deuterium targets. An extension of the fixed-target kinematic region down to 0.0008 in  $x$

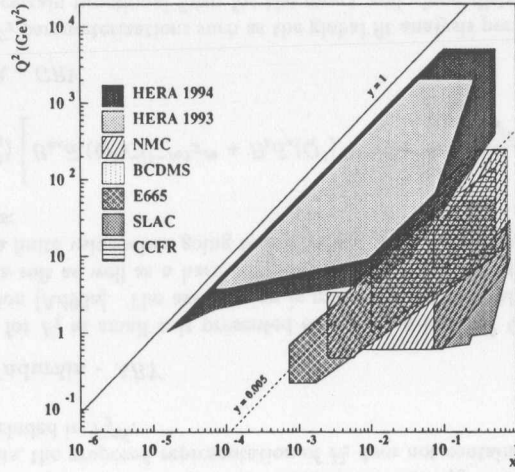


Figure 2.4: Kinematic coverage in the  $Q^2 - x$  plane for various fixed-target experiments and the HERA collider experiments H1 and ZEUS as of 1994.

and  $0.23 \text{ GeV}^2$  in  $Q^2$  was possible. A neutrino beam of  $30 < E_\nu < 600 \text{ GeV}$  on an iron target is used in the CCFR experiment at FNAL which allowed a measurement of structure functions as low as 0.01 in  $x$ .

The HERA experiments provided a drastic increase of the available kinematic region by almost two orders of magnitude in  $x$  and  $Q^2$  due to the much larger center-of-mass energy at HERA compared to the fixed-target experiments. The region of very small values in  $x$  ( $10^{-6} < x < 10^{-4}$ ) and  $Q^2$  ( $Q^2 < 1.5 \text{ GeV}^2$ ) has not been covered by any experiment before 1994. A measurement of the proton structure function  $F_2$  at H1 and ZEUS with an upgrade of both detectors in 1995 allowed to investigate this unexplored region which was referred to in the last sections as the transition region.

## 2.4 Reconstruction of kinematic variables at HERA

The accurate reconstruction of the Lorentz-invariant variables  $x$ ,  $y$  and  $Q^2$  is one of the major ingredients in measuring  $F_2(x, Q^2)$  and  $\sigma_{tot}^{\gamma^*p}$ . The final state in NC  $eP \rightarrow eX$  scattering consists of the scattered electron and the hadronic final state system  $X$ . Both systems alone or any combination among them can be used to reconstruct the event kinematics. Aiming at a precision measurement of  $F_2(x, Q^2)$  and  $\sigma_{tot}^{\gamma^*p}$  at low  $Q^2$ , places tight constraints on the reconstruction of the kinematic variables  $x$ ,  $y$  and  $Q^2$ , on the choice of the kinematic reconstruction methods and therefore on the measurable quantities. This then defines the requirements of an experimental configuration with which a measurement of  $F_2(x, Q^2)$  and  $\sigma_{tot}^{\gamma^*p}$  with high precision at low  $Q^2$  can be achieved. It is therefore of vital importance to obtain a solid understanding of kinematic reconstruction methods before discussing the requirements on the experimental device to perform a measurement at low  $Q^2$  (Chapter 5). The main emphasis in the following discussion will be placed on the region of low  $Q^2$ .

Figure 2.5 shows, to lowest order perturbation theory, the  $ep$  process with the final state electron

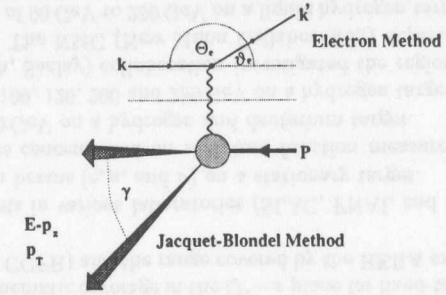


Figure 2.5: Schematic of the neutral current  $ep$  scattering process with the final state electron and the hadronic final state.

scattered under a polar angle  $\theta'_e$  having an energy  $E'_e$ . The hadronic final state consists of the current jet under the angle  $\gamma$  and the proton remnant jet which, in the Quark-Parton Model, originate from the fragmentation of the struck quark and the proton remnant, respectively. In the ZEUS coordinate system (Section 4.1), the four vectors of the initial and final state of the process  $e(k) + P(p) \rightarrow e(k') + X(p')$  are given as follows:

$$k = \begin{pmatrix} E_e \\ 0 \\ 0 \\ -E_e \end{pmatrix} \quad k' = \begin{pmatrix} E'_e \\ E'_e \sin \theta'_e \cos \phi'_e \\ E'_e \sin \theta'_e \sin \phi'_e \\ E'_e \cos \theta'_e \end{pmatrix} \quad p = \begin{pmatrix} E_P \\ 0 \\ 0 \\ E_P \end{pmatrix} \quad p' = \begin{pmatrix} \sum_h E_h \\ \sum_h p_{X,h} \\ \sum_h p_{Y,h} \\ \sum_h p_{Z,h} \end{pmatrix} \quad (2.95)$$

where  $E'_e$ ,  $\theta'_e$  and  $\phi'_e$  are the energy, polar angle and azimuthal angle of the scattered electron and  $\sum_h E_h$  and  $(\sum_h p_{X,h}, \sum_h p_{Y,h}, \sum_h p_{Z,h})$  are the energy and momentum of the hadronic final state system  $X$  which requires a summation over all hadronic final state particles  $h$ .

The following provides an overview of various reconstruction methods including a comparison of these methods to perform an inclusive measurement at low  $Q^2$ .

### Electron Method

The Electron method is the prime method in  $ep$  scattering experiments to reconstruct the event kinematics. This method relies solely on the final state electron. It is therefore applicable to NC events only. Using the above four vectors for the initial and final state electron,  $k$  and  $k'$ , the kinematic variables  $x$ ,  $y$  and  $Q^2$  in terms of  $E'_e$  and  $\theta'_e$  yield the following expressions:

$$x_e = \frac{Q_e^2}{s y_e} = \frac{E'_e \cos^2 \frac{\theta'_e}{2}}{E_p (1 - \frac{E'_e}{E_e} \sin^2 \frac{\theta'_e}{2})} \quad (2.96)$$

$$y_e = 1 - \frac{E'_e}{2E_e} (1 - \cos \theta'_e) = 1 - \frac{E'_e}{E_e} \sin^2 \frac{\theta'_e}{2} \quad (2.97)$$

$$Q_e^2 = 2E_e E'_e (1 + \cos \theta'_e) = 4E_e E'_e \cos^2 \frac{\theta'_e}{2} = \frac{p_{T,e}^2}{1 - y_e} \quad (2.98)$$

These expressions can be used to plot  $Q^2$  as a function of  $x$  keeping either  $E'_e$  or  $\theta'_e$  fixed. This is essential in order to understand which values in  $E'_e$  and  $\theta'_e$  correspond to which region in the

$$\cos \gamma = \frac{p_{T,h}^2 - (E - p_Z)_h^2}{p_{T,h}^2 + (E + p_Z)_h^2} \quad (2.108)$$

In the Naive Quark-Parton model, the energy  $F$  and the polar angle  $\gamma$  correspond to the energy and polar angle of the struck quark. The angle  $\gamma$  can therefore be associated with the angle of the current jet.

Using the above formulas, the kinematic variables can then be re-written in terms of  $F$  and  $\gamma$ :

$$y_{JB} = \frac{F(1 - \cos \gamma)}{2E_e} \quad (2.109)$$

$$Q_{JB}^2 = \frac{F^2 \sin^2 \gamma}{1 - y_{JB}} \quad (2.110)$$

These expressions can be used in the same manner as for the Electron method to plot  $Q^2$  as a function of  $x$  keeping either  $F$  or  $\gamma$  fixed:

$$Q^2(x, \gamma) = \frac{sx}{1 + \left(\frac{E_e}{xE_p}\right) \cot^2(\gamma/2)} \quad (2.111)$$

$$Q^2(x, F) = \frac{sx(1 - \frac{F}{xE_p})}{1 - \left(\frac{E_e}{xE_p}\right)} \quad (2.112)$$

Figure 2.6 shows isolines of constant energy  $F$  (c) and constant polar angle  $\gamma$  (d) as well as lines of constant  $y$  values (1, 0.1, 0.01).

For  $Q^2 < 1 \text{ GeV}^2$  and  $x < 10^{-4}$ , the polar angle  $\gamma$  is well above  $160^\circ$  and reaches quickly the detector acceptance limits for  $y \rightarrow 1$ . The energy  $F$  is in this region well below the electron beam energy of  $27.5 \text{ GeV}$ . For  $Q^2 < 1 \text{ GeV}^2$  and  $x > 10^{-4}$ , the angle  $\gamma$  is larger compared to  $x < 10^{-4}$  which avoids the problem of reaching the detector acceptance limits. The energy  $F$  remains below  $27.5 \text{ GeV}$  for  $x < E_e/E_p$ .

The above expressions for  $F$  and  $\gamma$  can be used as well to determine the dependencies of the kinematic variables on the measured quantities  $F$  and  $\gamma$ . The relative errors of the kinematic variables are given as follows:

$$\left(\frac{\delta x_{JB}}{x_{JB}}\right) = \left(\frac{1}{1 - y_{JB}}\right) \frac{\delta F}{F} \oplus \left[2 \cot \gamma + \left(\frac{2y_{JB} - 1}{1 - y_{JB}}\right) \cot\left(\frac{\gamma}{2}\right)\right] \delta \gamma \quad (2.113)$$

$$\left(\frac{\delta y_{JB}}{y_{JB}}\right) = \frac{\delta F}{F} \oplus \cot\left(\frac{\gamma}{2}\right) \delta \gamma \quad (2.114)$$

$$\left(\frac{\delta Q_{JB}^2}{Q_{JB}^2}\right) = \left(\frac{2 - y_{JB}}{1 - y_{JB}}\right) \frac{\delta F}{F} \oplus \left[2 \cot \gamma + \left(\frac{y_{JB}}{1 - y_{JB}}\right) \cot\left(\frac{\gamma}{2}\right)\right] \delta \gamma \quad (2.115)$$

The resolution in  $x_{JB}$  and  $Q_{JB}^2$  diverges for  $y_{JB} \rightarrow 1$  and no longer for  $y_{JB} \rightarrow 0$  as it is the case for the Electron method. For large values of the angle  $\gamma$ , the resolution in  $x_{JB}$  and  $Q_{JB}^2$  is dominated by the angular resolution. A precise angular measurement of the hadronic final state at low  $Q^2$  is necessary. The reconstruction of  $y$  using the Jacquet-Blondel method has the clear advantage that no divergent terms in  $y$  for  $y \rightarrow 0$  are present.

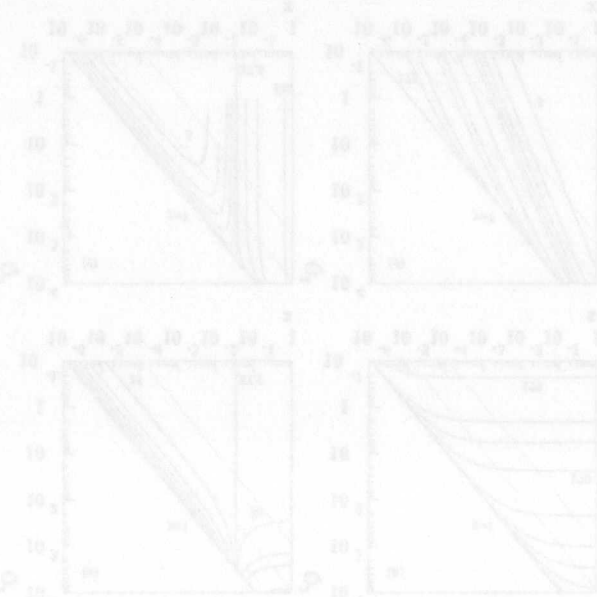
Besides the electron method and the Jacquet-Blondel method, two other methods are commonly used.

The *Double Angle method* reconstructs the kinematic variables using the angles  $\theta'_e$  and  $\gamma$ . It shows a degradation of the resolution in both  $x$  and  $Q^2$  for very large angles of  $\theta'_e$  and  $\gamma$ . At

low  $Q^2$ , a good angular resolution is therefore necessary. This method is restricted as well by the limited acceptance of a particular detector for  $\theta'_e \rightarrow 180^\circ$  and  $\gamma \rightarrow 180^\circ$ .

The  $\Sigma$  method uses the energy and angular information of the scattered electron and  $\sum_A(E_h - p_{z,h})$  from the hadronic final state. The divergence in  $y$  for  $y \rightarrow 1$  is no longer present. The angular resolution is for  $\theta'_e \rightarrow 180^\circ$  the dominant contribution of the resolution in both  $x$  and  $Q^2$ . Both the measurement of the electron as well as the measurement of  $\sum_A(E_h - p_{z,h})$  is restricted due to possible detector acceptance limitations.

To explore the region of small values in  $x$  and  $Q^2$ , a particular detector has to provide an acceptance for very large scattering angles of the scattered electron and/or the angle  $\gamma$  which can be associated with the scattering angle of the current jet. It requires to measure the energy and angle of the scattered electron and/or of the current jet with high precision. These constraints are of vital importance in the actual design of a particular detector to provide an acceptance for very small values in  $x$  and  $Q^2$ . This will be discussed in detail in section 5.3.



kinematic  $Q^2 - x$  plane. Figure 2.6 shows isolines of constant electron energy (a) and constant scattering angles (b) as well as lines of constant  $y$  values (1, 0.1, 0.01). Those curves can be determined using the following formulas:

$$Q_e^2(x, \theta'_e) = \frac{sx}{1 + (x \frac{E_p}{E'_e}) \tan^2(\frac{\theta'_e}{2})} \quad (2.99)$$

$$Q_e^2(x, E'_e) = \frac{sx(1 - \frac{E'_e}{E_e})}{1 - (x \frac{E_p}{E'_e})} \quad (2.100)$$

Small electron energies give rise to high  $y$  values. The kinematic limit  $y = 1$  as shown in Figure 2.6, is given by  $Q^2 = sx$ , i.e. the kinematic limit is determined by the center-of-mass energy. The low  $Q^2$  region can only be reached if one measures the final state electron under very large angles  $\theta'_e$ . For  $Q^2 < 1 \text{ GeV}^2$ , the energy of the scattered electron is limited to be below the electron beam energy of 27.5 GeV for  $x < E_e/E_p$  which is known as the kinematic peak position  $x = E_e/E_p$ . In this region the lines of constant  $y$  values are essentially parallel to lines of constant energy of the scattered electron. Going from small values of the scattered electron energy towards the kinematic peak point, the isolines start to be further apart from each other compared to the region of small electron energies. This indicates that small changes in  $E'_e$  lead to large changes of the kinematic variables.

The above expressions can be used to determine the dependencies of the kinematic variables on the measured quantities  $E'_e$  and  $\theta'_e$ . The relative errors of the kinematic variables are given as follows:

$$\left(\frac{\delta x_e}{x_e}\right) = \left(\frac{1}{y_e}\right) \frac{\delta E'_e}{E'_e} \oplus \left[\frac{x_e}{E_e/E_p} - 1\right] \tan\left(\frac{\theta'_e}{2}\right) \delta\theta'_e \quad (2.101)$$

$$\left(\frac{\delta y_e}{y_e}\right) = \left(1 - \frac{1}{y_e}\right) \frac{\delta E'_e}{E'_e} \oplus \left(\frac{1}{y_e} - 1\right) \cot\left(\frac{\theta'_e}{2}\right) \delta\theta'_e \quad (2.102)$$

$$\left(\frac{\delta Q_e^2}{Q_e^2}\right) = \frac{\delta E'_e}{E'_e} \oplus \tan\left(\frac{\theta'_e}{2}\right) \delta\theta'_e \quad (2.103)$$

The resolution in  $x_e$  and  $y_e$  diverges for  $y_e \rightarrow 0$ . The effect of  $y_e \rightarrow 0$  is to enhance the relative error of the energy measurement. The Electron method is therefore restricted to the region of high  $y$  values due to the singular structure of the resolution in  $x_e$  and  $y_e$  for  $y_e \rightarrow 0$ . The lower bound in  $y_e$  for which the resolution in  $x_e$  and  $y_e$  is still acceptable highly depends on the resolution with which the energy of the scattered electron can be measured.

The resolution in  $Q_e^2$  diverges for  $\theta'_e \rightarrow 180^\circ$ . The angular resolution at high values of the electron scattering angle  $\theta'_e$  is the dominant contribution for the resolution in  $Q^2$ .  $\theta'_e \rightarrow 180^\circ$  requires the capability of a particular detector to measure the energy and angle of the scattered electron under very large angles.

A precise measurement of  $x$ ,  $y$  and  $Q^2$  at low  $Q^2$ , using the Electron method, requires therefore a precise energy and angular measurement at large electron scattering angles  $\theta'_e$  and restrict its usage to a region of high  $y$  values.

### Jacquet-Blondel Method

The Jacquet-Blondel method provides a reconstruction of the kinematic variables using the hadronic final state only. This requires that the reconstructed kinematic variables are independent of the final state fragmentation process as well as insensitive to the loss of final state

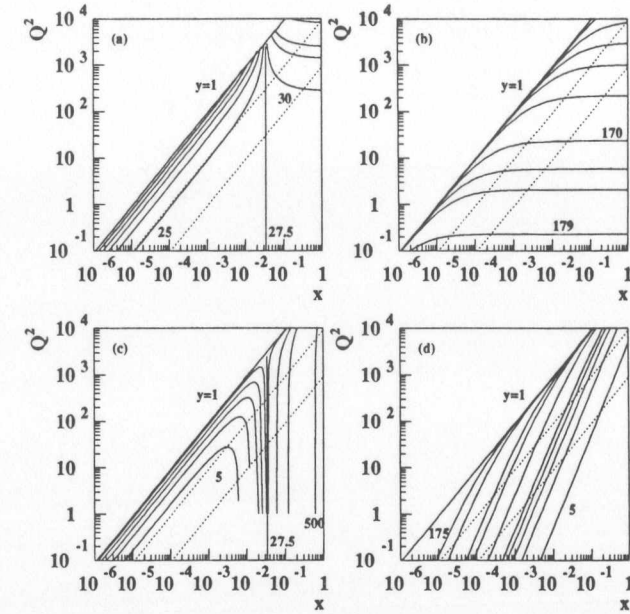


Figure 2.6: The dashed lines represent lines of constant  $y$  values (1, 0.1, 0.01). The electron beam energy amounts to 27.5 GeV whereas the proton beam energy is 820 GeV. Isolines of constant electron energies (5–30 GeV in steps of 5 GeV and 40, 50, 100, 200 GeV) (a), electron scattering angles ( $30^\circ - 150^\circ$  in steps of  $30^\circ$  and  $170^\circ, 175^\circ, 177^\circ, 179^\circ$ ) (b), jet energies (5–30 GeV in steps of 5 GeV and 50, 100, 500 GeV) (c) and hadronic angles ( $5^\circ - 45^\circ$  in steps of  $10^\circ$  and  $90^\circ, 135^\circ, 150^\circ, 170^\circ, 175^\circ$ ) (d).

particles in dead areas of a detector such as beam pipe holes. It was shown in [Ja79] that the transverse momentum  $p_{T,h}^2 = (\sum_h p_{X,h})^2 + (\sum_h p_{Y,h})^2$  as well as the difference of the energy and the longitudinal momentum of the hadronic final state  $(E - P_Z)_h = \sum_h (E_h - p_{Z,h})$  satisfy these requirements. Using the above four vectors with  $p' = (\sum_h E_h; \sum_h P_{X,h}; \sum_h P_{Y,h}; \sum_h P_{Z,h})$  and the definitions for the kinematic variables, one finds:

$$x_{JB} = \frac{Q_{JB}^2}{s y_{JB}} \quad (2.104)$$

$$y_{JB} = \frac{(E - P_Z)_h}{2E_e} \quad (2.105)$$

$$Q_{JB}^2 = \frac{p_{T,h}^2}{1 - y_{JB}} \quad (2.106)$$

$p_{T,h}$  as well as  $(E - p_Z)_h$  can be used to define the energy  $F$  and the polar angle  $\gamma$  [Be91] of a massless object which describes the hadronic final state:

$$F = \frac{p_{T,h}^2 + (E - p_Z)_h^2}{2(E - p_Z)_h} \quad (2.107)$$

*[Faint, illegible text from the reverse side of the page, appearing as bleed-through.]*



## Chapter 3

### Chapter 3

#### HERA

##### 3.1 The electron-proton collider HERA

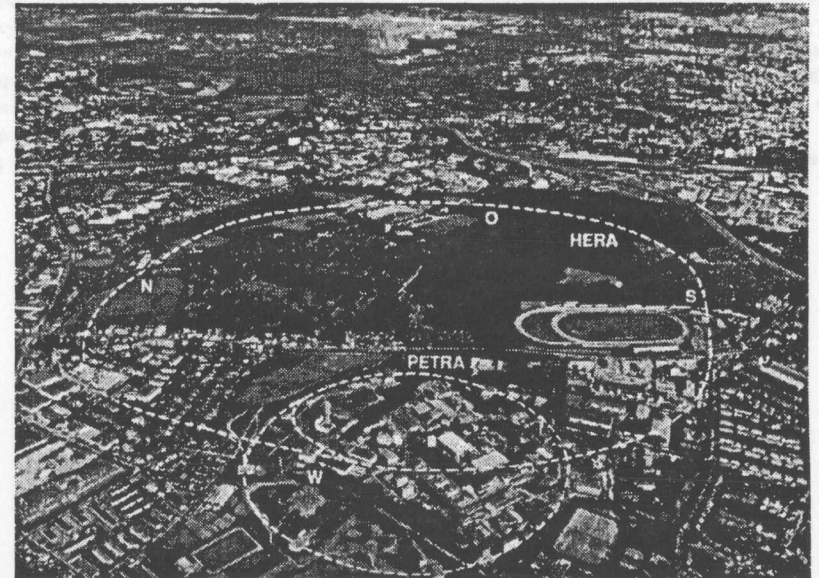


Figure 3.1: The 'Volkspark' in Hamburg surrounded by the HERA collider shown with the ZEUS experiment located in the South experimental hall (S). The pre-accelerator PETRA, enclosing the main DESY site, is shown in the foreground.

HERA, the Hadron-Elektron-Ring-Anlage (Figure 3.1), is the world's first electron-proton collider located at the DESY laboratory in Hamburg, Germany.

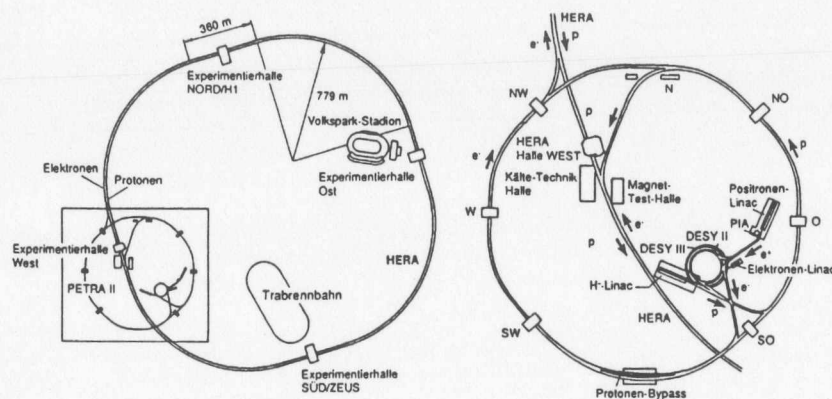


Figure 3.2: The HERA accelerator complex.

The proposal for an  $ep$ -facility in Europe was approved in April 1984. The first  $ep$ -collisions were observed on October 19th 1991 at a center-of-mass energy of  $\sqrt{s} = 152$  GeV. HERA began its operation to study inelastic electron-proton scattering with the two collider experiments H1 and ZEUS in spring 1992 at an electron beam energy of 26.6 GeV and a proton beam energy of 820 GeV which yields a center-of-mass energy of  $\sqrt{s} = 295$  GeV.

The HERA collider consists of two storage rings to accommodate at its design performance 30 GeV electrons or positrons and 820 GeV protons. Figure 3.2 shows the layout of the HERA accelerator complex. The HERA tunnel which is located 15–30 m below ground consists of four 90° arcs and 360 m long straight sections in between. The energy of the electron beam at its design value of 30 GeV is limited by the radio frequency power which is needed to compensate the energy loss due to synchrotron radiation. The magnetic field of the bending sections of the electron storage ring amounts to 0.165 T. Superconducting magnets are used for the proton storage ring. They are cooled with liquid and gaseous helium which is distributed around the HERA ring by a central He-plant located on the DESY site. The proton beam energy of 820 GeV (design value) is limited by the 4.65 T bending field of the dipole magnets<sup>1</sup> [Wi82].

The HERA collider allows to accommodate two collider experiments, H1 in the North experimental hall and ZEUS in the South experimental hall, as seen on Figure 3.2. In both interaction regions, electrons and protons are brought to collisions head-on at zero crossing angle. In addition, two fixed-target experiments, HERMES in the East experimental hall and HERA-B<sup>2</sup> in the West experimental hall, have been installed.

The HERMES experiment [HE93] is designed to explore the spin structure of the nucleons by employing inelastic scattering of longitudinally polarized electrons or positrons on polarized gas jet targets such as hydrogen, deuterium or He<sup>3</sup>. Spin rotators which are installed before and after the EAST experimental hall are used to cause a spin flip of transverse and longitudinal polarized electrons, respectively. The naturally occurring transverse polarization within an electron storage ring described by the Sokolov-Ternov effect [Te64] is the basis of this experiment.

<sup>1</sup>Some feasibility studies have been made to investigate the possibility of raising the proton beam energy up to 1 TeV [Ho97].

<sup>2</sup>The HERA-B experiment has not been fully completed at the time of writing this thesis.

HERA parameters	Design Values		Values of 1995	
	e-ring	p-ring	e-ring	p-ring
Circumference (m)	6336			
Energy (GeV)	30	820	27.5	820
Center-of-mass energy (GeV)	314		300	
Injection energy (GeV)	14	40	12	40
Injection time (min)	15	20	45	60
Energy loss per turn (MeV)	127	$1.4 \cdot 10^{-10}$	127	$1.4 \cdot 10^{-10}$
Current (mA)	58	160	30	55
Magnetic field (T)	0.165	4.65	0.165	4.65
Number of bunches	210	210	174+15	174+6
Bunch crossing time (ns)	96			
Horizontal beam size (mm)	0.301	0.276	0.239	0.185
Vertical beam size (mm)	0.067	0.087	0.055	0.058
Longitudinal beam size (mm)	0.8	11	0.8	11
Specific luminosity ( $\text{cm}^{-2}\text{s}^{-1}\text{mA}^{-2}$ )	$3.6 \cdot 10^{29}$		$5.0 \cdot 10^{29}$	
Instantaneous luminosity ( $\text{cm}^{-2}\text{s}^{-1}$ )	$1.6 \cdot 10^{31}$		$4.3 \cdot 10^{30}$	
Integrated luminosity per year ( $\text{pb}^{-1}/\text{a}$ )	35		12.5	

Table 3.1: HERA parameters [Ho96].

The HERA-B experiment [HB94] aims to study  $CP$ -violation in the  $B^0\bar{B}^0$ -system using a wire target in the halo of the HERA proton beam for the production of  $B$ -mesons.

Figure 3.2 shows the HERA accelerator complex. The injection of protons start with a H<sup>-</sup> 50 MeV linear accelerator. Before injecting the H<sup>-</sup>-ions into the DESY III storage ring, the H<sup>-</sup>-ions are stripped. The DESY III storage ring is then filled with 11 bunches with a bunch spacing of 96 ns which is identical to the HERA bunch spacing and accelerated to 7.5 GeV. The proton bunches are then transferred to the PETRA II storage ring. 70 bunches are accumulated within PETRA II and accelerated to 40 GeV. Finally, the proton bunches are transferred to HERA. This procedure is repeated three times until HERA is filled with 210 proton bunches which takes about 20 minutes at design performance. Within HERA, the proton bunches are accelerated to 820 GeV.

The electron (positron) injection begins with a 500 MeV linear accelerator to fill a small storage ring, the positron intensity accumulator (PIA), with a single bunch of about 60 mA. This bunch is then transferred to DESY II, accelerated to 7 GeV and afterwards injected into the PETRA II storage ring until 70 bunches are accumulated. Within PETRA II, the electron (positron) bunches are accelerated to 14 GeV and afterwards transferred to HERA. This procedure is repeated until HERA is filled with 210 electron (positron) bunches which takes about 15 minutes at design performance. The electron (positron) bunches are then accelerated to their final energy. The design performance of HERA is summarized in Table 3.1.

### 3.2 HERA parameters in the year 1995

During the HERA run in the year 1994, severe lifetime problems of the electron beam were observed. The maximum electron current was limited to 25 mA and the typical lifetime was only two to three hours. The reason for this effect is most likely due to capturing positively charged dust which originates from ion getter pumps from the HERA electron vacuum system by the

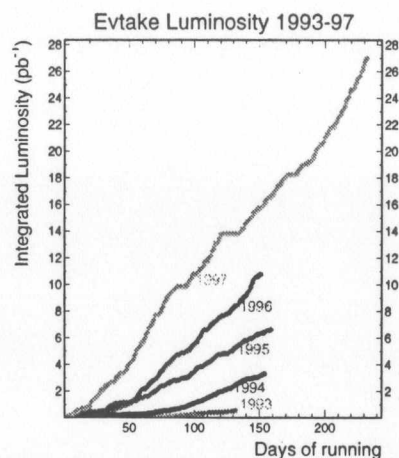


Figure 3.3: Integrated luminosity delivered by HERA plotted as a function of time in days from the years 1993 until 1997.

electron beam. In 1994, the HERA operation was therefore changed to accelerate positrons instead of electrons which resulted in a much larger lifetime of typically eight hours [DESY94]. The HERA runs during the years 1995 to 1997 were carried out as well using positrons instead of electrons. The main parameters of the HERA operation in 1995 can be seen from Table 3.1. During the HERA run in 1995, HERA was operated with 174 colliding bunches, 15 positron-pilot bunches and 6 proton-pilot bunches.

Figure 3.3 shows the HERA integrated luminosity from 1993 until 1997. It shows a continuous increase of the integrated luminosity delivered by HERA.

A typical HERA luminosity running period over 24 hours is shown in Figure 3.4 with the positron and proton current in mA plotted as a function of time in hours (h). It shows the end of a luminosity run at around 10:45. After the subsequent new fill of protons and positrons which started at approximately 12:45 and 16:15 respectively, both beams were lost which required a new fill of protons and positrons at around 14:30 and 17:30, respectively. A new luminosity

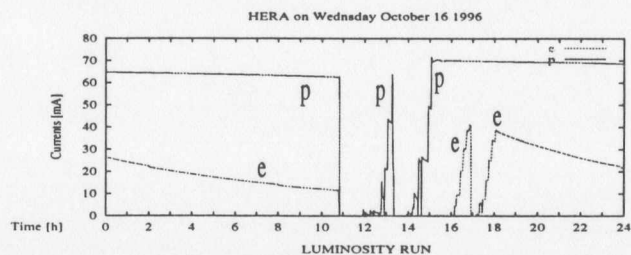


Figure 3.4: Electron and proton current (in mA) within HERA as a function of time (in h) during a typical 24 h luminosity operation.

run with stable beam conditions started at around 18:30. The performance of various detector components within an experiment such as ZEUS depends crucially on the reliability of the collider operation. This is important in particular for detector components which are installed close to the HERA electron and proton beams. The injection, dumping and accidental loss of the HERA beams are potential periods during the accelerator operation which can lead to significant higher background rates compared to the normal luminosity operation in between. The dumping scheme for the protons consists of a fast kicker magnet system which is installed in the West area of the HERA collider. Such a dumping scheme does not exist for the electron beam and one relies on other procedures [Ho97]. Some of them have been shown to cause a significant radiation background for the Beam Pipe Calorimeter (BPC) at ZEUS (Chapter 5) as will be discussed in detail in section 7.2. This has raised the question to install a kicker magnet system for the electron beam as well [Wi96].

## Chapter 4

# ZEUS - A Detector for HERA

### 4.1 Overview

The ZEUS detector at HERA is a general purpose magnetic detector which has been in operation since 1992 [Ho93]. It has been designed to study various aspects of electron-proton scattering. The design incorporates the large forward-backward asymmetry of the  $ep$  final-state system due to the significant difference in the energy of the electron and proton beam which results in a center-of-mass system which is moving in direction of the proton beam relative to the lab-frame system. The ZEUS detector consists of various sub-components to characterize the  $ep$  final-state in terms of energy, direction and type of the produced final-state particles, i.e. hadrons and leptons.

The coordinate system of the ZEUS detector is a right-handed coordinate system with the origin ( $X = Y = Z = 0$ ) at the nominal interaction point, the  $Z$  axis pointing in the proton beam direction, the  $Y$  axis pointing upwards and the  $X$  axis pointing horizontally towards the center of HERA. The polar angle  $\theta$  is measured with respect to the positive  $Z$  axis and the azimuthal angle  $\phi$  relative to the positive  $X$  axis. Thus, the polar angle of the proton and electron beam is equal to  $0^\circ$  and  $180^\circ$ , respectively.

Figure 4.1 and 4.2 show a cross-section of the ZEUS detector along and perpendicular to the beam direction, respectively.

The tracking system consists of a cylindrical drift chamber (CTD) which surrounds the interaction point. In the forward direction, three sets of planar drift chambers (FTD) are installed with transition radiation detectors (TRD) in between. A single arrangement of one planar drift chamber with three layers (RTD) is installed in the rear direction. This tracking system provides the necessary tracking information, i.e. the measurement of the momentum and direction of electrons and charged hadrons which allows a precise determination of the event vertex. Using the TRD as well as  $dE/dx$  measurements among the CTD provides some means of particle identification. The whole tracking system is enclosed by a superconducting solenoid which produces an axial magnetic field of 1.43 T. A vertex detector (VXD) which was in operation until 1994 was removed during the winter shutdown 1995/96.

The tracking system is surrounded by a high resolution uranium calorimeter (UCAL) which is the prime device for the energy measurement of electrons and hadrons. It is subdivided into three parts: the forward calorimeter (FCAL), the barrel calorimeter (BCAL) and the rear calorimeter (RCAL). A small angle rear tracking detector (SRTD) is mounted in front of the RCAL and covers an area of  $68 \times 68 \text{ cm}^2$ . Presampler detectors, RPRES and FPRES, which consist of single layers of scintillator plates, are installed in front of the RCAL and FCAL modules.

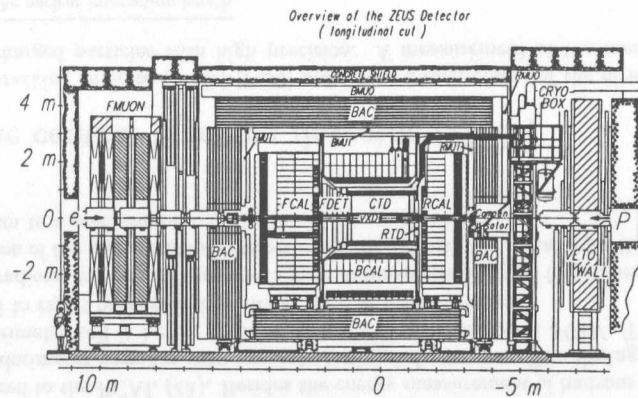


Figure 4.1: Cross-section of the ZEUS detector along the beam direction.

An iron yoke made of 7.3 cm thick iron plates surrounds the main calorimeter (UCAL) which provides a return path for the solenoid magnetic field flux. It is instrumented with proportional chambers to provide a measurement of energy leakage from the main calorimeter and serves therefore as a backing calorimeter (BAC). The iron yoke itself is magnetized to 1.6 T by copper coils to deflect muons. Limited streamer tubes are mounted inside and outside of the barrel (BMUI, BMUO) and the rear (RMUI, RMUO) iron yoke and are used for the muon momentum measurement. In the forward direction, limited streamer tubes which are mounted on the inside of the iron yoke (FMUI) as well as drift chambers and limited streamer tubes (FMUO) mounted outside the iron yoke are used for the forward muon momentum measurement within a toroidal magnetic field of 1.7 T which is produced by two iron toroids.

An iron/scintillator vetowall at  $Z = -7.3$  m is used to reject beam-related background. Two lead/scintillator electromagnetic calorimeters in the electron beam direction at  $Z = -34$  m and  $Z = -107$  m are used to measure electrons from bremsstrahlung and photoproduction events and photons from bremsstrahlung events, used for the luminosity determination at ZEUS, and radiative events, respectively.

In the forward direction, a lead/scintillator counter at  $Z = 5.1$  m, the proton remnant tagger (PRT), allows to obtain information about the hadronic final state in the forward direction for a range in pseudorapidity<sup>1</sup> of  $4.3 < \eta < 5.8$ . A leading proton spectrometer (LPS) at  $Z = 26 - 96$  m is used to measure very forward scattered protons (transverse momentum  $< 1$  GeV/c) using six stations of silicon strip detectors which are mounted very close to the beam. A forward neutron calorimeter (FNC) of a lead/scintillator sandwich type is installed at  $Z = 105.6$  m to detect very forward produced neutrons.

In 1995, the ZEUS-experiment at HERA significantly enhanced the kinematic coverage for low  $Q^2$  and low  $x$   $e^+p$  scattering by extending the acceptance for small positron scattering angles in the rear direction. The upgrade included the modification of the beam pipe with low mass exit windows and the installation of a small electromagnetic sampling calorimeter, the Beam Pipe Calorimeter (BPC) (Chapter 5), to explore the region in  $Q^2$  of  $0.11 \leq Q^2 \leq 0.65$  GeV<sup>2</sup>. A shift of two rear uranium calorimeter (RCAL) modules and the small rear tracking detector (SRTD) closer to the beam, extended the  $Q^2$  coverage of the main detector down to 0.65 GeV<sup>2</sup>.

<sup>1</sup>The pseudorapidity is defined as  $\eta = -\ln(\tan \frac{\theta}{2})$  with  $\theta$  the polar angle associated to the hadronic final state.

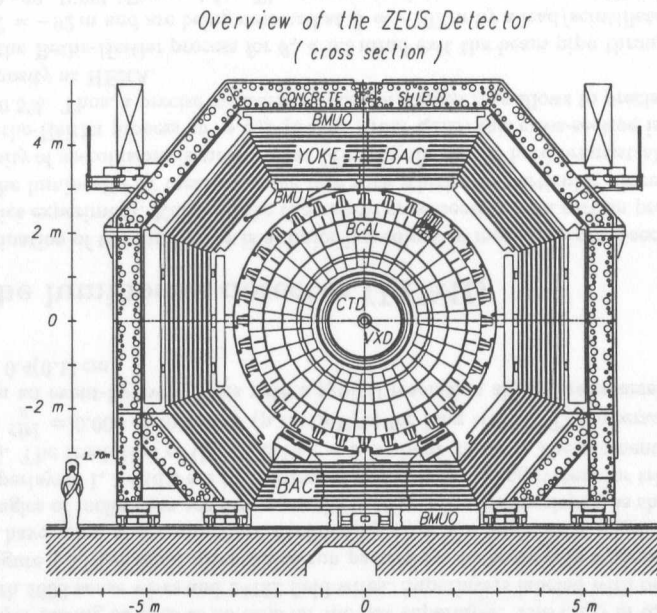


Figure 4.2: Cross-section of the ZEUS detector perpendicular to the beam direction.

The following sections provide a brief description of those detector components which are relevant for the physics analysis presented in this thesis.

## 4.2 The uranium calorimeter (UCAL)

The three parts of the ZEUS calorimeter [An91, De91, Be93], FCAL, BCAL and RCAL, cover the polar angle regions of  $2.2^\circ$  to  $39.9^\circ$ ,  $36.7^\circ$  to  $129.1^\circ$ , and  $128.1^\circ$  to  $176.5^\circ$  respectively.

The ZEUS calorimeter is a sampling calorimeter which consists of alternating layers of 3.3 mm thick depleted uranium and 2.6 mm thick plastic scintillator plates (SCSN38). The calorimeter provides compensation, i.e. the energy response to electrons and hadrons is equalized ( $e/h = 1.00 \pm 0.02$ ). Compensation is of particular importance for the energy resolution of hadrons. Under test-beam conditions, the energy resolution was measured to be  $\sigma_E/E = 0.35/\sqrt{E}$  for hadrons and  $\sigma_E/E = 0.18/\sqrt{E}$  for electrons with the impact energy  $E$  in GeV.

The three calorimeter parts are subdivided into single modules (Figure 4.3). The 32 BCAL modules (Figure 4.2) have a wedge-shaped design. Each module covers an angle of  $11.25^\circ$  in  $\phi$ . Each calorimeter module is transversally separated into towers which are longitudinally subdivided into one electromagnetic (EMC) and two (one in RCAL) hadronic sections (HAC1, HAC2). Each EMC section is further segmented transversally into four cells for the FCAL and BCAL and two cells for the RCAL. Each cell is read out on two sides (Figure 4.3) by wavelength shifters which are coupled to photomultiplier tubes. The energy information within one cell measured on two sides of each cell provides a means of position reconstruction of the incoming particle, uniformity in the response and redundancy for the readout system.  $3 \times 3$  cm<sup>2</sup> silicon diodes are installed at a longitudinal depth of  $3X_0$  in the RCAL to provide a way to

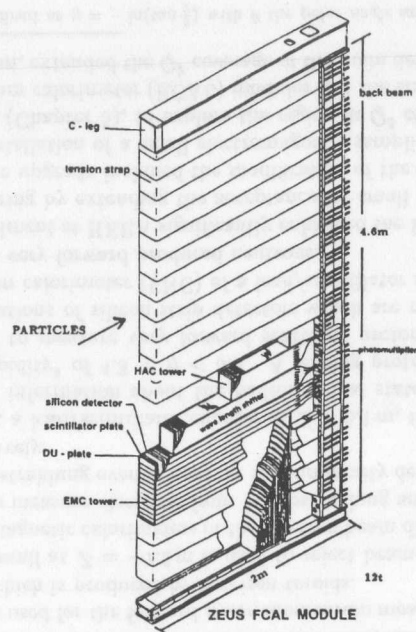


Figure 4.3: Layout of a FCAL module.

discriminate electromagnetic from hadronic showers.

In the forward and rear direction, the calorimeter modules have a non-projective geometry, i.e. the modules are planar and perpendicular with respect to the beam axis (Figure 4.1). In the barrel region, only the EMC sections are projective in the polar angle. The HAC towers of the BCAL are as well non-projective.

The large forward-backward asymmetry of the  $ep$ -final state is reflected in the depth of the three components of the ZEUS calorimeter which is significantly larger in case of the FCAL ( $7\lambda$ )<sup>2</sup> compared to the RCAL ( $4\lambda$ ). Besides the energy measurement of hadrons and electrons, the ZEUS calorimeter provides very accurate timing information. The timing resolution for a single calorimeter cell is better than  $\sigma_t = 1.5/\sqrt{E} \oplus 0.5$  ns above 3 GeV. This provides a powerful tool to reject background events already at the trigger level.

The natural radioactivity of  $U^{238}$  provides a very stable reference signal for calibration purposes. The calibration of the photomultiplier tubes is monitored with the signal from the radioactivity of the uranium to a precision of  $< 0.2\%$ .

### 4.3 The central-tracking detector (CTD)

The central-tracking detector (CTD) [Fo93] provides a measurement of the direction and momentum of charged particles with high precision. A measurement of the mean energy loss

<sup>2</sup> $\lambda$  denotes the nuclear interaction length.

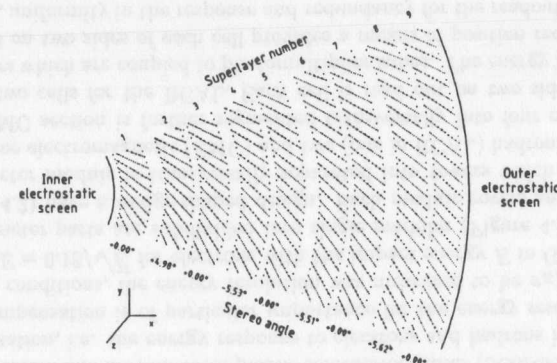


Figure 4.4: Layout of a CTD octant.

$dE/dx$  of charged particles within the gas-chamber volume of the CTD provides in addition a means of particle identification.

The CTD is a cylindrical drift chamber. Its active volume has a length of 205 cm, an inner radius of 18.2 cm and an outer radius of 79.4 cm. It has a polar angle coverage of  $15^\circ < \theta < 164^\circ$  and a full coverage of the azimuthal angle  $\phi$ . The chamber is filled with a mixture of argon,  $CO_2$  and ethane. Figure 4.4 shows the cross-section of an octant of the CTD. The CTD is designed as a multi-cell stereo superlayer chamber. It consists of nine superlayers which are built out of single cells with eight sense wires each. The number of cells increases from the first superlayer having 32 cells to 96 cells for the last superlayer. The CTD in total consists of 576 cells with 4608 sense wires and 24192 field wires. Superlayers labeled with odd numbers as shown in Figure 4.4 have sense wires which run parallel to the beam axis whereas even labeled superlayers have sense wires which are declined by a certain angle with respect to the beam axis. The angles of inclination are drawn on the bottom of each superlayer, as shown in Figure 4.4. The superlayers 1, 3 and 5 are instrumented with a  $z$ -by-timing system for trigger purposes ( $\sigma_z \simeq 4$  cm). The resolution of the CTD in  $r - \phi$  is about  $230 \mu m$ . The momentum resolution amounts to  $\frac{\sigma(p)}{p} = 0.005 \cdot p \oplus 0.0016$  ( $p$  in GeV/c) for long tracks. The interaction vertex is measured on an event-by-event basis with a typical resolution along (transverse) to the beam direction of  $0.4(0.1)$  cm.

### 4.4 The luminosity detector (LUMI)

The determination of the luminosity is a major ingredient to measure a cross-section in a high energy physics experiment. Knowing the theoretical cross-section for a certain process, one can determine the luminosity by measuring the rate with which this particular process occurs.

The luminosity of  $ep$ -collisions is measured at ZEUS by the rate of hard bremsstrahlung photons from the Bethe-Heitler process  $ep \rightarrow e\gamma p$  [Be34]. From QED, this cross-section is known to an accuracy of 0.5%. Thus, a precise measurement of the photon rate allows to precisely determine the  $ep$ -luminosity at HERA.

Photons of the Bethe-Heitler process for  $\theta_\gamma < 0.5$  mrad exit the beam pipe through a Cu - Be window at  $Z = -92$  m and are being detected at  $Z = -107$  m by a lead/scintillator calorimeter (LUMIG) [An92, Pi93] (Figure 4.5). The energy resolution amounts to  $18\%/\sqrt{E}$  under test

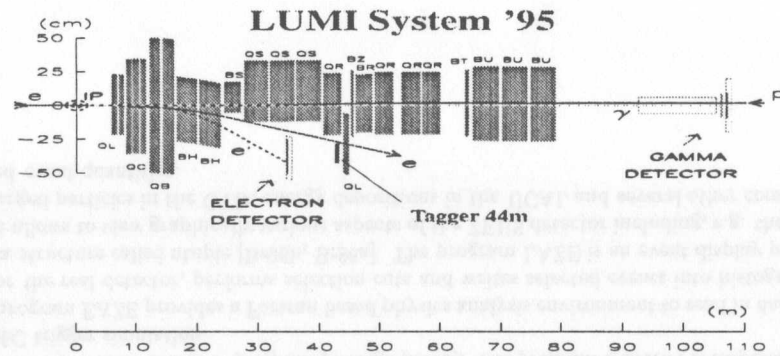


Figure 4.5: Layout of the luminosity monitor.

beam conditions. A carbon/lead filter which is installed in front of the LUMIG detector for shielding against synchrotron radiation reduces the achieved energy resolution under test-beam conditions to  $23\%/\sqrt{E}$ . Two layers of orthogonal 1 cm wide scintillator strips are installed within the LUMIG detector at a depth of  $7X_0$  and provide a means of position reconstruction of the incoming photon. The position resolution has been determined to be 0.2 cm in  $X$  and  $Y$ . Besides determining the position and energy of hard photons resulting from the Bethe-Heitler process, the LUMIG detector is used in addition to measure photons from initial-state-radiation processes.

A small electromagnetic lead/scintillator (LUMIE) [An92, Pi93] calorimeter at  $Z = -35$  m detects electrons for energies between 7 and 20 GeV which are produced under polar angles less than 5 mrad with respect to the electron beam direction. These electrons are deflected by the HERA magnet system and leave the beam pipe at  $Z = -27$  m (Figure 4.5). The energy resolution has been determined to be  $18\%/\sqrt{E}$  under test-beam conditions. The electron LUMIE detector allows to tag photoproduction events in a limited kinematic range of  $0.2 < y < 0.6$  and  $Q^2 < 0.01$  GeV<sup>2</sup> by measuring the electron scattered under very small angles.

## 4.5 The trigger and data acquisition system

The ZEUS detector with its subcomponents has a total of 250000 readout channels. The majority of events which leave a detectable signal in these subcomponents are not  $ep$  events. The total interaction rate is dominated by interactions of the proton beam with the residual gas in the beam pipe with a rate on the order of 10 – 100 kHz whereas the rate for  $ep$  physics events is only a few Hz. Other sources of non  $ep$  physics events are beam halo interactions, electron beam gas interactions and cosmic ray events.

A sophisticated trigger decision during data taking is necessary to filter out  $ep$  physics event candidates despite the large background rate. Such a trigger decision cannot be executed within the HERA bunch spacing time of 96 ns.

ZEUS has a three-level trigger system to select potential  $ep$  physics event candidates efficiently while reducing the input rate to a few Hz [Sm89, Yo92]. Figure 4.6 shows schematically, the readout system of each component with the three level trigger system.

To avoid dead time, both the components readout and first-level trigger system are pipelined. The data are stored in 10.4 MHz pipelines. Each local first level trigger analyzes within 25

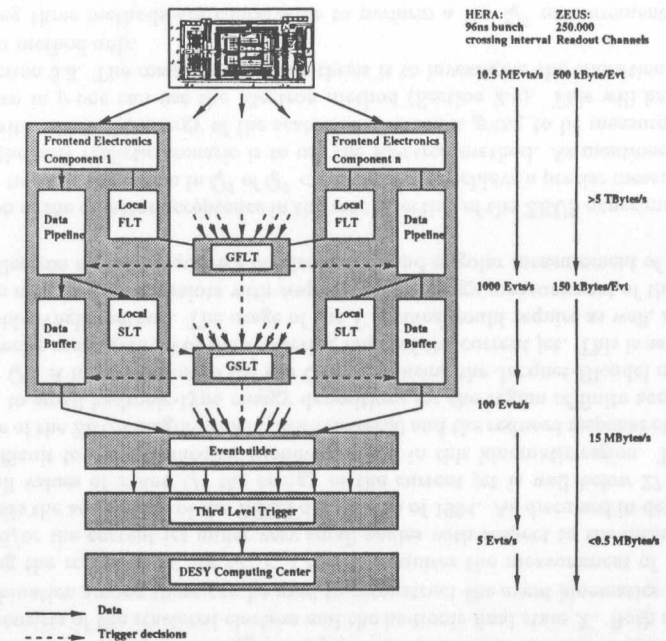


Figure 4.6: Schematic diagram of the ZEUS trigger and data acquisition system.

clock cycles a particular event and sends its information to a global first level trigger (GFLT). The GFLT issues a global trigger decision based on various logical combinations among the components input which takes additional 20 bunch crossings. In case of a positive trigger decision, the data stored in pipelines of each component are read out and processed further. The first level trigger at ZEUS is designed to reduce the input rate below 1 kHz.

The second-level trigger (SLT) is designed to reduce the input rate of at most 1 kHz to below 100 Hz. Each component has its own local second-level trigger which stores the data to be analyzed in a memory buffer. The component SLTs are based on a network of programmable transputers. Sophisticated algorithms can be used to identify and reject background events. The result of the local SLTs are combined in the global second level trigger (GSLT) [Ui92] to execute a final decision.

Once a positive decision of the GSLT has been issued, the data from each component is sent to the Eventbuilder to combine the component data in one single data set. The Eventbuilder makes the event information accessible to the third level trigger (TLT) and formats the components data in the ADAMO format [Gr89] which is used at the TLT and in the off-line reconstruction and analysis.

The TLT consists of a processor farm of Silicon Graphics CPUs. Part of the off-line reconstruction code runs on this processor farm to filter out  $ep$ -physics events to reduce the input rate to a few Hz.

Events which are accepted by the TLT are written to tape. After the TLT, the amount of data to be stored is less than 0.5 MBytes/s.

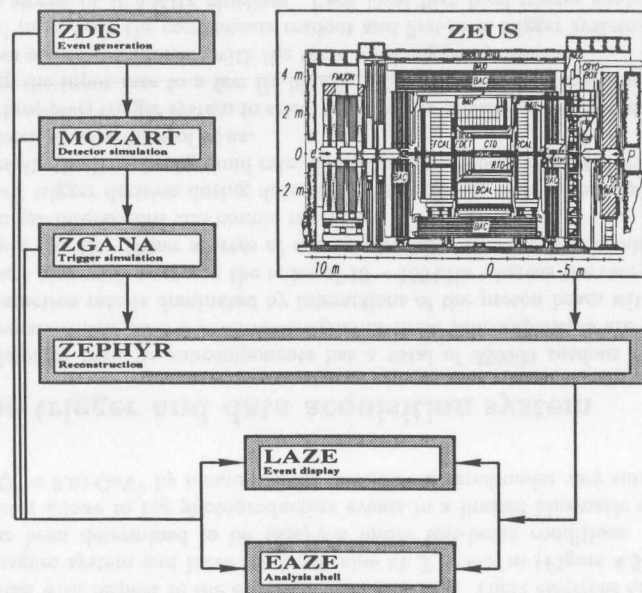


Figure 4.7: ZEUS off-line and Monte Carlo (MC) programs.

## 4.6 Event reconstruction and analysis

An overview of the physics analysis environment of the ZEUS experiment can be found in [Ba95a].

Figure 4.7 shows a scheme of the ZEUS off-line and Monte Carlo (MC) programs (Chapter 6) and their interrelationship. Events are reconstructed by the program ZEPHYR using the data of each component from either the real detector or MC.

The generation of MC events starts with the program ZDIS which contains a shell environment to steer various MC generator programs and stores the output data in the ADAMO format. This provides the proper input for the ZEUS detector simulation program MOZART which is based on the CERN GEANT program package [Br89]. The program ZGANA is responsible for the MC trigger simulation.

The program EAZE provides a Fortran based physics analysis environment to read in data from MC or the real detector, performs selection cuts and writes selected events into histograms or a data structure called ntuple [Br96b, Br96a]. The program LAZE is an event display program which allows to view graphically various aspects of the ZEUS detector including, e.g. the tracks of charged particles in the CTD, energy depositions in the UCAL and several other component related event quantities.

## Chapter 5

# The Beam Pipe Calorimeter (BPC)

### 5.1 Introduction

The investigation of the transition region between photoproduction and deep-inelastic scattering at small value of  $x$  and large values of  $W$  respectively, by measuring the proton structure function  $F_2(x, Q^2)$  and the total virtual photon-proton cross-section  $\sigma_{tot}^{\gamma^*p}(W^2, Q^2)$  respectively, is the main focus of this thesis. As pointed out in section 2.3.5, the investigation of this transition region implies the measurement of a  $Q^2$  region ( $Q^2 < 1.5 \text{ GeV}^2$ ), which has not been covered by the HERA experiments H1 [Ai96] and ZEUS [De96a] until 1994. The following section will motivate the experimental configuration to achieve such a measurement.

The accurate reconstruction of the Lorentz-invariant variables  $x$ ,  $y$  and  $Q^2$  is one of the key steps in measuring  $F_2(x, Q^2)$  and  $\sigma_{tot}^{\gamma^*p}(W^2, Q^2)$ . The final state in neutral current  $ep \rightarrow eX$  scattering consists of the scattered electron and the hadronic final state  $X$ . Both systems alone or any combination among those can be used to reconstruct the event kinematics (Section 2.4). Investigating the region in  $Q^2$  for  $Q^2 < 1.5 \text{ GeV}^2$  requires the measurement of the scattered electron and/or the current jet under very small angles with respect to the incoming electron which exceeds the acceptance of the ZEUS detector as of 1994. As discussed in detail in section 2.4, at small values of  $x$  and  $Q^2$  the energy of the current jet is well below  $27.5 \text{ GeV}$  which makes it difficult to use the Jacquet-Blondel method in this kinematic region. This is due to the presence of the ZEUS magnetic field, dead material and the reduced response of the uranium calorimeter to small hadronic-type energy depositions for the region of finite acceptance as of 1994 at low  $Q^2$ . A measurement in the low  $Q^2$  region using the Jacquet-Blondel method would require a precise measurement of the scattering angle of the current jet. This is as well the case for the Double Angle method. The usage of the  $\Sigma$  method would require as well, a very careful study of the mentioned constraints with respect to the energy measurement of the current jet. Using the Electron method requires a precise energy and angular measurement of the scattered electron.

An extension of the detector acceptance in the rear direction of the ZEUS experiment as of 1994 is necessary to cover the region in  $Q^2$  of  $Q^2 < 1.5 \text{ GeV}^2$ . To achieve a precise measurement of  $F_2$  at low  $Q^2$ , the only realistic scenario is to use the Electron method. As mentioned before, the resolution with which the energy of the scattered electron is going to be measured determines how far down in  $y$  one can use the Electron method (Section 2.4). This will be discussed in detail in section 5.3. The main focus of this thesis is to investigate the transition region using the Electron method only.

The following three methods are conceivable to perform a low  $Q^2$  measurement as shown in Figure 5.1. Method 1 requires a small electromagnetic calorimeter to measure the final state

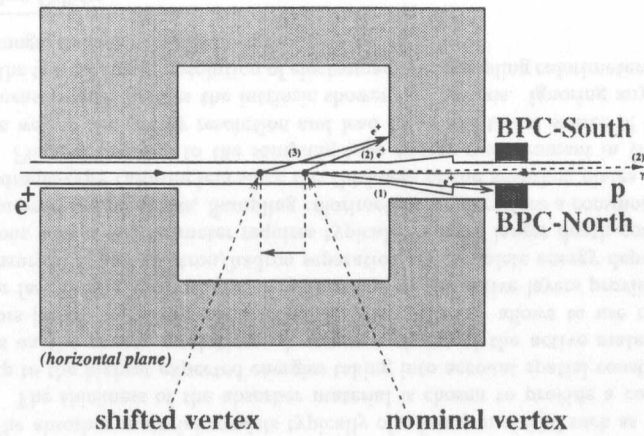


Figure 5.1: Schematic description of three methods to study the low  $Q^2$  region showing within the horizontal plane of the ZEUS detector the beam pipe, two small electromagnetic calorimeter modules (BPC-North and BPC-South) (Method 1) and the main calorimeter (CAL).

electron under very small angles and thus reaching low values in  $Q^2$ . Spatial constraints restrict the location of such a new detector within the existing ZEUS-detector and therefore the kinematic coverage in  $Q^2$ . In Method 2, a hard photon with energy  $E_\gamma$  in the initial state (ISR<sup>1</sup> events) is measured using the LUMIG photon calorimeter. This results in  $ep$  scattering at reduced center-of-energy and thus at lower values of  $Q^2$  keeping the electron scattering angle fixed. Method 3 requires shifting the event vertex in the direction of the incoming proton. For a fixed impact position in the RCAL, one obtains smaller angles of the scattered electron and thus smaller values in  $Q^2$ . Method 3 is limited by the geometrical acceptance of the RCAL.

The clear advantage of using Method 1 and 2 is that one can use the full data sample at nominal vertex for a low  $Q^2$  analysis. The systematic uncertainties on a measurement of  $F_2$  using Method 2 are fairly large [Fr96]. Method 3 is limited to dedicated runs and thus to a relatively small data sample. In 1995, a shift of two rear uranium calorimeter (RCAL) modules and the small rear tracking detector (SRTD) closer to the beam, together with a data sample taken with a shifted event vertex, extended the  $Q^2$  coverage of the main detector down to  $0.65 \text{ GeV}^2$  which corresponds to the central value of the lowest, single bin in  $Q^2$ . The two next  $Q^2$  bins are at  $0.92 \text{ GeV}^2$  [Su97]. Employing Method 2 has a similar restriction in  $Q^2$ .

To investigate the behavior of  $F_2$  within the transition region requires a measurement of  $F_2$  with high precision over several bins in  $Q^2$  and several bins in  $x$ . Only Method 1 could enable such a measurement. It requires the design, construction and operation of a small electromagnetic calorimeter. As will be shown in detail in section 5.4.1, spatial constraints for such a calorimeter within the existing ZEUS detector restrict the kinematic coverage in  $Q^2$  to  $0.1 < Q^2 < 0.8 \text{ GeV}^2$ . Together with data taken during the HERA run in 1995 with a shifted event vertex using the ZEUS RCAL and SRTD, allowed a continuous  $Q^2$  coverage of  $Q^2 > 0.1 \text{ GeV}^2$  [Su97].

Figure 5.2 shows isolines of constant polar angles of the scattered electron for the case of the BPC (ZEUS BPC 1995) and the main detector (ZEUS SVTX 1995) in comparison to the detector acceptance as of 1994 (ZEUS 1994 and ZEUS SVTX 1994).

<sup>1</sup>Initial State Radiation.

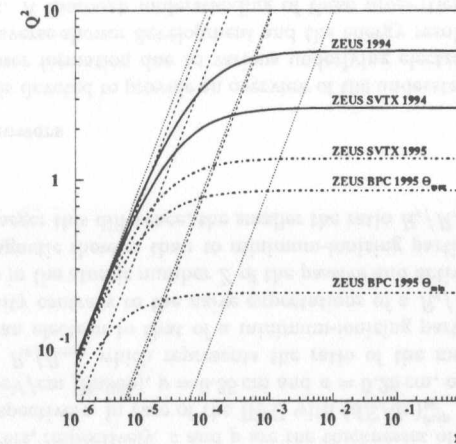


Figure 5.2: Isolines of constant polar angles (solid and dashed-dotted lines) and constant energy of the scattered electron (5, 15 and 25 GeV) (dashed lines). Lines of constant  $y$  values ( $y = 0.01, 0.1, 1$ ) are shown as well (dotted lines).

The design of a small electromagnetic calorimeter, the Beam Pipe Calorimeter (BPC), started in the summer of 1994. The construction was completed by the spring of 1995. The BPC participated then successfully for the first time at the 1995 HERA run to collect data for the first  $F_2$  measurement at low  $Q^2$  and very low  $x$  at ZEUS presented in this thesis<sup>2</sup>.

The following section provides an overview of basic concepts in calorimetry which are relevant for the design of a small electromagnetic calorimeter. The requirements on the design are focused on in section 5.3. The actual design and construction will be discussed in detail in section 5.4 followed by a brief overview of the readout and trigger electronics, the monitoring system and the survey of this new component within the existing ZEUS detector.

## 5.2 Basic concepts in calorimetry

### Principle idea of calorimetry

A calorimeter is conceptually the prime device to measure the energy of high energy particles [Fa82]. The incident particle deposits its energy within the calorimeter volume which is basically a block of matter through the formation of a shower of decreasingly lower-energy particles. This requires that the detector volume is deep enough to absorb the energy of the incident particle. Most of the deposited energy is dissipated and appears in the form of heat and only a small fraction of the deposited energy is converted into a measurable signal (e.g. scintillation light, Cherenkov light or ionization charge) depending on the type of material being used for the conversion. Provided that this fraction is constant, the measurable signal is proportional to the energy of the primary particle. Using a particle beam of known incident energy provides a means of absolute energy scale calibration. A calorimeter offers a variety of unique properties:

<sup>2</sup>The new BPC replaced a previous calorimeter described in [Lo96].

- The longitudinal dimension of the detector necessary to absorb the energy  $E$  of the primary particle scales only logarithmically with the energy  $E$ .
- The fast time response of calorimeters, depending on the type of readout, allows to accept very high event rates and provides information for a trigger decision at a very early stage.
- The energy resolution of well designed calorimeters improves with increasing energy and behaves like  $\sigma_E/E \propto 1/\sqrt{E}$ .
- The response of a calorimeter depends on the particle type. The shower formation of hadrons is very different from those of electrons. Together with a spatial and/or longitudinal segmentation of the calorimeter design, employing the different spatial and/or longitudinal energy depositions of electromagnetic and hadronic showers, provides a means of electron/hadron separation. In addition, spatial segmentation allows to measure the impact position of the incident particle.

### Calorimeter design

Two calorimeter designs are commonly used. In a *homogeneous calorimeter*, the whole detector is made out of one medium which serves as the main absorber as well as the active medium to produce a measurable signal. Heavy crystals such as BGO ( $\text{Bi}_4\text{Ge}_3\text{O}_{12}$ ), NaI (detection mechanism: scintillation) or lead glass (detection mechanism: Cherenkov light) are well known materials used for a homogeneous calorimeter. Using individual crystals with a transverse dimension of typically a few centimeters in a matrix arrangement allows not only to measure the energy of the incident particle, but also its impact position and respective shower shape. The energy resolution is superior to other calorimeter designs and is mostly dominated by instrumental limitations over the intrinsic shower fluctuations. To maintain the capability of crystal-type calorimeters, to measure electron and photon energies with high precision in a high-radiation environment such as at LHC<sup>3</sup>, places very tight constraints on the radiation hardness and precision calibration [Gr94].

In a *sampling calorimeter*, two different materials are used for the energy dissipation and measurement. Passive absorber plates and active detector layers are arranged in a sandwich structure. The absorber material consists typically of a heavy material such as lead, tungsten or uranium. The thickness of the absorber material is chosen to provide a complete energy deposition up to the highest expected energies taking into account spatial constraints and the requirements on the energy resolution. A common choice of the active material is the use of scintillators [Sc81]. The fast time response of scintillators allows to use calorimeters of such type for fast timing applications. Segmentation of the active layers provides a means of position measurement and electron/hadron separation. A complete energy deposition of high energy hadrons within a calorimeter requires typically a much larger depth compared to the energy measurement of electrons. Sampling calorimeters are therefore a common choice in the design of hadronic-type calorimeters since the thickness of the absorber plates can be chosen accordingly. Fluctuations due to the sampling-type energy measurement in the active layer contribute as well to the energy resolution and lead to an additional source of uncertainty in the energy measurement besides the intrinsic shower fluctuations. Ignoring any instrumental limitations, the typical energy resolution of electromagnetic sampling calorimeters is worse than those for homogeneous calorimeters.

<sup>3</sup>Large Hadron Collider.

The deposited energy within the active layers of a sampling calorimeter is only a small fraction of the total deposited energy. This fraction is known as the *sampling fraction*  $R^i$ :

$$R^i = \frac{E_{\text{active}}^i}{E_{\text{active}}^i + E_{\text{passive}}^i} \quad (5.1)$$

where  $E_{\text{active}}^i$  and  $E_{\text{passive}}^i$  are the total energies deposited in the active and passive layers, respectively. The index  $i$  denotes the particle type. This fraction amounts to about 4% ( $i = e$ , electrons) for the Beam Pipe Calorimeter. Only a small fraction of the latter is in turn available to be converted into a measurable signal such as scintillation light.

The mean energy deposition within the active and passive layers due to ionization caused by a charged particle is given by the *Bethe-Bloch formula* [Ro61]:

$$\frac{dE}{dx} = \frac{4\pi N_0 z^2 e^4 Z}{mv^2 A} \left[ \ln \frac{2mv^2}{I(1-\beta^2)} - \beta^2 \right] \quad (5.2)$$

where  $m$  is the electron mass,  $z$  and  $v$  are the charge (in units of  $e$ ) and velocity of the ionizing particle,  $\beta = v/c$ ,  $N_0$  is the Avogadro constant,  $Z$  and  $A$  are the atomic number and atomic weight of the medium, and  $x$  is the path length in the medium measured in  $\text{g}/\text{cm}^2$ . The quantity  $I$  is an effective ionization potential, approximately given by:  $I = 10 \cdot Z$  [eV].

The above formula describes only the ionization loss within gases. To account for the ionization loss within solid materials a *density correction*  $\delta$  has to be applied to equation 5.2. The effect of the density correction  $\delta$  is to damp the rise of  $dE/dx$  at high energies.

The sampling fraction  $R$  is typically normalized relative to the sampling fraction of a hypothetical *minimum ionizing particle* (*mip*) whose energy loss  $(dE/dx)^{\text{mip}}$  corresponds to the minimum in  $(dE/dx)^i$  which is common to all particles  $i$ .  $R^{\text{mip}}$  is given as follows:

$$R^{\text{mip}} = \frac{a(dE/dx)_{\text{active}}^{\text{mip}}}{a(dE/dx)_{\text{active}}^{\text{mip}} + p(dE/dx)_{\text{passive}}^{\text{mip}}} \quad (5.3)$$

where  $(dE/dx)_{\text{active}}^{\text{mip}}$  and  $(dE/dx)_{\text{passive}}^{\text{mip}}$  are the mean ionization losses per unit length in the active and passive layers, respectively.  $a$  and  $p$  are the thicknesses of the corresponding active and passive layers, respectively. In case of the BPC with  $(dE/dx)_{\text{W}}^{\text{mip}} = 22.4 \text{ MeV}/\text{cm}$  [Ba96b],  $(dE/dx)_{\text{SCI}}^{\text{mip}} = 2.01 \text{ MeV}/\text{cm}$  [Ba96b],  $p = 0.35 \text{ cm}$  and  $a = 0.26 \text{ cm}$ , one obtains  $R_{\text{mip}} = 0.062$ . The relative fraction  $R_e/R_{\text{mip}}$  which represents the ratio of the measurable fraction of the deposited energy for an electron to that of a minimum-ionizing particle is equal to 0.64 and therefore less than unity contrary to the naive expectations of a  $R_e/R_{\text{mip}}$  ratio to be equal to one. Large differences in the atomic number  $Z$  of the passive and active layers lead to a smaller response to electromagnetic showers than to minimum-ionizing particles of equivalent energy ( $R_e/R_{\text{mip}} < 1$ ). The larger this difference, the smaller the ratio  $R_e/R_{\text{mip}} < 1$  (*transition effect*) [Wi87].

### Electromagnetic showers

The following section is devoted to provide an overview of the understanding of electromagnetic showers, i.e. the shower formation due to various underlying electromagnetic processes, the longitudinal and transverse shower development and the energy resolution of electromagnetic sampling calorimeters. A thorough understanding of these properties are of vital importance in the design of an electromagnetic sampling calorimeter.

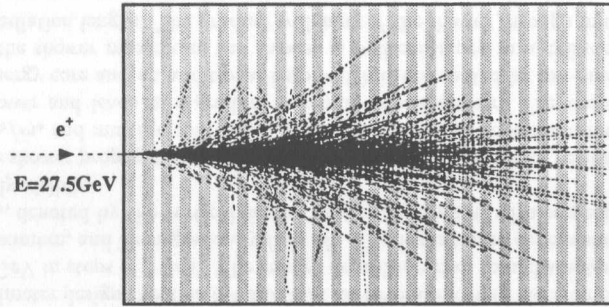


Figure 5.3: Simulation of an electromagnetic shower within a sampling calorimeter (BPC) due to a 27.5 GeV positron. The shaded layers denote the absorber plates (tungsten) and the white layers the active plates (scintillator).

A high energy electromagnetic particle which is intercepted by a calorimeter loses its energy through the formation of an electromagnetic shower and the subsequent energy deposition within the calorimeter volume. During the formation of a shower, secondary particles are produced with decreasing energy such as electrons/positrons and photons. The underlying processes which lead to the actual shower formation and the energy deposition in the active layers have a characteristic energy dependence which determines their relative importance during the history of an electromagnetic shower. A detailed understanding of the interactions of electrons/positrons and photons with matter is therefore essential. Electrons and positrons lose their energy through the following channels: Ionization, bremsstrahlung, positron annihilation, Møller scattering and Bhaba scattering. At energies above 100 MeV, the main mode of energy loss is bremsstrahlung. This process becomes energy independent above approximately 1 GeV. Below 100 MeV, electrons/positrons start to lose their energy dominantly through ionization. The three main interactions of photons in matter are: pair production, Compton scattering and photoelectric effect. For energies above 100 MeV, the pair production process is the dominant mode and becomes approximately energy independent above 1 GeV. Photons are by far more penetrating in matter than charged particles due to the much smaller cross-section of the above three processes. A photon beam is not degraded in energy like an electron/positron beam since the initial photon is removed in all the above three interaction modes. A photon beam is only degraded in its intensity:

$$I(x) = I(0)e^{-\mu/x} \quad (5.4)$$

where  $I(0)$  is the incident beam intensity,  $x$  the thickness of the absorber penetrated by the photon beam and  $\mu$  the absorption coefficient which is related to the total cross-section in terms of pair production, Compton scattering and photoelectric effect.

The formation of an electromagnetic shower results from the combined effect of these energy loss (electron/positrons) and interaction (photons) mechanisms. Let the incident particle be a positron with a primary energy well above 1 GeV. The development of the electromagnetic shower in matter will then be dominated by bremsstrahlung in the first step and the succession of bremsstrahlung and pair production among secondary produced electrons/positrons and photons, respectively. The number of particles will therefore drastically increase from the first interaction onwards. A cascade of particles is formed around the incident direction of the primary positron. The propagation of the cascade stops when the mean energy of the

shower particles reaches a critical value  $\epsilon_0$ .  $\epsilon_0$  is defined as the energy for which the energy loss caused by bremsstrahlung is equal to the ionization loss. The energy loss through ionization for electrons/photons and the interactions of photons by Compton scattering and the photoelectric effect will then dominate.

Figure 5.3 shows a cut view in the  $X - Z$ -plane<sup>4</sup> of the BPC indicating the sandwich structure of the tungsten and scintillator layers (Section 5.4). Tracks of secondary produced particles clearly display the cascade-type structure of an electromagnetic shower.

All above mentioned processes of electrons/positrons and photons in matter are well-understood processes in quantum electrodynamics (QED) and allow a detailed quantitative shower description via Monte-Carlo simulations (Chapter 6).

The amount of energy loss per unit length through bremsstrahlung is mainly determined by the density of electrons in the medium under consideration. The mean energy loss due to bremsstrahlung can be written in the following form:

$$\frac{dE}{E} = -\frac{dx}{X_0} \Leftrightarrow E = E_0 e^{-x/X_0} \quad (5.5)$$

where  $x$  is the thickness of the material,  $X_0$  the radiation length and  $E_0$  the impact energy. If the distance  $x$  is measured in units of  $X_0$ , the energy loss  $dE/dx$  becomes material independent.  $X_0$  measures the distance for which the mean energy of an incoming electron/positron beam dropped down by a factor  $1/e$  due to bremsstrahlung. The radiation length is given as follows [Ro61]:

$$\frac{1}{X_0} = 4\alpha \frac{N_A}{A} \frac{Z(Z+1)r_e^2 \ln(183Z^{-1/3})}{1 + 0.12(Z/82)^2} \quad (5.6)$$

where  $X_0$  is given in units of  $\text{g}/\text{cm}^2$ .  $\alpha$  is the fine structure constant,  $A$  the atomic weight,  $Z$  the atomic number,  $N_A$  the Avogadro constant and  $r_e$  the classical electron radius. An approximate estimate for  $X_0$  yields [Am81]:

$$X_0 \simeq 180 \frac{A}{Z^2} \left[ \frac{\text{g}}{\text{cm}^2} \right] \left( \frac{\Delta X_0}{X_0} < \pm 20\% \quad 13 \leq Z \leq 92 \right) \quad (5.7)$$

The critical energy  $\epsilon_0$  determines the end of the actual shower formation and the beginning of the energy loss within a medium via ionization:

$$\left( \frac{dE}{dx} \right)_{\text{bremsstrahlung}} = \left( \frac{dE}{dx} \right)_{\text{ionization}} \quad (5.8)$$

$\epsilon_0$  is approximately given by [Am81]:

$$\epsilon_0 \simeq \frac{550}{Z} [\text{MeV}] \left( \frac{\Delta \epsilon_0}{\epsilon_0} < \pm 10\% \quad 13 \leq Z \leq 92 \right) \quad (5.9)$$

Besides detailed MC-simulations of electromagnetic showers, it is often useful to evaluate approximate quantities concerning the shower formation such as the depth  $t_{\text{max}}$  corresponding to the maximum number of shower particles  $N_{\text{max}}$  and the mean depth  $t_{\text{med}}$  for which half of the total energy is deposited. Rossi provided an analytical description of the electromagnetic shower formation based on various simplifications [Ro61]. The cross-section of ionization is assumed to be energy independent and multiple and Compton scattering are neglected. This approximation is known as *Rossi's approximation B*. With  $y = E/\epsilon_0$  and  $t = x/X_0$ , Rossi provided the following quantities given in Table 5.1.

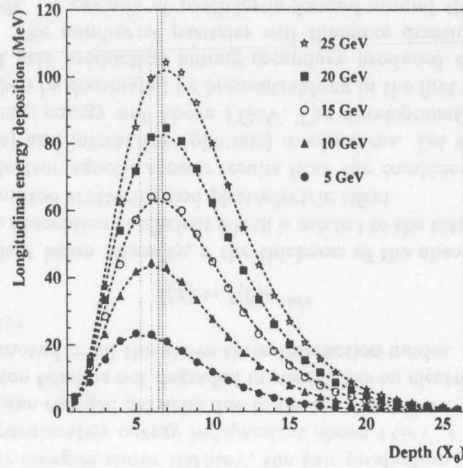


Figure 5.4: Longitudinal shower profile for different electron energies using an EGS4 MC-simulation of the BPC.

quantity	incident electron	incident photon
$t_{max}$	$\ln y - 1$	$\ln y - 0.5$
$t_{med}$	$t_{max} + 1.4$	$t_{max} + 1.7$
$N_{max}$	$\frac{0.3y}{\sqrt{\ln y - 0.37}}$	$\frac{0.3y}{\sqrt{\ln y - 0.31}}$

Table 5.1: Electromagnetic shower quantities based on the approximation B by Rossi.

The longitudinal shower profile  $dE/dt$  where  $t$  is the calorimeter depth measured in units of  $X_0$  has been parameterized in the following form [Lo75]:

$$\frac{dE}{dt} = E_0 \frac{b^{\alpha+1}}{\Gamma(\alpha+1)} t^\alpha e^{-bt} \quad (5.10)$$

The parameters  $\alpha$  and  $b$  are related through the position of the shower maximum  $t_{max} = \alpha/b$ . Figure 5.4 shows the longitudinal shower profile as determined from an EGS4 MC-simulation of the BPC calorimeter design (Section 5.4 and 6.2) for several incident electron energies between 5 GeV and 25 GeV in steps of 5 GeV. The energy deposition rises to a characteristic maximum, the shower maximum, and then gradually falls off. The logarithmic dependence of the shower maximum  $t_{max}$ , denoted by the vertical dotted lines in Figure 5.4, with respect to the incident energy is clearly visible.

The transverse shower propagation is determined by the typical angle of bremsstrahlung emission  $\theta_{brems} \sim p_e/m_e$  and multiple scattering. Multiple scattering is dominant for the low-energy part of the shower and leads to a gradual widening of the shower. The shower consists of a central high-energy core and an additional halo which is dominated by low-energy shower particles. Up to the shower maximum, the shower is well contained in a cylinder with a radius less than one radiation length. The gradual widening of the shower through multiple scattering

<sup>4</sup>See section 4.1 for a definition of the ZEUS coordinate system.

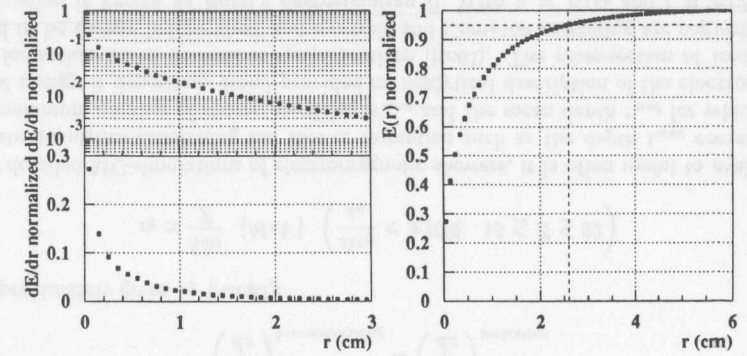


Figure 5.5: Differential and integrated radial shower distribution using an EGS4 MC-simulation of the BPC for an electron impact energy of 25 GeV.

scales with a characteristic quantity known as *Molière radius*  $R_M$ . Multiple scattering theory allows to estimate  $R_M$ :

$$R_M = E_s \frac{X_0}{c_0} \quad (5.11)$$

with  $E_s = 21$  MeV. An approximate formula for  $R_M$  is given as follows [Am81]:

$$R_M \simeq 7 \frac{A}{Z} \left[ \frac{\text{g}}{\text{cm}^2} \right] \left( \frac{\Delta R_M}{R_M} < \pm 10\% \quad 13 \leq Z \leq 92 \right) \quad (5.12)$$

Approximately 95% of the total energy of an electromagnetic shower is contained within a radius of  $R(95\%) \simeq 2R_M$  [Fa85]. Several parameterizations can be found in the literature for the transverse shower profile (Section 8.4). Common to most of them is the sum of two exponentials to take into account the central core surrounded by a halo of low-energy shower particles. Such a parameterization has been suggested by [Fe88].

$$\frac{dE}{dr} = \frac{1}{N} [e^{-\sqrt{r/\lambda_1}} + C_{12} e^{-r/\lambda_2}] / r \quad (5.13)$$

where  $\lambda_1$  and  $\lambda_2$  are attenuation coefficients describing the two transverse shower components,  $C_{12}$  measures their relative contribution,  $N$  is a normalization constant and  $r$  is the radial distance to the shower center in units of  $R_M$ . Figure 5.5 shows the differential ( $dE/dr$ ) and the integrated ( $E(r)$ ) radial shower distribution using an EGS4 simulation of the BPC with  $r$  measured in cm. The dashed lines on the right plot indicate the case for  $R(95\%)$  which is equal to 26 mm. Using the approximation  $R(95\%) \simeq 2R_M$  yields  $R_M \simeq 13$  mm.

For a medium with  $N$  compounds, the radiation length  $X_0$  and the Molière radius  $R_M$  can be evaluated as follows applying Bragg's rule [Le87]:

$$\frac{1}{X_0} = \sum_{i=1}^N w_i \left( \frac{1}{X_{0i}} \right) \quad (5.14)$$

$$\frac{1}{R_M} = \sum_{i=1}^N w_i \left( \frac{1}{R_{Mi}} \right) \quad (5.15)$$

$$w_i = \frac{a_i A_i}{\sum_{i=1}^N a_i A_i} \quad (5.16)$$

where  $a_i$  is the number of atoms and  $A_i$  the atomic weight of the  $i$ th element.

The principle idea for the energy measurement within a calorimeter can be understood through the term track length  $T$ .  $T$  is defined as the total length of all charged particle tracks within a calorimeter. It depends on the minimum detectable energy  $E_{min}$ . For  $E_{min} = 0$ ,  $T$  is simply given by the ratio of the incident energy  $E_0$  to the critical energy  $\epsilon_0$ ,  $T = E_0/\epsilon_0$ . With increasing  $E_{min}$ , the total track length  $T$  will decrease as one would expect it for the case of a realistic detector. To take into account a finite minimum detectable energy  $E_{min}$ , a correction factor  $F(z)$  has to be applied to the ratio of  $E_0/\epsilon_0$ . The following empirical parameterization of  $F(z)$  provides an approximation for the total track length  $T$  in a realistic detector environment [Am81]:

$$T = F(z) \frac{E_0}{\epsilon_0} \quad (5.17)$$

$$F(z) = e^z \left[ 1 + z \ln \left( \frac{z}{1.526} \right) \right] \quad (5.18)$$

$$z = 4.58 \frac{Z E_{min}}{A \epsilon_0} \quad (5.19)$$

The total track length is proportional to the incident energy  $E_0$ . Thus, the total energy deposited through ionization is proportional to the total incident energy  $E_0$ . This is the main ingredient of the energy measurement of high-energy particles using a calorimeter.

Fluctuations among the total track length  $T$  lead to fluctuations in the measured energy. The characteristics of these *intrinsic fluctuations* can be understood as follows. The total number of energy depositions can be estimated as follows:  $N_{max} = E_0/E_{min}$ . Using Poisson statistics among the total number of energy depositions one obtains:

$$\left( \frac{\sigma_E}{E} \right) \sim \left( \frac{\sigma_{N_{max}}}{N_{max}} \right) = \frac{1}{\sqrt{N_{max}}} \propto \frac{1}{\sqrt{E_0}} \quad (5.20)$$

The energy resolution is proportional to  $1/\sqrt{E_0}$ . This holds only for an ideal situation of negligible instrumental effects, full shower containment and a homogeneous calorimeter design. Shower leakage results in a degradation of the energy resolution where longitudinal shower leakage compared to transverse shower leakage has been shown to have a much larger impact on the energy resolution [Fa85]. A sampling calorimeter design leads to an additional component of the energy resolution due to the sampling-type energy measurement.

In a sampling calorimeter, one determines not the total track length  $T$  but only a fraction of it depending on the thickness of passive and active absorber plates. The total number of crossings  $N_x$  which determine the size of the measurable signal is then given by:

$$N_x = \frac{T_d}{d} = F(z) \frac{E_0}{\Delta E} = F(z) \frac{E_0}{\epsilon_0 d} \quad (5.21)$$

where  $T_d$  is the sum of all charged particles tracks in the active layers,  $\Delta E$  the energy loss per-unit-cell and  $d$  the gap between two active layers. Assuming that the number of crossings  $N_x$  are not correlated and their number follows a normal distribution,

$$\left( \frac{\sigma_E}{E} \right)_{\text{sampling}} \sim \left( \frac{\sigma_{N_x}}{N_x} \right) = \frac{1}{\sqrt{N_x}} \quad (5.22)$$

one can determine the *intrinsic sampling fluctuations* as follows [Fa85]:

$$\left( \frac{\sigma_E}{E} \right)_{\text{sampling}} = 3.2\% \sqrt{\frac{\Delta E}{F(z) \langle \cos \theta \rangle E_0}} \quad (5.23)$$

The factor  $\langle \cos \theta \rangle$  takes into account that the crossing of the sampling layers can occur under angles different from  $90^\circ$ . A parameterization of  $\langle \cos \theta \rangle$  is given as follows [Am81]:

$$\langle \cos \theta \rangle = \cos \left( \frac{E_s}{\pi \epsilon_0} \right) \quad (5.24)$$

Sampling fluctuations become smaller the larger the number of crossings  $N_x$  and thus the sampling frequency.

Additional sources which lead to a degradation of the energy resolution are due to *Landau fluctuations* and *path-length fluctuations* [Fa85]. The energy deposition through ionization follows an asymmetric Landau-distribution. This leads to an additional contribution to the energy resolution known as *Landau fluctuations*. This effect plays an important role for very thin layers such as gaseous detectors with energy deposition of a few keV. It can be ignored in the case of scintillator or silicon active layers with energy depositions of a few MeV.

Path length fluctuations arise due to the fact that low-energy electrons have a high probability to be multiply scattered into the active layers. These electrons are then able to pass larger distances within the active layers and deposit therefore more energy. This leads to additional fluctuations for the energy deposition in the active layers. This effect is much larger in gas than in solid detectors [Am81].

Landau and path length fluctuations give only a small contribution to the intrinsic sampling fluctuations in dense active layers.

It should be noted that the formula given above to determine the intrinsic sampling fluctuations provide only a rough estimate and are mainly to illustrate the qualitative understanding of the relation between the intrinsic shower processes and the actual detector performance. They are not meant to replace detailed studies using a MC-simulation.

All above sources of uncertainty on the energy measurement are specific properties of the energy measurement within a calorimeter (intrinsic shower fluctuations) and the sampling-type calorimeter design (sampling fluctuations).

Instrumental effects represent additional sources of uncertainty on the energy measurement and have to be well understood in order to limit their impact on the overall energy resolution within a calorimeter. These instrumental uncertainties can arise from: energy leakage (transverse and longitudinal), non-uniformities and photocathode statistics in PMT<sup>5</sup>-readout based calorimeters. In PMTs the release of photoelectrons on the photocathode due to photons and the subsequent photoelectron multiplication is a statistical process which is governed by Poisson statistics. The contribution of the photocathode statistics therefore decreases with increasing number of produced photoelectrons.

To account for various sources of uncertainties which do not necessarily decrease as  $1/\sqrt{E}$ , one can expand the variance of the energy distribution in a power series of  $E$  [Go81]:

$$\sigma_E^2 = \sigma_0^2 + \sigma_1^2 E + \sigma_2^2 E^2 + \dots \quad (5.25)$$

If one divides this expansion in  $E$  by  $E^2$ , one obtains an expression for the energy resolution  $\sigma_E/E$ :

$$\left( \frac{\sigma_E}{E} \right)^2 = \frac{\sigma_0^2}{E^2} + \frac{\sigma_1^2}{E} + \sigma_2^2 + \dots \quad (5.26)$$

<sup>5</sup>Photomultiplier tube.

Any additional sources of uncertainty will then be represented by one of the constants  $\sigma_i$  and can be obtained from a fit to the measured energy resolution for various impact energies such as in a test-beam environment. Calorimeter specific uncertainties (intrinsic shower fluctuations, sampling fluctuations) are represented by the constant  $\sigma_1$  known as the stochastic term. In addition, photocathode statistics in PMT-readout based calorimeters contribute as well to the constant  $\sigma_1$ . The  $\sigma_0$ -term arises from contributions which are only important at small energies such as electronics noise. The  $\sigma_2$ -term (constant term) affects the whole energy resolution curve as a function of  $E$ . It includes therefore imperfections of the calorimeter design and the calibration. The  $\sigma_2$ -term also includes intrinsic shower fluctuations, e.g. the electromagnetic/hadronic response in hadronic calorimeters.

### 5.3 Requirements

#### General

A precise energy and position reconstruction at low  $Q^2$  using a small electromagnetic calorimeter, the Beam Pipe Calorimeter (BPC), imposes several tight constraints on the energy and position resolution as well as the understanding of the energy calibration, the intrinsic position bias of the type of position reconstruction algorithm and the detector alignment. The following discussion will be restricted to the two independent kinematic variables  $y$  and  $Q^2$  to describe the  $ep$  inelastic scattering process at low values of  $Q^2$  (Section 2.4). The goal is to develop a set of minimum requirements on the energy and position measurement using a small electromagnetic calorimeter to achieve a precise measurement of the proton structure function  $F_2$  over several bins in  $y$  and  $Q^2$ .

In case of very small electron scattering angles, the kinematic variables  $y$  and  $Q^2$  can be written in the following form using  $\vartheta'_e = \pi - \theta'_e$  instead of  $\theta'_e$ :

$$Q^2 = 4E_e E'_e \sin^2 \left( \frac{\vartheta'_e}{2} \right) \simeq E_e E'_e \vartheta_e'^2 \quad (5.27)$$

$$y = 1 - \frac{E'_e}{E_e} \cos^2 \left( \frac{\vartheta'_e}{2} \right) \simeq 1 - \frac{E'_e}{E_e} \quad (5.28)$$

This approximation shows that  $y$  is to first order independent of the scattering angle  $\vartheta'_e$ , provided that  $\vartheta'_e$  is very small. The relative errors on  $y$  and  $Q^2$  at low values of  $\vartheta'_e$  are given as follows:

$$\left( \frac{\delta Q^2}{Q^2} \right) = \left( \frac{\delta E'_e}{E'_e} \right) \oplus \left( \frac{2}{\vartheta'_e} \right) \delta \vartheta'_e \quad (5.29)$$

$$\left( \frac{\delta y}{y} \right) = \left( 1 - \frac{1}{y} \right) \left( \frac{\delta E'_e}{E'_e} \right) \oplus \left( \frac{1}{y} - 1 \right) \left( \frac{\vartheta'_e}{2} \right) \delta \vartheta'_e \quad (5.30)$$

The proton structure function  $F_2(x, Q^2)$  is extracted from the double differential inelastic  $ep$  cross-section  $d^2\sigma/dy dQ^2$  over a certain bin size  $(\Delta y, \Delta Q^2)$  in the  $y - Q^2$  phase space. The size of the chosen bins are primarily restricted by the experimental resolution of the kinematic variables  $y$  and  $Q^2$  provided that the number of measured events are large enough that statistical fluctuations are small. In this case, the resolution of the kinematic variables  $y$  and  $Q^2$  and therefore the resolution of the measured energy and angle define the number of bins in a particular kinematic region for which the proton structure function  $F_2(x, Q^2)$  can be extracted.

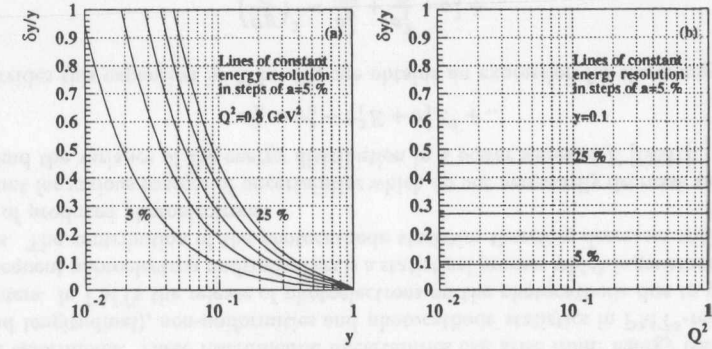


Figure 5.6: Relative error on  $y$  as function of  $y$  (a) and  $Q^2$  (b) for constant values of the energy resolution  $\delta E'_e/E'_e = a/\sqrt{E'_e}$  with  $a = 5, 10, 15, 20$  and  $25\%$ .

The relative error on the angle  $\vartheta'_e \simeq r/Z$  is determined by the error on the position measurement  $r = \sqrt{X^2 + Y^2}$  and the error on the  $Z$  position ( $Z = Z_{\text{vertex}} + Z_{\text{BPC}}$ ) and is given by:

$$\left( \frac{\delta \vartheta'_e}{\vartheta'_e} \right) = \left( \frac{\delta r}{r} \right) \oplus \left( \frac{\delta Z}{Z} \right) \quad (5.31)$$

where  $Z_{\text{BPC}}$  is the surveyed  $Z$  position of the BPC and  $Z_{\text{vertex}}$  the  $ep$  vertex position with respect to the ZEUS coordinate system. Provided that the  $Z$  vertex position using the ZEUS CTD (Section 4.3) can be well reconstructed, the contribution from the  $Z$  vertex resolution can be ignored. As will be shown later, the angle of the scattered electron to be measured within the BPC does not leave any track in the ZEUS CTD. One therefore relies on the hadronic final state to determine the  $Z$  vertex position which in turn depends on the topology of the event. If there is no information from the CTD on the  $Z$  vertex position available, the width in the  $Z$  vertex distribution of the proton beam profile will then dominate the  $Q^2$  resolution.

Figure 5.6 shows the relative error  $\delta y/y$  as a function of  $y$  (a) and  $Q^2$  (b) for constant values of the energy resolution  $\delta E'_e/E'_e = a/\sqrt{E'_e}$  with  $a = 5, 10, 15, 20$  and  $25\%$ . The relative error on  $y$  depends drastically on the energy resolution.  $\delta y/y$  increases as expected for  $y \rightarrow 0$  and the energy resolution determines how low in  $y$  one can go. For  $\delta E'_e/E'_e = 0.15/\sqrt{E'_e}$  and  $y > 0.1$ , the relative error on  $y$  remains well below  $30\%$ . The relative error on  $y$  is as expected independent of  $Q^2$  as shown in Figure 5.6 (b) for  $y = 0.1$ .

The relative error on  $Q^2$ , as shown in Figure 5.7 (a) as a function of  $y$  for  $\delta E'_e/E'_e = a/\sqrt{E'_e}$  with  $a = 5, 10, 15, 20$  and  $25\%$ , shows for  $y < 0.8$  only a moderate dependence. For  $\delta E'_e/E'_e = 0.15/\sqrt{E'_e}$ , the relative error in  $Q^2$  is approximately  $6\%$  for  $0.1 < y < 0.8$  and  $Q^2 = 0.1 \text{ GeV}^2$ . The relative error on  $Q^2$  as a function of  $Q^2$  (Figure 5.7 (b)) for  $y = 0.8$  is almost flat up to  $Q^2 = 0.1 \text{ GeV}^2$  and drastically increases from there onwards. Figure 5.7 (c) and 5.7 (d) display the resolution in  $Q^2$  for fixed angular resolution of  $\delta \vartheta'_e = 0.03, 0.17, 0.33, 0.67$  and  $1.67 \text{ mrad}$  which translates into a position resolution of  $0.1, 0.5, 1.0, 2.0$  and  $5.0 \text{ mm}$  ignoring the contribution from the  $Z$  vertex resolution. For  $y < 0.8$ , the resolution in  $Q^2$  is well below  $7\%$  provided that the angular resolution is less than  $0.33 \text{ mrad}$  (Figure 5.7 (c) for  $Q^2 = 0.1 \text{ GeV}^2$ ). For  $Q^2 > 0.1 \text{ GeV}^2$  and an angular resolution of better than  $0.33 \text{ mrad}$ ,  $\delta Q^2/Q^2$  is flat in  $Q^2$  (Figure 5.7 (d) for  $y = 0.8$ ).

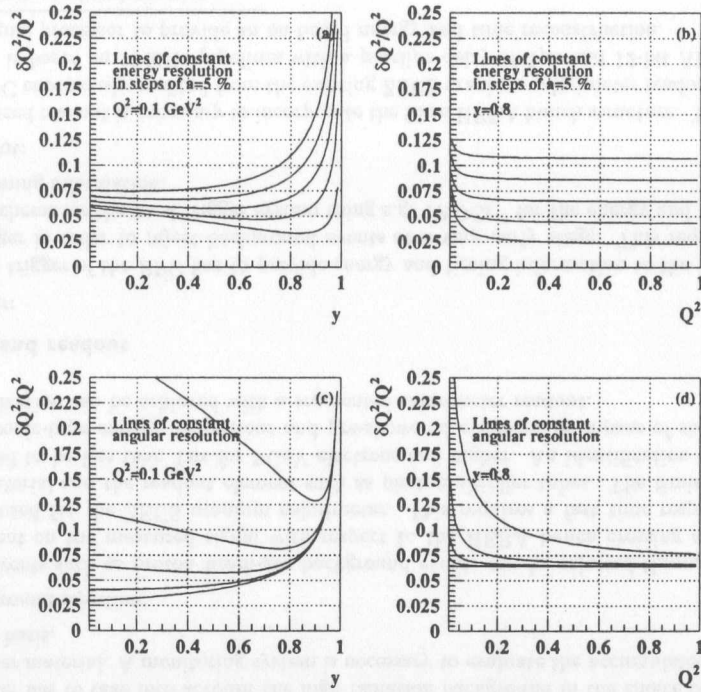


Figure 5.7: Relative error on  $Q^2$  as a function of  $y$  (a) and  $Q^2$  (b) for constant values of the energy resolution  $\delta E'_e/E'_e = a/\sqrt{E'_e}$  with  $a = 5, 10, 15, 20$  and  $25\%$  whereas  $\delta\vartheta'_e = 0.33$  mrad and as a function of  $y$  (c) and  $Q^2$  (d) for constant values of the angular resolution  $\delta\vartheta'_e = 0.03, 0.17, 0.33, 0.67$  and  $1.67$  mrad whereas  $\delta E'_e/E'_e = 0.15/\sqrt{E'_e}$ .

The accessible kinematic region for a small electromagnetic calorimeter (BPC) is shown in Figure 5.2. To achieve a measurement of  $F_2(x, Q^2)$  for  $y > 0.1$  and  $Q^2 > 0.1 \text{ GeV}^2$  over approximately eight bins in  $y$  and  $Q^2$ , an energy resolution of approximately  $15\%/\sqrt{E}$  and an angular resolution of less than  $0.33$  mrad is required. The latter requirement translates into a position resolution to be better than  $1$  mm ignoring the contribution from the  $Z$  vertex resolution.

Besides resolution effects, the accuracy of the energy calibration and the position bias of a small electromagnetic calorimeter is of vital importance to control systematic shifts in the determination of  $y$  and  $Q^2$  and therefore in  $F_2(x, Q^2)$ . The term position bias refers to the intrinsic position bias of the position reconstruction algorithm itself as well as to the accuracy of the detector alignment. Figure 5.8 shows the bias in  $y$  and  $Q^2$  as a function of  $y$  and  $Q^2$ , respectively. In Figure 5.8, (a) lines of constant energy shift  $\delta E'_e/E'_e$  of  $0.1, 0.5, 1.0, 2.5$  and  $5.0\%$  are drawn. Limiting systematic biases on  $y$  to be less than  $5\%$  translates into knowing the absolute energy scale to an accuracy of about  $0.5\%$  for  $y > 0.1$ . The bias on  $y$  drastically increases for  $y < 0.1$ . Exploring the region of low values of  $Q^2$  and  $y < 0.1$  using the Electron method provided that the energy resolution is well below  $0.15/\sqrt{E'_e}$  requires an extremely

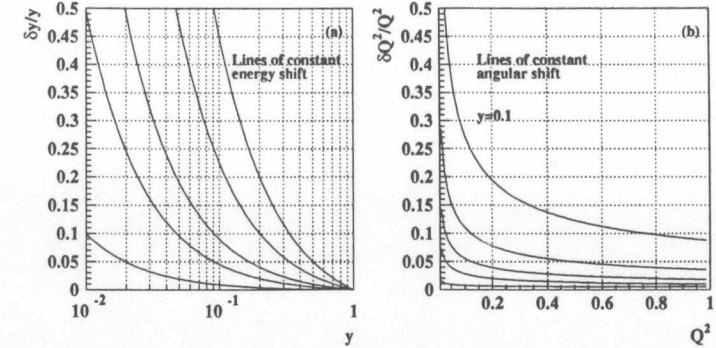


Figure 5.8: Systematic shift on  $y$  (a) (lines of constant energy shift  $\delta E'_e/E'_e$  of  $0.1, 0.5, 1.0, 2.5$  and  $5.0\%$ ) and  $Q^2$  (b) (lines of constant values in the position bias of  $0.1, 0.5, 1.0, 2.0$  and  $5.0$  mm) as a function of  $y$  and  $Q^2$ , respectively.

precise energy calibration of less than  $0.5\%$  to limit the bias on  $y$  to be at most  $10\%$  for  $y > 0.01$ . The bias in  $Q^2$ , as shown in Figure 5.8 (b) as a function of  $Q^2$  for constant values in the position bias of  $0.1, 0.5, 1.0, 2.0$  and  $5.0$  mm, increases towards low values of  $Q^2$ . For  $Q^2 > 0.1 \text{ GeV}^2$ , the bias in  $Q^2$  remains below  $5\%$  provided that a position bias of better than  $1$  mm can be achieved. For  $Q^2 > 0.1 \text{ GeV}^2$ , the difference in the bias on  $Q^2$  between a position bias of  $0.1$  mm and  $0.5$  mm is well below  $1\%$ .

Both the requirement on the energy calibration of  $0.5\%$  as well as the position bias to be less than  $1$  mm places very tight constraints on the energy and position reconstruction (Chapter 8).

### Calorimeter performance specifications

The following list provides an overview of various requirements on the specifications of a small electromagnetic calorimeter.

⇒ Energy and position resolution:

The energy resolution is expected to be at the level of  $15\%/\sqrt{E}$ . The design of a small electromagnetic calorimeter has to provide the capability of a position reconstruction via a segmented calorimeter readout with a position resolution to be better than  $1$  mm.

⇒ Longitudinal dimension:

As can be seen from Figure 2.6 (a), the energy of the scattered electron is kinematically limited to be less than  $27.5 \text{ GeV}$  in the low- $x$ -low- $Q^2$  region. The design has therefore to be such that it contains electron energies up to  $27.5 \text{ GeV}$  to avoid any degradation in the energy resolution due to longitudinal energy leakage. It has been shown by using an EGS4 MC-simulation that at least  $24X_0$  are necessary to sufficiently contain electron energies up to  $27.5 \text{ GeV}$ . In this case, the longitudinal energy leakage is approximately  $0.5\%$  (Figure 5.4). An overall spatial limitation in  $Z$  of about  $30$  cm restrict the type of possible absorber materials to those having a very small radiation length.

⇒ Transverse dimension:

The restricted space for a small electromagnetic calorimeter in both transverse directions  $X$  and  $Y$  requires a calorimeter such that the transverse spread of the electromagnetic shower and therefore the Molière radius is as small as possible to maximize the angular acceptance and thus the acceptance in  $Q^2$ . As can be seen from Figure 5.5, a Molière radius of approximately 13 mm can be achieved within a tungsten-scintillator calorimeter design based on an EGS4 MC-study. This is of particular importance to accept electrons as close as possible to the calorimeter edge to provide an acceptance towards very low values in  $Q^2$ .

⇒ Linearity:

The linearity is required to be well below 1%. This ensures an accurate energy measurement over the whole energy range of the scattered electrons up to the highest expected energies at the kinematic peak of 27.5 GeV.

⇒ Magnetic field:

The readout of a calorimeter using PMTs requires magnetic shielding since it has to be operated in the presence of the magnetic field of the ZEUS compensator and central magnet.

⇒ Radiation background:

The new calorimeter will be operated very close to the electron and proton beam at HERA. The radiation background is expected to be considerably higher compared to locations within the ZEUS detector at larger distances from the HERA beam [Ho93]. The design of the new calorimeter has to take into account the high radiation background in the choice of the active calorimeter material. A monitoring system is necessary to evaluate the accumulated dosage on a regular basis.

⇒ Background rejection:

Non  $ep$  events such as proton beam-gas background events can be rejected through a timing requirement on the measured signal with respect to the HERA bunch crossing as it is successfully used for the ZEUS uranium calorimeter. This requires a fast time response of the active material and the readout element such as photomultiplier tubes. The timing accuracy is expected to be less than 1 ns for 5 GeV electrons and higher. An identification of electrons over hadronic-type energy depositions and pre-showered electrons by means of shower width characterization can be achieved with a segmented calorimeter readout.

### Trigger and readout

⇒ Trigger:

The local trigger of the BPC has to provide energy and timing information to the ZEUS first-level trigger in order to reject background events at a very early stage. This requires a fast readout scheme for the local trigger system using e.g. FADCs<sup>6</sup> for the energy and fast TDCs<sup>7</sup> for the timing information.

⇒ Readout:

A specialized readout is necessary to incorporate the 96 ns HERA bunch structure. The readout of the BPC enormously profited from the existing ZEUS uranium calorimeter readout electronics which is based on 10 MHz pipelines with a pipeline delay of 5  $\mu$ s and 12-bit ADCs with a digital signal processor to provide an on-board energy and time reconstruction.

<sup>6</sup>Flash analog-to-digital converter.

<sup>7</sup>Time-to-digital converter.

### Calibration

⇒ Energy scale calibration:

To limit systematic biases in  $y$  to be less than 5%, the energy scale has to be determined at the level of 0.5%. Furthermore, the energy uniformity is expected to be at the level of 0.5%. Kinematical peak events as well as elastic  $\rho^0$  events will be used for the energy calibration of the new calorimeter.

⇒ Intrinsic position bias:

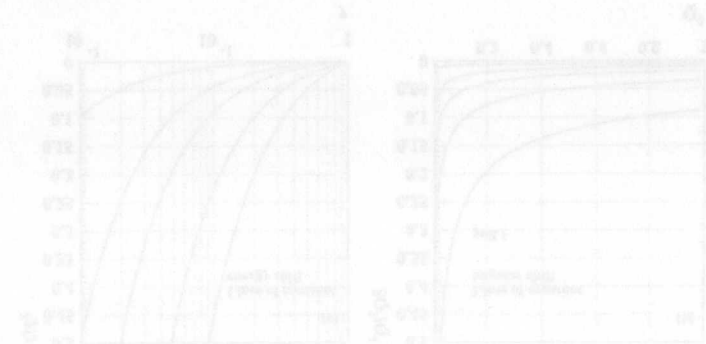
Any intrinsic position biases related to the position reconstruction algorithm are expected to be less than 1 mm.

⇒ Detector alignment:

The alignment accuracy of the BPC is expected to be well below 1 mm. This requires a precise optical survey procedure and possibly an in-situ alignment scheme. It will be shown in section 8.3.4 that elastic QED Compton events provide a means of in-situ position calibration.

⇒ Monitoring:

The operation of the BPC requires a set of calibration tools to monitor and calibrate the readout system which has been adapted from the readout monitoring system of the ZEUS uranium calorimeter. Furthermore, it requires various techniques to monitor the amount and effect of the high radiation background, such as radiation dose measurements using passive and active elements (TLD<sup>8</sup> meter, Si-diode radiation monitor) and <sup>60</sup>Co scans.



<sup>8</sup>Thermo-luminescence dosimeter

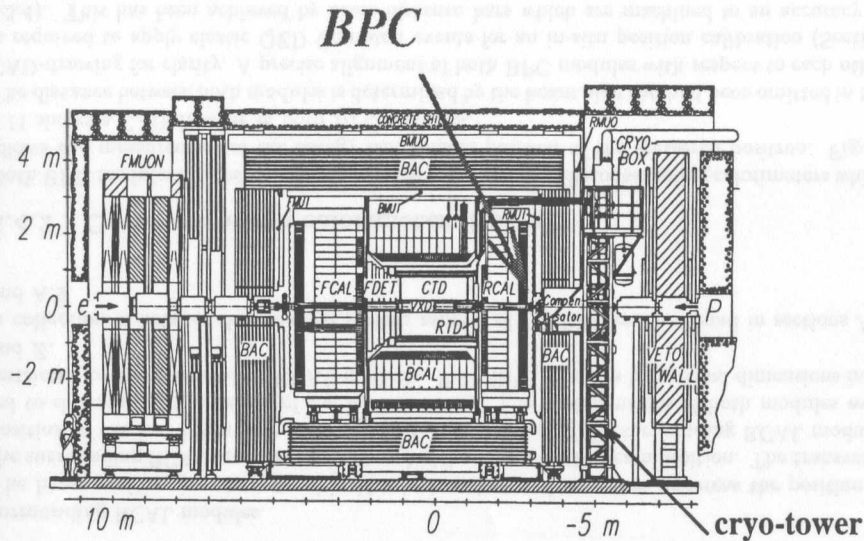


Figure 5.9: Longitudinal cut of the ZEUS detector. The upper arrow indicates the location of the BPC behind the RCAL and in front of the compensator magnet. The lower arrow points to the location of the BPC front-end electronics inside the cryo-tower.

## 5.4 Design and construction

Following the requirements on a Beam Pipe Calorimeter (BPC) for the ZEUS-experiment, the next sections are devoted to a detailed discussion on the actual design and construction of the BPC.

### 5.4.1 Geometry

The dimensions of the BPC are constrained in all three spatial coordinates due to various existing detector components in the rear (positron) direction<sup>9</sup>.

The BPC is located at 2937 mm from the interaction point in the rear direction. It is mounted in front of the compensator magnet and behind the RCAL. Figure 5.9 shows a longitudinal cut through the ZEUS-detector indicating the position of the BPC with respect to the ZEUS-detector and the location of the BPC front-end electronics inside the cryo-tower.

The design of the BPC incorporates a new beam pipe which was installed during the winter shutdown 1994/95 [Lo96].

In longitudinal direction, the BPC had to fit in the available space between the compensator magnet and the RCAL. In order to enlarge the limited available longitudinal space, the collimator C5, which had originally movable jaws, was replaced by fixed collimators. A new C5-counter was installed as well during the winter shutdown 1995/96 which requires much less space in

<sup>9</sup>See section 4.1 for a definition of the ZEUS coordinate system.

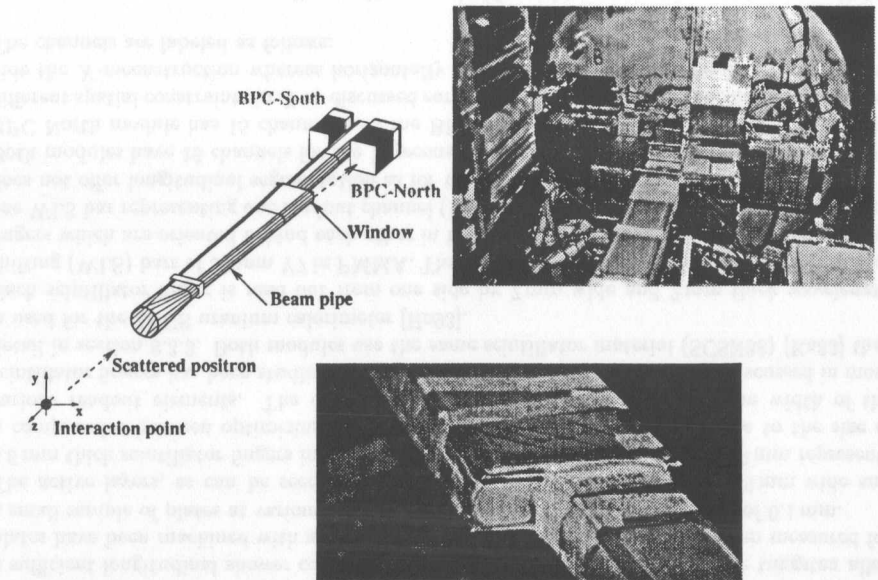


Figure 5.10: Schematic layout of the BPC and the new beam pipe (left) and photographs of the BPC modules and the North beam pipe exit window (right).

longitudinal direction than the previous C5-counter. The total available space in  $Z$  amounts to approximately 30 cm.

The transversal dimensions are determined by the position of the surrounding RCAL modules and the location of the new beam pipe. Two BPC modules were built and installed on either side of the new beam pipe. Following the geographical location of the ZEUS-experiment with respect to the HERA collider, one module is called BPC North and the other one BPC South. This design of two modules on either side of the beam pipe incorporates the two exit windows of the new beam pipe at 2498 mm from the interaction point in the direction of the positrons. Figure 5.10 shows a schematic layout of the new rear beam pipe section with the two BPC modules. The two photographs on the right side in Figure 5.10 show the two BPC modules within the ZEUS detector as seen from the interaction point with the RCAL being open. The lower photograph shows, in direction of the proton beam, the North beam pipe exit window.

The beampipe exit windows are made of 1.5 mm thick aluminum which equals to  $0.016 X_0$  and meets the requirement to have as little dead material in front of the BPC as possible. This enables positrons to exit the beam pipe with minimal interference. The transversal size of the exit windows determine the actual *fiducial volume* for the BPC modules which is substantially smaller in case of the BPC South module.

The inner diameter of the central beampipe was determined by the requirement that no part can be hit by direct or backscattered synchrotron radiation. This is the reason why the inner diameter of the South-window is at  $-75$  mm, whereas at the North-side it is at 39 mm. The outer dimensions as well as the height of the window on both sides were determined by the

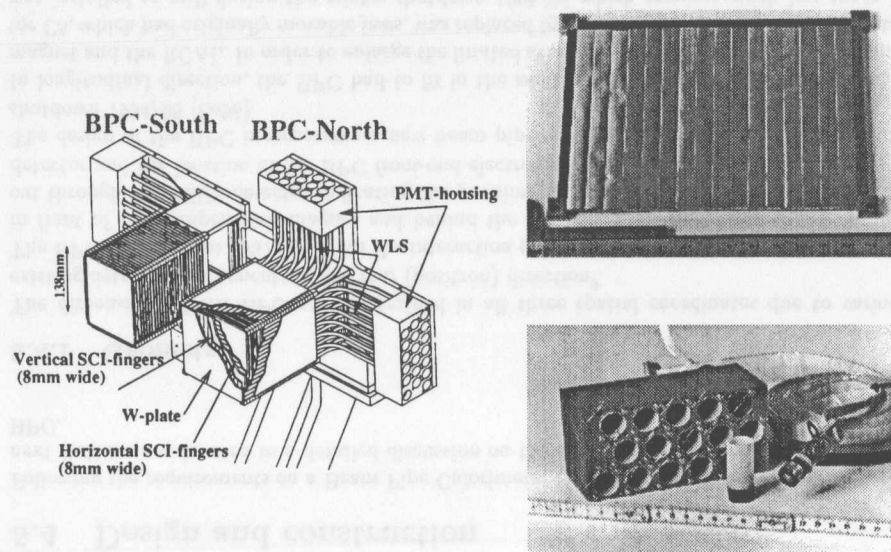


Figure 5.11: CAD drawing of both BPC modules (left) and photographs of a single plate (BPC South module) and a PMT support block with a PMT (Hamamatsu R5600-03) in the foreground.

surrounding RCAL modules.

The beam position is not centered inside the rear beam pipe section, whereas the position of the surrounding RCAL modules are centered with respect to the beam position. The transverse position of the rear beam pipe with respect to the position of the surrounding RCAL modules led to different  $X$ -dimensions of the BPC modules. The  $Y$  dimensions of both modules were restricted by the surrounding RCAL modules. Both BPC modules have equal dimensions in  $Y$  and  $Z$ .

A collection of detailed drawings on various aspects of the BPC can be found in sections A.1 and A.2.

#### 5.4.2 Overview of the calorimeter design

Both BPC modules are designed as segmented tungsten-scintillator sampling calorimeters which allows the measurement of the energy and impact position of the scattered positron. Figure 5.11 shows a CAD-drawing of both BPC modules.

The distance between both modules is determined by the beam pipe and had been omitted in the CAD-drawing for clarity. A precise alignment of both BPC modules with respect to each other is required to apply elastic QED Compton events for an in-situ position calibration (Section 8.3.4). This has been achieved by brass distance bars which are machined to an accuracy of 0.2 mm. Figure 5.12 shows a closeup view of both BPC modules with two of four brass distance bars on top of the beam pipe. The two other distance bars are mounted below the beam pipe

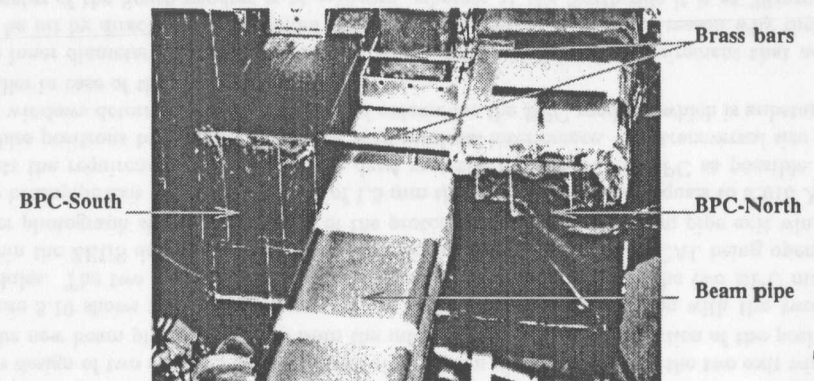


Figure 5.12: Closeup view of both BPC modules indicating the position of the upper two brass distance bars.

between both BPC modules. The brass bars are machined such that their respective ends fit into precisely machined holes on the BPC support structure.

The passive layers consist of 26 3.5 mm tungsten alloy plates (DENSIMET D18K) [P194]. The fraction of pure tungsten amounts to about 95.5%. The rest is given by a nickel-copper binder. This type of tungsten alloy offers improved machinability compared to pure tungsten and high densities similar to pure tungsten. The chosen tungsten alloy has a density of  $18 \text{ gcm}^{-3}$  and a radiation length of 3.87 mm. This yields an overall length of  $24X_0$  which is required to provide a sufficient longitudinal shower containment for electrons up to 27.5 GeV. The tungsten alloy plates have been machined with an accuracy of 0.1 mm. The thickness has been measured for a small sample of plates at various locations to confirm the required precision of 0.1 mm.

The active layers, as can be seen from Figure 5.11, consist of alternating 7.9 mm wide and 2.6 mm thick scintillator fingers in  $X$  and  $Y$ -direction. The chosen width of 7.9 mm represents a compromise between optimizing the position resolution and limitations due to the size of various readout elements. The dependence of the position resolution on the width of the scintillator fingers has been studied using an EGS4 MC-sample. This will be discussed in more detail in section 8.3.3. Both modules use the same scintillator material (SCSN38) [Ka83] that is used for the ZEUS uranium calorimeter [Ho93].

Each scintillator finger is read out from one side by 7 mm wide and 2 mm thick wavelength shifting (WLS) bars of 30ppm Y7 in PMMA. The scheme of the readout is such that scintillator fingers which are oriented behind each other in longitudinal direction are read out together by one WLS bar representing one readout channel (Figure 5.11). The chosen WLS-readout scheme does not offer longitudinal segmentation as for the ZEUS-calorimeter.

Both modules have 16 channels for the  $Y$ -reconstruction whereas for the  $X$ -reconstruction the BPC North module has 15 channels and the BPC South modules has 11 channels due to the different spatial constraints in  $X$  as discussed earlier. Vertically oriented scintillator fingers provide the  $X$ -reconstruction whereas horizontally oriented fingers provide the  $Y$ -reconstruction. The channels are labeled as follows:

$$X_{N1} \dots X_{N15} \text{ and } Y_{N1} \dots Y_{N16} \quad (5.32)$$

$$X_{S1} \dots X_{S11} \text{ and } Y_{S1} \dots Y_{S16} \quad (5.33)$$

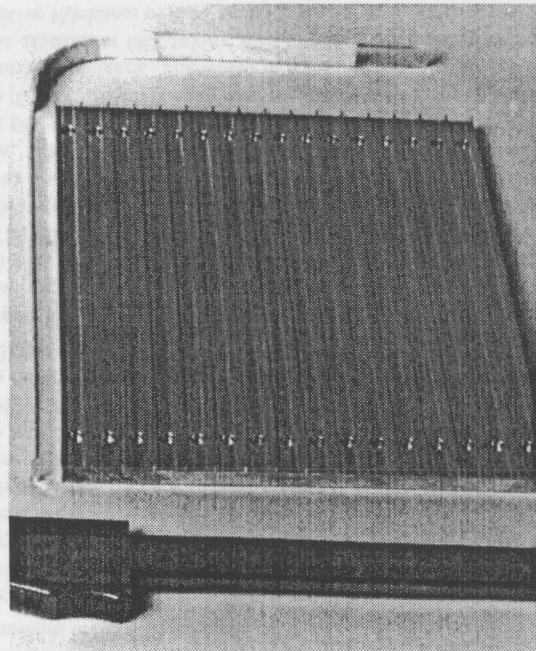


Figure 5.14: WLS (left) and WLS cassette (right). The aluminum lamellas are 0.5 mm wide.

using a lucite fibre light distribution system. This is an important tool to monitor the performance of each PMT.

Each BPC module has a single scintillator tile with a thickness of 5 mm at the back of the calorimeter with two sheets of 2 mm thick lead plates in the front and the back. It is being read out from two sides by WLS-bars which in turn, are read out by the same PMTs as the main BPC calorimeter modules. The back tile was included inside each BPC module as a possible tool to reject background events. It has not been included in the physics analysis of this thesis.

This design of the BPC modules incorporates all minimal requirements on a Beam Pipe Calorimeter for the ZEUS experiment. Some decisions on various aspects of the detector design represent a compromise between a precise measurement of  $F_2(x, Q^2)$  at low  $Q^2$  and very low  $x$  over several bins and the goal to achieve a first measurement of  $F_2(x, Q^2)$  on a short time scale. The design took advantage of the expertise in existing technologies at ZEUS in sampling calorimetry and the availability of various materials such as the scintillator and wavelength shifting material of the ZEUS uranium calorimeter to construct a tungsten-scintillator sampling calorimeter. This enormously reduced the time from the beginning of the design to the actual beginning of data taking with the BPC at ZEUS in 1995. It is understood that using a crystal-type calorimeter design could provide a better energy resolution such as the use of  $\text{PbWO}_4$  crystals which are expected to be sufficiently radiation hard. Several details on the performance of this type of crystal is still open and requires a detailed understanding [CMS94]. The  $Z$  vertex reconstruction in the  $Q^2$  range of the BPC relies on the hadronic final state. An independent tracking system in front of the BPC such as the use of several layers of silicon strip

BPC specification	BPC performance	reference
Depth	$\simeq 24 X_0$	5.2 and 5.4.2
Molière radius	$\simeq 13$ mm	5.2
Energy resolution	$17\%/\sqrt{E}$ (stochastic term)	8.5.4
Energy scale calibration	$\pm 0.5\%$	8.5.3
Energy uniformity	$\pm 0.5\%$	8.5.3
Linearity	$\leq 1\%$	8.5.4
Position resolution	$< 1$ mm	8.3.3
Intrinsic position bias	$< 1$ mm	8.3.3
Alignment accuracy	$\pm 0.5$ mm	5.8 and 8.3.4
Time resolution	$< 1$ ns	8.6

Table 5.2: BPC performance specifications.

detectors would be desirable to provide an independent  $Z$  vertex reconstruction. The last two items have been considered in an upgrade program<sup>10</sup> of the current BPC [Ca96].

The next section will concentrate on several details of the design and construction of the BPC. Table 5.2 summarizes the BPC performance specifications. The performance of the BPC, along with a detailed discussion of the energy and position reconstruction, will be discussed in chapter 8.

### 5.4.3 Details on the design and construction of the BPC

#### Magnetic field measurements

The magnetic field in the vicinity of the BPC (PMT-location of the BPC South  $Y$ -readout channels) has been measured in all three spatial coordinates using  $3 \times 3$  Hall probes. The Hall probes have been calibrated using a dipole magnet at the DESY II test-beam facility. The accuracy of the measurement has been estimated to be approximately 10%. Table 5.3 summarizes the magnitude of the measured magnetic field along with the location of the Hall probes. The  $Z$  component of the magnetic field is larger than all other components and reaches a value of 413 G. According to the specifications of the manufacturer of the chosen miniature PMTs (Hamamatsu R5600-03) [Ha94], the PMTs are expected to be insensitive to magnetic fields up to 100 G. The effectiveness of the ARMCO magnetic iron blocks has been investigated in a similar location as the ones for the BPC modules. The measured field inside the PMT support within the iron block did not exceed 20 G in  $Y$  and  $Z$  direction. The performance of the PMTs are therefore expected not to be degraded. This has been confirmed using LED test trigger runs employing the BPC LED monitoring system with the magnetic field of the compensator and central magnet turned on in sequence. The measured signal of the PMTs has been found to be completely insensitive to the surrounding magnetic field.

Furthermore, the ARMCO magnetic iron block was mounted on a strain gauge to measure the force on the iron block in the presence of the magnetic field. The measured net force was found to be as well completely negligible.

<sup>10</sup>Two layers of silicon strip detectors have been installed in September 1997 in front of the BPC North module.

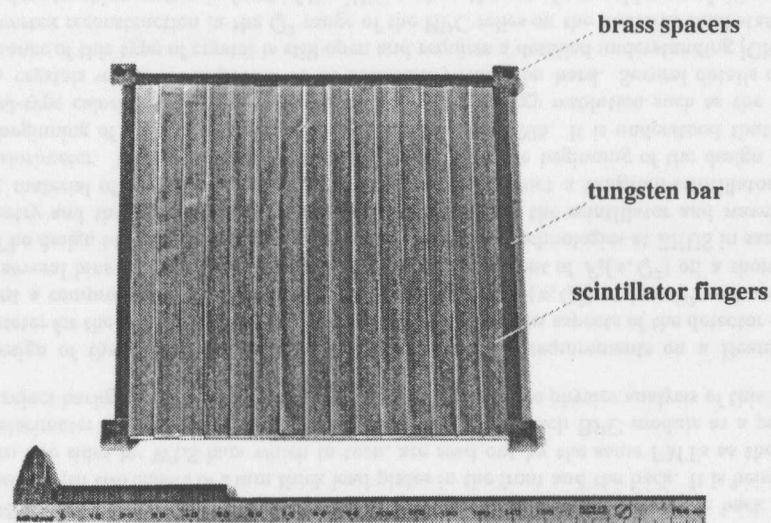


Figure 5.13: Single plate of the BPC North module showing the three 5 mm thick tungsten bars, 15 scintillator fingers wrapped in aluminum foil and the four brass spacers at each corner.

where the  $X$ -readout channels are counted from the beam pipe away and the  $Y$ -readout channels are counted from bottom to top (Figure 5.11).

The side of each scintillator finger which is not read out is aluminized to provide an efficient end reflector. Each scintillator finger has to be optically decoupled from each other. This was achieved along the scintillator fingers by wrapping them in 27.5  $\mu\text{m}$  thick aluminum foil which in turn increases the attainable light yield. It has been found that aluminum foil has a lower reflectivity than Tyvek-paper by about 10% depending on the type of Tyvek paper used. This has been confirmed by [Mo94] as well. On the other hand, aluminum foil has a completely smooth surface whereas Tyvek paper has a rather coarse surface. Aluminum foil can be bent precisely at the edges of each scintillator finger which yields very sharp edges. This is fairly difficult to do with Tyvek paper. Using aluminum foil allows a precise positioning of the wrapped scintillator fingers.

The scintillator fingers are kept in place, in transverse direction, by 5 mm wide tungsten bars which were glued on each tungsten plate by epoxy glue (Figure 5.13). The distance between respective tungsten bars determines the accuracy of the alignment of scintillator fingers in one particular layer. The gluing procedure has been therefore performed in a precisely machined support structure in order to hold the tungsten bars in place during the gluing procedure. The relative distance was checked before and after the gluing procedure and was controlled to an accuracy of 0.1 mm. The tungsten-bars also define the minimum distance of the scintillator fingers to the beam pipe edge which is 5 mm. The scintillator fingers have been machined to an accuracy of 0.1 mm [Ge94]. This has been confirmed by measuring the thickness and width of a small sample of scintillator fingers. The width of the scintillator fingers of 7.9 mm together with the thickness of the aluminum foil, taking into account the gap between respective tungsten bars, yields an effective thickness of each scintillator finger of 8.0 mm including air gaps.

Brass spacers which were machined with an accuracy of 0.1 mm were glued on each corner of a

tungsten plate and are used to mount individual tungsten-scintillator units together by inserting stainless steel bolts through each of the four brass spacers. The height of each brass spacer exceeds the thickness of the scintillator fingers within one layer by approximately 0.2 mm (Figure 5.13). This is to avoid any pressure on the scintillator layers within a completed calorimeter stack.

The attenuation of scintillator light along scintillator fingers has not been corrected directly using a particular correction pattern. The attenuation effect is being corrected for off-line (Section 8.5). To ensure a uniform response of the scintillator fingers, the mechanical cutting and polishing procedure has to be done with high accuracy since any surface imperfections spoil the uniformity of the scintillator fingers [Ge94]. The uniform response was confirmed by scanning a small sample of the scintillator fingers (Section 5.4.3).

To ensure that the response of the calorimeter depends only on the deposited energy of the positron and not on the depth of the energy deposition, one has to account for the attenuation of light along the wavelength shifting bars. This was achieved using the fact that a certain fraction of light which is being inserted from each scintillator finger into the WLS escapes the WLS on the backside. Tuning the amount of light which is reflected back into each WLS, one can achieve a uniform response along the WLS provided that the amount of light which escapes the backside of each WLS is large enough to account for the attenuation along the WLS. It has been confirmed that 30 ppm Y7 in PMMA allows to correct for this effect. All WLS were scanned to measure their individual attenuation length (Section 5.4.3). These measurements were then used to develop a pattern printed on Tyvek-paper which was placed on the backside of each WLS inside an aluminum cassette which provided at the same time the fixation of each WLS-bar. Aluminum lamellas between each WLS-bar decouple each SCI-finger (Figure 5.14). To ensure a constant air gap of about 1 mm between the scintillator fingers and the WLS-bars, plastic distance pieces were glued on three locations along the calorimeter stack on tungsten bars between SCI-fingers (Section 5.4.3).

As seen in Figure 5.11, each WLS-bar is bent by 90° with a radius of 30 mm away from the calorimeter and coupled to a photomultiplier tube. This was necessary to avoid placing the PMTs used for the WLS readout close to the beam pipe where the magnetic field as well as the radiation background is higher. The loss in light yield due to the WLS bending amounts to about 10%. This has been determined by comparing scanning results of a straight and bent WLS.

The miniature Hamamatsu R5600-03 PMTs [Ha94] (Figure 5.16) were used which exhibit in the presence of magnetic fields up to 100 G no performance degradation. The PMTs are placed inside an ARMCO-magnetic iron block ( $\mu \approx 1000$  for  $B = 800$  G) [Ar95] to provide in addition an effective magnetic shielding. The PMTs inside the ARMCO-magnetic iron block are surrounded by a 2 mm-thick PVC cover to electrically decouple the PMTs from the surrounding iron block. The orientation of the PMTs inside the iron block is diagonal due to spatial constraints. Therefore, three different lengths of the WLS of 32, 34 and 36 cm were required. The actual length of the calorimeter itself amounts to about 16 cm. The photoelectron yield has been estimated to be approximately 200 photoelectrons/GeV (Section 8.5.4).

A completed stack of 26 tungsten-scintillator units was mounted onto a 10 mm thick stainless steel plate using four stainless steel bolts inserted into each of the four brass spacers. The stainless steel plate itself as well as the ARMCO magnetic iron blocks are attached to an aluminum support structure which is used to mount the BPC inside the ZEUS detector on a support structure attached to the compensator magnet support (Figure 5.11).

An LED light distribution system was incorporated inside each BPC module by inserting light from a yellow LED (Hewlett Packard, HLMA-DL00, Amber) onto the front face of each PMT

Hall probe	X (cm)	Y (cm)	Z (cm)	$B_x$ (G)	$B_y$ (G)	$B_z$ (G)
1,2,3	-13.5	-25.0	-323.0	97	48	313
4,5,6	-13.5	-35.0	-323.0	51	133	370
7,8,9	-13.5	-45.0	-323.0	83	242	413

Table 5.3: Results of magnetic field measurements in the vicinity of the BPC (PMT-location of the BPC South Y-readout channels).

### Photomultiplier tubes and HV-system

Spatial constraints in the design of the BPC required a PMT which is significantly smaller in size than other known PMTs such as the ones used for the EMC sections of the ZEUS uranium calorimeter [Ho93].

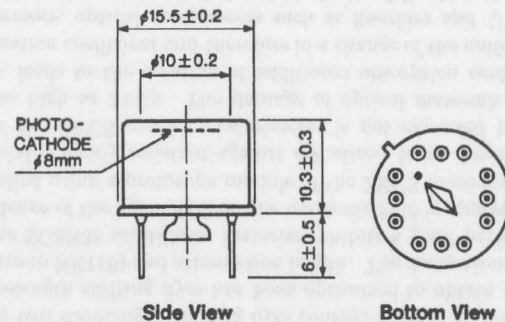


Figure 5.15: Side and bottom view of the Hamamatsu R5600-03 miniature PMT.

The miniature PMTs Hamamatsu R5600-03 (Figure 5.15 and 5.16) have an overall diameter of 15.5 mm and a height of 16.3 mm and have been advertised as the smallest PMTs in the world. The diameter of the photocathode amounts to 8 mm which is only slightly larger than the width of the wavelength shifting bars of 7 mm. The type used has a UV-glass window and a bialkali photocathode material with a spectral response in the range of 185 – 650 nm with a maximum at approximately 480 nm which equals to the maximum in the emission spectra of the wavelength shifter used. The dynode structure consists of an eight stage metal channel dynode arrangement built inside a standard TO-8 type metal package.

Fast timing characteristics of the BPC readout elements are extremely important to provide a means of background rejection based on timing requirements. The Hamamatsu R5600-03 PMT offers unique timing properties with a rise time of approximately 0.6 ns and a fall time of 1.0 ns. An output current of 30 mA is attained at a 5% deviation from the ideal linearity.

The characteristics of all PMTs have been evaluated in an extensive test program on the bench evaluating their gain and dark current properties [Mo97b]. The gain performances have been determined by measuring the yield of each PMT injecting light from a yellow LED (Hewlett Packard, HLMA-DL00, Amber) inside a dark box onto each PMT as a function of the applied high voltage (HV). Figure 5.17 shows a typical gain curve. Gain factors of typically  $5 \cdot 10^5$  have been achieved at an applied HV of 700 V. All PMTs have been grouped according to their respective performance. The best performing tubes have then been chosen for those readout

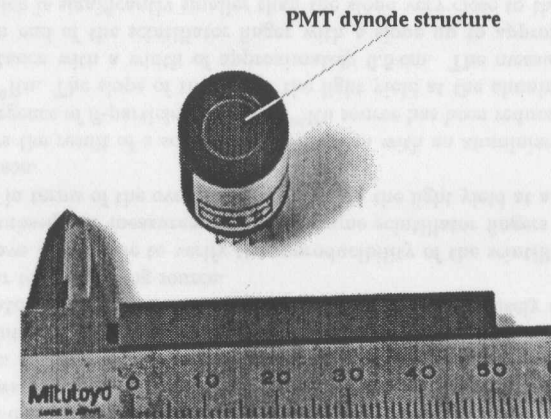


Figure 5.16: Photography of the Hamamatsu R5600-03 miniature PMT.

channels covering the fiducial volume. The nominal operating HV for all PMTs ranges from 700 V to almost 1000 V.  $^{60}\text{Co}$ -scans among the BPC (Section 5.7) have been used to equalize the response of each BPC readout channel by adjusting the HV for each readout channel accordingly. In addition, the HV for each readout channel was set such that a single readout channel saturates the readout electronics (Section 5.5) due to an incoming electron of 35 GeV. This estimate has been carried out prior to the installation of the BPC using a cosmic-ray experiment.

Figure 5.18 shows one of the ARMCO magnetic iron blocks with a photomultiplier tube in front plugged inside the corresponding base together with the PVC cover and a flat cable for the PMT HV supply. The cross-section of a wavelength shifting bar, together with a lucite fibre, can be seen in one of the PMT support within the iron block. The WLS bars and the lucite fibres are attached to the iron block using a PVC fixation. The overall light yield depends on the orientation of the cross-section of the WLS bar with respect to the PMT which is due to the dynode structure which can be seen from Figure 5.16. According to the manufacturer, the light yield is maximized if the longer side of the WLS cross-section is oriented in parallel to the PMT dynode structure. This has been verified on the bench by turning the PMT in steps of  $5^\circ$  with respect to a fixed WLS bar. The difference between a parallel to a perpendicular orientation has been found to be approximately 10%. The distance between the front face of each PMT and the WLS and the lucite fibre respectively, amounts to a fraction of a millimeter. The HV for all BPC PMTs is generated using a remote controlled Cockroft-Walton (CW) type HV power supply [Go96]. The voltage division among the PMT dynodes is performed inside the HV supply itself as  $\frac{1}{2} : 1 : 1 : 1 : 1 : 1 : 1 : 1$ . The divided HV is then supplied on a 5 m flat cable to the PMT dynodes of the BPC. The CW HV-power supply provides a security logic to set a maximum anode current beyond which the HV-supply is turned off and restarted after a certain time period if the problem of high anode currents disappeared. The maximum current is set to 100  $\mu\text{A}$ . The output voltage is stable within 1%.

### Scintillator fingers

The scintillator material used for the active layers of the BPC is the same as the one for the ZEUS uranium calorimeter (SCSN38) [Ka83]. It consists of a cross-linked polystyrene base

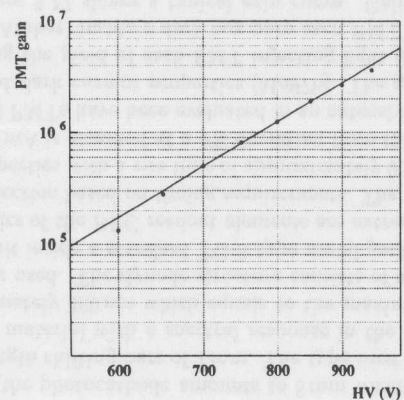


Figure 5.17: Measured gain curve for a typical Hamamatsu R5600-03 miniature PMT. The measured gain values have been fitted in the range of 700 – 900 V to a functional form of:  $\text{gain} = 10^a \cdot \text{HV}^b$ .

which is doped with two wavelength shifting dyes (buthyl-PDB (1%) and BDB (0.02%)). The composition of wavelength shifting dyes has been optimized to obtain the best possible light output (112% relative to NE110) and attenuation length. The decay time is given as 2 ns. It has been shown that the SCSN38 scintillator material exhibits a good performance against aging effects. The dependence of the light yield on the magnetic field is approximately 1% at 1000 G which has been studied using a prototype module of the ZEUS uranium calorimeter [Ho93]. The SCSN38 material is highly resistant against radiation. It has been shown in [Da96] that the performance of the ZEUS uranium calorimeter is not expected to be degraded for an accumulated dose as high as 3 kGy. The damage of optical materials, i.e. scintillators and wavelength shifters, leads to the creation of additional absorption centers which results in a change of the attenuation coefficient and therefore in a change of the uniformity of the measured light yield. Furthermore, optical components such as fluorides and UV-absorbers are being destroyed which reduces the attainable light yield. In the following, the main features of the radiation damage will be briefly summarized for the scintillator SCSN38. The results have been obtained assuming a homogeneous irradiation of examined scintillator samples in an air atmosphere [Da96]. No dependence of the actual damage on the dose rate between 3 Gy/h and 3 kGy/h has been observed. The ratio of the intensity of fluorescence light yield before  $I_b$  and after  $I_a$  irradiation has been parameterized as follows:

$$\left(\frac{I_b}{I_a}\right) = 1 - (9 \pm 2) \cdot 10^{-6} \text{Gy}^{-1} \cdot D \quad (5.34)$$

The change in the absorption coefficient  $\Delta\mu$  is given by:

$$\Delta\mu = (0.8 \pm 0.2) \cdot 10^{-6} \text{Gy}^{-1} \text{cm}^{-1} \cdot D \quad (5.35)$$

These parameterizations have been determined to be independent of the particular scintillator geometry. For accumulated doses of 1, 5 and 10 kGy, the intensity of fluorescence light is expected to decrease by 1%, 4% and 9%. It should be noted again that these results have been

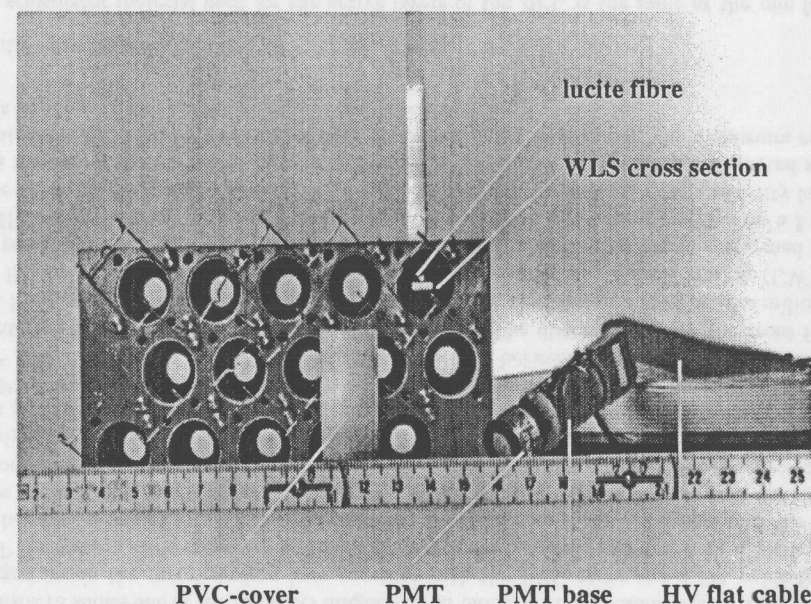


Figure 5.18: Photography of an ARMCO magnetic iron block with a Hamamatsu R5600-03 PMT in the foreground.

obtained for a homogeneous irradiation. Any non-uniform radiation damage will result in a position dependent loss of fluorescence light and absorption coefficient  $\Delta\mu$  (Section 7.2).

A sample of non-irradiated scintillator fingers have been scanned to verify their uniform response and light yield which is of particular importance as mentioned earlier since no internal attenuation correction is made which enormously simplified the construction of the BPC modules. It will be shown in detail in section 8.5.3 that the attenuation effect can be corrected to obtain a uniform energy response of the BPC at the level of 0.5%.

Figure 5.19 shows schematically, the setup to measure the response of scintillator fingers [Bo96a]. A  $^{106}\text{Ru}$  source was mounted on a computer controlled stepping motor plate to allow the movement of the radioactive source in all three spatial coordinates. The aluminum wrapped scintillator fingers have been fixed inside a groove of a precisely machined aluminum bar perpendicular to the moving source.

Several checks have been made to verify the reproducibility of the scintillator finger scans. It was found that subsequent measurements of the same scintillator fingers are reproducible at the percent level in terms of the overall uniformity and the light yield at a fixed position to be used for comparison.

Figure 5.20 shows the result of a scintillator finger scan with an aluminized end using a  $^{106}\text{Ru}$  source. The divergence of  $\beta$ -particles from the  $^{106}\text{Ru}$  source has been reduced using a collimator in front of the  $^{106}\text{Ru}$ . The slope of the rise of the light yield at the aluminum end occurs over a very small distance with a width of approximately 0.5 cm. The measured light yield rises towards the open end of the scintillator finger with a slope up to approximately 3 cm from the open end which is significantly smaller than the slope very close to the edge. This can be understood given the fact that the wavelength dependent attenuation coefficient is significantly

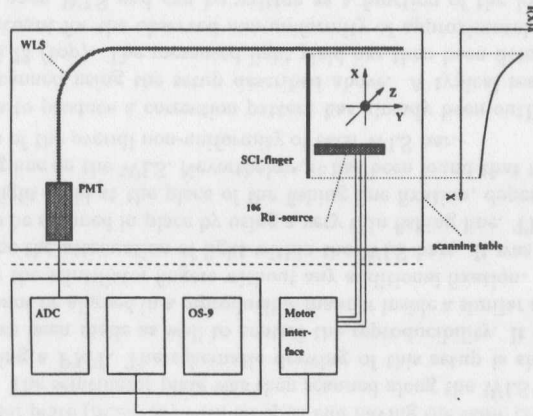


Figure 5.19: Setup for scanning the BPC scintillator fingers.

higher for small wavelengths compared to larger wavelengths which then leads to the observed behavior of the measured light yield. The measured light yield at the open end can be written in the following form:

$$I(x) = \int A(\lambda) \cdot I(x, \lambda) d\lambda \quad (5.36)$$

where  $A(\lambda)$  accounts for the sensitivity spectra of the experimental setup of the scintillator finger readout, i.e. the WLS-PMT arrangement.  $I(x, \lambda)$  denotes the intensity at the open end of the scintillator finger depending on the wavelength of the emitted scintillation light and the location  $x$  of the primary produced scintillation light by the  $^{106}\text{Ru}$  source. Taking into account the direct and reflected light,  $I(x, \lambda)$  has been parameterized in the following form:

$$I(x, \lambda) = \frac{I(x=0, \lambda)}{1 + R(\lambda) \cdot e^{-2\mu(\lambda)L}} (e^{-\mu(\lambda)x} + R \cdot e^{-\mu(\lambda)(2L-x)}) \quad (5.37)$$

The overlaid function represents a fit to the observed light yield using a fit of the following form:

$$\bar{I}(x) = \bar{I}_{01}(e^{-x/\mu_1} + R e^{-(2L-x)/\mu_1}) + \bar{I}_{02}e^{-x/\mu_2} \quad (5.38)$$

This ansatz is motivated by the description of the propagation of scintillator light as given by equation 5.37 assuming that the integrated distribution as given in equation 5.36 can be described by an exponential-type ansatz. The coefficients  $\mu_1$  and  $\mu_2$  cannot be associated with the attenuation coefficients  $\mu(\lambda)$  in equation 5.37.  $\mu_1$  and  $\mu_2$  represent effective values of the attenuation of scintillator light of a characteristic spectra, where  $\mu_1$  accounts for the low attenuated part and  $\mu_2$  for the large attenuated part of the scintillator light. This is a simplification provided that the main emphasis is placed on the integrated attenuation effect along a particular scintillator finger. The result of this fit shows that this ansatz describes the integrated attenuation rather well. The steep rise of the measured light yield towards the open end characterized by  $\mu_2$  occurs for all scintillator fingers outside the fiducial volume and therefore enormously simplifies the off-line attenuation correction procedure.

The use of an end reflector significantly improves the overall uniformity along a scintillator finger. This effect can be easily understood plotting the function in equation 5.38 for several values of  $R$ . Ignoring the second term in equation 5.38, one obtains for  $R = 1$ ,  $\bar{I} \propto \cosh(\mu_1 x)$

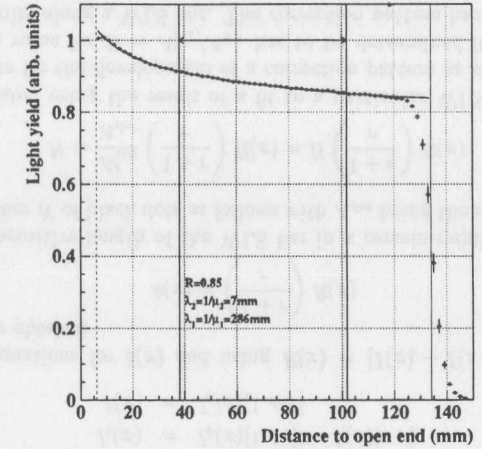


Figure 5.20: Scan of a scintillator finger using a  $^{106}\text{Ru}$  source. The horizontal arrow denotes the fiducial volume covered by the scanned X-scintillator finger.

which yields an overall smaller slope compared to  $R < 1$  and exhibits a slope of naught at  $x = L$ . The BPC scintillator fingers require the use of end reflectors of equal response which is of significant importance since any attenuation effect will be corrected off-line. It has been found that this can be best achieved by aluminizing each scintillator finger end instead of using small pieces of aluminum. The aluminization of all scintillator fingers had been carried at the Astronomical Observatory at the University of Hamburg within an aluminization apparatus which is normally used for the production of mirrors within telescopes for astronomical applications. Scanning a sample of scintillator fingers after aluminizing their respective ends verified their uniform response.

#### Wavelength shifter readout

The WLS material used for the BPC has also been used for the ZEUS uranium calorimeter. It consists of a PMMA base doped with a fluorescent dye of 30 ppm Y7. The absorption and emission spectra of the fluorescent dye Y7 matches well with those for the emission spectra of the SCSN38 scintillator and the spectral sensitivity of the bialkali photocathode (Hamamatsu R5600-03), respectively. The effect of radiation damage for the WLS material has been parameterized as follows [Da96]:

$$\left(\frac{I_b}{I_a}\right) = 1 - (3 \pm 1) \cdot 10^{-6} \text{Gy}^{-1} \cdot D \quad (5.39)$$

The change in the absorption coefficient  $\Delta\mu$  is given by:

$$\Delta\mu = (0.6 \pm 0.2) \cdot 10^{-6} \text{Gy}^{-1} \text{cm}^{-1} \cdot D \quad (5.40)$$

These results have been obtained based on the same assumptions as discussed in the previous section for the case of the scintillator material SCSN38.

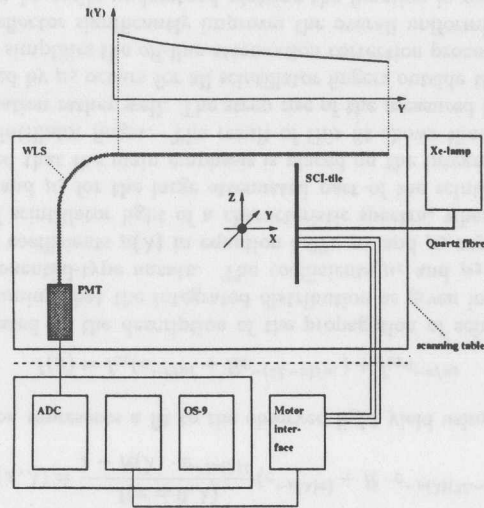


Figure 5.21: Setup for scanning the BPC WLS.

The WLS bars were also aluminized at the end which considerably reduced the WLS non-uniformity from 15% with an open end to approximately 8% with an aluminized end over the whole length of the actual calorimeter of 16 cm.

Figure 5.22 shows the effect of longitudinal non-uniformity on the linearity of the absolute energy scale. These results have been obtained using an EGS4 MC-simulation of the BPC. A longitudinal non-uniformity of maximum 5% is required to limit the linearity of the absolute energy scale to be well below 1%.

A correction pattern was developed to correct for the attenuation of light along the WLS bars. For that, each of the WLS bars was scanned using a similar setup to the one for the scintillator fingers. The light from a Xenon-lamp (Hamamatsu L2175) was guided using a flexible Quartz fibre to a scintillator plate (SCSN38) with an open end having the same cross-section as a BPC scintillator finger. The scintillator plate was then scanned along the WLS bar while measuring the light yield using a PMT. The schematic drawing of this setup is shown in Figure 5.21. Several checks have been made as well to control the reproducibility. It has been found that the bent WLS cannot be aligned in a reproducible manner inside a similar aluminum support as it was the case for the scintillator fingers without any additional fixation. This is important to correctly determine the attenuation of light within the WLS bars. It was therefore decided to keep each WLS to be scanned in place by using a very thin fishing line. This led to a reduction in the measured light yield at the place of the fishing line fixation, depending on the applied force of the fishing line on the WLS. Nevertheless, it has been found that this does not degrade the determination of the overall non-uniformity of each WLS bar.

The principle idea to produce a correction pattern has already been outlined in section 5.4.2. Each WLS was scanned using the setup described above. A typical result of these scans is shown in Figure 5.23 (top). The measured light yield has then been fitted for simplicity by a straight line to account for the observed non-uniformity of approximately 8%. The measured light yield at the open WLS end can be written as a function of the location  $x$  in terms of a primary component  $I_p$  and a secondary component  $I_s$ , which is due to the fraction of the

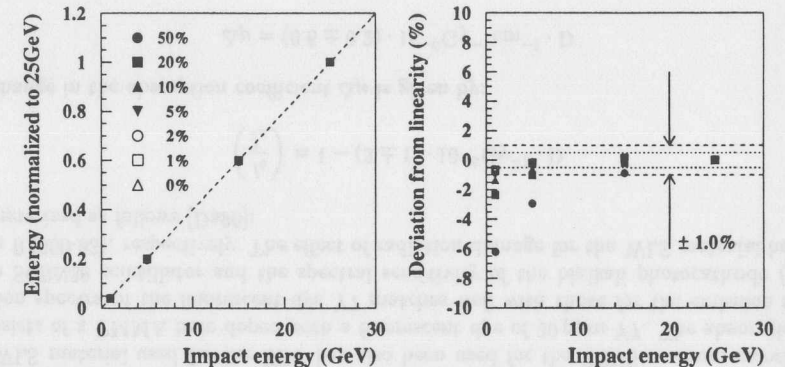


Figure 5.22: Deviation from linearity of the absolute energy scale due to a WLS non-uniformity of 50, 20, 10, 5, 2, 1 and 0% using an EGS4 MC-simulation. For a WLS non-uniformity of less than 5%, the deviation from linearity is well below 1% for impact energies of 1 GeV using an impact energy of 25 GeV to establish the energy scale.

primary component which is reflected back into the WLS due to a particular back reflector. The measured light yield at the open WLS can then be written as:  $I(x) = I_p + I_s = I_p(1 + r)$ , where  $r$  depends on the amount of dye Y7. In case of the BPC WLS,  $r$  is approximately 0.38 which has been determined using a spectral photometer. If no light is reflected back, i.e. in case of a black back reflector,  $I(x)$  decreases. By tuning the amount of back reflected light, one is able to achieve a uniform WLS response. Let  $b$  be the amount of 'blackness', i.e.  $0 < b < 1$  and  $I_b$  and  $I$  be the measured light yield with and without a black reflector of 'blackness'  $b$ .  $I_b$  and  $I$  are given as follows:

$$I_b(x) = I_p(x)[1 + (1 - b(x)) \cdot r] \quad (5.41)$$

$$I(x) = I_p(x)[1 + r] \quad (5.42)$$

Solving these two equations for  $b(x)$  and using  $R(x) = [I(x) - I(x = L)]/I(x = L)$  with  $I_b(x) = I(x = L)$  one obtains:

$$b(x) = \left(\frac{1+r}{r}\right) R(x) \quad (5.43)$$

Dividing the whole sensitive length of the WLS bar in a certain number of bins of size  $A_{bin}^i$ , one obtains the number  $N$  of black dots as follows with  $A_{dot}$  being the size of a particular black dot:

$$N = \frac{A_{bin}^i}{A_{dot}} \left(\frac{1+r}{r}\right) R(x) = B \left(\frac{1+r}{r}\right) R(x) \quad (5.44)$$

where  $R(x)$  is evaluated using the result of a fit to a particular WLS. This scheme provides an appropriate ansatz for the development of a correction pattern as shown in Figure 5.23. In practice, the precise value for  $B = A_{bin}^i/A_{dot}$  has to be determined iteratively to obtain the best possible uniformity along a WLS bar. The correction pattern has been printed on Tyvek paper using a high resolution plotter from a postscript file which has been created using the graphics package PAW [Br96a]. The final result is shown in Figure 5.23. With this scheme, a

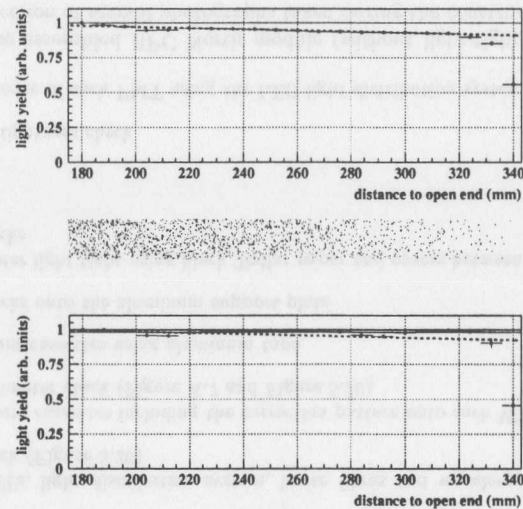


Figure 5.23: WLS scanning result (top), pattern (middle) and result of a WLS scan including the correction pattern (bottom).

WLS uniformity of 2% has been achieved. In this case, any deviations from the linearity of the absolute energy scale are completely negligible as can be seen from Figure 5.22.

The correction patterns printed on Tyvek paper were cut out including a 2 mm side reflector for each WLS bar and placed inside each aluminum slot as shown in Figure 5.14. These aluminum cassettes, including the WLS, were then placed on the actual calorimeter stack as will be discussed in more detail in the next section. The interface between scintillator fingers and WLS bars can be seen in Figure 5.24. Three plastic distance pieces were glued on three locations along the calorimeter stack to provide an approximately 1 mm air gap between each scintillator finger and a respective WLS bar. The aluminum lamellas within the aluminum cassettes were colored black and precisely positioned between each scintillator finger to avoid cross-talk of scintillator light between neighboring scintillator fingers. It was not possible to experimentally quantify the quality of the interface connection to verify the absence of cross-talk using for example a muon test-beam due to time constraints.

### LED monitoring system

A simple LED light distribution system was implemented to monitor the performance of the PMTs of the BPC. It allows to inject light from an LED and the ZEUS laser calibration system [Ho93] onto the front face of each PMT.

The light from a Yellow LED (Hewlett Packard, HLMA-DL00, Amber) or from the ZEUS laser calibration system is injected onto the front face of a  $8 \times 8 \times 80 \text{ mm}^3$  large polished lucite block. Lucite fibres for each PMT are glued inside a lucite cylinder and placed as shown in Figure 5.25 on the opposite side of the rectangular lucite block. The lucite block and the lucite cylinder are mounted inside a plastic cylinder inside the NY (North Y-channels) and SY (South Y-channels) iron blocks, respectively. Figure 5.25 shows a schematic drawing of the main elements of the

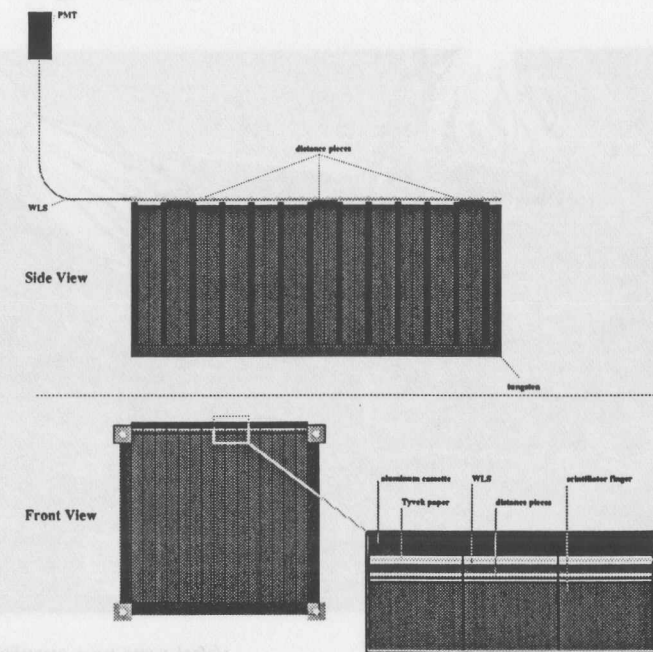


Figure 5.24: Side view and front view of the interface between longitudinally oriented scintillator fingers and a respective WLS bar.

light distribution system inside each BPC module.

The light is then distributed to the front face of each PMT as shown in Figure 5.18. The LED is driven by a pulser with a pulse height of  $-4 \text{ mV}$  and a width of 6 ns [Ro96]. The BPC light distribution system allows to monitor possible gain variations of the BPC PMTs at the level of 1 – 2%.

### Calorimeter assembly

The actual calorimeter assembly included the following steps:

#### 1. Preparation:

- gluing of tungsten bars and brass spaces onto each tungsten plate
- aluminization of scintillator fingers and wavelength shifting bars
- wrapping of scintillator fingers using precisely cut (accuracy: 0.5 mm) aluminum foil
- scan of wavelength shifting bars (Figure 5.21), optimization of correction patterns and preparation of correction patterns (Figure 5.23) to be placed inside the aluminum cassettes (Figure 5.14)
- wrapping of wavelength shifting bars using Tyvek paper among the WLS neck

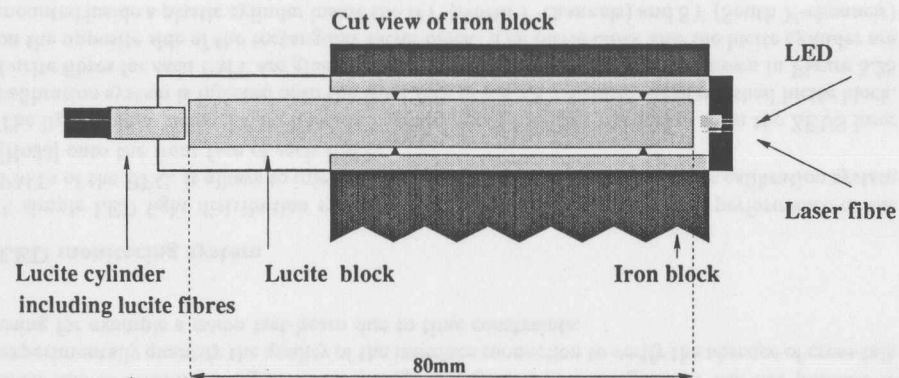


Figure 5.25: Schematic drawing of the LED light distribution system.

- placing scintillator fingers inside each tungsten plate (Figure 5.13)
  - measure performance of each PMT and classify them [Mo97b]
2. Calorimeter stacking:
- stacking tungsten plates including scintillator fingers on a flat metal surface including four long bolts from front to back of the calorimeter with the aluminum support structure at the end (Figure A.8)
  - insert bolts through all four brass spacers and align the calorimeter with respect to the flat metal surface, tighten bolts and turn stack around onto the aluminum support structure (Figure A.9)
  - glue plastic distance pieces for scintillator finger WLS interface onto the calorimeter stack
  - mounting PMTs, light distribution system, lucite fibres and wavelength shifting bars inside PMT iron block (Figure 5.26)
  - attach aluminum cassettes including the correction pattern onto each WLS bar and align them onto the calorimeter stack (Figure A.7 and Figure 5.26)
  - fix all aluminum cassettes using aluminum tape
  - screw iron blocks onto the aluminum support plate
  - make calorimeter light tight using black Tedlar paper and covers between calorimeter stack and PMT iron blocks
3. Quality checks:
- perform light tightness check
  - check performance of each PMT using the LED light distribution system

A front view of the assembled BPC North module (without light-tight covers) is shown in Figure 5.27. A collection of several photographs taken during the construction of the BPC can be found in section A.4.

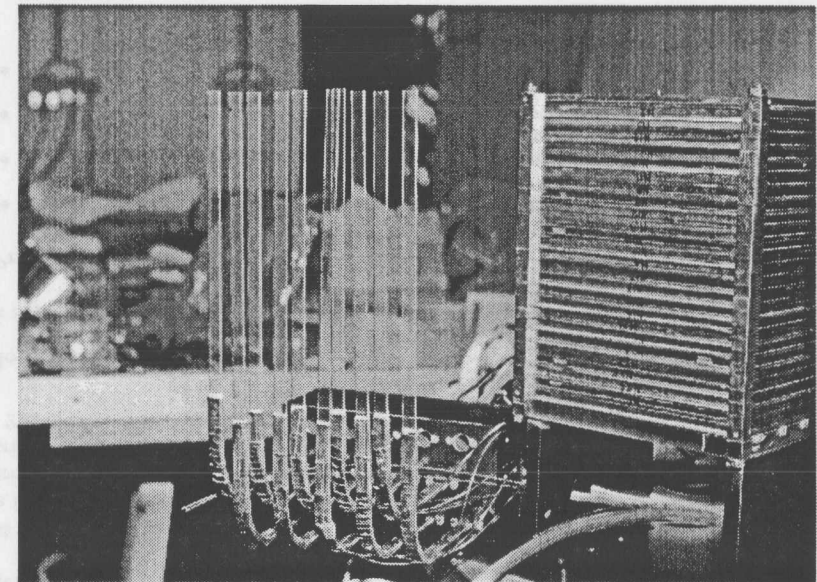


Figure 5.26: Photography of the calorimeter stack (right) and the WLS bars mounted to an ARMCO magnetic iron block (left).

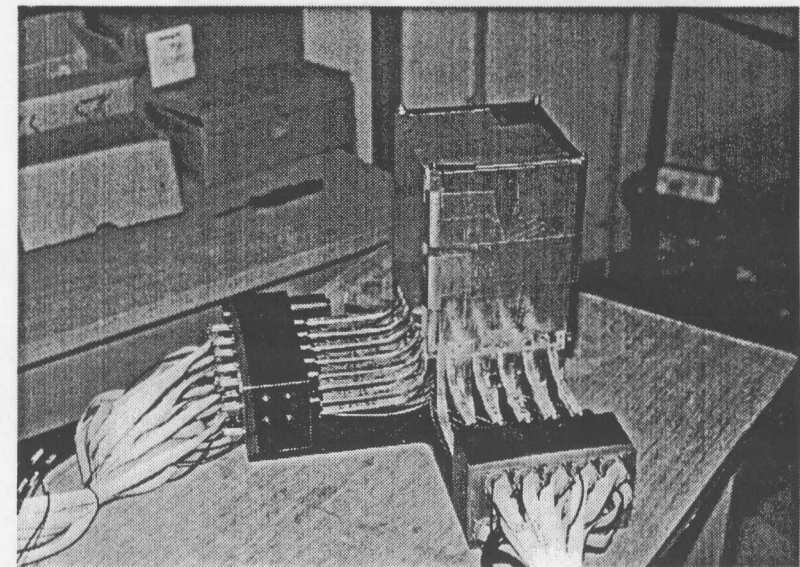


Figure 5.27: Photography of assembled BPC North module.

## 5.5 Readout

Figure A.14 displays the location of various components of the BPC readout system. The BPC front-end electronics is mounted inside the ZEUS cryo-tower (Figure 5.9). The BPC PMT pulses are sent on 5 m coaxial cables to the trigger summing cards which split off a charge of approximately 10% for each of the BPC PMT pulses to be used for the BPC first-level trigger (Section 5.6). The rest is sent to the BPC analog cards. These, together with the digital cards in the ZEUS electronics rucksack, represent the whole BPC readout system. The BPC readout system was implemented as a subcomponent of the readout chain of the main calorimeter.

The architecture of the analog cards reflect the design of the readout electronics of the ZEUS uranium calorimeter [Ca93]. The analog cards used for the BPC have been laid out in a standard Eurocard dimension to allow a compact installation inside a Eurocrate [Kö95]. Since a 12 bit dynamic range is sufficient for the case of the BPC, a single gain channel has been used instead of a two-gain channel as it is the case for the analog cards of the ZEUS uranium calorimeter. Figure A.12 displays an overview of the BPC readout system. One analog card integrates and shapes up to twelve PMT signals, samples the shaped signal at a rate of 96 ns and stores the samples in a 5  $\mu$ s deep analog pipeline. In case of a positive trigger decision from the GFLT, the samples are transferred to a one-event buffer which stores up to eight samples from a pipeline. The samples are then multiplexed to the digital cards.

The digital cards are identical to those of the ZEUS uranium calorimeter [Ca93]. Each digital card has four 12 bit ADCs which digitize the analog samples. A DSP<sup>11</sup> processor is used to provide on-board pedestal and gain corrections and to reconstruct the energy and time of an event. These variables are then made available to the second level processor. Each digital card allows to process the signals from 24 PMTs. Input and output buffers take into account fluctuations in the first-level trigger rate and in the second level trigger decision time, respectively.

## 5.6 Trigger

The measurement of the final state electron in  $ep$  collisions using the BPC as a new component of the ZEUS experiment requires a trigger scheme to reduce background events at a very early stage while efficiently selecting physics events of interest. This is of particular importance for an inclusive measurement using the BPC. Non  $ep$  background events are expected to arise from:

- electron/proton collisions with residual gas molecules or the beam pipe wall,
- synchrotron radiation and
- background events due to electrons having lost part of their energy due to bremsstrahlung which are then being bent by the HERA interaction lattice into the BPC.

The last item will be discussed in more detail in chapter 7 which required a modification of some of the collimator positions within the ZEUS interaction region after the implementation of the BPC trigger scheme. The rate of this type of background events was not known at the beginning of the design of the BPC first-level trigger scheme and therefore required a careful investigation at the startup of the 1995 HERA run including the BPC as a new component. The amount of synchrotron radiation background is expected to be completely negligible taking into account the respective rate of synchrotron radiation. The energy of synchrotron radiation

<sup>11</sup>Digital Signal Processor.

photons peaks at very small energies (keV-range) and are therefore expected to be stopped already after the first tungsten layers.

Proton beam gas background events typically occur out of time with  $ep$  scattering events and can therefore be rejected by requiring a proper timing from the measured BPC signal relative to the  $ep$  bunch crossing. Electron beam gas background events typically occur in-time with  $ep$  scattering events and are expected to decrease towards large energies of the candidate electron. The BPC trigger scheme is intended to provide energy and timing information to the GFLT which will be then used via an energy threshold cut and a cut on the measured timing information from the BPC to reduce the rate of background events. The precise energy and timing cuts will be discussed in section 7.1. The following section is devoted to provide an overview of the hardware of the BPC trigger scheme.

Several analog sums are formed among the BPC readout channels taking into account the fiducial region of the BPC due to the restricted size of the beam pipe window. This is achieved by resistively splitting approximately 10% of the charge of the BPC readout channels and adding them together using current mode operational amplifiers [Ri94]. The summing circuits have been laid out on standard NIM cards which are located inside a NIM crate within the ZEUS cryo-tower (Figure A.14). The following analog sum signals are provided from the North (South) module:

- Vertical sum:  $N(S)V = \sum_{i=2}^{10(6)} N(S)X_i$
- Horizontal sum:  $N(S)H = \sum_{i=3}^{14} N(S)Y_i$
- Outer sum:  $N(S)O = \sum_{i=11(7)}^{15(11)} N(S)X_i + N(S)Y_1 + N(S)Y_2 + N(S)Y_{15} + N(S)Y_{16}$
- Inner sum:  $N(S)I = N(S)X_1$
- Back tile sum:  $N(S)B = \sum_{i=1}^2 N(S)B_i$

The actual sum signal and its corresponding inversion are sent on 30 m long BNC cables to the ZEUS electronics rucksack. Figure A.13 shows the setup of the BPC first-level trigger scheme. The sum signals are fed into differential receivers which are used as a filter for 50 Hz noise and also to provide a 1-to-4 fanout of the corresponding input signal. The trigger scheme for both BPC modules is divided into an energy and timing part.

In case of the BPC North module, the energy information for the GFLT is derived using a 4-bit FADC<sup>12</sup> based on the CAMAC LeCroy Model 4504 which allows four analog input signals to be digitized into a 4-bit digital word at a frequency of up to 100 MHz and a sampling time as short as 4 ns. The fast conversion process is required to use the BPC at the ZEUS first-level trigger. The digitized signals are sent on twisted-pair cables to the GFLT to be used in various first-level trigger applications, as will be shown in detail in chapter 7. The strobe signal is derived from the ZEUS clock signal associated with the  $ep$  bunch crossing. A problem with the strobe-signal discriminator during the 1995 data taking caused the strobe signal for the FADC to get lost for some of the runs which resulted in a decrease of the trigger efficiency. This problem has been examined in detail as part of the off-line physics analysis and will be discussed in section 9.2.

Only one FADC-module was available at the time of the startup for the BPC first-level trigger. Since the BPC South module is not explicitly used for the physics analysis presented in this thesis, it was decided to simply form a lower and upper threshold among the BPC South sum

<sup>12</sup>Flash Analog-to-Digital converter.

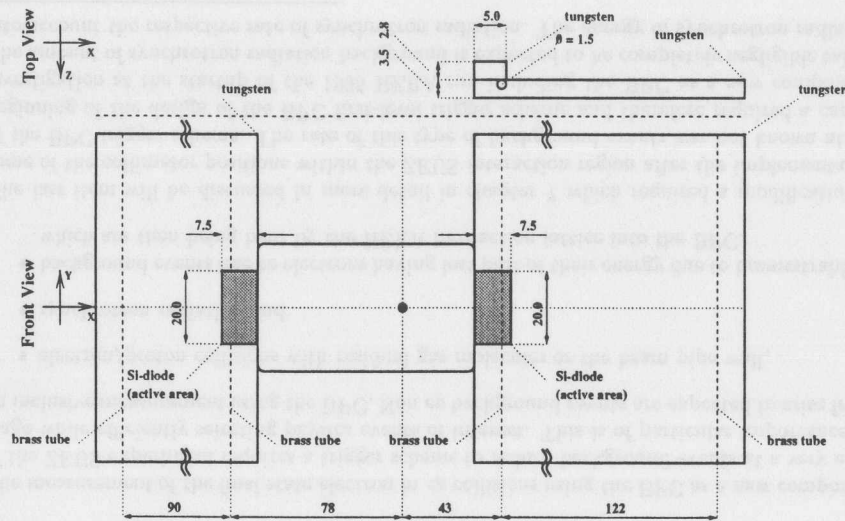


Figure 5.28: Top and front view of both BPC modules showing the location of TLDs and the Si-diodes for the BPC radiation monitoring. All dimensions are in mm.

signals, SH and SV, using a discriminator and send the NIM-ECL converted NIM-signals on twisted pair cables to the GFLT. The same procedure has been followed for the BPC North backtile sum signal.

The timing information for both BPC modules are derived using conventional LeCroy discriminators whose respective logic output signals are fed into 4-bit TDCs<sup>13</sup> with a 5 ns step at the GFLT.

The implementation of the BPC into the 1995 ZEUS trigger scheme, the calibration of the FADC-digitized energy to the off-line calibrated measured energy in the BPC North module as well as the efficiency of the BPC North energy and timing cut will be discussed in detail in sections 7.1 and 9.2. Apart from a problem with the strobe-signal discriminator, the BPC first-level trigger was found to work reliably.

## 5.7 Monitoring

Several tools have been implemented to monitor the performance of the BPC readout electronics, the performance of the BPC photomultiplier tubes and in particular the effect of radiation damage on the optical components of the BPC.

Daily test trigger runs are taken in between luminosity periods to evaluate the integrity of the readout electronics by means of charge injection and pedestal test triggers. A full electronics calibration is performed once per week. The stability of the readout electronics has been found to be at the level of 0.1% [Ho93]. On-line charge injection and pedestal test triggers, as well as LED and laser test triggers, are used in addition to monitor on-line the performance of the readout electronics and the BPC photomultiplier tubes. Details on these monitoring and calibration tools of the readout electronics can be found in [Ho93].

<sup>13</sup>Time-to-Digital Converter.

Monitoring the accumulated radiation dose using passive and active radiation monitors is of vital importance since the BPC is located at a fixed distance of only 38.7 mm (Section 5.8) from the beam contrary to the rear and forward uranium calorimeter at ZEUS which are retracted by 40 cm from the beam during injection and ramping periods in HERA. Figure 5.28 shows a front view of both BPC modules as seen from the interaction point. Groves with a cross-section of  $1.5 \times 1.5 \text{ mm}^2$  have been machined on two sides of the first and the last tungsten plates. Prior to the assembly of the BPC modules, brass tubes with a diameter of 1.5 mm were glued inside these groves in such a way that their respective ends are accessible from the outside of both BPC modules. These tubes are filled with TLD<sup>14</sup> crystals (Harshaw TLD-700) on a regular basis as will be discussed in more detail in section 7.2. The type of TLD crystals used are based on a Lithium-7 isotope fluoride ( $\text{LiF}_2$ ) which are useful to measure doses up to 3 kGy. The TLD crystals are calibrated using a  $^{137}\text{Cs}$  source and analyzed using an automated apparatus by measuring the glow curve of exposed TLD crystals. The accuracy of the measured dose has been estimated to be approximately 10% which significantly decreases if the range of applicability is reached.

As will be discussed in detail in section 7.2, the measurement of the radiation background of the BPC by means of a dark current measurement using a Si-diode was essential to determine the origin of the measured accumulated dose as a function of the HERA operation. Two Hamamatsu silicon photodiodes (Hamamatsu S2662) with a sensitive area of  $7.5 \times 20 \text{ mm}^2$  enclosed inside a light-tight cover were installed in front of both BPC modules, as shown in Figure 5.28. These two diodes were read out by a simple pre-amplifier circuit [We92]. It has been laid out on a standard NIM card located inside the cryo-tower and read out by a voltage-sensitive ADC [Lo96]. The readout scheme was implemented to be completely independent of the ZEUS data acquisition system. A bias voltage of 27 V was chosen to allow a maximum sensitivity to the incoming particle flux.

Two standard monitoring tools have been used to investigate the performance of the optical components of the BPC:

- $^{60}\text{Co}$ -scans [Be92] of both BPC modules and
- a scan of individual scintillator fingers.

Prior to the installation of the BPC both BPC modules were scanned using  $^{60}\text{Co}$  scans. A point-like  $^{60}\text{Co}$  source emitting  $\gamma$  rays of 1.17 MeV and 1.33 MeV was moved using a stepping motor on the opposite side of the WLS-bars along the BPC within a brass tube as shown in Figure 5.29. The plot above the schematic drawing shows the response of one particular readout channel as a function of the location of the  $^{60}\text{Co}$  source. These scans have been performed moving the  $^{60}\text{Co}$  source for each readout channel on the respective opposite side. It allowed to determine assembly faults and a first relative calibration. For that, the response for each readout channel has been integrated and used to adjust the HV of the respective PMT using the gain measurements of the BPC PMTs. This allowed a first relative calibration at the level of approximately 7% (Section 8.5.3).

The BPC North modules was scanned after the 1995 data taking to evaluate the effect of radiation damage on the optical components. The  $^{60}\text{Co}$  results before the installation of the BPC modules within the ZEUS experiment served as a reference. A comparison of these results will be presented in section 7.2.

Besides a scan using a movable  $^{60}\text{Co}$  source, several scintillator fingers have been scanned using the same setup as described in section 5.4.3. A comparison of scanning results among individual scintillator fingers before and after the 1995 HERA run will be discussed in section 7.2.

<sup>14</sup>Thermo-luminescence dosimeter.

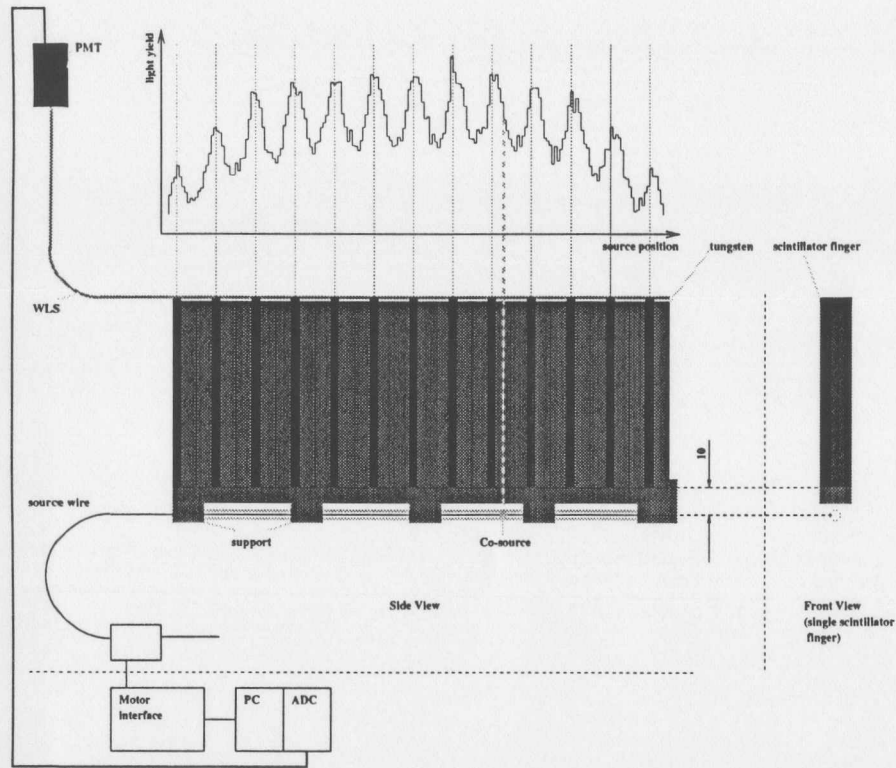


Figure 5.29: Schematic drawing to illustrate the BPC  $^{60}\text{Co}$  scans.

## 5.8 Survey

The absolute position of the BPC was determined through an optical survey procedure at the end of the 1995 data taking period besides an in-situ position calibration using elastic QED Compton events (Section 8.3.4).

The top of the compensator magnet has two reference platforms which have been surveyed prior to the actual survey of the BPC with respect to the CTD frustum with an accuracy of approximately 0.5 mm. These two reference points have then been used to survey both BPC modules, i.e. the distance as well as the polar and azimuthal angle of a particular survey mark on the BPC with respect to the reference platforms. The tilt of both BPC modules have been measured as well. The tilt of the nominal beam axis (Figure A.6) with respect to the horizontal plane has been measured to be 5.875 mrad. Both BPC modules have been installed within ZEUS such that they are tilted with respect to the horizontal plane by approximately 6 mrad.

Since the polar angles turned out to be too steep and not visible by the theodolite used, a precisely machined survey platform was mounted on top of each BPC module which allowed to insert two survey marks, as shown in Figure 5.30 for one of the reference points. These

BPC module	X (mm)	Y (mm)	Z (mm)
North	38.7	1.8	-2936.6
South	-74.7	1.4	-2936.8

Table 5.4: Survey results of the BPC North and South modules in 1995.

survey marks have been then surveyed from both reference points on top of the compensator magnet. The survey platform including the two survey marks were later surveyed on the bench to an accuracy of 0.1 mm. Using the internal alignment of the scintillator fingers known to an accuracy of 0.1 mm (Section 5.4.2), it was possible to calculate among the survey results the absolute position of the BPC ( $X$ : front beam pipe edge;  $Y$ : interface between 8th and 9th scintillator finger;  $Z$ : front face of first tungsten plate) with respect to the mechanical axis of the CTD and therefore to the ZEUS coordinate system. The accuracy of the BPC survey has been estimated to be at best 0.5 mm [We96]. The major source of uncertainty is due to the difficulty in the determination of the absolute position of the reference platforms on top of the compensator magnet with respect to the ZEUS coordinate system. The compensator magnet is subject to horizontal movements of up to 0.5 mm depending on the position of the ZEUS RCAL modules. An independent measurement of the reference platforms prior to the actual BPC survey is essential.

To achieve an accuracy of the absolute positioning of the BPC of 0.5 mm, an independent position calibration via elastic QED Compton events is necessary (Section 8.3.4).

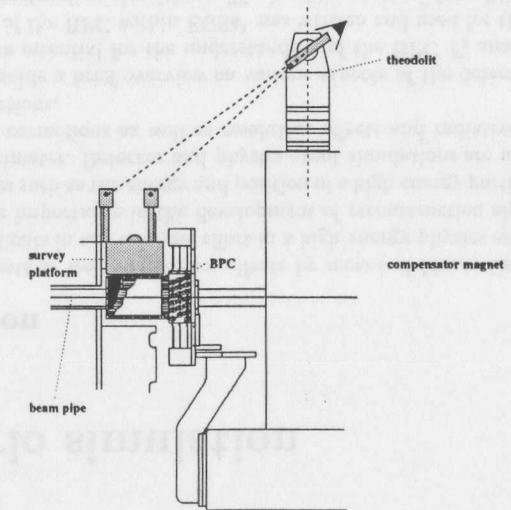


Figure 5.30: Side view of the BPC survey setup.

## Chapter 6

### Monte-Carlo simulation

#### 6.1 Introduction

Simulation of physics events as well as detector effects by means of Monte-Carlo (MC) techniques are essential ingredients in any analysis effort in a high-energy-physics experiment. This includes for example their importance in the development of reconstruction algorithms to extract measurable quantities such as the energy and position of a high energy particle from energy depositions within a calorimeter. Detector and physics event simulations are used to evaluate acceptance and efficiency corrections as well as resolution effects and radiative corrections in order to measure cross-sections.

The following sections provide a brief overview on various aspects of the detector and physics event simulation which are essential for the understanding of the BPC  $F_2$  analysis. A stand-alone detector simulation of the BPC within EGS4<sup>1</sup> was written and used for the development of energy and position reconstruction algorithms. The implementation of the BPC within EGS4 and the optimization of various tracking parameters will be focused on in the next section. The detector simulation of the ZEUS detector including the BPC based on the simulation package GEANT [Br89] will be briefly summarized in section 6.3. Basic elements of the simulation of  $ep$  physics events such as electroweak radiation at the lepton vertex as well as the simulation of the hadronic final state will be discussed in section 6.4. An overview of the MC event generators used for the physics analysis, in particular the modifications of some MC generators to generate physics events in the kinematic region of the BPC, will be given in section 6.5.

#### 6.2 Simulation of the BPC within EGS4

The EGS4 code is a general purpose MC simulation package for the coupled transport of electrons/positrons and photons in an arbitrary geometry which can consist of any element, compound, or mixture [Bi94]. The simulation only concerns electromagnetic processes which are theoretically well understood and calculatable within the framework of QED. The simulation of electromagnetic processes using EGS4 therefore allows precise estimates of event quantities such as the energy deposition within a calorimeter which have been cross checked in numerous applications. The processes simulated within EGS4 which refer to interactions of electrons in matter are (Section 5.2): bremsstrahlung, positron annihilation, Bhabha and Møller scattering, multiple scattering and energy loss due to excitation and ionization. The following photon processes are simulated within EGS4: pair production, Rayleigh scattering, Compton scattering,

<sup>1</sup>Electron Gamma Shower (Version 4).

15 GeV, 20 GeV and 25 GeV).

3. Energy uniformity scan (5 GeV, 10 GeV, 15 GeV, 20 GeV and 25 GeV) with varying normal incident impact position in  $X$  with an incident angle of  $88^\circ$  and  $90^\circ$  respectively, with respect to the BPC front face.
4. Implementation of the degradation of each scintillator strip due to radiation damage (5 GeV, 10 GeV, 15 GeV, 20 GeV, 25 GeV and 27.5 GeV) (Section 7.2 and 8.5.4).

These samples (1-3) are used for the development of the BPC energy and position reconstruction algorithms (Chapter 8). The fourth sample is used to evaluate the effect of radiation damage on the linearity of the absolute energy scale of the BPC. This will be discussed in detail in section 8.5.4.

### 6.3 Simulation of the ZEUS detector within MOZART

The ZEUS detector simulation [Ho93] is based on an extensive software chain which provides a description of various detector components representing their geometry, the materials they consist of and their position. Electromagnetic and hadronic type particles can be tracked through these simulated detector volumes taking into account various electromagnetic and hadronic interactions which these particle undergo within a particular media. The detector simulation is based on the GEANT program [Br89]. The ZEUS detector simulation, together with various trigger simulation related software packages, is called MOZART (MOnte Carlo for ZEUS Analysis, Reconstruction and Trigger).

The BPC detector simulation based on GEANT was incorporated within the program MOZART including several additions among the simulation of the rear section of the ZEUS detector such as the new asymmetric beam pipe (Section 5.4) and the movement of two RCAL modules R12T and R12B closer to the beam. The impact of tracking parameters such as the step length and the shower energy thresholds on the energy resolution, sampling fraction and CPU time has been extensively studied and optimized for the BPC detector simulation. Figure 6.2 shows a 3D view of the BPC North module as implemented within MOZART using GEANT. Similar to the case of the simulation of the BPC within EGS4, several readout elements such as the WLS have been omitted for simplicity in the BPC detector simulation. It was shown as well that the energy responds across the simulated scintillator fingers as well as the energy resolution is not affected by ignoring the  $100\ \mu\text{m}$  gap between adjacent scintillator fingers [Ti97].

The tracking of particles from simulated  $ep$  physics events starts with a list of particles for a particular event which includes for each particle its type, four vector and production vertex. MC event information, characteristic to each detector component such as the energy depositions in the BPC scintillator fingers, are used to fill the same type of ADAMO tables (Section 4.6) as for real data. True MC event information such as the true energy of a positron hitting the BPC is provided in additional ADAMO tables.

### 6.4 Basic elements of the simulation of $ep$ physics events

The double differential cross-section describing inelastic  $ep$  scattering,  $d\sigma^2/dy dQ^2$ , has been discussed in detail in section 2.2.2 to lowest order perturbation theory, i.e. only terms of order  $\alpha^2$  have been taken into account. This double differential cross-section is known as the Born

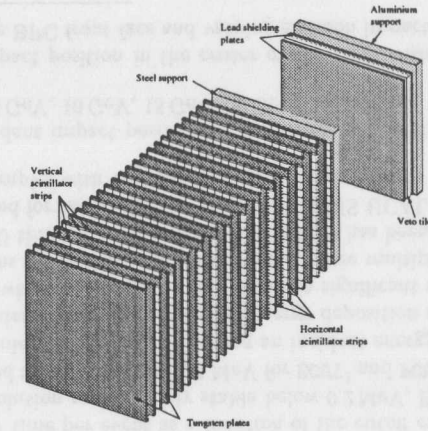


Figure 6.2: Implementation of the BPC design within GEANT.

differential cross-section. The proton structure functions  $F_1$  and  $F_2$  are defined with respect to the Born differential cross-section.

Figure 6.3 (a) shows the Born-level  $ep$  Feynman diagram. Higher order diagrams lead to corrections which have to be taken into account in order to extract the Born differential cross-section and thus the proton structure function  $F_2$ . These corrections arise from the emission of additional real or virtual photons from either the lepton or the quark line. Corrections at the quark line are proportional to the square of the quark charge and are therefore smaller than leptonic corrections. The quarkonic corrections are included in the definition of parton distribution functions. Corrections due to lepton-quark interference have been shown to be significantly smaller than leptonic corrections. Contributions which involve the heavy gauge bosons  $Z^0$  and  $W^\pm$  can be completely ignored in the kinematic region covered in this thesis [Sp92].

The dominant contributions to higher order corrections above the Born level are therefore QED corrections. Figure 6.3 (b-e) show the Feynman diagrams at order  $\alpha^3$  which refer to QED corrections. In case of initial state radiation, the emitted photon travels collinearly with the electron beam and remains therefore undetected in the main detector. The energy of the electron at the leptonic vertex is therefore less than the beam energy. If the electron beam energy is used to evaluate the kinematic variables  $x$ ,  $y$  and  $Q^2$  (Electron method), one obtains the so called apparent values ( $x_{app}$ ,  $y_{app}$  and  $Q_{app}^2$ ) which are different from the true values at the hadronic vertex. In case of final state radiation, the emitted photon travels close to the outgoing electron. Provided that the angle of emission is small, the energy of the final-state-radiated photon is included in the energy measurement of the outgoing electron using a calorimeter. One therefore obtains the true kinematic variables  $x$ ,  $y$  and  $Q^2$ . In summary, the emission of a photon at the lepton line will shift the kinematic variables which are therefore systematically different from the kinematic variables at the hadronic vertex where the proton is being probed. To infer from the observed cross-section the Born cross-section, one has to take these systematic shifts into account. Radiative corrections [Mo69] are included through the term  $\delta_{RC}(y, Q^2)$  which is defined as follows:

and the photoelectric effect. EGS4 allows the simulation of incident electrons/positrons in the range of a few tens of keV up to a few thousand GeV. In case of photons, simulations can be performed for photon energies between 1 keV and several thousand GeV. Energy depositions within a particular detector volume such as the active layers of the BPC can be scored and read out on an event-by-event basis. Thus, the response of a detector to a particular incident electromagnetic particle can be simulated.

The EGS4 code, written in FORTRAN, is provided by a set of subroutines and block data statements. Before performing a simulation using EGS4 the material data, i.e. the material cross-section and branching ratio data have to be created by the program PEGS4.

The user has to provide a main program which has to proceed through the following steps by calling various EGS4 subroutines:

- initialization of requested material data by calling the subroutine HATCH,
- initialization of the radiation transport: charge, position, angle and energy of incident particle,
- call to the subroutine SHOWER which controls the whole simulation which requires
- the user routine HOWFAR to specify the detector geometry and
- the user routine AUSGAB to score and output various event quantities.

Within the user routine HOWFAR, any auxiliary volume such as planes, cylinders, cones, spheres, etc. can be specified. The user has access to a variety of event quantities which specify the particle type, energy, position and media type. Using this information, the user has to determine within the subroutine HOWFAR if a particular particle leaves the current volume having a certain size and therefore enters another volume and the tracking of the particle is continued in the new volume or the tracking should be stopped since the particle under consideration leaves the detector volume. The definition of volumes is performed through various constraints among the position of particles being tracked.

The subroutine AUSGAB is used to score and output for each tracking step a variety of quantities on request of the user such as the position of particles, particle type, type of interaction and the amount of energy deposited during the last tracking step. In the case of simulation of an electromagnetic sampling calorimeter, the deposited energy information for each step can be summed for each active sampling layer and recorded after the simulation of the whole shower is finished. The simulation for a particular particle in a shower is terminated if its energy falls below a certain energy cutoff which has to be specified in the initialization of the material data. The simulated geometry of the BPC reflects the size of the BPC North module (Section 5.4). Figure 6.1 shows the implemented geometry of the BPC within EGS4. 26 layers of 3.5 mm thick tungsten alloy plates (ID: 1, 3, 5, ..., 51) are separated by layers of 2.6 mm thick scintillator sheets (ID: 2, 4, 6, ..., 52) which in turn are separated by 8 mm wide scintillator fingers to provide a segmented energy deposition. The 5 mm wide tungsten bars on the edge of each tungsten plate are simulated as well. Each volume needed has the shape of a cube. The geometry definition within HOWFAR has therefore been enormously simplified by writing a single subroutine which specifies the general geometrical layout of a cube with the size of each individual layer stored in a data statement. Depending on the position of a particular shower particle, the corresponding dimensions of the current layer is picked up from this data statement. Any details concerning the WLS readout, the brass spacers and the aluminum wrapping of scintillator fingers have been omitted for simplicity. As pointed out in Section 5.4, the gap between

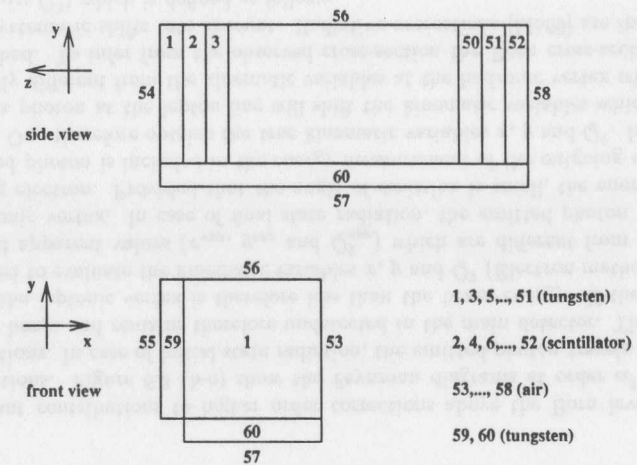


Figure 6.1: Implementation of the BPC design within EGS4.

scintillator fingers amounts to  $100\ \mu\text{m}$ . It has been verified that the energy response across the simulated scintillator fingers as well as the energy resolution is not affected by ignoring the gap in the geometry definition of the active layers of the BPC. This enormously simplifies the simulation, in particular the execution time.

The tungsten material is specified as a mixture of 95.5% tungsten and 4.5% copper with a density of  $18.0\ \text{gcm}^{-3}$  (Section 5.4.2). The scintillator layers are represented by polystyrene with a ratio of the number of hydrogen to carbon atoms of one and a density of  $1.032\ \text{gcm}^{-3}$ . Several tracking parameters within EGS4 can be tuned and optimized for a particular application.

The energy cutoff parameters of electrons ECUT and photons PCUT determine below which energy the tracking is terminated and the energy of a particle is deposited on the spot. The energy cutoff parameters have been optimized by examining the sampling fraction, the energy resolution and the CPU time per event as a function of the cutoff energy. The sampling fraction and the energy resolution remain fairly stable below 0.2 MeV. Based on this optimization procedure, it was decided to use a value of 0.1 MeV for ECUT<sup>2</sup> and PCUT. These parameters have been chosen for the simulation of electrons having an incident energy above 1 GeV.

The parameter ESTEPE determines the amount of energy deposition per simulated step length. Choosing a step length which is too large could result in significant uncertainties in particular in multilayer applications. Very small step lengths can cause multiple scattering to be turned off and increase the CPU time. The optimization of ESTEPE has been performed according to a procedure which was used for the parameter study of a ZEUS UCAL prototype module [Jo99]. The generated EGS4 samples with 10000 events each are as follows:

1. Fixed normal incident impact position in the center of the BPC with varying electron impact energies (5 GeV, 10 GeV, 15 GeV, 20 GeV, 25 GeV and 30 GeV).
2. Fixed incident impact position in the center of the BPC with an incident angle of  $88^\circ$  with respect to the BPC front face and varying electron impact energies (5 GeV, 10 GeV,

<sup>2</sup>EGS4 requires the electron rest mass to be included in ECUT, i.e. ECUT is set to 0.611 MeV.

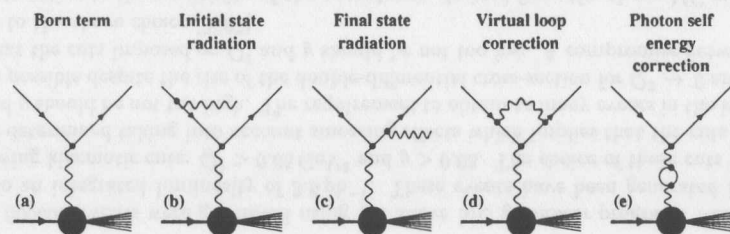


Figure 6.3: QED radiative corrections.

$$\left(\frac{d\sigma^2}{dydQ^2}\right) = \left(\frac{d\sigma^2}{dydQ^2}\right)_{\text{Born}} \cdot [1 + \delta_{RC}(y, Q^2)] \quad (6.1)$$

The Monte Carlo generator HERACLES [Kw91] provides a simulation of the NC process  $eq \rightarrow eq\gamma$  which includes initial and final state radiation and the full one-loop virtual corrections.

Figure 6.4 shows the size of radiative corrections in % as a function of  $y$  for  $Q^2 = 0.3 \text{ GeV}^2$ . The solid line refers to the LLA<sup>3</sup> order  $\alpha^3$  radiative correction. The dashed line represents the sum of LLA order  $\alpha^3$  and  $\alpha^4$  radiative corrections together with higher order terms from soft photon exponentiation. The difference between both estimates is well below 1% for  $0.08 < y < 0.74$  which represents the kinematic range in  $y$  covered by the physics analysis presented in this thesis. These corrections have been evaluated using the program HERACLES [Kw91] in the HELIOS mode [BI91]. It has been shown that the amount of radiative corrections varies only slowly within the  $Q^2$  range of the BPC. The amount of radiative corrections drastically increases towards high values in  $y$  to be well above 30%. This can be significantly reduced by imposing a cut on the variable  $E - P_z$  reconstructed from the hadronic final state which will be discussed in detail in section 10.2. This cut is equivalent to imposing a cut on the energy of the initial state photon.

A MC prediction for  $\delta_{RC}(y, Q^2)$  is used for the radiative correction procedure. This can be done explicitly by correcting the measured cross-section or implicitly by using a MC sample which was generated with radiative corrections. The implicit radiative correction procedure will be discussed in more detail in section 11.3.

The hadronic final state has to be as well simulated using MC techniques which turns out to be significantly more complicated. This is because of the QCD dynamics which affects the struck quark which carries a certain color. Figure 6.5 displays the development of the hadronic final state of the  $ep$  scattering process. The formation of hadrons which are being measured in the detector out of a collection of quarks and gluons cannot be calculated within QCD. Phenomenological models are necessary to provide a description of the parton shower process as well as the final hadronization. The formation of a parton shower is being simulated using for example the Color Dipole Model (CDM) [An89]. A color dipole is formed between the struck quark and the proton remnant which can radiate gluons which in turn form additional dipoles. Quark-antiquark pairs are created from the break up of color dipoles. This shower process is terminated after the participating quarks and gluons reach a certain minimum momentum.

<sup>3</sup>Leading Logarithmic Approximation [Mo69].

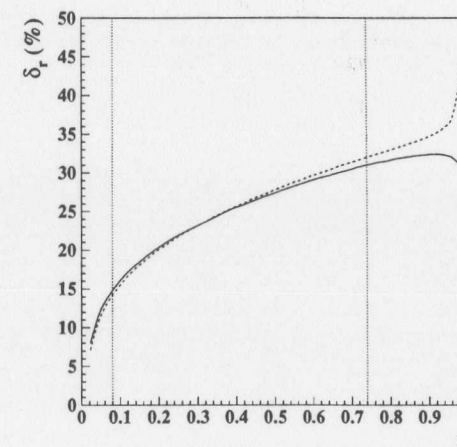


Figure 6.4: Magnitude of radiative corrections. The solid line refers to the LLA order  $\alpha^3$  radiative correction. The dashed line represents the sum of LLA order  $\alpha^3$  and  $\alpha^4$  radiative corrections together with higher order terms from soft photon exponentiation. The vertical dotted lines refer to the kinematic range in  $y$  covered by the physics analysis presented in this thesis.

This mechanism is implemented in the MC generator ARIADNE [Lö92]. ARIADNE also allows the simulation of diffractive events with a large rapidity gap on the basis of a color singlet exchange assuming that the struck quark originates from a colorless state within the proton. An alternative approach to describe the formation of a parton shower is given by the parton shower (PS) model [Be88]. The hadronization among the produced quarks and gluons is simulated within the program JETSET [Be87b] which uses the LUND string fragmentation model [An83]. A color string is formed between quarks moving apart. Provided that the string energy is large enough, a string can break apart into shorter pieces. This procedure stops as soon as the energy of a string is no longer enough to create additional strings. In the final step, these strings are converted into hadrons.

## 6.5 MC event generators and samples

The starting point for the simulation of  $e^+p$  collisions in the kinematic region of the BPC is the program package DJANGO 6.22 which combines the programs LEPTO 6.4.1 [In96], HERACLES 4.5.1 [Kw91] and ARIADNE 4.06 [Lö92].

The MC-generator HERACLES calculates the structure functions  $F_2$  and  $F_L$  from an input set of parton density functions from which it calculates the differential cross-section including initial and final state radiation and the full one-loop virtual corrections. The description of the parton shower formation is taken into account using the program ARIADNE. The program JETSET, as implemented in LEPTO, is then used to perform the LUND string fragmentation and hadronization.

The measurement of the proton structure function  $F_2$  requires to know the longitudinal structure function  $F_L$ , since both cannot be measured separately at fixed center-of-mass energy  $\sqrt{s}$ .

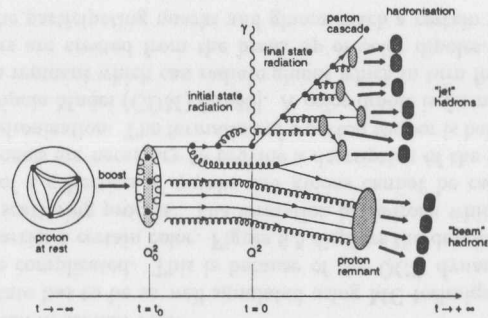


Figure 6.5: Formation of the hadronic final state of the  $ep$  scattering process.

The contribution from  $F_L$  to the double-differential cross-section  $d\sigma^2/dy dQ^2$  is kinematically suppressed at low  $y$ .  $F_L$  is expected to vanish like  $F_L \propto Q^4$  for  $Q^2 \rightarrow 0$  (Section 2.3.1). Since the contribution from  $F_L$  to  $d\sigma^2/dy dQ^2$  is expected to be small,  $F_L$  has been set to naught for the generation of MC events for the analysis presented in this thesis. This implies that the extracted  $F_2$  values from data are those for which  $F_L = 0$ . Any other assumption on  $F_L$  can later be used to correct the extracted  $F_2$  ( $F_L = 0$ ) values from data (Section 11.3.2).

Several modifications were necessary for the simulation of  $e^+p$  events in the kinematic region of the BPC. The DL parameterization (Section 2.3.4) was used to evaluate  $F_2$  in the kinematic region of the BPC. This parameterization yields in the limit  $Q^2 \rightarrow 0$  the total photoproduction cross-section which is well described by the DL model. HERACLES requires a set of parton distribution functions as input. These have been calculated by re-weighting MRSA [Ma94] parton distribution functions using the following weight factor:  $F_2(\text{DL})/F_2(\text{MRSA})$ .

Diffractive events were generated using the program ARIADNE according to  $d^2\sigma/dtdM_X^2 \sim e^{bt}/(M_X^2 + Q^2 - M_\rho^2)^{\alpha_{IP}}$  with  $b = 6 \text{ GeV}^{-2}$  and  $\alpha_{IP} = 1.1$  where  $t$  is the square of the four-momentum transferred to the outgoing proton.  $M_X$  is the invariant mass of the hadronic final state.

Elastic vector meson production contribute to the total photoproduction cross-section to about 12%. The relative fraction of the light vector mesons in photoproduction amounts to  $\rho^0 : \omega = 12 : 1$  and  $\rho^0 : \phi = 15 : 1$ , respectively [De96c]. The elastic  $\rho^0$  vector meson contribution is therefore expected to dominate. This event class was generated in the kinematic range of the BPC using a similar procedure as for the generation of large  $M_X$  diffractive events [Ti97].

The fraction of diffractive and elastic  $\rho^0$  used in the final sample will be discussed in section 9.5.

In total, 600000 events were generated using the above MC generator programs which corresponds to an integrated luminosity of  $3.6 \text{ pb}^{-1}$ . These events have been generated imposing the following kinematic cuts:  $Q^2 > 0.05 \text{ GeV}^2$  and  $y > 0.03$ . The choice of these cuts has been carefully determined taking into account smearing effects which implies that the cuts imposed on  $Q^2$  and  $y$  should be not too high. The requirement to obtain as many events in the kinematic region as possible despite the rise of the double-differential cross-section for  $Q^2 \rightarrow 0$  and  $y \rightarrow 0$  means that the cuts imposed on  $Q^2$  and  $y$  should be not too low. A compromise between both gave rise to the above choice [Ti97].

In order to estimate the sensitivity of the acceptance, derived from the above MC sample for the determination of the proton structure function  $F_2$ , on the simulation of various underlying MC processes with respect to several constraints among the hadronic final state (Section 10.2),

the acceptance determination was compared to those of different MC generators (Section 9.5). The program EPSOFT [Ka95] was used to generate a non-diffractive sample of minimum bias events as well as resolved and direct di-jet events was generated using the PYTHIA [Be87a] program. Single and double dissociate diffractive events as well as elastic  $\rho^0$  events were generated using the HERWIG MC generator [Ti96].

Photoproduction background events were generated using the PYTHIA program [Be87a] using an ALLM [Ab90] cross-section parameterization. The contributions from various sub-processes have been taken from [De94]. Events were generated in the range of  $Q_{\text{min}}^2 < Q^2 < 0.05$  and  $0.5 < y < 1.0$  whereas  $Q_{\text{min}}^2 = m_e^2 y^2 / (1 - y)$ . The generated background sample of 60000 events corresponds to an integrated luminosity of  $0.59 \text{ pb}^{-1}$ .

Both MC samples were passed through the complete ZEUS simulation chain and processed using the same off-line reconstruction software as for data. A simulation of the BPC trigger has been omitted. The BPC trigger efficiency has been taken into account off-line (Section 9.2).

## Chapter 7

### The 95-running conditions

#### 7.1 Trigger configuration and implementation

##### Introduction

The hardware part of the BPC first-level trigger was discussed in detail in section 5.6. Energy and timing information of the BPC trigger is used at the ZEUS Global First Level Trigger (GFLT). The trigger logic formed from the BPC trigger information together with the first-level trigger input from other detector components defines a particular BPC GFLT trigger slot. This provides the BPC related input at the next trigger levels within the ZEUS trigger scheme (Section 4.5) which is used in a variety of physics applications. The BPC trigger configuration was designed to incorporate the following physics interests:

- BPC  $F_2$  measurement,
- study of elastic  $\rho^0$  vector meson production,
- study of BPC tagged high  $E_T$  jet events,
- study of BPC tagged radiative events,
- study of elastic QED Compton events tagged in both BPC modules,
- study of BPC tagged elastic  $e^+p$  events and
- study of the photoproduction background for high  $Q^2$  events with a reconstructed positron in the main calorimeter.

This list underlines the physics potential of the BPC at ZEUS. The following section provides an overview of the implementation of the BPC trigger within the ZEUS trigger scheme, in particular the definition of energy and timing cuts, a discussion of the BPC trigger rate and an overview of the configuration of the BPC trigger within the ZEUS three-level trigger scheme to incorporate the above physics interests. The following discussion will focus on the BPC North module which is the main component used for the physics analysis presented in this thesis.

##### Implementation

A series of test trigger runs have been taken prior to the actual BPC data taking in 1995 to examine the TDC spectra for the BPC timing and the FADC spectra for the BPC energy in order to establish proper cuts at the GFLT for the BPC North module. Among the various



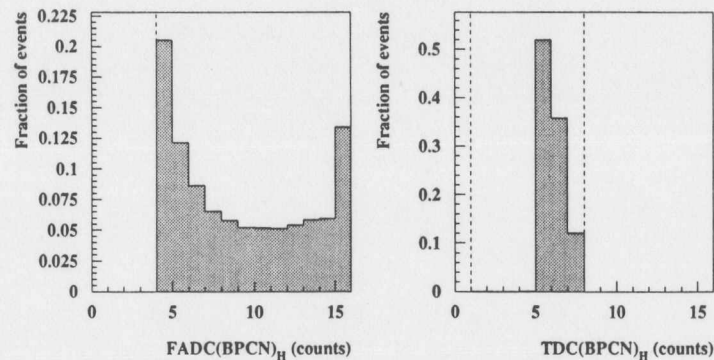


Figure 7.1: FADC (left) and TDC (right) spectra for events passing the GFLT SLOT 52 requirements ( $FADC(BPCN)_H \geq 4$  and  $1 \leq TDC(BPCN)_H < 8$ ).

trigger sums provided by the BPC trigger hardware (Section 5.6), only the horizontal sum was used to derive a trigger signal for the energy and timing information. This choice was made over the vertical sum to minimize the influence of a possible degradation of the inner most vertical strips due to radiation damage which is expected to increase towards the beam pipe edge of the BPC (Section 7.2). All other trigger sums have not been used for any trigger decision at the GFLT. This enormously simplified the understanding of the BPC trigger. The main emphasis will be placed in the following on the BPC  $F_2$  trigger configuration. The design of an inclusive trigger for the BPC  $F_2$  measurement was driven by the requirement to only impose cuts on the BPC energy and timing information available at the GFLT. This concept had to be somewhat modified due to unexpected high background rates.

Figure 7.1 shows the FADC and TDC spectra. Figure 7.2 displays the correlation between the FADC digitized energy for the horizontal trigger sum and the final off-line reconstructed energy of the BPC North module. Events to be triggered had to pass a timing window of  $1 \leq TDC(BPCN)_H < 8$ . The calibration of the FADC energy spectra using the off-line reconstructed energy which was determined to an accuracy of 0.5% yields a calibration factor of approximately 1.8 GeV per FADC count. This value has been determined from a linear fit to the correlation plot in Figure 7.2. The last FADC bit has not been included in the straight line fit since the FADC was already saturated. The small offset is due to the voltage offset in the differential receiver cards (Section 5.6). The chosen energy cut amounts to  $FADC(BPCN)_H \geq 4$ . The chosen cuts represent a compromise between reducing the rate of background events at the trigger level which is expected to increase towards small positron energies and still having a large enough acceptance for small positron energies to achieve a maximum possible coverage of the region of small  $x$  values. The initial setup of the BPC trigger as a pure inclusive trigger, i.e. using only the BPC energy and timing information, is very sensitive to any background events which occur in time to an  $e^+p$  collision. It turned out that a vast amount of the unexpected high background rate in the BPC North and the BPC South module was due to off-momentum positrons.

A series of dipole and quadrupole magnets of the straight section downstream of the ZEUS detector is used to deflect and focus the positron beam onto the interaction point to yield a head-on collision between positrons and protons. A simulation of positrons losing energy via

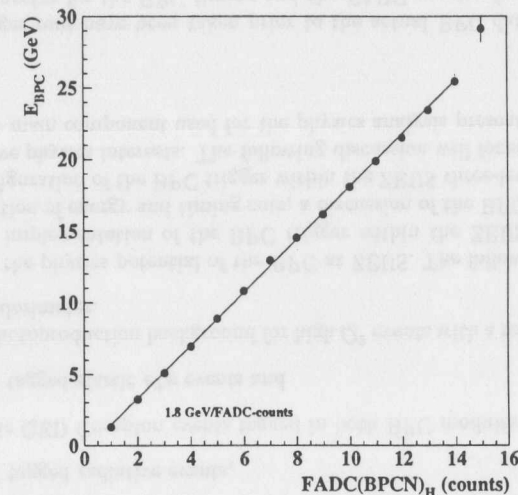


Figure 7.2: Correlation between the FADC digitized energy for the horizontal trigger sum and the final off-line reconstructed energy of the BPC North module. A linear fit yields 1.8 GeV per FADC count.

bremstrahlung was used to track these off-momentum positrons through the HERA machine lattice [Kö97]. It was found that a lattice arrangement which would only consist of dipole magnets would only give rise to a significant background in the BPC North module, since the magnetic field within the dipole magnets has to bend the positron beam towards the interaction point. Quadrupole magnets are responsible for the fact that positrons having lost part of their energy through bremsstrahlung are being tracked through the lattice arrangement in such a way that they can end up on the opposite side, i.e. towards the side of the BPC South module which allows to understand the high background rate observed in the BPC South module. The result of the simulation of off-momentum positrons provided a qualitative understanding of the observed high background rate. A detailed quantitative understanding is rather difficult due to the complex dependence on the precise lattice layout, the  $Z$  position where the energy loss due to bremsstrahlung occurs and in particular the quality of the vacuum downstream of the ZEUS detector.

Figure A.3 shows a top view of the ZEUS interaction region. The positron beam which is being bent towards the interaction point is a strong source of synchrotron radiation. The collimators (C1-C4) are used to shield the central tracking detector as well as the calorimeter from synchrotron radiation. It was found that moving the inner (outer) collimator C4 towards the HERA beams cuts into the stream of off-momentum positrons and thereby significantly reduces the high background rate for the BPC North (South) module. Using a machine condition with only positrons in HERA and the C4 collimator being open, the measured energy in the BPC North module peaks at almost half the positron beam energy which gave rise to a significant background rate in the BPC North module based on the timing and energy cuts mentioned above. Closing the inner collimator C4 reduces these type of events and the BPC North energy spectra is dominated by low energy positrons well below 7 GeV. The inner and outer collimator

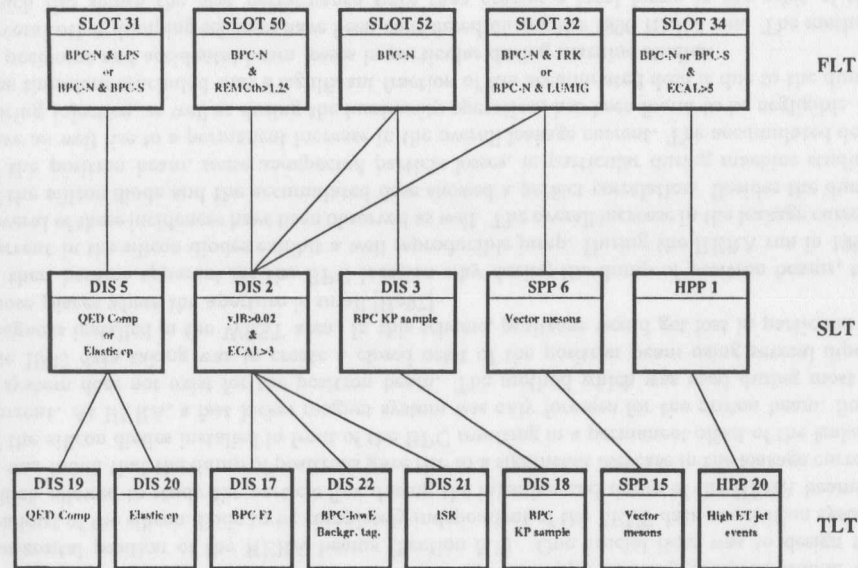


Figure 7.3: Use of the BPC in the 1995 trigger configuration.

C4 and the inner jaw of C3 had been open during the HERA runs from 1992 to 1994. With the installation of the BPC in 1995, the inner jaw of C4 was closed by 15 mm, the outer C4 jaw by 6 mm and the inner C3 jaw by 4 mm during luminosity operation. With this new collimator configuration, the background was reduced by approximately two orders of magnitude in the BPC North module.

The BPC FLT rate was between 10 and 30 Hz for the 1995 running period, taking into account the cuts on the energy and timing information as well as the new collimator position. No BPC trigger information was available for the 1995 HERA run at the Second and Third Level trigger. The rate of the BPC inclusive trigger turned out to be still not at an acceptable level at the Third Level Trigger. This necessitated imposing two additional cuts on two non-BPC quantities at the Second Level Trigger. The total energy measured in the main calorimeter (CAL) was required to be greater than 3 GeV. An approximate value of  $y_{FB}$  which was determined from the energy measured in the main calorimeter assuming an interaction vertex at  $Z = 0$ , was required to be greater than 0.02.

### Configuration

Figure 7.3 displays the 1995 BPC trigger configuration at all three trigger levels. This scheme takes into account the above mentioned physics items to be examined using the BPC. The following list provides a brief description of the individual GFLT trigger slots:

- **GFLT SLOT 31:** This GFLT SLOT is intended to study elastic QED Compton events tagged in both BPC modules and BPC tagged elastic  $e^+p$  events. For the first item, energy as well as timing cuts were imposed on the BPC South and BPC North modules. The second item required energy and timing cuts on the BPC North module and a hit in the LPS.

- **GFLT SLOT 50:** At the end of the 1995 HERA run, the GFLT SLOT 50 was implemented to study the photoproduction background for high  $Q^2$  events by requiring energy and timing cuts in the BPC North module and energy in the RCAL EMC sections.
- **GFLT SLOT 52:** This GFLT SLOT is the main BPC  $F_2$  GFLT trigger slot. It imposes energy as well as timing cuts on the BPC North module.
- **GFLT SLOT 32:** The study of elastic  $\rho^0$  vector meson production and BPC tagged radiative events is the main focus of this trigger. It requires energy as well as timing cuts on the BPC North module together with either a good track at the CTD FLT or energy in the LUMIG detector above 1 GeV.
- **GFLT SLOT 34:** BPC tagged high  $E_T$  jet events are studied by requiring energy as well as timing cuts in the BPC North or South module and energy in the main calorimeter (CAL).

The precise cuts imposed on the energy and timing information for SLOT 52 are the ones which have been discussed in the last section.

A brief description of the GFLT slots (DIS5, DIS2, DIS3, SPP6, HPP1) as well as the TLT slots (DIS19, DIS20, DIS17, DIS22, DIS21, DIS18, SPP15, HPP20) can be seen in Figure 7.3. A prescale factor 2 at the TLT slot DIS 17 was moved during the 1995 run from the GFLT SLOT 52 to the TLT slot DIS 17.

The trigger efficiency of the BPC  $F_2$  trigger (GFLT SLOT 52) will be discussed in detail in section 9.2. The GFLT SLOTS 31 and 32 have been exclusively used for alignment and calibration purposes. A detailed trigger efficiency study among those triggers was therefore omitted. The impact of the main calorimeter cuts on the acceptance determination will be focused on in section 9.5.

## 7.2 Radiation dose measurements

The BPC North module is located only 38.7 mm away from the beam. The accumulated dose was measured on a regular monthly basis using the TLDs mounted inside brass tubes within the BPC (Section 5.7). After the first months of data taking in 1995, a very high accumulated dose was measured on a monthly basis in the front inner brass tube of the BPC North module. Figure 7.4 shows the accumulated dose as a function of the central position of each TLD crystal within the front inner brass tube. The alignment accuracy of the TLD crystals was estimated to be approximately 2 mm. Over the whole 1995 data taking period, a characteristic dose profile was measured which shows a clear peak in the horizontal plane of the beam which falls off towards larger distances. The measured peak values reached the limits of the TLDs. It has been measured over a period of one month that the accumulated dose across the front face of the BPC North module shows approximately an exponential falloff in  $X$ .

Figure 7.5 shows a front and back view of both BPC modules as seen from the interaction point. Vertical lines indicate the position of the brass tubes containing the TLD crystals. The plotted values correspond to the accumulated dose measured over the whole 1995 HERA run in Gray. The position of the plotted dose values correspond to the approximate position of the TLD crystals. The accumulated dose in the BPC North module drops down significantly for larger distances away from the beam. It shows as well, a significant difference between the front and the back plane of the BPC North module which suggests that the particle flux leading to such a high dose has to be in direction of the positron beam. The dose in the BPC South

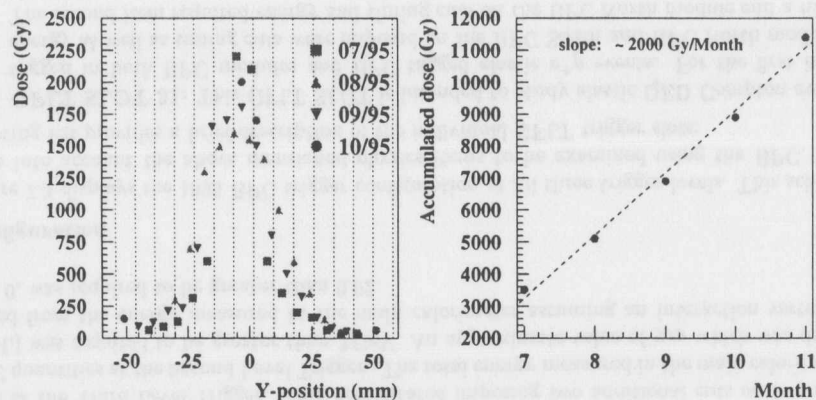


Figure 7.4: Dose profile (left) and accumulated dose for the maximum in  $Y$  (right) measured inside the front inner tube of the BPC North module for the HERA run in 1995.

module, measured over a period of one month, amounts to approximately 50 Gy which is lower by a factor 40 compared to the monthly dose measured in the BPC North module.

Over the first few months, several attempts have been made to understand the origin of such a high accumulated dose using various background monitoring devices in the RCAL region. It was not possible with these existing tools to trace the origin of the measured monthly dose as a function of the HERA operation, i.e. injection, luminosity run and dump or loss of particle beams. With the measured dose profile in mind, it was decided to install a silicon diode having a large sensitive area in front of the BPC North module approximately centered around the horizontal position of the HERA beams (Section 5.7). One crucial item was to design the readout of the silicon diode to be completely independent of the ZEUS data acquisition system which allowed to study the particle flux during the injection and dump of the HERA beams.

It was found that the dump of positrons gave rise to a significant increase in the leakage current of the silicon diodes installed in front of the BPC resulting in a permanent offset of the leakage current. At HERA, a fast kicker magnet system was only foreseen for the proton beam. Such a system does not exist for the positron beam. The method which was used during most of the 1995 data taking was to create a closed orbit of the positron beam using several dipole magnets installed in the WEST area. In this scheme, positrons would get lost in particular in those places where the aperture is small [Ho97].

It then became apparent for the BPC location why during the dump of positron beams, the current in the silicon diodes exhibit a well reproducible jump. During the HERA run in 1996, several of these incidences have been observed as well. The overall increase in the leakage current of the silicon diode and the accumulated dose showed a perfect correlation. Besides the dump of the positron beam, some unexpected particle losses, in particular during machine studies, gave as well rise to a permanent increase in the overall leakage current. The accumulated dose during injection, as well as during the luminosity operation, has been found to be negligible. It was therefore concluded that a significant fraction of the accumulated dose is due to the dump of positrons and accidental beam losses in particular during machine studies.

Several other dumping schemes have been considered during the 1996 HERA run. The method which has shown the best performance since then creates a local bump in the orbit of the

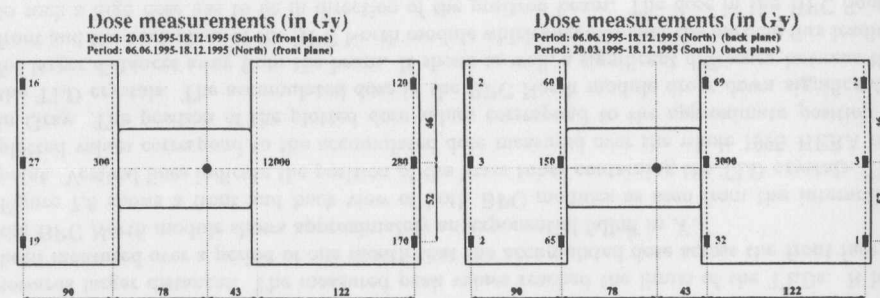


Figure 7.5: Measured dose in the front (left) and back (right) of the BPC modules for the HERA run in 1995.

positron beam using a series of dipole magnets in the WEST area [Ho97].

The significant difference between the accumulated dose measured within the BPC North module and the BPC South module has not been fully understood.

The total accumulated dose during the HERA run in 1995 amounted to about 12 kGy and 10 kGy during 1996 measured in the center of the front inner brass tube of the BPC North module. The amount of radiation damage in the BPC North module was determined using  $^{60}\text{Co}$ -scans. Radiation damage was clearly identified which showed a non-uniform structure as expected from the dose profile measurements. It was therefore decided to disassemble the BPC North module after the HERA run in 1995 and 1996 to investigate the response of individual scintillator fingers and replace damaged scintillator fingers.

In the following, results of  $^{60}\text{Co}$ -scans and of scintillator finger scans will be briefly summarized. The use of  $^{60}\text{Co}$ -scans as a calorimeter monitoring tool has been discussed in detail in section 5.7. The results of  $^{60}\text{Co}$ -scans among the BPC North module prior to its installation provides a reference which will be used to compare the  $^{60}\text{Co}$ -scans of the BPC North module after the 1995 data taking with. Scintillator strips which are closest to the beam as well as scintillator strips around the central position of the BPC are expected to be more damaged compared to scintillator strips being further away from the beam and the central position. Figure 7.6 shows results of four  $^{60}\text{Co}$ -scans of the X2 and X5 channels as well as among the Y9 and the Y13 channels (dashed line) in comparison to the reference  $^{60}\text{Co}$  measurements (solid line). One clearly notices the loss of light yield in individual scintillator fingers towards the front of the BPC for the channels X2 and Y9. This effect is no longer visible for the channels X5 and Y13.

A sample of scintillator fingers have been scanned using the setup as described in section 5.4.3. Figure 7.7 shows results of scans among X scintillator fingers from the first active layer (a) and the seventh active layer (c). Figure 7.7 displays as well the case for Y fingers from the second (b) and eighth (d) active layer. Horizontal arrows indicate the location of the fiducial volume of the BPC North module. The amount of radiation damage increases towards the beam pipe edge of the BPC and the central position of the BPC associated with a characteristic loss of light yield. It was found that the amount of light yield loss increases from the first active layers towards approximately the shower maximum and then quickly decreases to the case of a reference sample. This underlines the fact that the particle flux has to be associated with high energy electromagnetic particles which have been found to result from the dump of positrons and accidental losses of positrons within HERA. The results of the scintillator finger scans follow the expectations from the dose profile measurements (Figure 7.4).

The shape of the curves in Figure 7.7 can be understood through the following qualitative ansatz

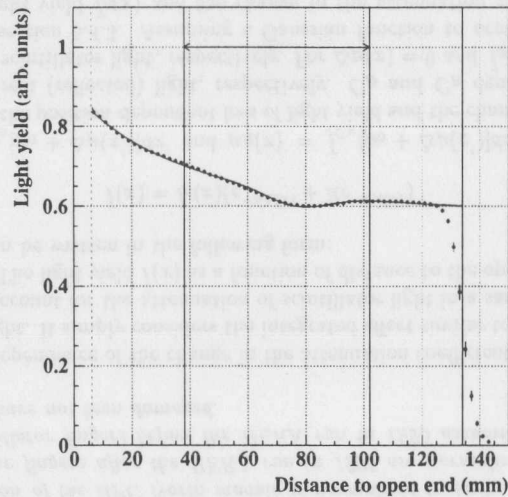


Figure 7.8: Scan of a X1 scintillator finger (seventh active layer) from the BPC North module after the HERA run in 1995. The horizontal arrow indicates the location of the fiducial volume of the BPC North module. The solid curve represents a fit to the observed light yield behavior due to radiation damage according to equation 7.1.

It should be noted that a detailed wavelength dependent quantitative understanding has been shown for the case of a homogeneous damaged scintillator material in [Da96]. It turns out that the strongly localized damage within a scintillator finger makes a detailed wavelength dependent quantitative understanding rather difficult. Several wavelength dependent studies have been carried out and can be found in [Bo97a].

## Chapter 8

# BPC Reconstruction and performance

### 8.1 Introduction

The key to studying inclusive  $e^+p$ -scattering at very small values of  $Q^2$  with the ZEUS detector is to tag the scattered positron under very small angles using the Beam Pipe Calorimeter (BPC) (Section 5.1). One has to identify the scattered positron and to precisely determine its energy and angle. The kinematic variables  $y$  and  $Q^2$  are then reconstructed from the energy and angle of the scattered positron. To limit systematic shifts on  $y$  and  $Q^2$  for  $y > 0.1$  and  $Q^2 > 0.1 \text{ GeV}^2$  to be less than 5%, the energy scale has to be determined at the level of 0.5% and the angle measurement with a precision of at least 0.3 mrad which requires the intrinsic position bias and the detector alignment to be well below 1 mm (Section 5.3). This places stringent requirements on the energy and position reconstruction as well as the detector alignment. The energy calibration was performed in-situ using kinematic peak (KP) events<sup>1</sup> and elastic  $\rho^0$  events. Elastic QED Compton events were used as a cross-check of an optical survey of the BPC modules to establish their absolute position. The performance of the BPC South module was examined in a test-beam experiment at DESY II prior to its installation within the ZEUS-detector. The experimental setup of this test-beam experiment will be discussed in the next section. The position and energy reconstruction will be focused on in detail afterwards along with a discussion of the transverse shower behavior. A discussion of the BPC energy resolution and linearity and the BPC timing reconstruction will be presented in the last two sections of this chapter.

### 8.2 DESY II test-beam measurements

#### 8.2.1 Introduction

The main purpose of the test-beam experiment at the DESY II test-beam 21 beam line was to investigate the performance of the BPC South module. The BPC North module was already installed within the ZEUS-detector at the time of the test-beam experiment. The BPC North module is the main component for the physics analysis presented in this thesis. In order to study the new BPC trigger, it was necessary to participate in the 1995 data taking period from the very beginning with the BPC North module. As discussed in detail in section 5.4, both modules are identical apart from their  $X$ -dimensions. Therefore, the conclusions which are drawn from the test-beam results are assumed to be valid for the BPC North module as well.

<sup>1</sup>See section 2.2.2 and 2.4.

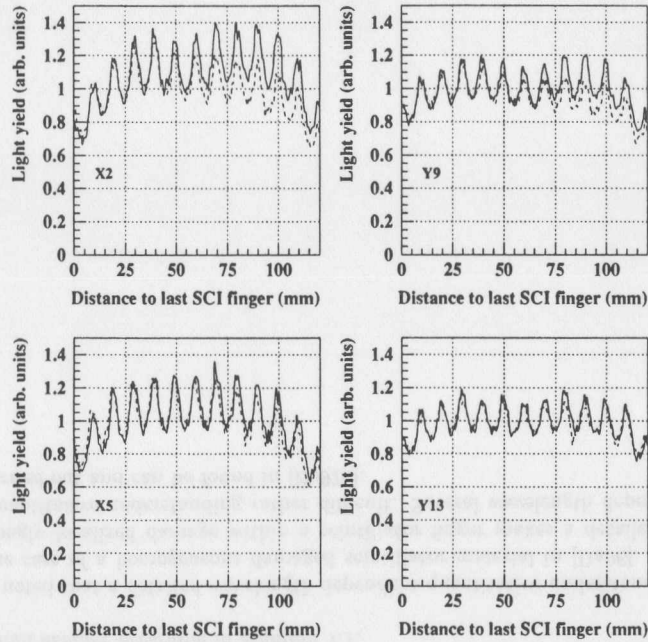


Figure 7.6:  $^{60}\text{Co}$ -scan of the BPC North module before (solid line) and after (dashed line) the HERA run in 1995. The distance is measured with respect to the last scintillator finger ( $X = 0$ ). The first scintillator finger corresponds to  $X = 120$  mm. The integrated light yield distribution before the installation of the BPC North module is normalized to unity. The response of the last three scintillator fingers after the HERA run in 1995 are normalized to the response of the respective scintillator fingers before the HERA run in 1995 assuming that the last three scintillator fingers have not been damaged.

which ignores any dependence of the change in the attenuation coefficient with the wavelength of the scintillator light. It simply considers the integrated effect similar to the ansatz discussed in section 5.4.3 to account for the attenuation of scintillator light in a sample of non-damaged scintillator fingers. The light yield  $\bar{I}(x)$  as a function of distance to the open end of a particular scintillator finger can be written in the following form:

$$\bar{I}(x) = \bar{I}_0(x)(e^{-\mu_D(x)} + R e^{-\mu_R(x)}) \quad (7.1)$$

where  $\mu_D(x) = \int_{C_D} [\mu_0 + \Delta\mu(x')] dx'$  and  $\mu_R(x) = \int_{C_R} [\mu_0 + \Delta\mu(x')] dx'$ .  $\bar{I}_0(x)$  and  $\mu_D(x)$  ( $\mu_R(x)$ ) account for the position dependent loss of light yield and the change in the attenuation coefficient of the direct (reflected) light, respectively.  $C_D$  and  $C_R$  denotes the path of the direct and reflected scintillator light, respectively. For  $\Delta\mu(x) = 0$  and  $\bar{I}_0(x) = \bar{I}_0$ , one obtains the ansatz used in section 5.4.3. Assuming a Gaussian function to account for the position dependent loss of light yield  $\bar{I}_0(x)$  and the change in the attenuation coefficient  $\Delta\mu(x)$ , the function  $\bar{I}(x)$  was used to fit the observed light yield behavior in various scintillator fingers.

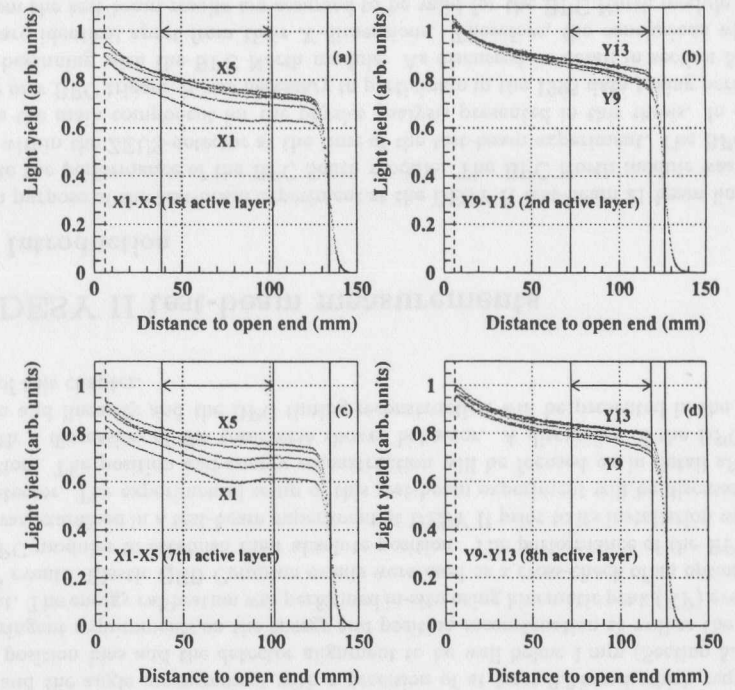


Figure 7.7: Scan of scintillator fingers from the BPC North module used for the HERA run in 1995. The horizontal arrows indicate the location of the fiducial volume of the BPC North module. The light yield of each scan at 6 mm from the open end is normalized using the results from the  $^{60}\text{Co}$ -scans. A drop in the overall light yield due to radiation damage from X5 to X1 and Y13 to Y9 is clearly visible.

Figure 7.8 shows the case for the X1 finger from the seventh active layer. The proposed ansatz in equation 7.1 provides a good description of the measured light yield in the radiation damaged scintillator fingers. The loss of light yield ( $\bar{I}_0(x)$ ) or the change in the attenuation coefficient ( $\Delta\mu(x)$ ) alone does not allow to describe the observed light yield behavior due to radiation damage. It is the effect of both items which have to be taken into account to provide a proper description, according to equation 7.1.

The loss of light yield for fingers close to the beam pipe edge has been as well observed towards the end of the 1995 run in data using a kinematic peak (KP) sample. The final reconstructed energy  $E_X$  as a function of  $Y$  within the fiducial volume showed as well a similar shape as the one shown in Figure 7.7 (a) and (c). After the relative strip-to-strip calibration, the energy uniformity across the whole fiducial volume is well within 0.5%, as will be shown in detail in section 8.5.3.

The result of these scintillator finger scans have been used to evaluate the effect on the linearity of the absolute energy scale of the BPC North module. This will be discussed in detail in section 8.5.4.

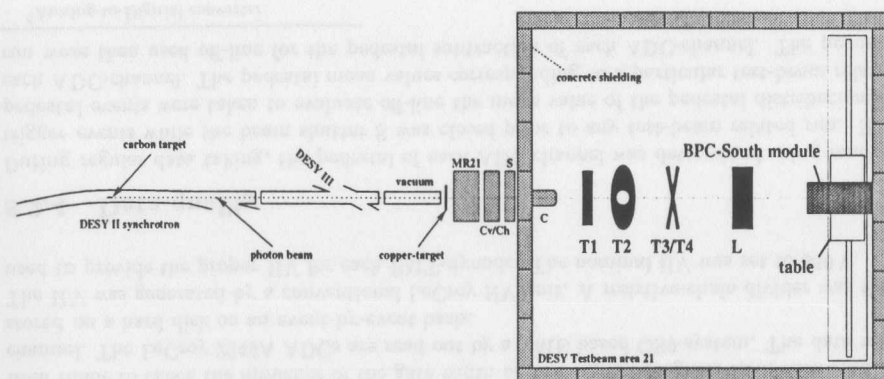


Figure 8.1: Schematic drawing of the DESY II test-beam area 21. The actual size of the trigger counters and other beamline related components are not meant to scale with the size of the test-beam area shown.

The main emphasis of the test-beam program is to investigate the energy resolution, uniformity and linearity as well as the position resolution of the BPC restricted to low electron energies (2 – 6 GeV) available at the DESY II test-beam. It should be stressed that the test-beam experiment was not used to establish the energy scale for the physics analysis. In detail, the following test-beam program was performed:

- Energy scan (2 – 6 GeV) at fixed beam impact position.  
The beam impact position was chosen to be approximately in the center of the calorimeter to provide a full transverse shower containment while changing the energy of the test-beam from 2 GeV to 6 GeV in steps of 1 GeV
- Energy uniformity scan varying the beam impact position in both transverse directions.  
At fixed beam energy, the calorimeter was moved across the incoming test-beam in steps of 1 mm in the horizontal and vertical direction while keeping the position of the calorimeter fixed at several vertical and horizontal coordinates, respectively.

## 8.2.2 Overview of the experimental setup

Figure 8.1 shows the experimental setup with emphasis on the location of the BPC South module, the beam defining trigger counters (T1, T2, T3, T4) and several beam line related components.

Electrons in the halo of the beam at the DESY II synchrotron are used to produce high energy photons within a carbon target. These photons traverse the DESY III proton synchrotron which is installed in the same horizontal plane as the electron synchrotron. The photons are then converted into electron-positron pairs using a copper conversion target. The dipole magnet MR21, right after the copper conversion target, directs electrons into the DESY II test-beam area 21. The choice of a certain dipole magnet (MR21) current setting and the position of the collimators Cv/Ch<sup>2</sup> and C<sup>3</sup> selects particles of a certain energy  $E$  and spread  $\sigma_E$ . The

<sup>2</sup>Cv/Ch are two tungsten-blocks in vertical and horizontal direction.

<sup>3</sup>Lead-collimator with a fixed opening.

resolution of the beam has been estimated in [Ba92b] to be  $\sigma_E/E < 5\%$ . After passing a beam shutter S, electrons enter the test-beam area 21.

The trigger definition for the electron test-beam is based on a coincidence of four scintillator counters (T1, T2, T3, T4). The relative positioning of these trigger counters with respect to the BPC South module can be seen in Figure 8.1. T1 is a  $5 \times 20 \text{ cm}^2$  large scintillator counter which is installed with its larger side along the horizontal direction. T2 is a  $20 \times 30 \text{ cm}^2$  scintillator tile with a 3 cm hole in the middle. T2 is used as a veto-counter. Both T3 and T4 are 1 cm-wide scintillator strip counters which are mounted 58 cm away from the BPC South module in the horizontal and vertical directions, respectively. All four trigger counters are read out via PMTs<sup>4</sup>.

A LUMI scintillator-finger counter<sup>5</sup> was installed in front of the BPC South module to restrict the transverse size of the electron test-beam. Four scintillator fingers, each with a width of 0.26 cm, are mounted within this counter in horizontal and vertical directions and are coupled to photodiodes [Pi96]. All eight channels are read out along with the BPC South module. To restrict the transverse size of the beam, one requires off-line a tag of only one of the four scintillator fingers. This restricts the beam size in the horizontal and vertical directions to  $2.6/\sqrt{12} \text{ mm} = 0.75 \text{ mm}$ .

The BPC South module was mounted on a remotely controllable table. The table can be moved in the horizontal and vertical directions with a precision of about 0.5 mm. This had been cross-checked with a direct measurement.

The nominal position of the electron beam is indicated by a survey mark on the concrete block wall opposite the collimator C. A string from the opening of collimator C to this survey mark was used to align the BPC South module with respect to the nominal position of the electron test-beam.

The main limitations of the test-beam experiment are first the lack of tracking information. The short time scale for the design and construction of the BPC modules did not allow a high resolution tracking chamber to be installed in front of the BPC South module in the test-beam experiment to provide a very precise determination of the true position of the test-beam on an event-by-event basis. Knowing the true position of the test-beam is necessary to study in detail the position resolution and the bias between the measured position using the BPC South module and the true position of the test-beam. The LUMI scintillator-finger counter was used to limit the transverse size of the test-beam in order to estimate the position resolution of the BPC South module.

The second limitation is due to the fact that it was not possible to verify the resolution and the calibration of the test-beam. In order to determine the energy spread, one can use a second dipole magnet after the first bending magnet. Measuring the beam profile with and without the magnetic field of the second dipole magnet and the corresponding shift in the beam profile, one can determine the energy spread of the test-beam. This second dipole magnet within the test-beam 21 area was not in operation. It was not possible to perform an independent determination of the energy scale of the test-beam. As it will be shown in section 8.5.4, it was found that the nominal beam energy of the test-beam should be lower by about 300 MeV which was also concluded by a test-beam experiment [Pi96] right after the one presented here. It was later confirmed by the DESY II test-beam administration [Me95].

Furthermore, it was not possible to use the same HV-distribution system and the same readout system as the one being used within the ZEUS-detector.

<sup>4</sup>Photo-multiplier tubes.

<sup>5</sup>Loan from the ZEUS LUMI-group.

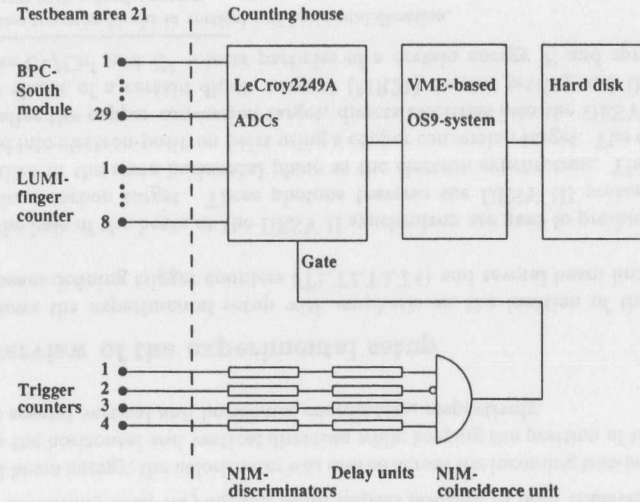


Figure 8.2: Trigger and DAQ setup for the DESY II test-beam experiment.

### 8.2.3 Electronics and Data Acquisition system

Figure 8.2 shows the complete trigger and DAQ setup for the test-beam experiment. The PMT-signals are sent to NIM-discriminators to provide a well-defined logic signal from each trigger counter above noise. A coincidence among these NIM-logic output signals is formed via a NIM-coincidence unit. The test-beam trigger has the following logic structure:

$$[T] = [T1] \cdot [\overline{T2}] \cdot [T3] \cdot [T4] \quad (8.1)$$

The trigger signal provides the gate signal for the digitization of the analog signals of the readout channels of the BPC South-module and the LUMI-scintillator finger counter via ADCs. Four LeCroy 2249A ADCs<sup>6</sup> were used for the digitization. The input sensitivity of the 2249A model is 0.25 pC/count for a full scale range of 256 pC. The gate width was set to 100 ns. This gate width is wide enough to contain more than 99% of the input analog signals. Several tests have been made to check the influence of the gate width on the digitized signals from each readout channel. The LeCroy 2249A ADCs are read out by a VME based OS9-system. The data were stored on a hard disk on an event-by-event basis.

The HV was generated by a conventional LeCroy HV-unit. A resistive-chain divider was then used to provide the proper HV for each PMT-dynode. The nominal HV was set to 850 V.

### 8.2.4 Data quality

During regular data taking, the pedestal of each ADC-channel was determined using random trigger events while the beam shutter S was closed prior to any test-beam related run. 1000 pedestal events were taken to evaluate off-line the mean value of the pedestal distribution for each ADC-channel. The pedestal mean values corresponding to a particular test-beam related run were then used off-line for the pedestal subtraction of each ADC-channel. The pedestal

<sup>6</sup>Analog-to-Digital converter.

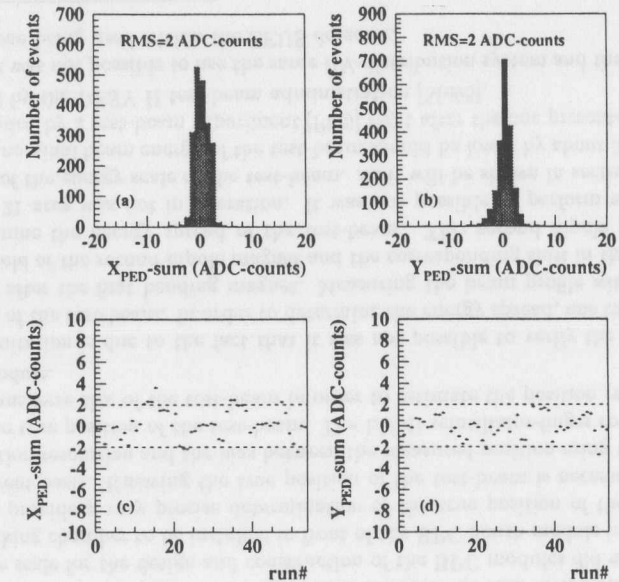


Figure 8.3: Pedestal distributions of the BPC test-beam experiment (Refer to text for further details).

distributions of the  $X$ -channel sum (11 channels) and the  $Y$ -channel sum (16 channels) for a typical pedestal run are shown in Figure 8.3 (a) and Figure 8.3 (b), respectively. The RMS in both cases is equal to 2 ADC-counts which is equivalent to an energy of 16 MeV (Section 8.5.4). The mean value of the  $X$ -channel sum and  $Y$ -channel sum for each pedestal run are shown in Figure 8.3 (c) and Figure 8.3 (d) respectively, as a function of the corresponding run number. The variations of the pedestal-sums over the whole three week data taking period are well within 2 ADC-counts which is equal to the RMS-value of the corresponding pedestal distributions of a typical single pedestal run.

The dependence of the energy resolution of the electron test-beam on the size of the collimator opening was studied prior to the test-beam data taking period. The collimator opening between the two tungsten-blocks (Cv/Ch) in vertical and horizontal directions was changed from  $2 \times 2 \text{ mm}^2$  to  $10 \times 10 \text{ mm}^2$  while keeping the opening of the lead collimator C fixed at  $5 \times 5 \text{ mm}^2$ . The second test was done keeping the opening of Cv/Ch fixed at  $5 \times 5 \text{ mm}^2$  changing the opening of the lead collimator C from  $2 \times 2 \text{ mm}^2$  to  $10 \times 10 \text{ mm}^2$ . The change in the energy resolution is negligible compared to the nominal setting of  $5 \times 5 \text{ mm}^2$  (Cv/Ch) and  $5 \times 5 \text{ mm}^2$  (C), respectively. This nominal setting was chosen for higher rate considerations.

The nominal PMT-HV of 850 V was lowered from 850 V to 700 V. The change in the measured ADC-counts for each BPC channel agreed well with the changes to be expected from the PMT-gain curves. Regular LED-runs using the BPC LED light distribution system (Section 5.4.3) were taken to monitor the stability of the PMTs and the HV-system. The changes over the three week test-beam period were less than 1%.

## 8.3 Position reconstruction

### 8.3.1 Introduction

Besides knowing the coordinates of the event vertex (Section 9.3), the angle reconstruction of the scattered positron using the BPC requires a precise measurement of its impact position in the BPC. The essential ingredients of the position reconstruction for the BPC as discussed in detail in section 5.3 are: a good position resolution, low bias between the measured and the true impact position of the scattered positron and a precise determination of the absolute position of the BPC with respect to the ZEUS coordinate system.

Two distinct methods for the position reconstruction are first qualitatively discussed in the following section which differ in the way the lateral energy depositions of the BPC readout channels are taken into account in the actual position reconstruction by either a linear or a logarithmic weighting. The importance between the functional form of the shower profile resulting in the lateral energy depositions and the way these energy depositions are taken into account will be stressed. It will be shown that a logarithmic weighting of the lateral energy depositions yield a smaller intrinsic position bias as well as a better position resolution. This qualitative discussion is then followed by various detailed studies in section 8.3.3 on the intrinsic position bias and the position resolution of the 'logarithmic-weighting method' employing an EGS4 MC-simulation. Section 8.3.4 will focus on the determination of the absolute position of the BPC using elastic QED Compton events. Some comments on the position and angle reconstruction of the BPC within the ZEUS-detector will be discussed in section 8.3.5.

### 8.3.2 Method

The design of the active layers of the BPC provides a lateral segmented measurement of energy deposits due to the shower formation caused by the incoming positron within the BPC. This is a common technique in high energy physics experiments used for position measurements within a calorimeter [Fa82].

The active layers of the BPC are laterally segmented into 7.9 mm-wide scintillator strips. The lateral segmentation allows to measure the energy deposition of the shower over distance intervals of 7.9 mm transverse to the shower axis. Taking all BPC readout channels together, one can then determine the centroid of the deposited energy and thus obtain an estimate of the impact position of the positron in the BPC.

In order to meet the stringent requirements on the position resolution and bias, a thorough understanding of various details of the position reconstruction is essential. Both position resolution and bias mainly depend on:

- the strip width,
- the impact energy,
- the impact position,
- the transverse shower size,
- the fluctuations in the shower formation,
- the relative calibration of each scintillator strip and
- the reconstruction method.

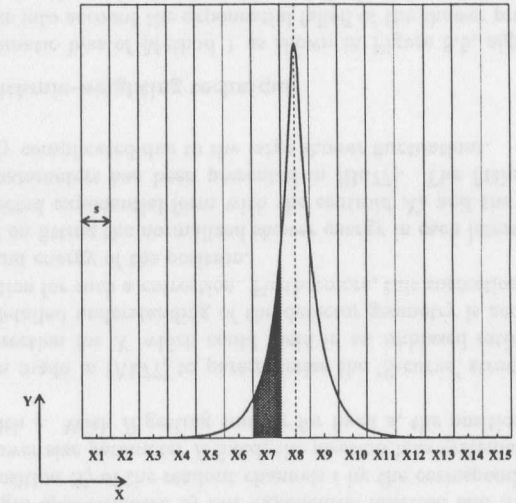
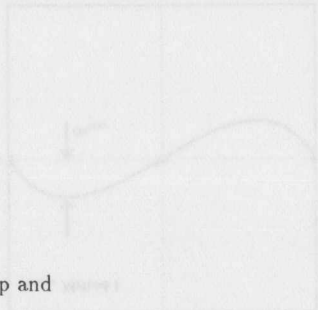


Figure 8.4: Schematic drawing of the X-scintillator readout with an overlaid exponential lateral shower profile.

The position resolution is of statistical nature whereas the position bias is of systematic nature. Both were studied by an EGS4 MC-simulation. In addition, an analytical approach was used to understand the position bias.

Several methods have been developed in the past to determine the shower central position from a lateral segmented calorimeter design [Bu77]. In the following, the qualitative behavior of the position bias for two distinct methods will be discussed postponing a detailed quantitative presentation to section 8.3.3. The difference between the two methods lies in the way the lateral segmented energy deposits in the readout channels are being used in the position reconstruction. The distinct features of the position bias for the two methods will be developed analytically which requires a description of the shower within the BPC resulting from energy depositions in the scintillator strip readout channels. For that purpose, the assumption is made that the lateral shower profile  $dE/dX$  can be described approximately by one exponential function (Section 8.4). This ansatz is primarily chosen to present in a simple way the qualitative behavior of the two methods with respect to the position bias:

$$\frac{dE}{dX} = E_D(0)e^{-|X-X_0|/R} \quad (8.2)$$

where  $E_D(0)$  is the energy per unit length at the impact position  $X_0$  and  $R$  denotes the distance from the impact position  $X_0$  for which the lateral shower profile  $dE/dX$  dropped down by a factor  $1/e$ .  $R$  therefore serves as a parameter to characterize the lateral shower size. It has been shown that using two exponential functions will not alter the conclusions of the following qualitative discussion.

Since the structure of the lateral segmentation of the BPC is identical in both directions  $X$  and  $Y$ , the following discussion will be restricted to  $X$  only.

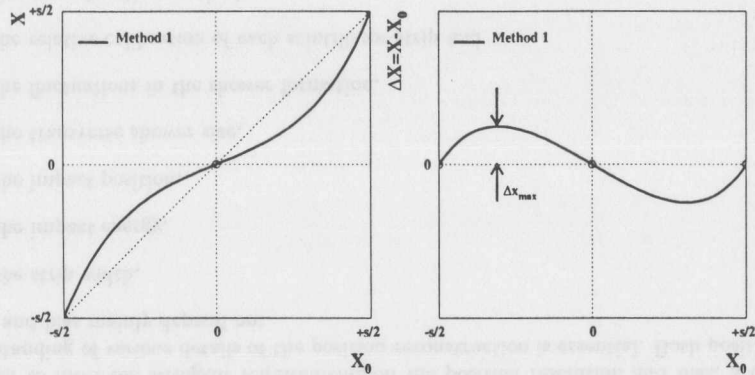


Figure 8.5: Bias between the measured position  $X$  as a function of the true position  $X_0$  for Method 1 (linear-weighting method).

Figure 8.4 shows schematically the  $X$ -scintillator strip readout channels ( $X_1 - X_{15}$ ,  $N = 15$ ) of the BPC North module with an exponential lateral shower profile given by equation 8.2. The width of the strips is denoted by  $s$ .  $X$  and  $Y$  are the two coordinates of the ZEUS-coordinate system describing the orientation of the  $X$ -scintillator strip readout channels.

Using the lateral shower profile given in equation 8.2, one can calculate for each readout channel the expected mean deposited energy  $E_i$ :

$$E_i = \int_{X_i - s/2}^{X_i + s/2} \left( \frac{dE}{dX'} \right) dX' = \int_{X_i - s/2}^{X_i + s/2} E_D(0) e^{-|X' - X_0|/R} dX' \quad (8.3)$$

The integration is performed for each readout channel  $i$  over the corresponding lateral boundaries.  $X_i$  is the coordinate center of the readout channel  $i$ . The gap width between adjacent scintillator strips of about 0.01 cm has been omitted for simplicity. It has been shown that the result of the following qualitative discussion does not depend on that. The size of the shaded area in Figure 8.4 corresponds schematically to the expected deposited energy  $E_i$  (here  $i = 7$ ).

#### Method 1 - linear-weighting technique

One of the most straightforward techniques is to estimate the shower central position  $X$  by simply calculating the center of gravity of the shower using a linear weighting of the lateral center position  $X_i$  of the readout channels  $i$  by the corresponding measured energy  $E_i$ :

$$X = \frac{\sum_{i=1}^N w_i X_i}{\sum_{i=1}^N w_i} \quad w_i = E_i \quad (8.4)$$

Using equation 8.3 and 8.4 together with the lateral shower profile given in equation 8.2, one then finds a simple expression for the measured position  $X$  as a function of the true position  $X_0$  of the positron in the BPC:

$$X = \left( \frac{s}{2} \right) \frac{\sinh\left(\frac{X_0}{R}\right)}{\sinh\left(\frac{s}{2R}\right)} \quad (8.5)$$

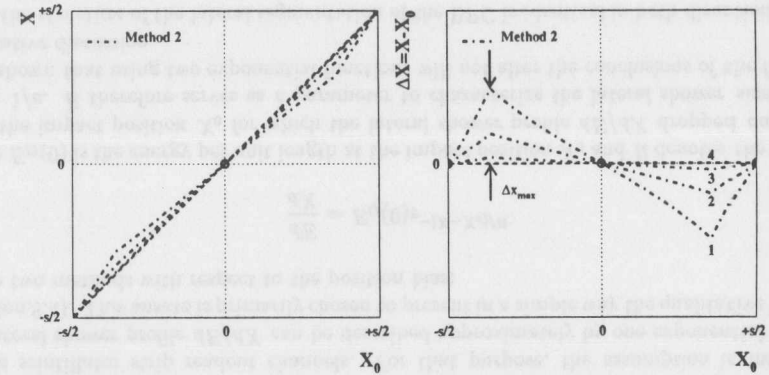


Figure 8.6: Bias between the measured position  $X$  as a function of the true position  $X_0$  for Method 2 (logarithmic-weighting method) for several values of  $W_{0i}$  ( $i = 1 \dots 4$ ) whereas  $W_{01} < W_{02} < W_{03} < W_{04}$ .

where  $X, X_0 \in [-s/2; s/2]$ . The dependence of  $X$  on  $X_0$  is not linear, but is systematically governed by:

$$X \propto \sinh\left(\frac{X_0}{R}\right) \quad (8.6)$$

Figure 8.5 shows  $X$  as a function of the  $X_0$  for Method 1. One clearly notices a 'S-curve' relation between  $X$  and  $X_0$ .  $X$  is an unbiased estimate of the true position  $X_0$  only in the middle of each scintillator strip and at the borders between two adjacent scintillator strips due to the symmetric arrangement of the scintillator strips in these two cases around the shower axis. The position bias in case of Method 1 as shown in Figure 8.5, is the result of the exponential-type energy per unit length approximated by one exponential function and the linear weighting of the lateral center position  $X_i$  of the readout channels  $i$  by the corresponding measured energy  $E_i$ . Keeping the shower size parameter  $R$  fixed, the position bias systematically increases with increasing strip width  $s$ . With  $R$  getting smaller for fixed  $s$ , the position bias systematically increases.

Attempts have been made in [Ak77] to parameterize the 'S-curve' structure between  $X$  and  $X_0$  to obtain a correction for  $X$  which could yield in an unbiased estimate for  $X_0$ . It was found that a very detailed understanding of the detector geometry is necessary to provide an accurate determination for such a correction. Furthermore, this correction method depends on the incident angle and energy of the positron.

An algorithm based on fitting the normalized shower energy in each lateral segmented readout channel to the expected exponential form with the centroid  $X_0$  and the width of the shower  $R$  taken as fitted parameters has been presented in [Bu77]. The fitting procedure is time consuming and fairly complicated due to the large shower fluctuations.

#### Method 2 - logarithmic-weighting technique

To reduce the systematic bias of Method 1 as shown in Figure 8.5, algorithms [Ak77] were developed which take into account the exponential falloff of the shower profile by weighting  $X_i$  not linearly in  $E_i$ , but rather using the logarithm of  $E_i$ . Several authors introduced in [Aw92] a logarithmic weighting technique of the observed energy deposition in lateral segmented cells

within a calorimeter which is similar to those methods presented in [Ak77]. The position measured using the lateral segmented BPC readout employing this method is then given as follows (Method 2):

$$X = \frac{\sum_{i=1}^N w_i X_i}{\sum_{i=1}^N w_i} \quad (8.7)$$

where

$$w_i = \begin{cases} W_0 + \ln\left(\frac{E_i}{E}\right) & \left(\frac{E_i}{E}\right) > e^{-W_0} \\ 0 & \left(\frac{E_i}{E}\right) \leq e^{-W_0} \end{cases} \quad (8.8)$$

and

$$E = \sum_{i=1}^N E_i \quad (8.9)$$

The requirement of  $w_i \geq 0$  makes it necessary to introduce the positive dimensionless parameter  $W_0$ .  $W_0$  serves as a threshold on the fraction of the total shower energy  $E$  which a strip  $i$  must exceed in order to be included in calculating the position  $X$ . It provides at the same time a way to control shower fluctuations and the inclusion of the shower tails in the position reconstruction. In the following, the qualitative behavior of Method 2 is discussed in the same framework as for Method 1. The expected deposited energy  $E_i$  is calculated using equation 8.3.

Using equations 8.7 and 8.8, one can then plot in the same manner the measured position  $X$  as a function of the true position  $X_0$  as shown in Figure 8.6.

In case of logarithmic weighting, the systematic bias between the measured position  $X$  and the true position  $X_0$  depends on the parameter  $W_0$ . The position bias is found to decrease with larger values of  $W_0$  ( $W_{01} < W_{02} < W_{03} < W_{04}$ ). In the limit of very large values of  $W_0 = W_{04}$ , the position bias is found to vanish. In the latter case, the value for  $W_0$  is chosen to be large enough to avoid any dependence on the strips to be included in the position reconstruction.

For  $W_0 \rightarrow 0$ , only the most energetic strips are included in the position reconstruction and one therefore expects the position bias to increase. For  $W_0 \rightarrow \infty$ , the shower tails are being taken into account in the position reconstruction. The weight factors corresponding to the shower tails are increased compared to linear weighting since  $W_0$  is very large although  $E_i/E$  is very small which makes their contribution for the linear weighting very small. The position resolution is expected to worsen. This will be shown in the next section. The determination of the precise value of  $W_0$  is therefore a compromise to keep both position resolution and bias as small as possible. As it will be shown in the next section, the position bias in case of logarithmic weighting with the optimized parameter  $W_0$  is significantly reduced over the linear weighting but does not vanish for the reasons explained above.

The simple ansatz made above using an exponential-type lateral shower profile showed the distinct qualitative behavior in calculating the measured position  $X$  by either using a linear weighting of the energy  $E_i$  (Method 1) or rather by using a logarithmic weighting technique (Method 2), taking into account the exponential falloff of the shower profile. Assuming a triangular shaped and therefore linear shower profile  $dE/dX$ , a linear weighting of  $X_i$  by  $E_i$  results in a vanishing position bias as it is the case for Method 2 for very larger values of  $W_0$ . This points to the importance of the relation between the functional form of the shower profile and the way the weighting of the positions  $X_i$  by the energy  $E_i$  is being done in order to control the position bias.

A detailed quantitative discussion based on an EGS4 MC-simulation and the DESY II test-beam results will be presented in the next section employing the logarithmic weighting technique. This method (Method 2) is the basis of the position reconstruction algorithm used for the BPC.

### 8.3.3 Detailed studies on position resolution and bias

The following section will focus on the following items:

- determination of  $W_0$ ,
- comparison of linear and logarithmic weighting,
- dependence of the position resolution on the impact position,
- position resolution results from the DESY II test-beam,
- effects of the position reconstruction at the BPC edge,
- dependence of the position resolution on the electron energy and
- dependence of the position resolution on the strip width.

All studies have been carried out using various EGS4 MC-samples. The impact of real detector related items on the position reconstruction such as the relative strip-to-strip calibration of the BPC, the influence of the ZEUS magnetic field and the correction of the reconstructed positions within the BPC to the impact position at the front face of the BPC as well as the polar angle reconstruction will be focused on in section 8.3.5.

#### Determination of $W_0$

The weight factors  $w_i$  which are used for the logarithmic-weighting method given by equation 8.8 contain  $W_0$  as a free parameter. It has to be determined by optimizing both the position resolution as well as the position bias as discussed in the previous section. The existence of a simultaneous optimum value of  $W_0$  on the position resolution as well as the position bias can be understood from the definition of  $w_i$ . The possible range of  $W_0$  is as follows:  $W_0 \in ]0, \infty[$ . For  $W_0 \rightarrow \infty$ , all laterally segmented readout channels are included in the determination of the measured position since  $e^{-W_0} \rightarrow 0$ . The position bias is expected to vanish and the position resolution to worsen.

In case of  $W_0 \rightarrow 0$ , only the most energetic readout channels are included in the position reconstruction since  $e^{-W_0} \rightarrow 1$ . Therefore, only a few readout channels dominate the position reconstruction. The position bias will increase. This can be understood by looking at two extreme cases of the impact position, namely first in the center of a scintillator strip and second between two adjacent strips. For  $W_0 \rightarrow 0$ , the actual number of strips being included in the position reconstruction changes in a discrete way from two for an impact position between two strips to one for an impact position in the center of one strip. This leads to a significant position bias when moving the impact position from one to the other of the two extreme points. The position resolution will also be very sensitive to the impact position and is expected to have a drastic difference for impact positions in the center of a strip compared to an impact position between two strips.

Choosing the optimum value for  $W_0$  was therefore performed by plotting the dependence of the position resolution as well as the position bias as a function of  $W_0$ . In both cases, the incident electron energies have been chosen between 10 GeV and 25 GeV to avoid any bias on the chosen incident energy. The position resolution values correspond to the  $\sigma$ -value of a Gaussian fit to the difference of the measured position  $X$  and the true position  $X_0$ .

The position resolution as a function of  $W_0$  is expected to have an absolute minimum, whereas the position bias as a function of  $W_0$  is expected to decrease towards larger  $W_0$ -values. The

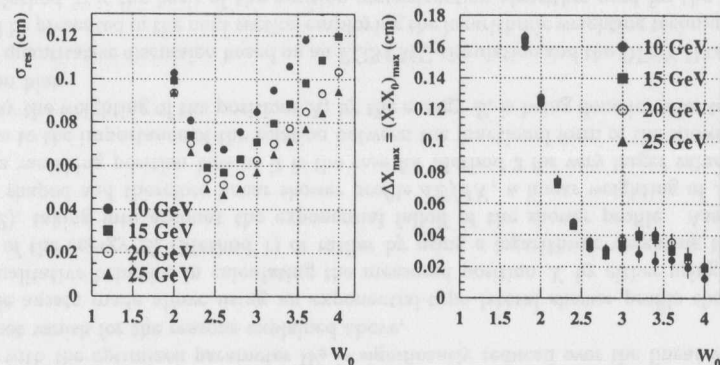


Figure 8.7: Position resolution  $\sigma_{res}$  (left) and maximum position bias  $\Delta X_{max}$  (right) as a function of  $W_0$  using an EGS4 MC-simulation.

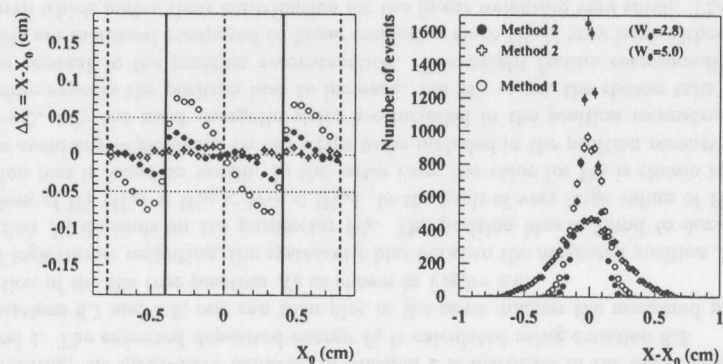


Figure 8.8: Position bias  $\Delta X$  as a function of  $X_0$  (left) and position spectra (right) for several position reconstruction methods for 10 GeV electrons from an EGS4 MC-simulation.

position resolution has been evaluated over the same range of the impact position, as the position bias, namely over one strip in order to avoid any systematic bias due to a fixed impact position.

Figure 8.7 (left) shows the dependence of the position resolution as a function of  $W_0$ . Figure 8.7 (right) displays the maximum difference between  $X$  and  $X_0$  as a function of  $W_0$ . The actual position bias as a function of  $X_0$  for several  $W_0$ -bins is shown in Figure 8.9. As can be seen, the position bias decreases and vanishes for large values of  $W_0$  as expected from the above discussion. The position resolution shows a clear absolute minimum in  $W_0$  of about 2.6. At  $W_0 = 2.8$ , one observes a local minimum of the maximum position bias as a function of  $X_0$ . The position resolution at  $W_0 = 2.8$  is only slightly higher compared to  $W_0 = 2.6$ . It has been verified that a change in the impact angle between  $88^\circ$  and  $90^\circ$  with respect to the BPC front face, to account for the expected range in impact angles for the BPC within ZEUS, has a negligible effect on this procedure.

Taking both criteria for the optimization together, a value of 2.8 was chosen for  $W_0$  for the BPC

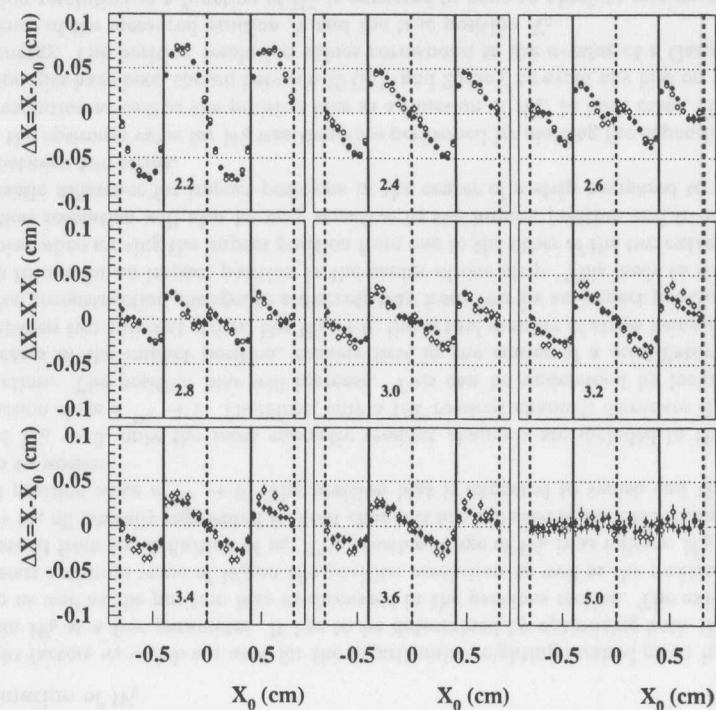


Figure 8.9: Position bias  $\Delta X$  as a function of  $X_0$  in several  $W_0$ -bins for 10 GeV (closed circles) and 20 GeV (open circles) electrons using an EGS4 MC-simulation. The vertical solid lines indicate the strip boundaries whereas the dashed lines indicate the strip centers. The actual  $W_0$ -values are plotted in the lower left corner of each plot.

position reconstruction. The sensitivity of the choice of  $W_0$  on the position resolution and bias and therefore on the position reconstruction has been taken into account in the determination of systematic errors on the physics results.

### Comparison of bias for linear and logarithmic weighting

The qualitative behavior of the linear-weighting method and the logarithmic-weighting method have been presented in section 8.3.2. Figure 8.8 shows the position bias as a function of  $X_0$  for 10 GeV electrons for the linear-weighting method (open circles) as well as for the logarithmic weighting method (closed circles) using the optimized value for  $W_0$  of 2.8. The bias in case of the linear weighting method is within 0.1 cm, whereas in case of the logarithmic weighting method the bias is well within 0.05 cm and therefore demonstrates the clear advantage of the logarithmic over the linear weighting method. The crosses in Figure 8.8 demonstrate the case of the logarithmic-weighting method with  $W_0 = 5.0$ , i.e.  $E_i/E > 0.7\%$ . No position bias is observed as expected. The position resolution is a factor of three larger compared to the case

of  $W_0 = 2.8$ . For the linear weighting method, the position resolution is about 30% larger compared to the logarithmic weighting method using  $W_0 = 2.8$ .

### Dependence of the position resolution on the impact position

The position bias between the true position  $X_0$  and the measured position  $X$  vanishes for the electron impact position either between two strips or in the center of one strip, as seen in Figure 8.10 (left) for 10 GeV electrons simulated by EGS4. Figure 8.10 (right) shows for 10 GeV electrons the position resolution as a function of the impact position over the same region of the impact position, as shown in Figure 8.10 (left). The position resolution is seen to decrease by about 0.04 cm when moving from the center of a strip to an impact position between two adjacent strips. The position resolution has a minimum between two adjacent strips.

### Position resolution results from the DESY II test-beam

Using the LUMI scintillator-finger counter in the DESY II test-beam experiment, the transverse size of the electron test-beam was restricted to 0.75 mm. Figure 8.11 shows the reconstructed position obtained from 5 GeV-test-beam electrons. The mean reconstructed value has been subtracted from each reconstructed position. The value for  $\sigma$  of the Gaussian fit, together with the beam width of  $\sigma_{\text{beam}} = 0.75$  mm, allows an estimate of the intrinsic position resolution of the BPC,  $\sigma_{\text{BPC}}$ , for 5 GeV test-beam electrons. The relation between them is given as follows:

$$\sigma = \sqrt{\sigma_{\text{BPC}}^2 + \sigma_{\text{beam}}^2} \quad (8.10)$$

One obtains a value for  $\sigma_{\text{BPC}}$  of 0.13 cm. The mean of the impact position lies in the center of one strip. An EGS4 MC-simulation was used to compare the position resolution between the DESY II test-beam and the simulation. The impact position, and therefore the mean of the reconstructed position, has been chosen for the EGS4 MC-simulation as well to be in the center of one strip. The position resolution of the EGS4 MC-simulation is equal to 0.13 cm and therefore the same as the one obtained from the DESY II test-beam result.

### Effects of the position reconstruction at the BPC edge

In order to have access to very small values in  $Q^2$ , it is necessary to accept positrons as close as possible to the beam pipe edge for the physics analysis. It is therefore necessary to evaluate how close one can approach the edge limiting the position bias to within 0.05 cm. Figure 8.12 shows the position bias as a function of the true position  $X_0$  for the logarithmic weighting method (closed circles) and the linear weighting method (open circles) for 10 GeV electrons from an EGS4 MC-simulation.

One can clearly see that the bias is well within 0.05 cm for the logarithmic-weighting method if one restricts the fiducial volume of the physics analysis to start from the second scintillator strip on, i.e. 0.8 cm from the edge. This is certainly not the case for the linear-weighting method. This demonstrates again the clear advantage of the logarithmic-weighting method over the linear-weighting method. The change in the position resolution using the logarithmic-weighting method has the same behavior in this fiducial volume region as discussed before.

### Dependence of the position resolution on the electron energy

The position resolution for energies higher than those available at the DESY II test-beam was determined by an EGS4 MC-simulation as well. The impact position was chosen uniformly

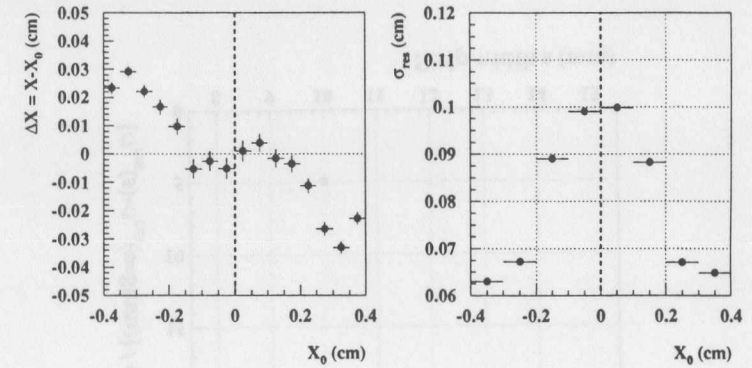


Figure 8.10: Position bias  $\Delta X$  (left) and position resolution  $\sigma_{\text{res}}$  (right) as a function of  $X_0$ . The dashed line indicates the strip center. The  $X_0$ -range in both plots is over one strip. These results have been obtained from an EGS4 MC-simulation of 10 GeV electrons.

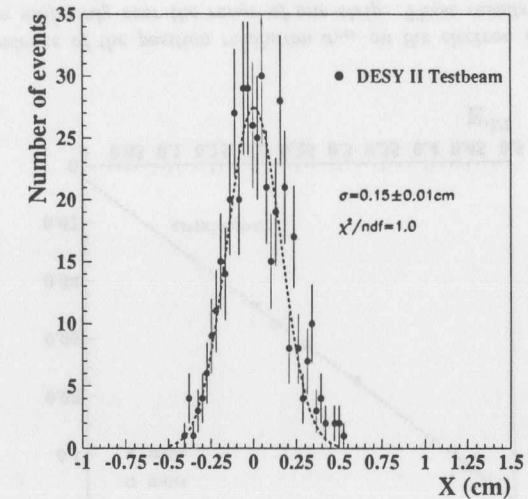


Figure 8.11: Reconstructed position from the DESY II test-beam experiment with 5 GeV electrons.

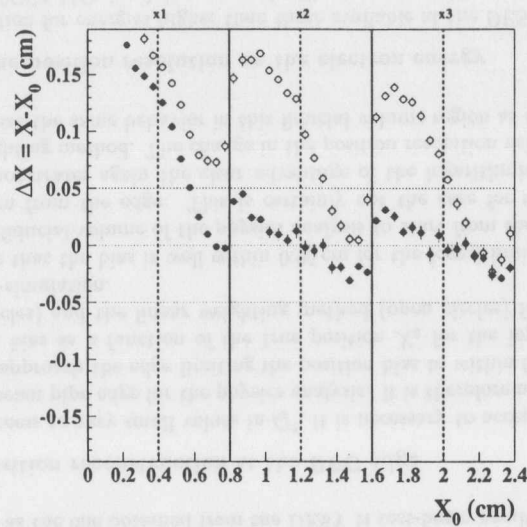


Figure 8.12: Position bias  $\Delta X$  a function of  $X_0$  for 10 GeV electrons from an EGS4 MC-simulation. The strip centers are denoted by dashed lines whereas the boundaries between two adjacent strips are denoted by solid lines. The strip indices (X1-X3) are plotted on top of the corresponding strip.  $X_0 = 0$  corresponds to the edge of the BPC. Closed circles are taken for the logarithmic-weighting method and open circles for the linear-weighting method.

over the range of one strip. The position resolution is expected to decrease with higher electron energies. In Figure 8.13, the position resolution is plotted as a function of  $1/\sqrt{E}$ , where  $E$  is the incident electron energy. Values for  $E$  have been chosen between 5 GeV and 25 GeV. One clearly notices the improvement in the position resolution for higher incident electron energies. One obtains a position resolution of 0.05 cm at 25 GeV.

#### Dependence of the position resolution on the strip width

The position resolution depends on the ratio of the width of the scintillator strips to the size of the shower. The position resolution as well as the position bias increases if this ratio gets large. In Figure 8.14, the position resolution is plotted as a function of the strip width. A steady improvement of the position resolution towards smaller values of the scintillator strip widths is clearly visible. These results have been obtained from a simulation of 10 GeV electrons using an EGS4 MC-simulation

As discussed in detail in chapter 5, the chosen width of the scintillator strips represents a compromise between optimizing the position resolution and experimental constraints due to the fixed size of several readout elements such as the PMTs.

#### 8.3.4 Determination of the absolute BPC position

The BPC modules have been surveyed within the ZEUS-detector by an optical survey procedure (Section 5.8) to determine their absolute position with respect to the ZEUS-coordinate system

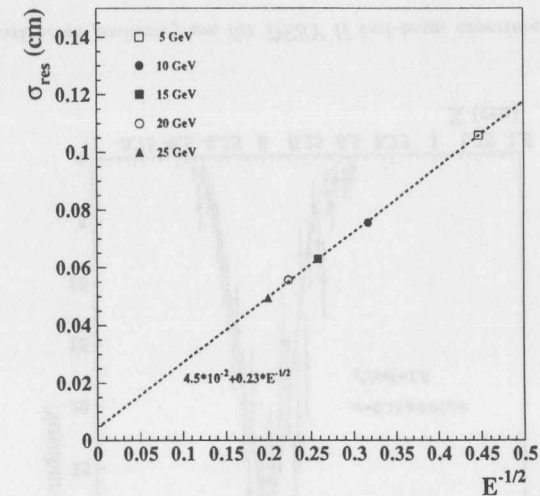


Figure 8.13: Dependence of the position resolution  $\sigma_{res}$  on the electron energy. The impact position was chosen uniformly over the range of one strip. These results have been obtained from an EGS4 MC-simulation.

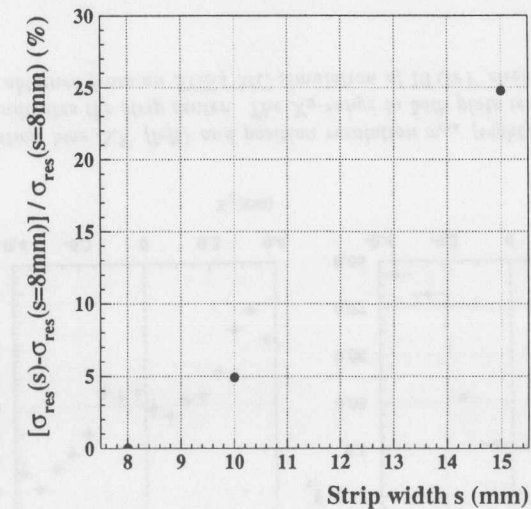


Figure 8.14: Percent deviation of the position resolution with respect to the position resolution of 8 mm scintillator strips, as a function of the respective strip width. These results have been obtained from a simulation of 10 GeV electrons using an EGS4 MC-simulation.

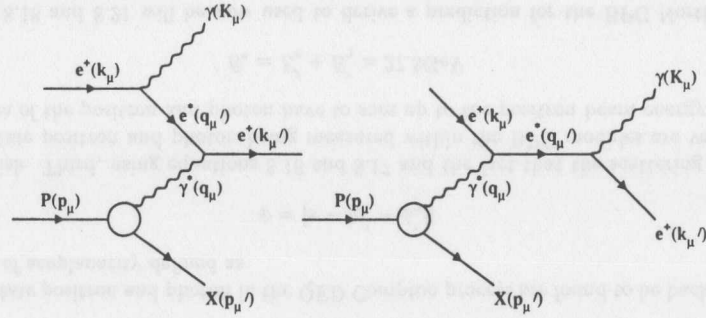


Figure 8.15: Lowest order Feynman diagrams describing the QED Compton process.

after the data taking period in 1995. The accuracy of that procedure suffers from various systematic uncertainties and was estimated to be at best 0.5 mm (Section 5.8). The requirement on the absolute position of the BPC is 0.5 mm (Section 5.3). To meet such a stringent requirement on the absolute position, an independent verification of the BPC position calibration is essential. Elastic QED Compton events [Co92] provide a way of an in-situ position calibration. In the QED Compton process as shown in Figure 8.15,

$$e^+p \rightarrow e^+\gamma X \quad (8.11)$$

the final state consists of two electromagnetic objects, a positron and a photon besides the hadronic final state system X. The QED Compton process corresponds to the case of  $q^2 \rightarrow 0$ , i.e.  $Q^2 \rightarrow 0$  and  $q'^2 > 0$ . The hadronic final state system X can be classified in the following way [Co92]:

- Elastic contribution:  $m_X = m_P$
- Resonant contribution:  $m_P + m_\pi < m_X < 1.8 \text{ GeV}$
- Continuum inelastic contribution:  $m_X > 1.8 \text{ GeV}$

The square of the mass of the hadronic final state is given by:  $m_X^2 = m_P^2 + Q^2(1-x)/x$  with  $0 \leq x \leq 1$ . For  $Q^2 \rightarrow 0$  (QED Compton condition), the elastic contribution will be the dominant contribution [B193].

The principle idea of using the elastic QED Compton process for the BPC position calibration is to measure the final state positron and photon in the BPC North and South module (Figure 8.16). Employing the precisely known relative distance between the two BPC modules, the reconstructed position of the final state positron and photon measured in the two BPC modules and the energy of either the positron or the photon measured in the BPC North module, one can determine the absolute position of the BPC modules with respect to the ZEUS coordinate system taking into account the positron beam tilt and the vertex position (Section 9.3).

The application of the QED Compton process for the BPC position calibration relies on various simplifications. The following part will focus on them in detail.

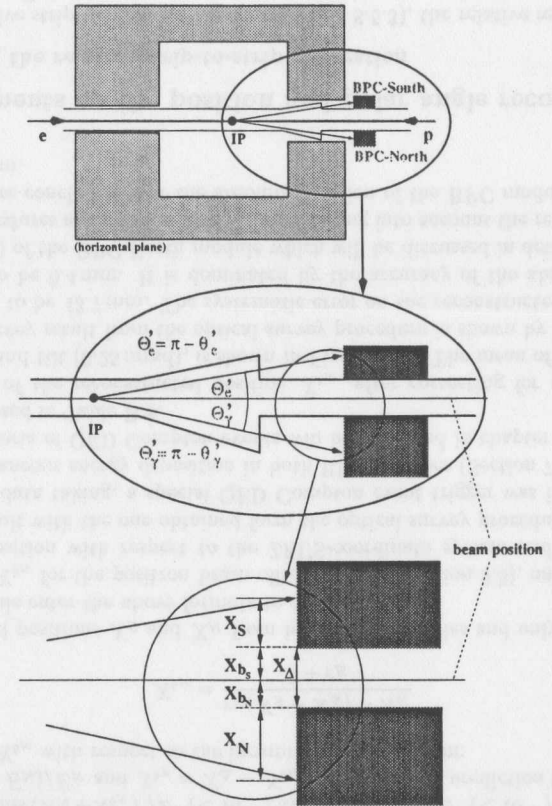


Figure 8.16: Schematic layout of the in-situ position calibration of the BPC using elastic QED Compton events.

Using four-momentum conservation among the initial and final state particles of the QED Compton process, one obtains the following equations:

$$E_e + E_P = E'_e + E'_\gamma + E_X \quad (8.12)$$

$$0 = E'_e \sin \theta'_e \cos \phi'_e + E'_\gamma \sin \theta'_\gamma \cos \phi'_\gamma + |\vec{p}_X \sin \theta_X \cos \phi_X \quad (8.13)$$

$$0 = E'_e \sin \theta'_e \sin \phi'_e + E'_\gamma \sin \theta'_\gamma \sin \phi'_\gamma + |\vec{p}_X| \sin \theta_X \sin \phi_X \quad (8.14)$$

$$-E_e + E_P = E'_e \cos \theta'_e + E'_\gamma \cos \theta'_\gamma + |\vec{p}_X| \cos \theta_X \quad (8.15)$$

With the QED Compton condition of  $Q^2 \approx 0$ , the angle of the elastically scattered proton will vanish, i.e.  $\cos \theta_X = 1$ . Using the above equations and employing the fact of  $\cos \theta_X = 1$ , one can write the energy of the positron  $E'_e$  and photon  $E'_\gamma$  in the final state as a function of the reconstructed angles  $\theta'_e$  and  $\theta'_\gamma$ :

$$E'_e = 2E_e \frac{\sin \theta'_\gamma}{\sin \theta'_e + \sin \theta'_\gamma - \sin(\theta'_e + \theta'_\gamma)} \quad (8.16)$$

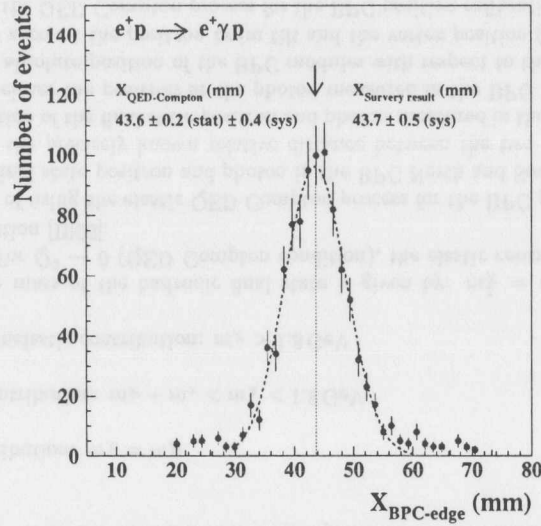


Figure 8.17: Distribution of the reconstructed BPC North position. The dotted vertical line indicates the result obtained from the optical survey.

$$E'_\gamma = 2E_e \frac{\sin \theta'_e}{\sin \theta'_e + \sin \theta'_\gamma - \sin(\theta'_e + \theta'_\gamma)} \quad (8.17)$$

Using equations 8.12-8.15 together with  $\cos \theta_X = 1$ , one obtains three characteristic conditions for the QED Compton events. First, the transverse momentum between the positron and photon in the final state has to be balanced:

$$E'_e \sin \theta'_e = E'_\gamma \sin \theta'_\gamma \Leftrightarrow P_{T,e} = P_{T,\gamma} \quad (8.18)$$

Second, the angles  $\phi'_e$  and  $\phi'_\gamma$  are connected via:

$$\phi'_e = \phi'_\gamma \pm \pi \quad (8.19)$$

The final state positron and photon in the QED Compton process are found to be back-to-back. The angle of acoplanarity defined as

$$\psi = |\pi - |\phi'_e - \phi'_\gamma|| \quad (8.20)$$

has to vanish. Third, using equations 8.16 and 8.17 and the fact that the scattering angles of the final state positron and photon being measured within the BPC modules are very small, the energies of the positron and photon have to sum up to the positron beam energy.

$$E_e = E'_e + E'_\gamma = 27.5 \text{ GeV} \quad (8.21)$$

Equations 8.18 and 8.21 will be now used to derive a prediction for the BPC North module position. Figure 8.16 illustrates all abbreviations to be used in the following derivation. The relative distance  $X_\Delta = X_{b_S} + X_{b_N}$  is given by the length of the brass distance bars (Section

5.4.2).  $X_\Delta$  is known to an accuracy of 0.02cm. Knowing  $X_{b_N}$ , one can determine  $X_{b_S}$  using  $X_\Delta$  as well.

Equation 8.18 can be re-written in the following form using the surveyed Z-position of the BPC (Section 5.8), the reconstructed positions  $X_S$  and  $X_N$  in the BPC South and North module, respectively and the distances  $X_{b_S}$  and  $X_{b_N}$  of the BPC South and North module, respectively to the incoming positron beam:

$$\frac{E'_e(X_N + X_{b_N})}{Z\sqrt{1 + \left(\frac{X_N + X_{b_N}}{Z}\right)^2}} = \frac{E'_\gamma(X_S + X_{b_S})}{Z\sqrt{1 + \left(\frac{X_S + X_{b_S}}{Z}\right)^2}} \quad (8.22)$$

Re-writing equation 8.22 in terms of the measured energy in the BPC North module  $E_N$  which replaces either  $E'_e$  or  $E'_\gamma$  depending on whether the final state positron or photon is being tagged by the BPC North module and the energy of the other final state particle which is not being measured in the BPC North module,  $E_e - E_N$ , yields:

$$E_N(X_N + X_{b_N}) = (E_e - E_N)(X_S + X_{b_S}) \quad (8.23)$$

where the two terms  $(X_N + X_{b_N})^2/Z^2$  ( $< 10^{-3}$ ) and  $(X_S + X_{b_S})^2/Z^2$  ( $< 10^{-3}$ ) have been ignored. With  $r_E = (E_e - E_N)/E_N$  and  $X_{b_S} = X_\Delta - X_{b_N}$ , one obtains a prediction for the BPC North module position  $X_{b_N}$  with respect to the incoming positron beam:

$$X_{b_N} = \frac{r_E(X_S + X_\Delta) - X_N}{1 + r_E} \quad (8.24)$$

The reconstructed positions  $X_S$  and  $X_N$  from both BPC modules and only the energy of the BPC North module enter the above formula to obtain  $X_{b_N}$ .

After correcting  $X_{b_N}$  for the positron beam offset and tilt (Section 9.3), one obtains the BPC North module position with respect to the ZEUS-coordinate system and can compare this in-situ survey result with the one obtained from the optical survey procedure.

During the 1995 data taking, a special QED Compton event trigger was implemented which required a simultaneous energy deposition in both BPC modules (Section 7.1).

The selection criteria of QED Compton events will be discussed in chapter ten. The selection cuts are summarized in Table B.3.

The distribution of the reconstructed position  $X_{b_N}$ , after correcting for the positron beam offset (1.15 mm) and tilt (0.25 mrad), is shown in Figure 8.17. The mean of the Gaussian fit is 43.6 mm. The survey result from the optical survey procedure is shown by the vertical dotted line and amounts to be 43.7 mm. The systematic error on the reconstructed position  $X_{b_N}$  has been estimated to be 0.4 mm. It is dominated by the accuracy of the absolute energy scale calibration (0.5%) of the BPC North module which will be discussed in detail in section 8.5.3. Both survey procedures agree well within 0.5 mm, taking into account the respective uncertainties. It is therefore concluded that the absolute position of the BPC modules is known to an accuracy of 0.5 mm.

### 8.3.5 Comments on the position and polar angle reconstruction

#### Dependence on the relative strip-to-strip calibration

Prior to the relative strip-to-strip calibration (Section 8.5.3), the relative response of all strips was adjusted using  $^{60}\text{Co}$ -scans to a level of about 7% (Section 5.7). The relative strip-to-strip

calibration procedure requires a fiducial volume cut. This implies that the position reconstruction for the fiducial volume cut of the relative strip-to-strip calibration procedure is based on a relative strip-to-strip uniformity of 7%. The systematic shift of the reconstructed position before and after the relative strip-to-strip calibration procedure has been found to be well below 0.5 mm. It has been verified that the extracted relative strip-to-strip calibration values are insensitive to systematic shifts of 0.5 mm in the definition of the fiducial volume. The final extracted relative strip-to-strip calibration values have been then used for any fiducial volume cuts, i.e. for the absolute energy scale calibration, as well as the physics analysis presented in this thesis.

### Dependence on the ZEUS-magnetic field

The scattered positron has to pass on its way from the interaction point to the BPC through a magnetic field resulting from the ZEUS central magnet. This magnetic field has essentially only an axial component in the central part of the detector, but a negative radial component in front of the RCAL. It was found that positrons are displaced in  $Y$  downwards. The displacement in  $X$  can be completely ignored. The displacement in  $Y$ , i.e. the difference between the true impact position and the reconstructed position in  $Y$  is proportional to  $X/E_{BPC}$  assuming a constant radial magnetic field component within the acceptance of the BPC. A straight line was fitted to the displacement in  $Y$  as a function of  $X/E_{BPC}$  using a MC simulation (Section 6.3). The extracted slope has then been used to correct the reconstructed  $Y$  position in data which amounts to about 0.5 mm for KP-events.

### Dependence of the longitudinal shower deposition

Within ZEUS, the angle of incidence of the scattered positron measured by the BPC is not exactly orthogonal to the front face of the BPC. The maximum energy deposition of a positron occurs at the shower maximum which amounts to about  $7X_0$  (Section 5.2). The impact position is therefore reconstructed at this depth. The reconstructed position has to be therefore projected to the front face of the BPC. It has been shown that the position of the shower maximum follows roughly the relation for  $t_{\max}$ , as given in Table 5.1. This relation has then been used to correct the reconstructed positions in  $X$  and  $Y$  to the front face of the BPC. The correction is well below 2.0%.

### Polar angle reconstruction

The reconstruction of the polar of the scattered positron within ZEUS has to take into account: the above corrections on the reconstructed  $X$  and  $Y$  positions measured in the BPC using the logarithmic-weighting method, offsets in the  $X$  and  $Y$  vertex positions using the ZEUS central-tracking detector (CTD) and the positron beam tilt  $\theta_X^{\text{tilt}} = 0.25$  mrad with respect to the ZEUS coordinate system. The determination of the event vertex position as well the positron beam tilt will be discussed in detail in section 9.3. The final reconstructed polar angle is then given by:

$$\vartheta_{\text{BPC}} = \sqrt{\left(\frac{X_{\text{corr}}}{|Z|} - \theta_X^{\text{tilt}}\right)^2 + \left(\frac{Y_{\text{corr}}}{|Z|}\right)^2} \quad (8.25)$$

where  $Z = Z_{\text{vertex}} + Z_{\text{BPC}}$ .  $Z_{\text{vertex}}$  is the reconstructed  $Z$  vertex position and  $Z_{\text{BPC}}$  the surveyed  $Z$  position of the BPC.  $X_{\text{corr}}$  and  $Y_{\text{corr}}$  are the corrected  $X$  and  $Y$  positions reconstructed in the BPC.

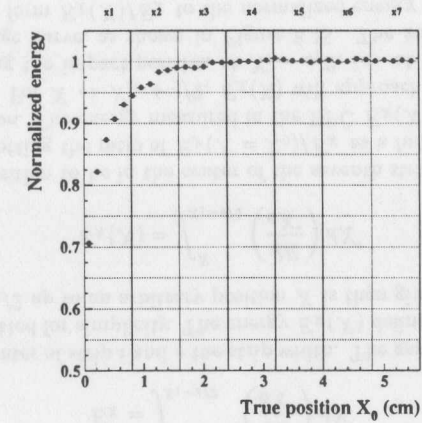


Figure 8.18: Normalized energy as a function of the true position  $X_0$  for 25 GeV electrons simulated by EGS4. The solid vertical lines indicate the strip boundaries.

## 8.4 Lateral shower behavior

### 8.4.1 Introduction

A detailed understanding of the lateral shower behavior of the BPC is important for the physics analysis for two reasons.

In order to have access to very small values in  $Q^2$ , it is necessary to accept positrons within the BPC as close as possible to the beam pipe edge. The BPC is being used for the position as well as for the energy measurement of the incoming positron. To limit the position bias to 0.05 cm, the fiducial volume has to start 0.8 cm away from the active layer edge towards the beam pipe, as discussed in detail in the previous section. For positrons being reconstructed as close as 0.8 cm to the active layer edge, transverse energy leakage cannot be avoided and has to be corrected for. The principle idea of the energy leakage correction is based on a fit to the normalized energy distribution as a function of the reconstructed  $X$ -position using a certain ansatz for the lateral shower distribution  $dE/dX$ . The result of the fit is then used for the relative strip-to-strip calibration as well as for the energy reconstruction (Section 8.5). Comparisons of two types of  $dE/dX$ -parameterizations and the dependence of the integrated lateral shower distribution on the positron energy will be presented in section 8.4.2.

The lateral segmentation of the active layers of the BPC allows, besides the reconstruction of the impact position of the incoming positron, the determination of the shower width through the second moment of the lateral shower distribution on an event-by-event basis. The shower width provides a means of positron identification employing the difference in the size of electromagnetic and hadronic showers. An observed discrepancy of the shower width between MC and data using a clean KP-sample gave rise to a correction of the transverse shower distribution in MC which will be discussed in detail.

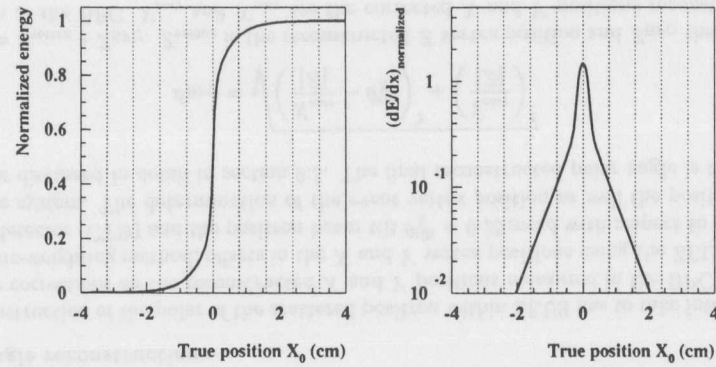


Figure 8.19:  $E_X(X = X_0)/E_X$  plotted as function of the true position  $X_0$  (left).  $dE/dX$  (normalized) using the sum of two exponential functions, plotted as a function of the true position  $X_0$  (right). The impact position is chosen to be in the center of the seventh strip. The central position of the seventh strip,  $X_7$ , has been subtracted such that the impact position appears at  $X_0 = 0$ . The dotted vertical lines indicate the strip boundaries.

### 8.4.2 Lateral shower distribution

The need to correct the reconstructed energy within the BPC for transverse energy leakage is illustrated in Figure 8.18. The normalized energy for 25 GeV electrons is plotted as a function of the true position  $X_0$  simulated by an EGS4 MC-sample. The true position  $X_0$  and not the measured position  $X$  has been chosen to illustrate the amount of energy leakage close to the active layer edge. Solid vertical lines indicate the scintillator strip boundaries. The left edge of the X2-strip corresponds to the 0.8 cm distance from the active layer edge towards the beam pipe which defines the beginning of the fiducial volume. The transverse energy leakage there is about 5%. The amount of transverse energy leakage depends on the cluster size used for the energy reconstruction which will be discussed in section 8.5.2. The following discussion is based on the final choice of the cluster size using four strips.

The most general description of the shower development in space is given by:

$$\rho_E^3(r, Z, \phi) = \frac{1}{E_0} \frac{\partial E(r, Z, \phi)}{\partial r \partial Z \partial \phi} \quad (8.26)$$

Cylindrical coordinates are the preferred coordinate system due to the corresponding symmetry of the shower development. The transverse position of the energy deposition  $dE$  is defined by  $r$ , the distance between the shower axis and the place of the energy deposition  $dE$ , the angle  $\phi$  and the longitudinal position  $Z$ . Provided that the angle of incidence of the incoming positron is orthogonal to the BPC, the energy deposition has no preferred direction in  $\phi$ . Positrons entering the BPC within ZEUS have polar angles measured in direction of the incoming positron of at most  $2^\circ$  and therefore angles of impact on the front face of the BPC of at least  $88^\circ$ . Asymmetries between the case of perpendicular incidence and the case of the BPC within ZEUS are expected to be small and have been ignored for the following discussion. Although the energy deposition  $dE$  depends on the depth  $Z$  within the BPC, the readout scheme of the BPC provides no longitudinal segmentation and energy depositions corresponding to one

particular readout channel are summed together in longitudinal direction. The above equation can be integrated over in  $\phi$  and  $Z$  and one obtains  $\rho_E^1$  which will be called the *transverse shower distribution*:

$$\rho_E^1 = \int_0^L \int_0^{2\pi} \rho_E^3(r, Z, \phi) dZ d\phi = \int_0^L \int_0^{2\pi} \frac{1}{E_0} \left( \frac{\partial E(r, Z, \phi)}{\partial r \partial Z \partial \phi} \right) dZ d\phi \quad (8.27)$$

where  $L$  corresponds to the total depth of the BPC. It is common to use normalized shower distributions. The normalization condition for the transverse shower distribution  $\rho_E^1$  is chosen as:

$$\int_0^\infty \rho_E^1 dr = 1 \quad (8.28)$$

The BPC provides a lateral segmentation in  $X$  and  $Y$ , each with an independent readout scheme. The preferred description of energy depositions  $dE$  is therefore in  $X$  and  $Y$ , respectively. The projection of energy depositions  $dE$  in  $dr$  onto the  $X$  and  $Y$  axis respectively, will then lead to the shower distributions  $dE/dX$  and  $dE/dY$ , respectively. These distributions will be called *lateral shower distributions*. The lateral shower distributions are normalized as follows:

$$\int_{-\infty}^{+\infty} \frac{1}{E_0} \left( \frac{dE}{dX'} \right) dX' = 1 \quad (8.29)$$

Due to the identical lateral structure of the BPC in  $X$  and  $Y$ , the following discussion will be restricted to  $X$ . As it will be shown in section 8.5.3, it is only the  $X$ -direction where the need arises to correct for transverse energy leakage.

Several parameterizations have been suggested in the literature to describe transverse as well as lateral shower distributions. It should be noted that most of the suggested parameterizations do not follow from 'first principles' but describe the energy distribution rather well. One ansatz which is common to most descriptions is an exponential-type shower distribution (Section 5.2). Several authors in [Ak77] parameterize the lateral shower distribution by the sum of two exponential functions which was used as well by [Fe88] for a description of the transverse shower distribution. The total energy  $E_X$  in the BPC is given by:

$$E_X = \int_{X_1 - s/2}^{X_{15} + s/2} \left( \frac{dE}{dX'} \right) dX' \quad (8.30)$$

where  $X_i$  denotes the center of strip  $i$  and  $s$  the strip width. The gap between individual strips of 0.01 cm has been omitted for simplicity. The energy  $E_X(X)$  defined as the sum of all energy depositions from  $X_1 - s/2$  up to an arbitrary position  $X$  is then given as follows:

$$E_X(X) = \int_{X_1 - s/2}^X \left( \frac{dE}{dX'} \right) dX' \quad (8.31)$$

Choosing the impact position to be in the center of the seventh strip as shown in Figure 8.19 (left), one obtains by plotting the ratio of  $E_X(X = X_0)/E_X$  as a function of  $X_0$  the *integrated lateral shower distribution*. The energy measured in the BPC  $E_X(X = X_7)$  is exactly one half of the total energy  $E_X$ . For  $X \rightarrow X_{15} + s/2$ ,  $E_X(X)$  will approach the total energy  $E_X$ , i.e.  $E_X(X) \rightarrow E_X$ . Choosing the impact position at  $X_1 - s/2$ , i.e. at the X1-edge, one obtains the typical energy leakage curve, as shown in Figure 8.18. The key to perform the leakage correction are fits of the form  $E_X(X)/E_X$  to the normalized energy distribution as a function of  $X$  using a given parameterization for  $dE/dX$ . As can be seen from equations 8.30 and

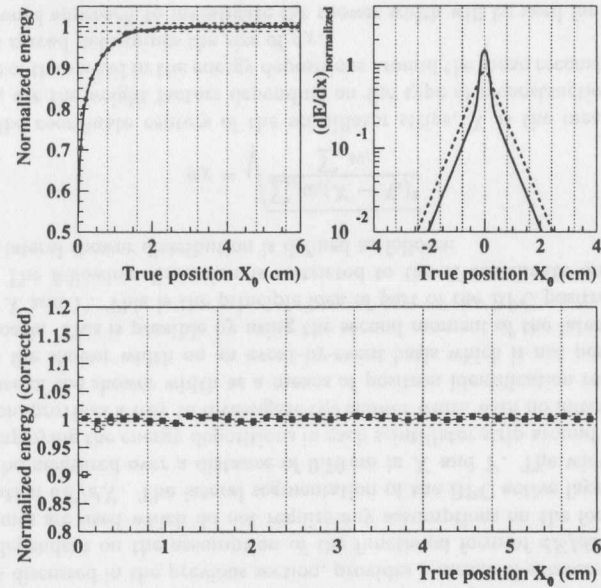


Figure 8.20: Normalized energy as a function of the true position  $X_0$  for 25 GeV electrons simulated by EGS4 (left). A fit to  $E_X(X = X_0)/E_X$  using one (dashed line) and two (solid line) exponential function is overlaid.  $dE/dX$  (normalized) plotted as a function of  $X_0$  for one and two exponential functions (right). Corrected normalized energy plotted as function of  $X_0$  using a correction based on one exponential (open squares) and two (closed squares) exponential functions (bottom).

8.31, the function  $E_X(X)/E_X$  which is used to fit the normalized energy distribution does not include a clustering of deposited energies. This ansatz results in a satisfactory description of the transverse energy leakage. The use of a cluster algorithm in the evaluation of  $E_X(X)/E_X$  has been therefore omitted.

These parameterizations of the lateral shower distribution are then used for the relative strip-to-strip calibration and the energy reconstruction. Table 8.1 summarizes the type of  $dE/dX$ -

$dE/dX$	$\int_{-\infty}^X (dE/dX') dX'$	normalization
$A_1 \exp(-X/\lambda_1)$	$0.5 \cdot [1 + \frac{X}{ \lambda_1 } (1 - \frac{1}{2} \exp(-\frac{ X }{\lambda_1}))]$	$2A_1\lambda_1 = 1$
$\sum_{i=1}^{N=2} A_i \exp(-X/\lambda_i)$	$0.5 \cdot [1 + \frac{X}{ \lambda_1 } (1 - ((\sum_{i=1}^{N-1} A_i \exp(-\frac{ X }{\lambda_i})) + (1 - \sum_{i=1}^{N-1} A_i) \exp(-\frac{ X }{\lambda_N})))]$	$\sum_{i=1}^N 2A_i\lambda_i = 1$

Table 8.1: Parameterization of lateral shower profiles.

ansatz and the corresponding lateral shower distribution  $E_X(X)/E_X$  which are used for the following discussion. It should be noted that no attempt was made to discriminate between different positron energies in the parameterization of the lateral shower distribution. As will

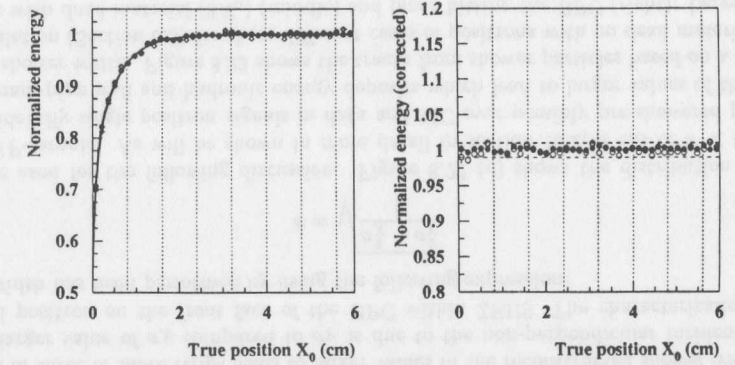


Figure 8.21: Normalized energy for 5 GeV (open circles) and 25 GeV (closed circles) electrons simulated by EGS4 (left). A fit to the 25 GeV electron case of  $E_X(X = X_0)/E_X$  based on two exponential functions is overlaid (solid line). Corrected normalized energy using a fit to the 25 GeV electron case as a function of  $X_0$  for 5 GeV (open circles) and 25 GeV (closed circles) electrons simulated by EGS4 (right).

be shown, a common leakage correction provides a flat energy distribution independent of the positron's impact energy.

Figure 8.20 (left) shows the result of two fits to the normalized energy distribution from 25 GeV electrons using an EGS4 MC-sample. The true impact position has been used for the position information to illustrate the behavior of the energy leakage as well as the quality of the fits close to the edge. Both parameterizations give a good description up to the right edge of the X1-strip. Going closer to the edge, a steeper energy distribution is preferred and only the sum of two exponential functions describes the energy falloff towards the active layer edge well. The difference between the two cases can be seen also in Figure 8.20 (right), where the result of the two fits have been used to plot the corresponding lateral shower distribution. For a distance of at least 0.8 cm away from the shower axis, the two distributions result in the same slope, but for distances very close to the shower axis, the sum of two exponentials yields a much steeper lateral shower distribution compared to one exponential function. The result of the fits have been used to correct for the observed energy leakage. The result of this correction is shown in 8.20 (bottom) and demonstrates that a leakage correction using the ansatz described above is very well able to yield a flat energy distribution up to the X2-strip. The uniformity is well within the statistical errors and amounts to about 0.5%. A one-exponential type fit has been used for the relative strip-to-strip calibration and the energy reconstruction.

It will be shown in the following that a common leakage correction for all electron energies provides a flat energy distribution. The leakage correction fit has been performed using 25 GeV electrons simulated by EGS4. The correction has been then applied to lower electron energies. The fit to the 25 GeV case is shown in Figure 8.21 (left). Using the same leakage correction provides for all energies in the range of 5 – 25 GeV a flat energy distribution. The open circles denote the case for 5 GeV electrons as shown in Figure 8.21. The energy uniformity is well within 0.5% using a common leakage correction for all electron energies.

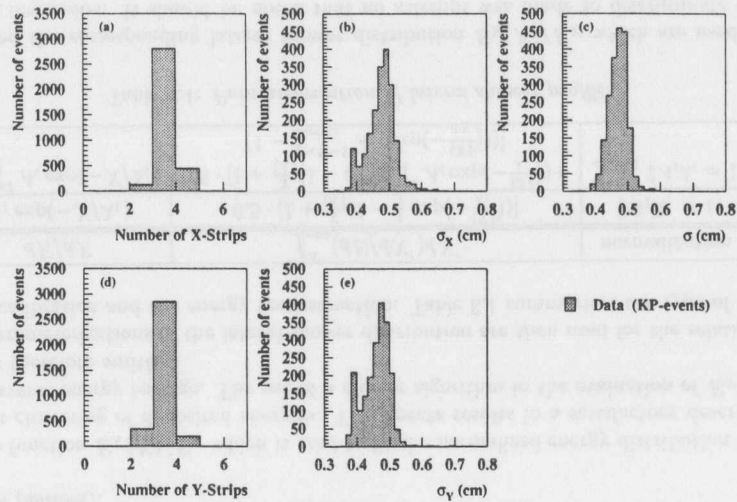


Figure 8.22: Number of X-strips (a) and number of Y-strips (d) included in the evaluation of the corresponding shower width  $\sigma_X$  (b) and  $\sigma_Y$  (e) and  $\sigma$  (c) for a KP-sample.

### 8.4.3 Details on the shower width reconstruction

The determination of the lateral shower profile  $dE/dX$  by fitting the integrated lateral shower distribution, as discussed in the previous section, provides a means of shower width characterization. It is dependent on the assumption of the functional form of  $dE/dX$ . Besides that, two other schemes are used which do not require any assumptions on the form of the lateral shower distribution  $dE/dX$ . The lateral segmentation of the BPC active layers allows energy depositions to be measured over a distance of 0.79 cm in X and Y. The width of the energy distribution, employing the energy depositions in each scintillator strip around the mean reconstructed position, provides a way to investigate the shower width with no initial assumption on  $dE/dX$ . The use of the shower width as a means of positron identification requires a method which provides the shower width on an event-by-event basis which is not possible employing the latter approach. This is possible by using the second moment of the lateral shower width distribution in X and Y. This is the principle idea of part of the BPC positron identification (Section 9.4). The following discussion is restricted to the X-coordinate only. The second moment of the lateral shower distribution is defined as follows:

$$\sigma_X = \sqrt{\frac{\sum_i w_i (X - X_i)^2}{\sum_i w_i}} \quad (8.32)$$

where  $X_i$  are the coordinate centers of the scintillator strips,  $X$  is the mean reconstructed position and  $w_i$  are the weight factors depending on the type of reconstruction method used.  $\sigma_X$  is a measure of the spread in the energy depositions around the mean reconstructed position. The size of this spread determines the size of  $\sigma_X$ .

The first mentioned approach to investigate the shower width will be used for a detailed comparison of the shower width between MC and data. The two distinct methods for the position

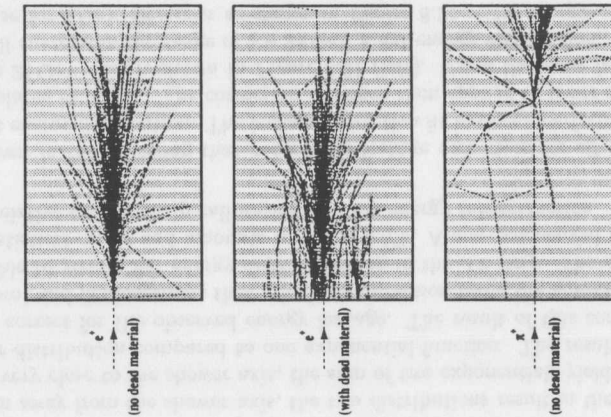


Figure 8.23: Tracks from shower particles for positrons with no dead material (left), positrons with dead material ( $3X_0$ ) (middle) and pions hitting the BPC (right) simulated within GEANT. The shaded layers denote the tungsten plates whereas the white layers denote the scintillator finger layers.

reconstruction show in the case of the shower width  $\sigma_X$  a similar feature as the position bias. The free parameter  $W_0$  in the logarithmic-weighting method has been determined in section 8.3.3 using an optimization of the position resolution and bias. The amount of bias on  $\sigma_X$  is also significantly reduced when using the logarithmic-weighting technique. The size of the bias in the shower width decreases for larger values in  $W_0$ . This has been investigated in detail using an EGS4-MC sample as well as an analytical approach. The free parameter  $W_0$  has been chosen to be the same as obtained in section 8.3.3 to be 2.8.

The non-vanishing bias of the shower width using  $W_0 = 2.8$  leads to a distribution in  $\sigma_X$  and  $\sigma_Y$  which is not smooth. Figure 8.22 (a) and 8.22 (d) show for a data KP-sample, the number of strips  $n_X$  and  $n_Y$  respectively, included in the position reconstruction. Including two strips in the evaluation of the shower width for almost equal energy depositions leads to a shower width of approximately 0.4 cm which shows up as a clear peak in Figure 8.22 (b) and 8.22 (e). The inclusion of three or more strips leads to larger values in the reconstructed shower width. The slightly larger value of  $\sigma_X$  compared to  $\sigma_Y$  is due to the non-perpendicular incidence of the scattered positron on the front face of the BPC within ZEUS. The characterization of the shower width has been performed by using the following expression:

$$\sigma = \sqrt{\frac{\sigma_X^2 + \sigma_Y^2}{2}} \quad (8.33)$$

$\sigma$  will be used for the following discussion. Figure 8.22 (c) shows the distribution of  $\sigma$  for a data KP-sample. As will be shown in more detail in section 10.2, a cut of  $\sigma < 0.7$  cm is used to identify single positron signals in data and MC over possibly pre-showered positrons on the beam-pipe wall and hadronic energy depositions which lead to larger values of the reconstructed shower width. Figure 8.23 shows the tracks from shower particles based on a GEANT MC-simulation (Section 6.3) for three different cases of positrons with no dead material (left), positrons with dead material ( $3X_0$ ) (middle) and pions hitting the BPC (right). Larger reconstructed values for  $\sigma$  from the last two cases compared to a single positron signal, can be clearly

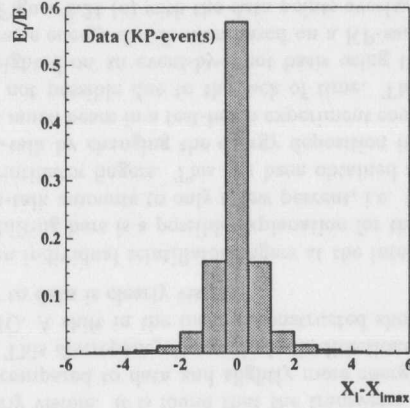


Figure 8.26:  $E_i/E$  versus  $X_i - X_{imax}$  for data from a KP-sample.

were found. This strongly supports the effectiveness of the shower width cut to reject events with positrons having pre-showered at the beam pipe wall which lead to significantly larger values of the reconstructed shower width.

## 8.5 Energy reconstruction

### 8.5.1 Introduction

The BPC energy reconstruction has to meet the requirements on the precision of the absolute energy scale and the energy uniformity of 0.5% (Section 5.3). Kinematic peak (KP) events and elastic  $\rho^0$  will be used for the energy calibration. The following section introduces the method of the BPC energy reconstruction and motivates the usage of a clustering among the lateral segmented BPC readout channels. The actual energy calibration will be discussed in detail in section 8.5.3, i.e. the relative strip-to-strip calibration taking into account transverse energy leakage and the attenuation of scintillator light along the scintillator strips as well as the absolute energy scale calibration. Section 8.5.4 will focus on the BPC energy resolution and linearity.

### 8.5.2 Method

The BPC consists conceptually of two independent readout schemes in  $X$  and  $Y$ . The laterally segmented readout channels in  $X$  and  $Y$  are used to reconstruct the energies  $E_X$  and  $E_Y$ , respectively. The total energy  $E_{BPC}$  is then obtained from the energies  $E_X$  and  $E_Y$ . The reconstruction of  $E_X$  and  $E_Y$  has to take into account

- transverse energy leakage,
- attenuation of scintillator light within the scintillator strips and
- relative strip-to-strip non-uniformities.

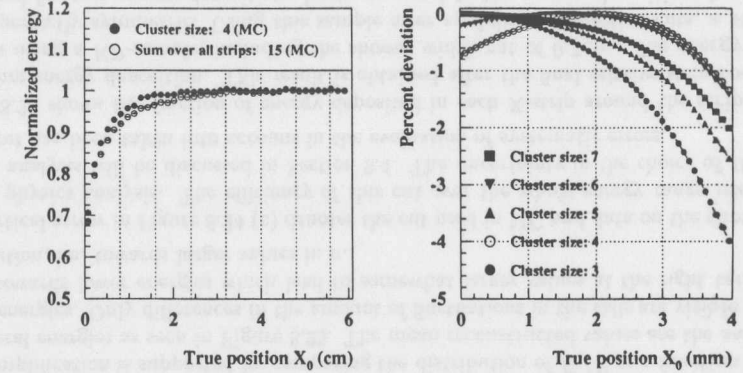


Figure 8.27: Normalized energy as a function of the true position  $X_0$  (left). Percent deviation of  $E_X$  with respect to the maximum of  $E_X$  within the shown interval as a function of the true position  $X_0$  for several cluster sizes (right) (See text for further details).

The energies  $E_X$  and  $E_Y$  are then given as follows:

$$E_X^j = l_X(X, Y) \cdot a_X(Y) \cdot \sum_{\text{cluster}} \alpha_X^i \cdot E_{X_{raw}}^i \quad (8.34)$$

and

$$E_Y^j = l_Y(X, Y) \cdot a_Y(X) \cdot \sum_{\text{cluster}} \alpha_Y^i \cdot E_{Y_{raw}}^i \quad (8.35)$$

where  $l_X(X, Y)$  and  $l_Y(X, Y)$  are the leakage correction functions and  $a_X(Y)$  and  $a_Y(X)$  are the attenuation correction functions. The constants  $\alpha_X^i$  and  $\alpha_Y^i$  are the relative strip-to-strip calibration constants. The index  $j$  denotes the strip  $j$  with the maximum energy deposition around which a cluster sum is performed. It will be used only for those cases where it is explicitly needed. The total energy  $E_{BPC}$  is then reconstructed as the energy scale weighted sum of  $E_X$  and  $E_Y$ :

$$E_{BPC} = s_X \cdot E_X + s_Y \cdot E_Y \quad (8.36)$$

The determination of the leakage and attenuation correction functions, the relative strip-to-strip calibration constants  $\alpha_X^i$  and  $\alpha_Y^i$ , are determined by the relative calibration [Mo96] and the scale values  $s_X$  and  $s_Y$  by the absolute energy scale calibration procedure.

The summation in equations 8.34 and 8.35 can be performed simply over all strips, i.e. 15 in  $X$  and 16 in  $Y$  (BPC North module) or as denoted by the term 'cluster' around the strip  $j$  with the maximum energy deposition using a certain cluster size  $N_c$ . As shown in Figure 8.26, the energy  $E_X$  is contained in only a few readout channels which is also the case for  $E_Y$ .

It will be shown in the following that using a clustering algorithm has clear advantages over the simple sum including all strips. The following discussion will be restricted to the  $X$ -direction. Using a similar ansatz for the lateral shower distribution  $dE/dX$  as given by equation 8.2, one can calculate using

$$E_i = \int_{X_i-(s-g)/2}^{X_i+(s-g)/2} \left( \frac{dE}{dX'} \right) dX' \quad (8.37)$$

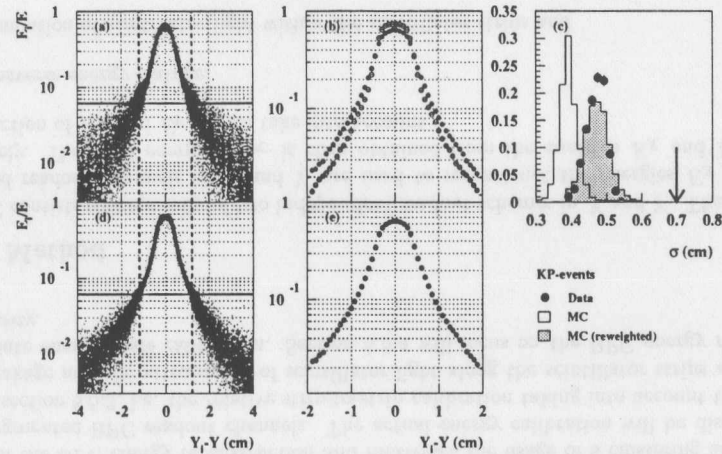


Figure 8.24:  $E_i/E$  versus  $Y_i - Y$  for MC (re-weighted) (a), mean  $E_i/E$  versus  $Y_i - Y$  for data (closed circles) and MC (open circles) (b),  $\sigma$  (c),  $E_i/E$  versus  $Y_i - Y$  for data (d), and mean  $E_i/E$  versus  $Y_i - Y$  for data (closed circles) and MC (open circles) (re-weighted) (e) for a KP-sample.

inferred from this graphical presentation.

Acceptance corrections used within the physics analysis which are derived from a MC-sample require that the shower width cut has a comparable efficiency in MC as well as in data. In order to use a common threshold for the shower width cut in MC and data requires in particular that the shower width distributions in MC and data have to agree. A discrepancy in the reconstructed shower width distribution for a KP-sample necessitates correcting the transverse energy distribution in MC. In Figure 8.24 (b), the fraction  $E_i/E$  is plotted as a function of  $Y_i - Y$  for MC (open circles) and data (solid circles) using a KP-sample. The difference in the overall shape is clearly visible. It is found that the transverse energy distribution in MC is narrower in the tails compared to data and slightly more energy is deposited close to the shower central position. This discrepancy is seen in both directions  $X$  and  $Y$ . Figure 8.24 (c) shows  $\sigma$  for data and MC. A shift in the mean reconstructed shower width towards smaller values for MC compared to data is clearly visible.

Cross-talk effects between individual scintillator fingers at the interface of the scintillator fingers to the wavelength shifting bars is a possible explanation for this discrepancy. It has been estimated that this cross-talk amounts to only a few percent, i.e. the loss of scintillator light into two neighbouring scintillator fingers. This has been obtained assuming the observed discrepancy is due to cross-talk by changing the energy deposition in the scintillator fingers in MC accordingly. Using a muon beam in a test-beam experiment could eventually have resolved this problem which was not possible due to the lack of time. The transverse energy distribution in MC was re-weighted on an event-by-event basis using the ratio of data to MC of the corresponding transverse energy distribution based on a KP-sample. The re-weighted MC distribution is shown in Figure 8.24 (e) with the data points overlaid. No difference is visible in the mean reconstructed values for  $E_i/E$  in bins of  $Y_i - Y$  between MC (re-weighted) and

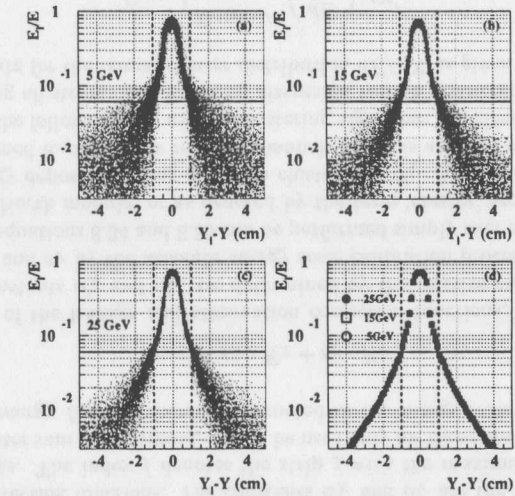


Figure 8.25:  $E_i/E$  versus  $Y_i - Y$  for 5 GeV (a),  $E_i/E$  versus  $Y_i - Y$  for 15 GeV (b),  $E_i/E$  versus  $Y_i - Y$  for 25 GeV (c) and mean  $E_i/E$  versus  $Y_i - Y$  for 5, 15 and 25 GeV (d) electrons using an EGS4 MC simulation.

data. The effect of this re-weighting procedure on  $\sigma$  is shown in Figure 8.24 (c). The mean reconstructed shower width for data and MC is now at the same place. The MC distribution in  $\sigma$  has a tendency to have somewhat larger tails towards larger values in  $\sigma$ . This has been identified due to the difference in the amount of shower fluctuations in MC and data as seen in Figure 8.24 (a) and 8.24 (d) for MC (re-weighted) and data, respectively. The amount of events in the tails above threshold ( $E_i/E > \exp(-2.8)$ ) denoted by the solid horizontal line is larger in case of MC compared to data. This discrepancy in MC and data leads to the difference in the right tails of  $\sigma$ .

The re-weighting of MC has been done independently of the energy of the scattered positron. This simplification is supported by comparing the distribution of  $E_i/E$  as a function of  $Y_i - Y$  for several energies as seen in Figure 8.25. The mean reconstructed values are the same for all shown energies. Only differences in the amount of fluctuations in the tails are visible which are larger towards lower energies which lead to somewhat larger values at the right tail of the  $\sigma$  distribution, i.e. towards larger values in  $\sigma$ .

The vertical arrow in Figure 8.24 (c) denotes the cut used in MC and data on the shower width for the physics analysis. The efficiency of this cut over the whole energy range used for the physics analysis will be discussed in Section 9.4. The uncertainty in the choice of the shower width cut has been taken into account in the evaluation of systematic errors.

Figure 8.26 shows the fraction of energy deposited in each X-strip around the strip with the maximum energy deposition. This result is obtained after the final relative strip-to-strip calibration using a KP-sample, including the shower width cut of 0.7 cm. The energy distribution is perfectly symmetric. Using this sample after applying all selection cuts, a search was performed for any energy depositions larger or equal to the energy depositions in the strips  $E(\text{imax})$ ,  $E(\text{imax} - 1)$  and  $E(\text{imax})$  for strips  $j$  with  $j > \text{imax} + 1$  or  $j < \text{imax} - 1$ . No events

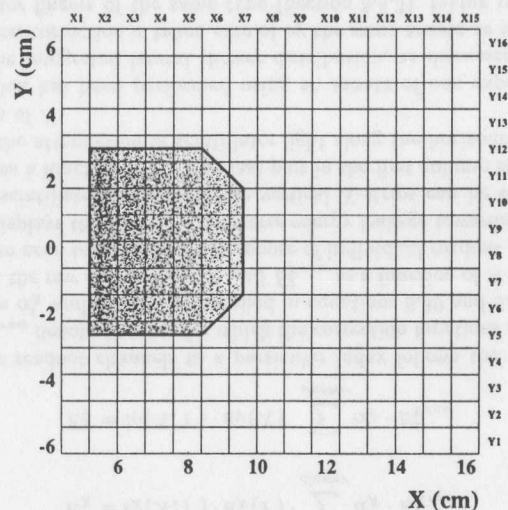


Figure 8.28: Fiducial volume of the BPC (North module). The solid horizontal and vertical lines denote the strip boundaries.

the energy  $E_X$  using a certain cluster size.  $X_i$  is the central position of strip  $i$ ,  $s$  is the width of the scintillator fingers including wrapping and  $g$  is the gap between two adjacent scintillator fingers.  $E_X$  can then be plotted as a function of the true position  $X_0$  as shown in Figure 8.27 (right) for several choices of  $N_c$  between 3 and 7. The impact position has been restricted to be between the center of a strip ( $X_0 = 0$ ) and the corresponding edge ( $X_0 = 4$  mm) due to the symmetry of the scintillator strip arrangement. The  $Y$ -axis denotes the percent deviation of  $E_X$  within that interval to the maximum value of  $E_X$  within the same interval. A clear correlation between the functional form and the use of either even or odd integers for  $N_c$  is visible. The maximum deviation has a tendency to get smaller for larger values of  $N_c$ . The deviation is found to be almost equal for  $N_c = 4$  and  $N_c = 6$  and clearly smaller compared to  $N_c \leq 7$  with  $N_c$  being odd. It has been verified that the relative difference in the deviation as a function of the impact position  $X_0$ , between the choices of  $N_c$ , is not dependent on the precise parameters used in the determination of the lateral shower distribution. This qualitative study shows that the energy uniformity depends on the cluster size and shows a minimal variation with  $N_c = 4$  for  $N_c \leq 7$ .

Figure 8.27 (left) shows the transverse energy leakage for 25 GeV electrons simulated with EGS4 for  $N_c = 4$  and the case performing the sum in equation 8.34 over all strips for  $E_X$  setting the term  $l_X(X, Y)$  to one. The sensitivity to transverse energy leakage is clearly reduced, as one would expect, by using a clustering algorithm.

As will be shown in the next section, relative strip-to-strip calibration values can be only obtained with the algorithm used for strips within the fiducial volume. A cluster algorithm reduces the influence of non-calibrated readout channels since only edge strips outside the fiducial volume are taken into account in the reconstruction of  $E_X$  and  $E_Y$ . Using a cluster algorithm also reduces the sensitivity to noise.

Taking these considerations into account, a cluster size of  $N_c = 4$  was chosen for the energy reconstruction of the BPC. It has been verified that the energy resolution stays constant for  $N_c \geq 4$ . Furthermore, it has been verified that for MC, the difference between the re-weighted and the non re-weighted transverse energy distribution has a negligible effect on the overall energy spectra using  $N_c = 4$  and has been therefore omitted for the energy reconstruction in MC. The excellent agreement between data and MC for a KP-sample, as will be shown in section 8.5.3, supports this as well.

### 8.5.3 Calibration

The energy calibration of the BPC consists of two steps:

- relative strip-to-strip calibration including leakage and attenuation corrections and
- absolute energy scale calibration.

Both steps are driven by the requirements on the calibration of the BPC, which have been discussed in section 5.3, namely that the uniformity of the energy measurement as well as the accuracy of the absolute energy scale, should be at the level of 0.5%. Both calibration steps are performed using KP-events. Due to reductions in the gain for some of the PMTs and the loss of light yield in some of the scintillator strips due to radiation damage (Section 7.2), the energy scale was not stable within 0.5% for the whole BPC 1995 data. The drop in the energy scale over the whole BPC running-period is at most 2.5% for regions closest to the beam determined by a KP-sample. To correct for this, the whole data sample was separated into four time periods and the calibration procedure, i.e. relative and absolute calibration performed separately for each time period. It was found that four periods are enough to ensure a stability of the energy scale at the level of 0.5% within each calibration period.

The selection criteria of KP events will be discussed in chapter ten. The selection cuts are summarized in Table B.2.

#### Relative strip-to-strip calibration

The relative strip-to-strip calibration has to equalize the response of the individual readout channels, taking into account the attenuation of scintillator light within the scintillator strips and the transverse shower leakage towards the edges of the BPC.

The beam pipe window determines the fiducial volume of the BPC. Figure 8.28 shows a scatter plot of reconstructed  $X$  and  $Y$  positions from a data KP-sample applying the final fiducial volume cuts for the calibration procedure. The solid horizontal and vertical lines denote the strip boundaries. One can see that six strips in  $X$  ( $X_2 - X_7$ ) and eight strips in  $Y$  ( $Y_5 - Y_{12}$ ) cover the actual fiducial volume. The upper and lower edges, as well as the right edge of the fiducial volume, are determined by the shape of the beam pipe window. The left edge is determined by the requirement to restrict the position bias to stay within 0.05 cm (Section 8.3.3).

The algorithm used for the relative strip-to-strip calibration only allows off-line calibration factors  $\alpha_X^i$  and  $\alpha_Y^j$  to be obtained for those strips which are within the fiducial volume. Since the cluster size for the energy reconstruction is four strips and the final fiducial volume cuts are quite restrictive, only the first strips outside the fiducial volume represent some uncertainty on the energy uniformity. However, the energy uniformity was determined to be  $\pm 0.5\%$  in both directions  $X$  and  $Y$  within the fiducial volume and the influence of non-calibrated edge strips does therefore not represent a systematic degradation of the energy uniformity.

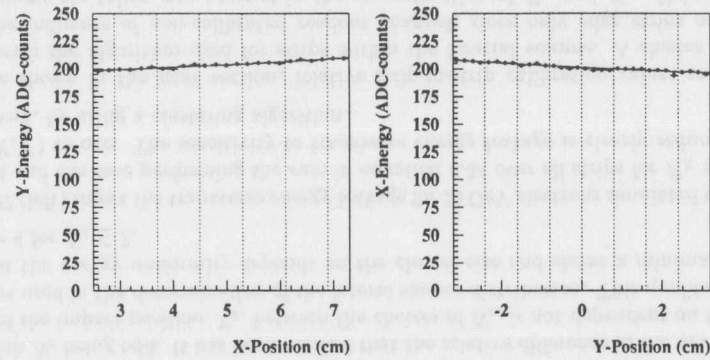


Figure 8.29: Results from the DESY II test-beam experiment on the attenuation of scintillator light in scintillator fingers of the BPC South module showing  $E_Y$  as a function  $X$  (left) and  $E_X$  as a function  $Y$  (right). A fit to the observed attenuation is overlaid using the first term in equation 5.38.

The relative response of all strips was adjusted prior to the installation of the BPC using a  $^{60}\text{Co}$ -scan to a level of about 7% as described in Section 5.7.

In the previous section it was shown that the total energy is obtained as the energy scale weighted sum of the reconstructed energies  $E_X$  and  $E_Y$ .

$$E_{BPC} = s_X \cdot E_X^j + s_Y \cdot E_Y^j \quad (8.38)$$

where,

$$E_X^j = l_X(X, Y) \cdot a_X(Y) \cdot \sum_{\text{cluster}} \alpha_X^i \cdot E_{X_{\text{raw}}}^{ji} \quad (8.39)$$

and

$$E_Y^j = l_Y(X, Y) \cdot a_Y(X) \cdot \sum_{\text{cluster}} \alpha_Y^i \cdot E_{Y_{\text{raw}}}^{ji} \quad (8.40)$$

The mapping of the readout channels to a particular index follows the convention in Figure 8.28.  $E_{X_{\text{raw}}}^j$  and  $E_{Y_{\text{raw}}}^j$  denote the case for which the correction functions as well as the relative calibration constants  $\alpha_X^i$  and  $\alpha_Y^i$  are not applied in equations 8.39 and 8.40. The first column in Figure 8.30 shows the raw energies  $E_{X_{\text{raw}}}^j$  and  $E_{Y_{\text{raw}}}^j$  as a function of  $X$  and  $Y$ . The first two plots clearly show the need to equalize the response of individual readout channels.  $E_{X_{\text{raw}}}^j$  as a function of  $X$  also displays the effect of transverse energy leakage towards the beam pipe edge. The attenuation of scintillator light along the vertical  $X$ -strips can be seen in the third plot with  $E_{X_{\text{raw}}}^j$  plotted as a function of  $Y$ . The last plot in the first column shows both transverse energy leakage and the attenuation of scintillator light along the horizontal  $Y$ -strips for  $E_{Y_{\text{raw}}}^j$  plotted as a function of  $X$ .

The leakage correction has been performed using an ansatz of one exponential function for  $dE/dX$  to obtain the integrated lateral shower distribution, as discussed in detail in section 8.4.2. The attenuation correction is taken care of by the same ansatz as used for a description of scans on scintillator fingers of the same type (Section 5.4.3), taking into account only the low attenuated part represented by  $\mu_1$  (Equation 5.38). Figure 8.29 shows such a fit of a scan

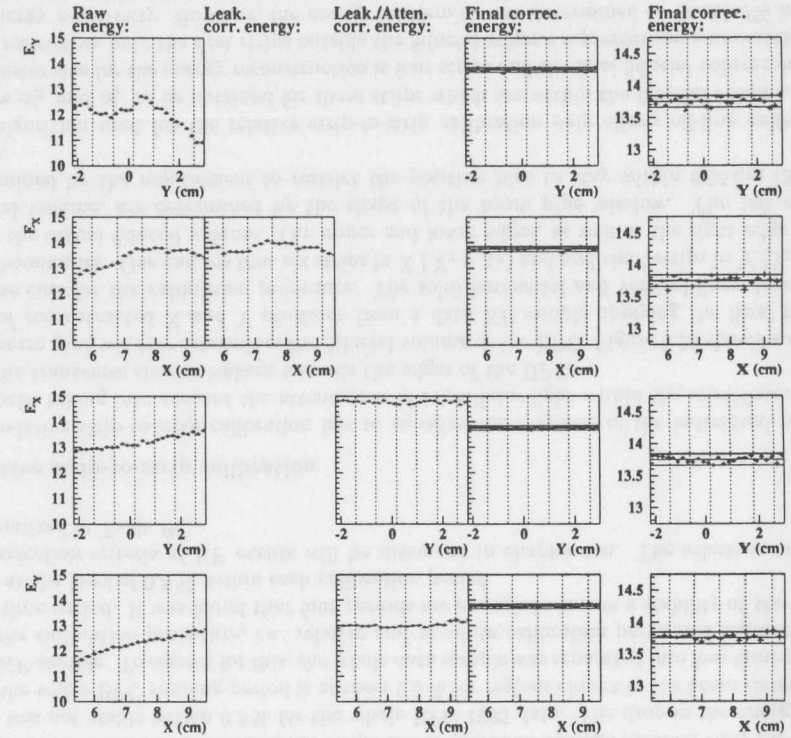


Figure 8.30: Relative strip-to-strip calibration procedure. The uniformity of the final reconstructed energies  $E_X$  and  $E_Y$  is well within  $\pm 0.5\%$ . The histograms shown are taken from the first calibration period.

using electrons from the DESY II test-beam data. This ansatz provides a good description of the observed attenuation within scintillator fingers. The scans using electrons from the DESY II test-beam data have been performed over several fixed positions. The attenuation lengths, using the mentioned ansatz, are well within  $\pm 5\text{cm}$  which has been as well confirmed by a sample of scanned scintillator fingers on the bench (Section 5.4.3). Using a single attenuation correction  $a_X(Y)$  and  $a_Y(X)$  for all positions  $X$  and  $Y$  provides a well justified simplification of the relative strip-to-strip calibration procedure to be discussed now in detail.

$E_{X_{\text{raw}}}^{ji}$  and  $E_{Y_{\text{raw}}}^{ji}$  are the raw energies in each BPC readout channel. Due to the restricted fiducial volume in  $Y$ , one can completely ignore any transverse energy leakage and the function  $l(X, Y)$  reduces to a correction function in  $X$  only, i.e.  $l(X)$ . The energy  $E_X^j$  depends on two correction functions,  $l(X)$  and  $a_X(Y)$ , which can be decoupled.  $a_X(Y)$  accounts for the attenuation of light along the vertical  $X$ -scintillator fingers. The correction function  $l(X)$  was determined by a fit to  $E_{X_{\text{raw}}}^j$  as a function of  $X$  whereas  $a_X(Y)$  was obtained by a fit to  $E_{X_{\text{raw}}}^j$  as a function of  $Y$ .

The readout schemes of the BPC in  $X$  and  $Y$  direction are identical in both transverse dimen-

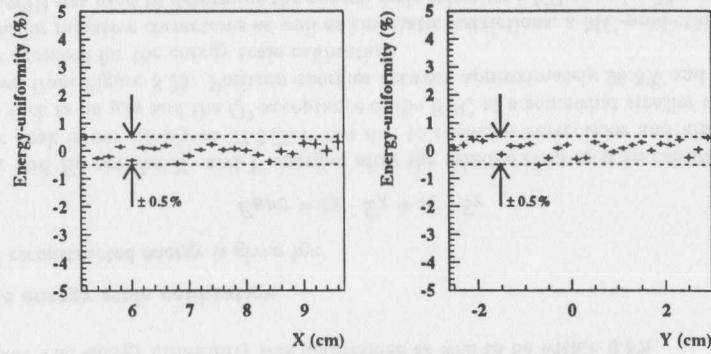


Figure 8.31: Uniformity of the final reconstructed energy  $E_{BPC}$  as a function of  $X$  and  $Y$  for the whole 1995 KP-sample.

sions. The correction function  $l(X)$  was therefore used for  $E_Y^j$  as well. The correction function  $a_Y(X)$  was then obtained by a fit to  $l(X)E_{Y_{raw}}^j$  as a function of  $X$ . The result of this correction procedure prior to the determination of the relative calibration factors  $\alpha_X^i$  and  $\alpha_Y^i$  can be seen in Figure 8.30.

This procedure has been performed for each of the four calibration periods.

The relative strip-to-strip calibration are taken into account by multiplicative factors  $\alpha_X^i$  and  $\alpha_Y^i$  as being discussed in the following.

If one moves the positron impact position along the BPC in direction of  $X$  or  $Y$  and therefore changing the index  $j$ , the reconstructed energy  $E_X^j$  and  $E_Y^j$  respectively, for the same event class should be strictly independent of the index  $j$ , i.e. the response of the BPC should be uniform. Selecting KP-events, one therefore sets  $E_X^j$  or  $E_Y^j$  to be  $13.75 \text{ GeV}$  which is half of the positron beam energy. This neglects radiative corrections as well kinematic cuts introduced by the cut on  $y_{JB}$  and the  $Q^2$ -acceptance of the BPC which leads to somewhat lower values than  $13.75 \text{ GeV}$ . This will be taken into account through the absolute energy scale calibration. It only ensures that the reconstructed energy  $E_X^j$  and  $E_Y^j$  are independent of the impact position of the positron by adjusting the individual response of the BPC readout channels by the relative strip-to-strip calibration factors  $\alpha_X^i$  and  $\alpha_Y^i$ .

The index  $j$  runs in principle from 1 to 15 in  $X$  and from 1 to 16 in  $Y$ . The cluster-sum index  $i$  runs over the same interval. One therefore obtains a matrix equation in which the solution vector corresponds to the fixed reconstructed energy which is set to be  $13.75 \text{ GeV}$  for strips within the fiducial volume. Strips outside the fiducial volume are assigned to have relative calibration factors of 1 during the whole calibration procedure. Let us define the following abbreviations for the matrix elements:

$$\bar{E}_X^{ji} = l(X) \cdot a_X(Y) \cdot E_{X_{raw}}^{ji} \quad (8.41)$$

and

$$\bar{E}_Y^{ji} = l(X) \cdot a_Y(X) \cdot E_{Y_{raw}}^{ji} \quad (8.42)$$

We can therefore rewrite the above equations as follows:

RMS=0.33							
							Y12
	0.0	0.4	0.4	0.2	-0.1		Y11
	-0.5	-0.1	-0.0	0.3	0.5		Y10
	-0.7	-0.3	0.2	0.5	0.2		Y9
	-0.3	-0.2	-0.2	0.3	0.1		Y8
	0.2	0.0	-0.1	-0.1	-0.2		Y7
	0.5	0.4	-0.2	-0.7	-0.4		Y6
							Y5
X1	X2	X3	X4	X5	X6	X7	X8

Figure 8.32: Percent deviation of the reconstructed mean energy in each 8 mm bin from the reconstructed mean energy over the whole fiducial volume for the whole 1995 KP-sample.

$$\bar{E}_X^{ji} \alpha_X^i = E_X^j = \begin{cases} 13.75 & \text{for } j \in V_{in} \\ 1 & \text{for } j \in V_{out} \text{ and } \bar{E}_X^{ji} = \delta^{ji} \end{cases} \quad (8.43)$$

and

$$\bar{E}_Y^{ji} \alpha_Y^i = E_Y^j = \begin{cases} 13.75 & \text{for } j \in V_{in} \\ 1 & \text{for } j \in V_{out} \text{ and } \bar{E}_Y^{ji} = \delta^{ji} \end{cases} \quad (8.44)$$

where the sum is being extended over double occurring indices.  $V_{in}$  denotes the fiducial volume and  $V_{out}$  the whole region outside the fiducial volume. If one inverts the matrix  $\bar{E}_X^{ji}$  and  $\bar{E}_Y^{ji}$ , one obtains the relative strip-to-strip calibration values via the following equations:

$$\alpha_X^i = (\bar{E}_X^{ji})^{-1} \cdot E_X^i \quad (8.45)$$

and

$$\alpha_Y^i = (\bar{E}_Y^{ji})^{-1} \cdot E_Y^i \quad (8.46)$$

Using an iteration in the evaluation of the relative calibration constants, the difference of these constants between the first and the second iteration is well below 0.1%. Applying these relative calibration factors, one obtains the final reconstructed energies  $E_X$  and  $E_Y$  plotted as a function of  $X$  and  $Y$  as shown in Figure 8.30. The energy uniformity of  $E_X$  and  $E_Y$  as a function of  $X$  and  $Y$  is well within 0.5%, denoted by the solid horizontal lines in Figure 8.30, which is the case for all four calibration periods.

Figure 8.31 shows uniformity of the final reconstructed energy  $E_{BPC}$ , including the absolute energy scale calibration to be discussed, as a function of  $X$  and  $Y$  over the whole data taking period. One clearly finds that in both transverse directions the uniformity is well within 0.5%. The uniformity in  $E_{BPC}$  for each of the four calibration periods is as well within 0.5%. There is no indication of a systematic change from the beginning to the end of the data taking period which has not been taken into account by the above relative calibration procedure which could

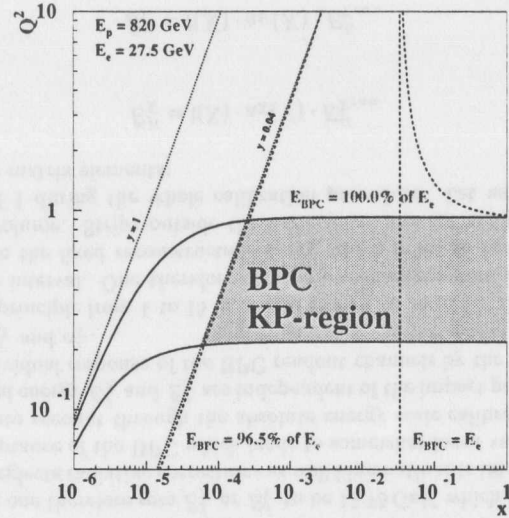


Figure 8.33: Selection of kinematic peak events in the BPC region including lines of constant positron energy (dashed lines) and constant polar angle with  $\vartheta'_e = 17$  and  $35$  mrad representing the BPC fiducial volume (solid lines). The dotted lines represent lines of constant  $y$  values (1 and 0.04).

lead to a systematic degradation of the energy uniformity. It indicates that the above relative calibration procedure ensures a uniform energy response for the whole 1995 BPC data by adjusting the attenuation correction as well as the relative strip-to-strip calibration constants. Figure 8.32 shows in bins of  $8$  mm for the whole 1995 data in a two-dimensional plot, the percent deviation of the reconstructed mean energy in each bin from the reconstructed mean energy in the whole fiducial volume. Vertical and horizontal lines indicate the position of the scintillator strips. The RMS-value of the percent deviations is, as shown,  $0.33\%$ .

The same relative calibration procedure has been applied to data from the DESY II test-beam experiment. The energy uniformity was determined as well to be within  $0.5\%$ .

#### Absolute energy scale calibration

The final reconstructed energy is given by:

$$E_{BPC} = s_X \cdot E_X + s_Y \cdot E_Y \quad (8.47)$$

where  $E_X$  and  $E_Y$  are the  $X$ - and  $Y$ -energies after the relative strip-to-strip calibration. The kinematic peak is not simply at  $27.5$  GeV but due to radiative corrections and kinematic restrictions such as on  $y_{JB}$  and the  $Q^2$ -acceptance of the BPC at a somewhat smaller value. This can be seen from Figure 8.33. Positron energies between approximately  $96.5\%$  and  $100.0\%$  of  $E_{BPC}$  are accepted for the energy scale calibration.

To account for radiative corrections as well as kinematic restrictions, a MC-prediction (HERACLES) [Kw91] was used to determine the energy scale selecting a KP-sample. The scale values  $s_X$  and  $s_Y$  for the independent reconstructed energies  $E_X$  and  $E_Y$  are adjusted separately. This

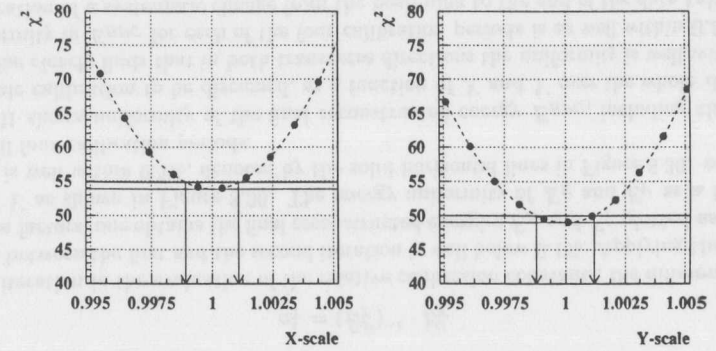


Figure 8.34: Determination of scale values  $s_X$  and  $s_Y$  for the first calibration period in 1995.

is being done by minimizing a  $\chi^2$  between the data and MC  $E_X$  and  $E_Y$  energy distributions, varying the scale values for the data distributions  $s_X$  and  $s_Y$ , respectively. Let  $N_{data}(j, k)$  be the number of events in bin  $j$  of the energy distribution  $E_X$  and  $E_Y$  respectively, where  $k$  denotes the scale value  $s_X$  and  $s_Y$  with which the array  $N_{data}(j, k)$  was filled.  $N_{MC}(j)$  is the same expression for MC for bin  $j$ . The scale values  $s_X$  and  $s_Y$  were then determined by minimizing the following expression by varying  $s_X$  and  $s_Y$ :

$$\chi^2 = \sum_{j=1}^{n_{bin}} \frac{(N_{data}(j, k) - N_{MC}(j))^2}{\sigma_{data}^2(j, k) + \sigma_{MC}^2(j)} \quad (8.48)$$

In Figure 8.34,  $\chi^2$  is plotted as a function of  $s_X$  and  $s_Y$ , respectively. The minimum appears at  $s_X = 1$  and  $s_Y = 1$ , since the final scale values have been already included. Changing the absolute value of  $\chi^2$  by one unit, one obtains an estimate of the statistical error which amounts to be in both cases about  $0.1\%$  of the scale values obtained, denoted by the vertical arrows in Figure 8.34.

In order to evaluate the systematic error on the obtained scale values using the above procedure, a whole series of checks have been performed changing the following quantities:

- binning of the energy distribution  $E_X$  and  $E_Y$ ,
- number of points used to calculate  $\chi^2$ ,
- structure function for the generation of HERACLES MC-events,
- fiducial volume cuts,
- UCAL noise suppression cuts (Section 10.2) which effects the reconstruction of  $y_{JB}$  and

period	$\chi^2/ndf$ for $E_X$	$\chi^2/ndf$ for $E_Y$
1	54/50	49/50
2	55/50	55/50
3	51/50	50/50
4	52/50	54/50

Table 8.2:  $\chi^2/ndf$  values for  $E_X$  and  $E_Y$  for all four calibration periods.

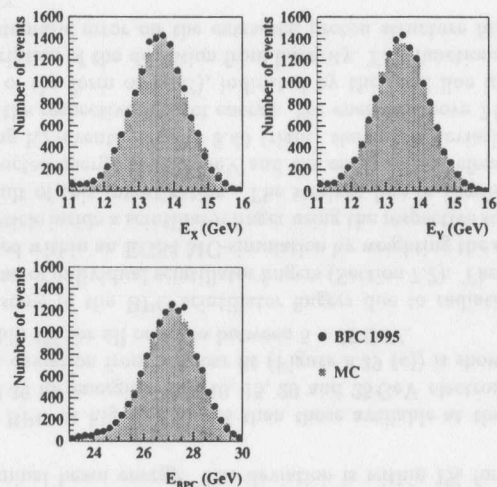


Figure 8.35: Comparison between MC and data for  $E_X$ ,  $E_Y$  and  $E_{BPC}$  for the whole BPC 1995 data.

- cut on  $y_{JB}$  to select KP-events.

The dependence on the underlying structure function in MC is expected to be small in the selected kinematic region of low values in  $y$ . This has been cross-checked by re-weighting the MC input structure function based on the DL-parametrization (Section 6.5) to the parameterization given by CKMT (Section 2.3.4). Taking these uncertainties into account, the systematic error of the above procedure was estimated to be 0.2%. This procedure has been performed for all four calibration periods. Table 8.2 provides the values of  $\chi^2/ndf$  for all four periods. There is no indication of a systematic change from the beginning to the end of the data taking period which has not been taken into account by the above calibration procedure. Figure 8.35 shows, for the whole BPC 1995 data, the reconstructed energies  $E_X$ ,  $E_Y$  and  $E_{BPC}$  comparing data and MC. In all three cases, one finds a good agreement between MC and data.

The absolute energy scale obtained with a KP-sample was checked using elastic  $\rho^0$  events,  $e^+p \rightarrow e^+\rho^0p$ . The  $\rho^0$  vector meson decays almost exclusively into two charged pions, i.e.  $\rho^0 \rightarrow \pi^+ + \pi^-$ . Those can be measured in the ZEUS central-tracking detector (CTD) (Section 4.3) over a limited kinematic region which amounts to  $0.004 < y < 0.09$  in case of the BPC. The position of the scattered positron was measured in the BPC. Using four momentum conservation, one can derive an expression for the energy of the scattered positron in terms of the scattering angle of the positron and the energy and momenta of the final state  $\rho^0$  decaying into two pions:

$$E'_e = \frac{2E_e - (E - P_Z)_{\rho^0}}{(1 - \cos \theta'_e)} \quad (8.49)$$

where  $E_e$  is the energy of the incoming positron taken to be  $27.5 \text{ GeV}$  ignoring initial-state radiation,  $(E - P_Z)_{\rho^0}$  are the energy and momenta of the final state  $\rho^0$  determined via its decay particles  $\rho^0 \rightarrow \pi^+ + \pi^-$ . The selection criteria of elastic  $\rho^0$  events will be discussed in chapter ten. The selection cuts are summarized in Table B.4.

Figure 8.36 shows an event display of a typical elastic  $\rho^0$  event. Two tracks coming from the two decay pions are clearly visible as well as the positron measured in the BPC.

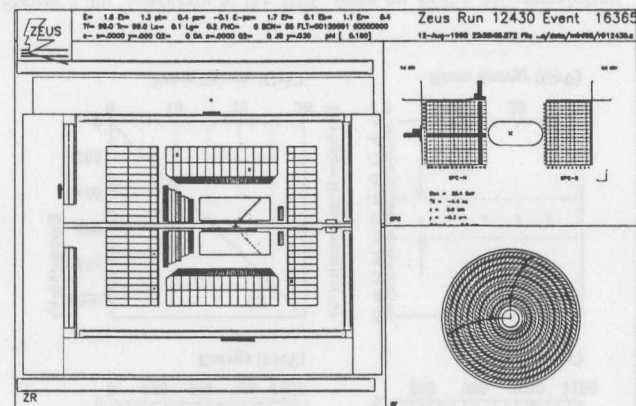


Figure 8.36: Event display of a typical elastic  $\rho^0$  event. Tracks from the two decay pions are clearly visible in the CTD. The upper right plot shows a cross section of the BPC modules as seen from the proton beam with the BPC North module on the left.

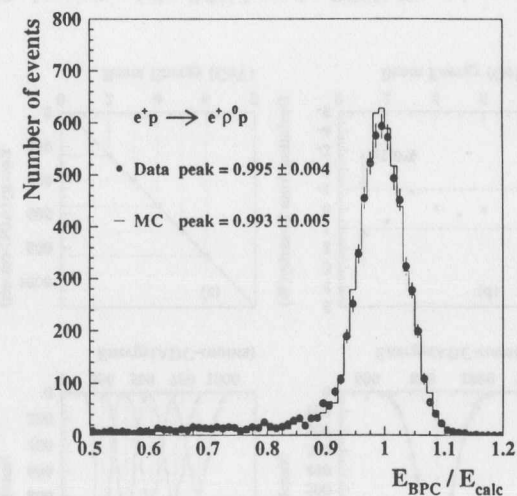


Figure 8.37: Comparison between MC and data of the ratio of the measured positron energy in the BPC,  $E_{BPC}$ , to the calculated positron energy,  $E_{calc}$ , using elastic  $\rho^0$  events.

Figure 8.37 shows the ratio of the measured energy of the scattered positron in the BPC to the energy determined using the above formula for both data and MC. Radiative corrections are responsible for the tail towards low values and the fact that both distributions peak below unity. The agreement between both spectra is good. The accuracy of the BPC energy reconstruction is within 0.5%, taking into account the energy uniformity and the comparison among the energy scale determined from KP-events and elastic  $\rho^0$  events between data and MC (Figure 8.37). The latter value has been used in the evaluation of systematic errors for the physics analysis of this thesis.

### 8.5.4 Energy resolution and linearity

The energy resolution and linearity of the BPC has been verified using results from the BPC South test-beam experiment restricted to electron energies between 2 – 6 GeV. An EGS4 MC-simulation was used to establish the energy resolution and linearity at higher energies. Furthermore, an EGS4 MC-simulation was used to estimate the effect on the linearity of the absolute energy scale due to radiation damage as discussed in detail in section 7.2.

#### Linearity

Figure 8.38 (a) displays the reconstructed energy in the BPC South module for energies of the test beam of 2 – 6 GeV using the energy reconstruction and calibration procedure as discussed in detail in section 8.5.3. The mean values of a Gaussian fit for all test-beam energies, as shown in Figure 8.38 (b) for 6 GeV test-beam electrons, is plotted in Figure 8.38 (c) as a function of the respective nominal beam energy. A linear fit is overlaid which does not pass through the origin. As discussed in section 8.2, this effect is due to a mis-calibration of the test-beam energy which should be lower by 300 MeV to force the linear fit as shown in Figure 8.38 (c) to pass through the origin. The deviation from the linear fit is shown in Figure 8.38 (d) as a function of the respective nominal beam energy. The deviation is within 1% for all energies between 2 – 6 GeV.

The linearity of the BPC at higher energies than those available at the DESY II test-beam is shown in Figure 8.39 for energies of 5, 10, 15, 20 and 25 GeV electrons based on an EGS4 MC-simulation. The deviation from a linear fit (Figure 8.39 (c)) is shown in Figure 8.39 (d). The deviation is within 1% for all energies between 5 – 25 GeV.

The degradation of some of the BPC scintillator fingers due to radiation damage has been determined from a scan of individual scintillator fingers (Section 7.2). The results of these scans have been incorporated within an EGS4 MC-simulation by weighting the energy deposition of a particular shower particle inside a scintillator finger using the respective scanning result. Figure 8.40 displays the result of this investigation. The straight line in Figure 8.40 (left) is drawn through the reconstructed energy at 27.5 GeV and the origin. This refers to the actual energy scale calibration using KP-events. Figure 8.40 (right) shows the deviation from this straight line as a function of the respective impact energy. For energies above 7 GeV, the deviation is less than 1%. A fit of the form  $\propto \ln(E)$ , indicated by the solid line in Figure 8.40 (right), provides a good description of the deviation from linearity. This functional form has been used to determine the systematic error on the extracted proton structure function  $F_2$  due to the observed non-linearity.

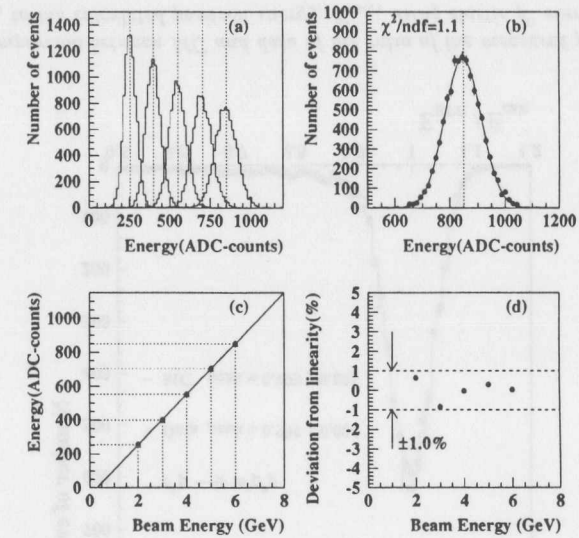


Figure 8.38: Linearity of the BPC from the DESY II test-beam experiment.

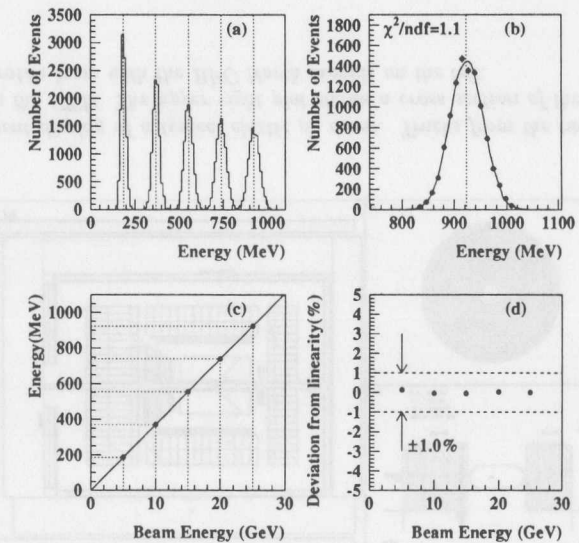


Figure 8.39: Linearity of the BPC from an EGS4 MC-simulation.

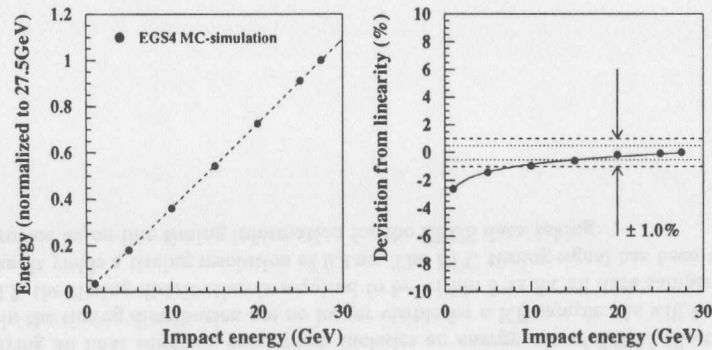


Figure 8.40: Deviation from linearity due to radiation damage.

### Energy resolution

Figure 8.41 shows the energy resolution as obtained from the BPC South test-beam experiment. The reconstructed  $\sigma/E$  values are plotted as a function of the respective beam energy subtracted by the beam energy offset of 300 MeV. The fractional energy resolution has been fitted by a functional form of  $(\sigma_E/E)^2 = (a^2/E^2) + (b^2/E) + c^2$ , as introduced in section 5.2, which yields the following parameters:  $a = 110 \pm 5.0$  MeV,  $b = 17.2 \pm 0.2\% \text{ GeV}^{1/2}$  and  $c = 2.1 \pm 0.2\%$ .

The energy spread of a 3 mm copper target amounts to approximately 100 MeV which contributes to the  $a$  term [Me95]. The impact of the finite collimator aperture has been estimated to be about 1–2%. The  $c$  term is compatible with this estimation. The sampling term together with the contribution from photocathode statistics amounts to  $17.2\%/\sqrt{E}$ . Using LED test-trigger data among the calibrated BPC North module, the photoelectron yield has been estimated to be about 200 photoelectrons/GeV which yields a photoelectron contribution to the stochastic term of  $7\%/\sqrt{E}$ . Taking this value as the contribution of the photoelectron statistics for the BPC South module, the sampling fraction of the BPC South module amounts to  $15.7\%/\sqrt{E}$ .

The reconstructed fractional energy resolution  $\sigma/E$  is shown in Figure 8.42 for an EGS4 MC-simulation with impact energies in the range of 5–25 GeV. The extracted sampling term amounts to  $16.0\%/\sqrt{E}$  which is in good agreement with the one extracted from the BPC South test-beam experiment.

Figure 8.43 shows for the BPC South module for 3 GeV test-beam electrons, the fractional resolution  $\sigma/E$  as a function of the respective reconstructed position measured with respect to the edge of the first scintillator strip. The energy resolution is flat to within 8 mm from the edge of the BPC.

The photoelectron yield of 200 photoelectrons/GeV has been taken into account in the simulation of the physics events using the ZEUS MC-program MOZART (Section 6.3). The good agreement between the final reconstructed energies  $E_X$ ,  $E_Y$  and  $E_{BPC}$  (Figure 8.35), reflects the fact that the energy resolution in data is well reproduced by the MC simulation.

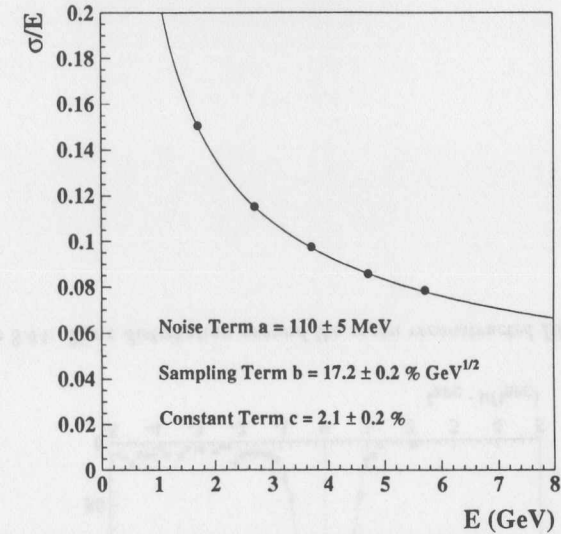


Figure 8.41: Energy resolution of the BPC from the DESY II test-beam experiment.

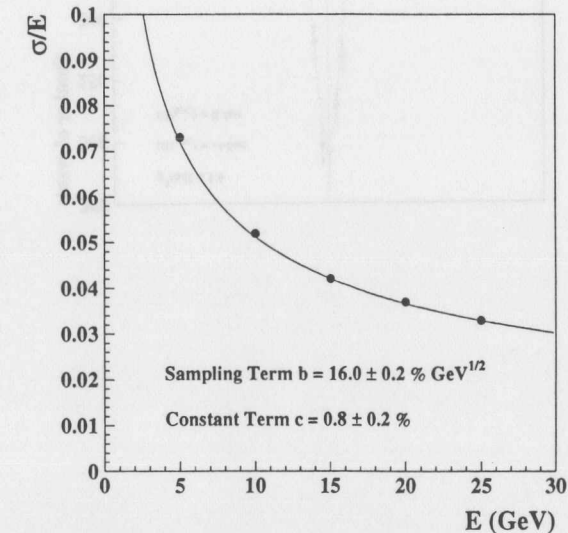


Figure 8.42: Energy resolution of the BPC from an EGS4 MC-simulation.

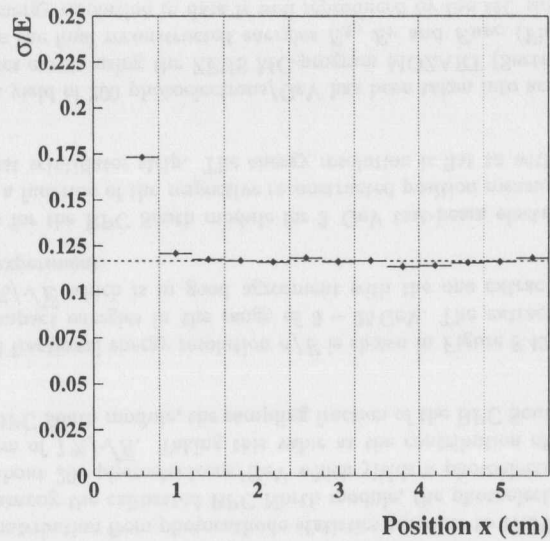


Figure 8.43: Energy resolution of the BPC at the BPC edge for 3 GeV electrons from the DESY II test-beam experiment.

## 8.6 Reconstruction of time

The DSP-reconstructed time (Section 5.5) for each BPC readout channel  $t_i$  has been used to determine a mean reconstructed time  $t_{BPC}$  for one particular BPC module on an event-by-event basis. Each timing information  $t_i$  has been linearly weighted by the respective deposited energy  $E_i$ , i.e.:

$$t_{BPC} = \frac{\sum_{i=1}^N E_i t_i}{\sum_{i=1}^N E_i} \quad (8.50)$$

with  $N$  being the number of readout channels for one particular BPC module (North:  $N = 31$ ; South:  $N = 27$ ).

Figure 8.44 shows the timing distribution for the BPC North module for one particular run after applying all final selection cuts which includes an energy cut of 7 GeV (Section 10.2). The tails in the timing distribution are no longer visible for a KP-sample. As will be shown in section 10.2, the timing distribution is required to be within 3 ns for all data samples.

A Gaussian fit yields a timing resolution of 0.4 ns. The BPC timing signal has been used since 1995 to provide an on-line timing information for the ZEUS data taking.

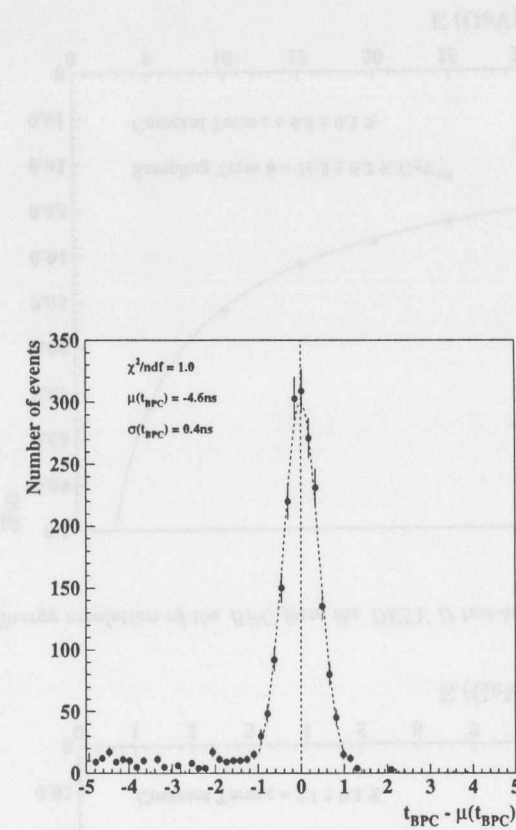


Figure 8.44: Time distribution around the mean reconstructed BPC time.

## Chapter 9

### Efficiencies and systematics

#### 9.1 Introduction

The following chapter will discuss in detail, several efficiency and systematic effects which are relevant for the determination of the proton structure function  $F_2$  and its systematic uncertainties as well as for the choice of some of the off-line selection cuts. This includes the study of the BPC trigger efficiency, the determination of the event vertex using the CTD, the efficiency of the shower width cut in data and MC, the dependence of the acceptance on the underlying physics process due to various requirements on the hadronic final state and the understanding of radiative corrections.

#### 9.2 Trigger efficiency

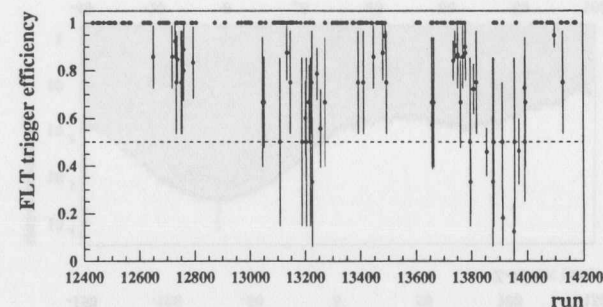


Figure 9.1: BPC FLT trigger efficiency as a function of run number for the HERA run in 1995.

The hardware of the BPC First-Level Trigger (FLT) and its implementation in the 1995 trigger configuration was presented in section 5.6 and 7.1, respectively. In order to evaluate the efficiency of the BPC FLT cuts on the FADC-digitized energy spectra of  $FADC(BPCN)_H \geq 4$  and the TDC-digitized timing information of  $1 \leq TDC(BPCN)_H < 8$ , an independently triggered sample was used which only required an energy deposit in the main calorimeter (CAL). All off-line selection cuts for the BPC  $F_2$  sample, except those which take into account the off-line reconstructed BPC energy, were imposed on this independently triggered sample (Section 10.2).

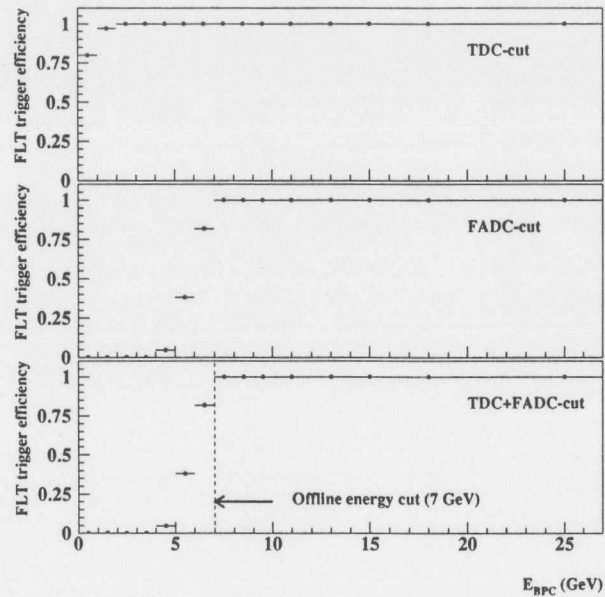


Figure 9.2: BPC FLT trigger efficiency as a function of the off-line reconstructed BPC energy imposing the TDC-cut (top), the FADC-cut (middle) and the TDC and FADC requirements together (bottom).

Using the BPC FLT requirements then allowed the determination of the trigger efficiency of the BPC FLT as a function of the BPC off-line reconstructed energy.

During the 1995 data taking, a hardware problem of the BPC FLT caused the HERA 10 MHz clock signal, derived from the GFLT, to be lost at the FADC which is used as the strobe input signal. This has been clearly identified as an intermittent problem with a NIM discriminator which caused the strobe signal at the FADC to be lost (Figure A.13). This resulted in a drop of efficiency for some of the runs. It has been verified that the loss of efficiency is independent of the reconstructed energy and position of the scattered positron and therefore of the respective kinematic variables.

Figure 9.1 shows the BPC FLT efficiency as a function of run number. The events are required to have an off-line reconstructed BPC energy of at least 10 GeV and are therefore expected to be 100% efficient, taking into account the calibration of the FADC energy spectra and the BPC FLT trigger requirements as discussed in detail in section 7.1. Those runs which suffered from the hardware problem can be clearly identified. Runs with an efficiency of less than 50% have been excluded from the physics analysis. 82% of the remaining runs have an efficiency of 100% whereas for 18% the overall efficiency amounts to  $81 \pm 4\%$ , which yields an overall efficiency for the whole data sample of  $96.6 \pm 0.7\%$ . The overall drop in the trigger efficiency from 100% to  $96.6 \pm 0.7\%$  has been taken into account in the luminosity determination. Figure 9.2 shows the trigger efficiency as a function of the BPC off-line reconstructed energy for the BPC FLT trigger requirements. The efficiency of the BPC FLT timing cut as a function of

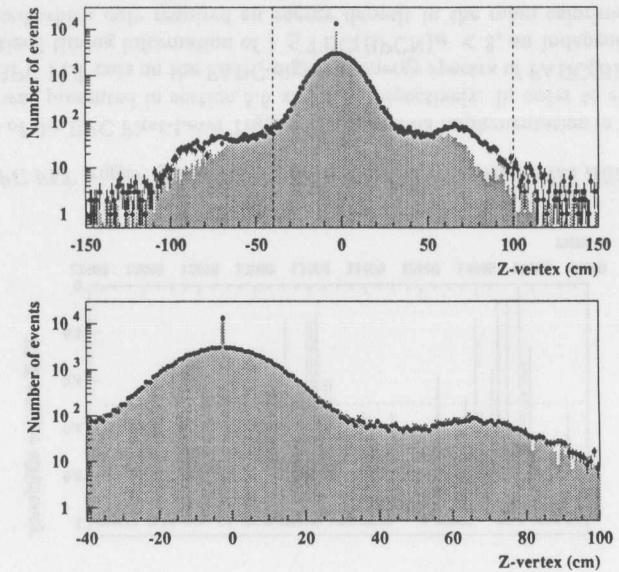


Figure 9.3: Comparison of the Z vertex distribution between data and MC before (top) and after (bottom) reweighting the MC input vertex distribution.

the BPC off-line reconstructed energy amounts to 100% above 2 GeV (Figure 9.2 (top)). The turn-on of the trigger efficiency around 7 GeV with respect to the FADC cut is clearly visible (Figure 9.2 (middle)). Figure 9.2 (bottom) shows the trigger efficiency of both BPC FLT trigger requirements. The efficiency amounts to 100% for energies above 7 GeV.

### 9.3 Vertex determination and positron beam tilt

The following section will focus on several items of the event vertex reconstruction. The tilt of the positron beam with respect to the ZEUS coordinate system and its impact on the kinematic reconstruction will be discussed as well.

The event vertex reconstruction using the ZEUS CTD is a major ingredient in the evaluation of the event kinematics through the reconstruction of the positron scattering angle (Electron method) using the CTD reconstructed vertex position and the impact position of the scattered positron in the BPC. The CTD vertex position is also needed to reconstruct the hadronic variables  $y_{JB}$  and  $E - P_z$ . Cuts on the reconstructed Z vertex position provide a means of background rejection, in particular for positron/proton beam gas events and cosmic ray events (Section 10.2).

In the case of the BPC, the final state positron cannot be used for the determination of the event vertex since it is far outside the acceptance of the CTD and one therefore relies on the hadronic final state. The topology of the hadronic final state introduces an additional dependence on the event vertex reconstruction. For events where the hadronic final state is lost in the forward

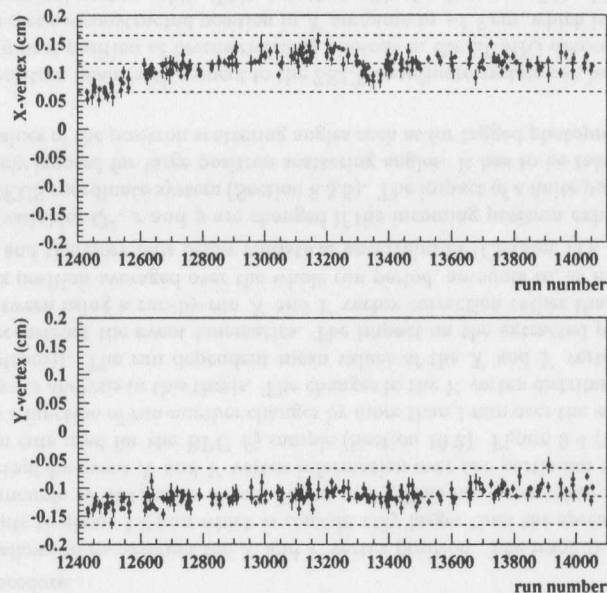


Figure 9.4: Mean  $X$  (top) and mean  $Y$  (bottom) vertex positions averaged over one run as a function of the respective run number.

direction (e.g. very low  $y$  events) or diffractive events which do not leave any tracks in the CTD, no event vertex information is available and the  $Z$ -position of the vertex is set for the full data sample to the nominal vertex position of  $\langle Z \rangle = -2.5$  cm. This leads to a worsening of the resolution of kinematic variables and therefore affects the migration among the chosen bins (Section 11.2).

The CTD requires at least one track for a vertex reconstruction to be possible. The quality of the vertex reconstruction increases with the number of tracks and reaches for events with two or more tracks a resolution in  $Z$  of about 4 mm.

The BPC acceptance changes with the position of the reconstructed  $Z$  vertex. The reconstructed  $Z$  vertex distribution in MC is therefore required to match those in data. Otherwise, systematic shifts in the distribution of kinematic variables between MC and data would result in a wrong acceptance correction and thus in errors when determining the proton structure function  $F_2$ . It is therefore important to provide a correct input vertex distribution to the MC simulation.

The input vertex distribution was determined from a measurement using a minimum-bias photoproduction sample [Ma96a]. Such a sample exhibits little bias in the  $Z$ -dependence of the vertex reconstruction and was therefore used to obtain the true vertex distribution as input for the MC simulation. Figure 9.3 (top) shows the reconstructed  $Z$  vertex distribution of data and MC. Stringent timing cuts on the main calorimeter in the determination of the input vertex distribution using a minimum-bias photoproduction sample resulted in a drop in the acceptance at large  $|Z|$  values, as can be seen from Figure 9.3 (top). The second peak in the

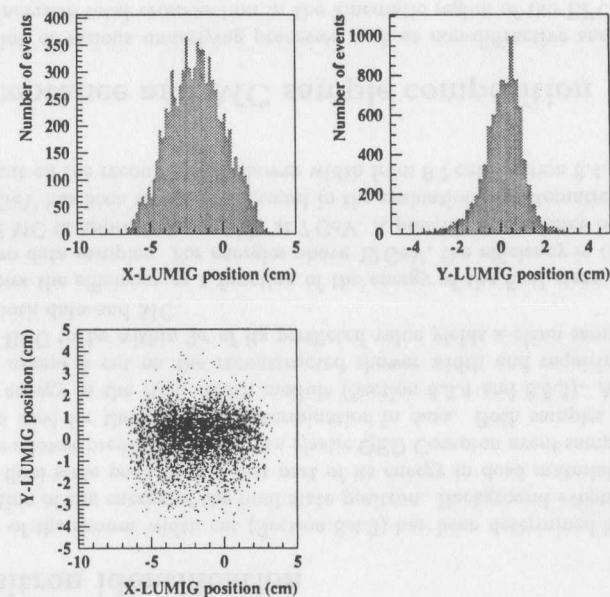


Figure 9.5:  $X$  and  $Y$  position distributions in the LUMIG detector. The mean reconstructed  $X$  position yields a tilt of the positron beam of  $-0.15$  mrad with respect to the nominal proton orbit.

vertex distribution, besides the central peak, is due to spill over protons from the main bunch. These satellite protons arrive approximately 4.8 ns earlier and give rise to  $e^+p$  interactions at  $Z = 70$  cm which enhance the acceptance for low  $Q^2$  events.

The spike in the center corresponds to events where no vertex has been found.

The obvious difference in the reconstructed  $Z$  vertex distribution between data and MC requires the input  $Z$  vertex distribution to be modified [Ti96]. The vertex reweighting procedure is based on the observation that the measured vertex distribution in MC is close to the MC input distribution. Reweighting the input distribution by the measured distribution in data provides therefore a way to obtain the proper measured vertex distribution in MC. For that, each MC event is assigned a weight factor depending on the true  $Z$  vertex position, as the ratio of the number of reconstructed events in data to those generated in MC at the same  $Z$  position. The weight factors are normalized such that the average  $Z$  vertex weight factor is one.

Besides the correction of the  $Z$  vertex distribution in MC, an additional correction has to be applied which is related to the discrepancy in the number of events without a reconstructed  $Z$  vertex between data and MC. This effect is dominated by the type of underlying process. The number of events with no reconstructed  $Z$  vertex amounts to 5% for non-diffractive and 39% for diffractive events in case of data. For MC, only 3% of non-diffractive and 21% of diffractive events are found to have no reconstructed vertex position. This difference leads to an overestimation of the resolution of kinematic variables in MC, in particular the  $Q^2$  resolution. This influences the smearing corrections derived from the MC sample. To match the number of events with no  $Z$ -vertex information in data and MC, a randomly chosen sample of MC events

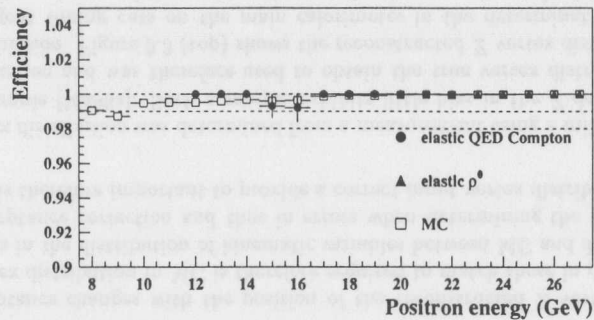


Figure 9.6: Efficiency of the positron shower width cut as a function of the off-line reconstructed energy in the BPC.

was selected and their vertex information was ignored by putting their reconstructed  $Z$  vertex strictly to the nominal vertex position. This was performed separately for non-diffractive and diffractive events. As a systematic check, the fraction of MC events whose  $Z$  vertex information was ignored was changed by  $\pm 50\%$  to investigate the impact on the reconstructed  $F_2$  values. The effect on  $F_2$  is negligible in all chosen bins (Section 11.5).

Including both corrections, Figure 9.3 (bottom) shows a good agreement in the reconstructed  $Z$  vertex distribution between data and MC. It has been verified that the  $Z$  vertex distribution between data and MC agrees for each of the chosen bins (Section 11.2) after the above reweighting procedure.

The CTD also allows to reconstruct the  $X$  and  $Y$  vertex position. The resolution in the  $X$  and  $Y$  vertex amounts to about 1.0 mm which is considerably larger than the spread of the HERA beams which amounts to  $300\ \mu\text{m}$  in  $X$  and  $70\ \mu\text{m}$  in  $Y$ . This has been taken into account by averaging the event-by-event  $X$  and  $Y$  vertex information over one particular run applying all off-line selection cuts used for the BPC  $F_2$  sample (Section 10.2). Figure 9.4 (top) shows that the  $X$  vertex as a function of run number changes by more than 1 mm over the whole run period used for the physics analysis in this thesis. The changes in the  $Y$  vertex distribution are smaller (Figure 9.4 (bottom)). The run dependent mean values of the  $X$  and  $Y$  vertex distributions were used to reconstruct the event kinematics. The impact on the extracted proton structure function  $F_2$ , between using a run-by-run  $X$  and  $Y$  vertex correction rather than using a mean  $X$  and  $Y$  vertex position averaged over the whole run period, amounts to, at most, 2% for the highest  $\theta'_e$  bins and therefore falls below statistical uncertainties (Chapter 11).

The kinematic variables  $Q^2$ ,  $x$  and  $y$  are changed if the incoming positron exhibits a tilt with respect to the ZEUS coordinate system (Section 8.3.5). The impact of a finite positron tilt angle can be completely ignored for large positron scattering angles. It has to be taken into account for very small values of the positron scattering angles such as for tagged photoproduction events [De94].

The tilt of the positron beam with respect to the ZEUS coordinate system can be determined by measuring the impact position of bremsstrahlung photons in the LUMIG detector, as shown in Figure 9.5. The mean reconstructed position in  $X$  amounts to  $-1.7\ \text{cm}$ , which is measured with respect to the nominal proton orbit. This, together with the distance of the LUMIG detector of 107 m from the ZEUS detector, yields a positron tilt angle of  $-0.15\ \text{mrad}$  with respect to the

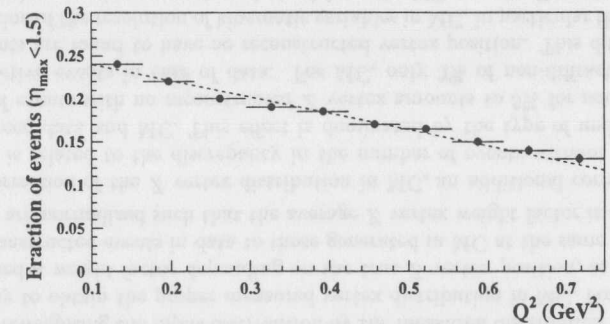


Figure 9.7: Fraction of events with  $\eta_{MAX} < 1.5$  as a function of  $Q^2$  in data.

nominal proton orbit in the  $X$ - $Z$ -plane, i.e the positron beam is tilted outwards with respect to the HERA ring. The nominal proton orbit has been surveyed [We96] with respect to the mechanical axis of the CTD and therefore to the ZEUS coordinate system. It exhibits a tilt in the  $X$ - $Z$ -plane of  $0.405\ \text{mrad}$  as shown in Figure A.6 with respect to the mechanical axis of the CTD. The positron beam therefore has an angle of  $0.25\ \text{mrad}$  with respect to the ZEUS coordinate system. Ignoring a correction for the positron beam tilt in data and MC leads to changes in the extracted  $F_2$  values by at most 2% for the highest  $\theta'_e$  bins which are less than statistical uncertainties (Chapter 11).

## 9.4 Positron identification

The efficiency of the shower width cut (Section 8.4.3) has been determined both in data and MC as a function of the energy of the final state positron. Background events or those events for which the final state positron has lost part of its energy in dead material before reaching the BPC, have a lower predicted energy. An elastic QED Compton event sample and an elastic  $\rho^0$  sample was used for the efficiency determination in data. Both samples allow to predict the measured energy in the BPC North module (Section 8.3.4 and 8.5.3). Applying all final selection cuts except a cut on the reconstructed shower width and requiring the measured energy in the BPC to be within  $2\sigma$  of its predicted value yields a clean sample of final state positrons for both data and MC.

Figure 9.6 shows the efficiency as a function of the energy of the final state positron for MC and for the two data samples. For energies above 12 GeV, the efficiency is close to 100%. It falls in case of MC to approximately 98% at 7 GeV. A possible discrepancy between data and MC below 12 GeV has been taken into account in the evaluation of systematic uncertainties by changing the cut on the reconstructed shower width from 0.7 cm (Section 8.4.3) to 0.8 cm.

## 9.5 Acceptance and MC sample composition

The contribution of various underlying processes such as non-diffractive and diffractive processes to the inclusive total cross-section in the kinematic region of the BPC has never been measured. Their fractional contribution was therefore unknown. The topology of these pro-

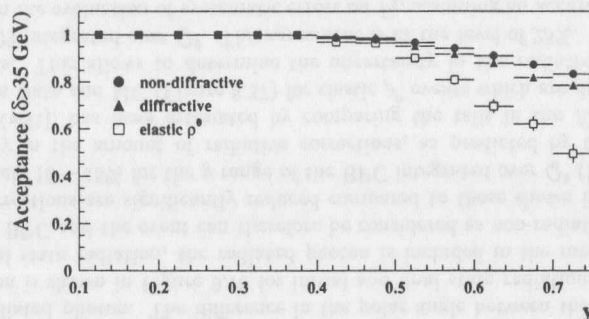


Figure 9.8: Fraction of events which pass the cut on  $\delta = E - P_z$  as a function of  $y$ .

cesses as anticipated from results in the photoproduction and deep-inelastic scattering (DIS) region are quite different. The overall acceptance in the kinematic region of the BPC for the measurement of the proton structure function  $F_2$  depends on their fractional contribution and the topology of these processes due to various constraints on the hadronic final state such as the cut on the total  $E - P_z$  and the cut on  $y_{JB}$  (Sections 10.2).

The fractional contribution of diffractive processes is completely different in the photoproduction region compared to the deep-inelastic scattering region. A common experimental way to quantify the fraction of diffractive over non-diffractive events is to use the variable called *pseudorapidity*  $\eta^1$ .  $\eta_{MAX}$  refers to the most forward deposited energy in the detector with at least 400 MeV energy.

10% of all DIS events exhibit  $\eta_{MAX}$  values of less than 1.5 whereas for photoproduction events, this fraction amounts to 35%. It is therefore expected that the contribution of diffractive events, based on the fraction of events with  $\eta_{MAX} < 1.5$  in the kinematic region of the BPC, is between 10% and 35%, depending on  $Q^2$ . The fraction of inelastic, high-mass diffractive events in MC (Section 6.5) was generated with a contribution of 30% to the total cross-section and reweighted later on. This reweighting procedure will be discussed below.

The fraction of diffractive events in the final MC sample used for the extraction of the proton structure function  $F_2$  (Chapter 11) was determined from the fraction of events with  $\eta_{MAX} < 1.5$  in data. This fraction was determined in data as a function of  $Q^2$ , as shown in Figure 9.7. It does not depend on  $y$ . Not all diffractively generated events in MC pass the cut on  $\eta_{MAX}$  of  $\eta_{MAX} < 1.5$ . The fraction of MC diffractive events was reweighted such that the fraction of events with  $\eta_{MAX} < 1.5$  agrees to those in data depending on  $Q^2$ . For that, a straight line was fitted to the fractional contribution of events in data with  $\eta_{MAX} < 1.5$  as a function of  $Q^2$ .

The fractional contribution of elastic  $\rho^0$  events (Section 6.5) was fixed at 5% for the generation of MC events and subsequently reweighted taking into account results from the cross-section measurement of elastic  $\rho^0$  production in the kinematic region of the BPC [Mo97a].

The  $W$  dependence of the elastic  $\rho^0$  cross-section was measured for a  $Q^2$  value of 0.47 GeV<sup>2</sup> with a slope in  $W$  which is consistent with the prediction by DL and therefore the same as the one used for the simulation of the total cross-section (Section 6.5). It has been used to evaluate the absolute contribution of the elastic  $\rho^0$  cross-section to the total cross-section. The

<sup>1</sup>The pseudorapidity is defined as  $\eta = -\ln(\tan \frac{\theta}{2})$  with  $\theta$  the polar angle associated to the hadronic final state.

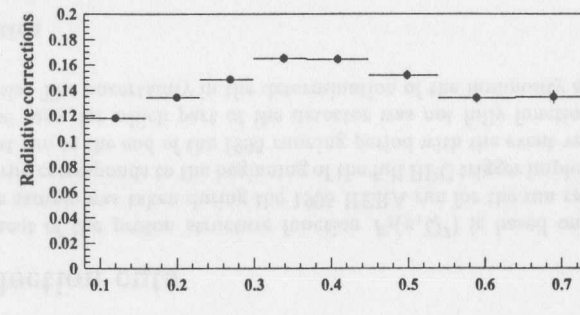


Figure 9.9: Radiative corrections as a function of  $y$ .

$Q^2$  dependence of the fractional elastic  $\rho^0$  contribution has been approximated by a simple straight line fit.

With this reweighting scheme in mind, each MC event used for the extraction of the proton structure function  $F_2$  was assigned a weight factor depending on the type of generated event, i.e. elastic  $\rho^0$ , inelastic high mass diffractive and non-diffractive events [Ti96]. The fraction of non-diffractive events is then determined such that the total weight of all MC event classes is one.

The uncertainty in the determination of the amount of diffractive events has been estimated to be 25% from varying the cut on  $\eta_{MAX}$  and the uncertainty to fit the fraction of events with  $\eta_{MAX} < 1.5$  as a function of  $Q^2$ . This uncertainty has been taken into account in the evaluation of systematic errors (Section 11.5).

The sensitivity of the acceptance, with respect to the two cuts of  $E - P_z$  and  $y_{JB}$  on the simulation of various underlying MC processes, has been estimated by comparing the acceptance as obtained from the MC sample described above to various different MC generators (Section 6.5) [Ti96].

A non-diffractive sample of minimum bias events, as well as resolved and direct di-jet events, was generated using the PYTHIA [Be87a] program. The program EPSOFT [Ka95] was used to generate a non-diffractive sample of minimum bias events. Single and double dissociate diffractive events as well as elastic  $\rho^0$  events were generated using the HERWIG MC generator [Ma92]. These MC samples were compared to the individual processes of the final MC sample. Figure 9.8 displays the fraction of events which pass the cut on the total  $E - P_z$  of the three underlying MC processes used for extraction of the proton structure function  $F_2$  as a function of  $y$ . Elastic  $\rho^0$  events exhibit a significantly smaller acceptance at high  $y$  compared to diffractive and non-diffractive events. At large values of  $y$ , i.e. in the rear direction of the ZEUS detector, the two decaying pions of the  $\rho^0$  are likely to be lost in the rear beam pipe section and therefore fail the cut on the total  $E - P_z$  which yields a drop in the acceptance for elastic  $\rho^0$  events at high  $y$ .

The non-diffractive sample of the final MC sample agrees well with the results obtained from the simulation of non-diffractive events based on PYTHIA. Differences of up to 4% were observed at high  $y$  between the non-diffractive sample generated by the program EPSOFT and the final non-diffractive MC sample.

The acceptance for resolved and direct di-jet events is found to be somewhat larger at high  $y$

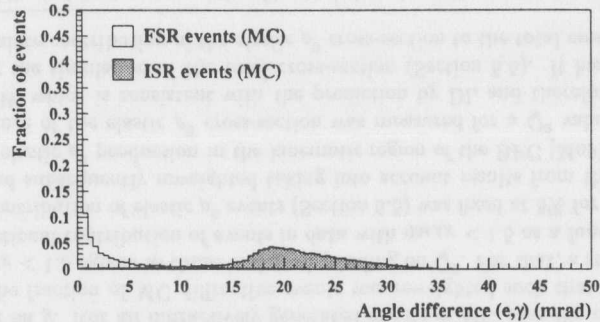


Figure 9.10: Positron and photon scattering angles in FSR and ISR events.

compared to the final non-diffractive MC-sample. This occurs since a  $p_T$  cut at the generator level ensures that the di-jets are not lost in the rear beam pipe section. Differences in the acceptance of up to 10% at high  $y$  were found among the diffractive and elastic  $\rho^0$  MC-samples. The effect on the overall acceptance is limited due to the fact that the diffractive and elastic  $\rho^0$  contribution to the total cross-section is approximately 10–20% and 5%, respectively. From the uncertainty in the acceptance determination due to the different fraction of events accepted by the cut on the total  $E - P_Z$  and the cut on  $y_{JB}$ , an uncertainty of 2% was assigned to the extracted values of  $F_2$  (Section 11.5) for  $y < 0.4$  rising linearly to 5% at  $y = 0.74$ .

## 9.6 Radiative corrections

QED radiative corrections at the lepton vertex lead to a systematic shift of kinematic variables reconstructed among the final state positron compared to those at the hadronic vertex where the proton is being probed (Section 6.4). As will be shown in section 10.2, a cut on the total  $E - P_Z$  of  $E - P_Z > 35$  GeV removes events with an energy of the initial state photon above approximately 10 GeV. This significantly reduces the amount of radiative corrections at large values of  $y$ .

The magnitude of the radiative corrections can be estimated by looking at the fraction of events passing all off-line selection cuts of the BPC  $F_2$  sample, as shown in Figure 9.9, with an initial state radiated photon. The difference in the polar angle between the radiated photon and the positron is shown in Figure 9.10 for initial and final state radiation, respectively. In the case of final state radiation, the radiated photon is included in the measurement of the positron in the BPC and the event can therefore be considered as non-radiative. The amount of radiative corrections are significantly reduced compared to those shown in Figure 6.4 and are approximately 10–15% for the  $y$  range of the BPC integrated over  $Q^2$  (Figure 9.9).

The uncertainty in the amount of radiative corrections, as predicted by the MC program HERACLES [Kw91], has been estimated by comparing the tails in the  $E_{BPC}/E_{calc}$  distributions between Data and MC (Figure 8.37) for elastic  $\rho^0$  events which are due to initial state radiation events. This allows to determine the uncertainty in the radiative corrections for  $0.004 < y < 0.09$  integrated over  $Q^2$ . The agreement is at the level of 25%. This uncertainty has been used in the evaluation of systematic errors on  $F_2$ , assuming an accuracy of 25% of the amount of radiative corrections as shown in Figure 9.9.

# Chapter 10

## The Data sample

### 10.1 Introduction

The measurement of the proton structure function  $F_2(x, Q^2)$  and the total  $\gamma^*p$  cross section  $\sigma_{tot}^{\gamma^*p}$  using the Beam Pipe Calorimeter (BPC) at ZEUS is based on a reconstruction of the kinematic variables employing the Electron method (Section 2.4 and 5.1). This requires to identify the final state positron in  $e^+p$ -collisions and to precisely measure its energy and angle. The on-line and off-line selection cuts for the measurement of the proton structure function  $F_2(x, Q^2)$  are chosen to provide a sample of identified final state positrons in a well-measured kinematic region while reducing background events such as beam gas and photoproduction events.

Throughout the analysis several data samples have been extracted such as for the measurement of the proton structure function  $F_2(x, Q^2)$  itself, for the relative and absolute energy scale calibration (Section 8.5), for a cross-check of the energy scale using elastic  $\rho^0$  events (Section 8.5) and for the alignment of the BPC using elastic QED Compton events (Section 8.3.4). The requirements on the final state positron are essentially common to all four samples, whereas the cuts imposed among the hadronic final state differ due to the different event topology and the requirements on the kinematic region to be accepted. An overview of the precise selection cuts will be given in the next section, where the emphasis will be placed on the extraction of the data sample for the measurement of the proton structure function  $F_2(x, Q^2)$ . Section 10.3 will present the effect of various selection cuts on the energy in the BPC, the total  $E - P_Z$  and the population of rejected events in the  $Q^2 - x$ -plane. Section 10.4 will discuss the understanding and subtraction of beam gas and photoproduction background events.

### 10.2 Selection cuts

The measurement of the proton structure function  $F_2(x, Q^2)$  is based on a data sample of  $1.65 \text{ pb}^{-1}$ . This sample was taken during the 1995 HERA run for the run range 12430 - 14054, where the first run corresponds to the beginning of the full BPC trigger implementation (Section 7.1) and the last run to the end of the 1995 running period with the event vertex at its nominal position. Those runs, for which part of the detector was not fully functioning, are excluded from the analysis. The uncertainty in the determination of the luminosity amounts to 1.5%.

#### On-line selection

The use of the BPC in the 1995 trigger configuration has been discussed in detail in section 7.1. The following on-line requirements have been used for the physics analysis presented in

this thesis:

- BPC  $F_2$  analysis: GFLT SLOT 52 & TLT DIS 17
- BPC kinematic peak events: GFLT SLOT 52 & TLT DIS18
- BPC elastic  $\rho^0$  events: GFLT SLOT 32 & TLT SPP15
- BPC elastic QED Compton events: GFLT SLOT 31 & TLT DIS19

The definition of each trigger slot has been discussed in detail in section 7.1. The energy and timing information provided by the BPC first-level trigger were used in all four cases at the GFLT. In the case of the BPC  $F_2$  analysis (GFLT SLOT 52), an energy cut was made and the timing was required to be consistent with  $e^+p$  collisions (Section 7.1). Scintillation counter arrays located along the beam-line at  $Z = -730, -315,$  and  $-150$  cm respectively, were used to reject proton-gas events.

No additional cuts were required at the Second and Third Level Trigger for the in-situ alignment sample as well as for the selection of kinematical peak events. As for the elastic  $\rho^0$  sample, several criteria are imposed on the track finding at the Second and Third Level Trigger.

In case of the BPC  $F_2$  sample, timing information from the main calorimeter (CAL) was used at the Second Level Trigger to reject non  $e^+p$  events. An approximate value for  $y_{JB}$ , which was determined from the CAL energy assuming the interaction vertex to be at  $Z = 0$ , was required to be greater than 0.02 and the total CAL energy to be greater than 3 GeV. Both cuts at the Second Level trigger are not simulated in the ZEUS trigger simulation. Off-line cuts imposed on  $y_{JB}$  to be greater than 0.06 and the total energy to be greater than 3.1 GeV, ensure the DIS2 slot at the Second Level Trigger to be 100% efficient. No additional cuts were required for the BPC  $F_2$  sample at the Third Level Trigger for the HERA run in 1995.

### Off-line selection

The off-line selection cuts fall into two categories of requirements among the final state positron and the hadronic final state. The following part provides a detailed overview of these two categories. Several cuts have already been justified earlier. For a more detailed description, we refer to the respective section of this thesis.

#### 1. Requirements on the final state positron:

These cuts are used to identify the final state positron within a well-measured fiducial region of the BPC while reducing background events.

##### 1a. BPC timing cut:

It has been shown in section 8.6 that the BPC time,  $t_{BPC}$ , is reconstructed as the energy-weighted time among all BPC readout channels. As shown in Figure 10.1 (b), the mean-reconstructed time for one particular run has considerable variations as a function of the respective run number. This is due to run-to-run variations in the HERA  $e^+p$  bunch crossing time which in turn is due to a shift of the relative phase of the proton and positron radiofrequency at HERA. These variations have been taken into account by using the reconstructed BPC time with the run dependent mean BPC time subtracted. The mean of the BPC time for one particular run is reconstructed from a Gaussian fit, as shown in Figure 10.1 (a), after

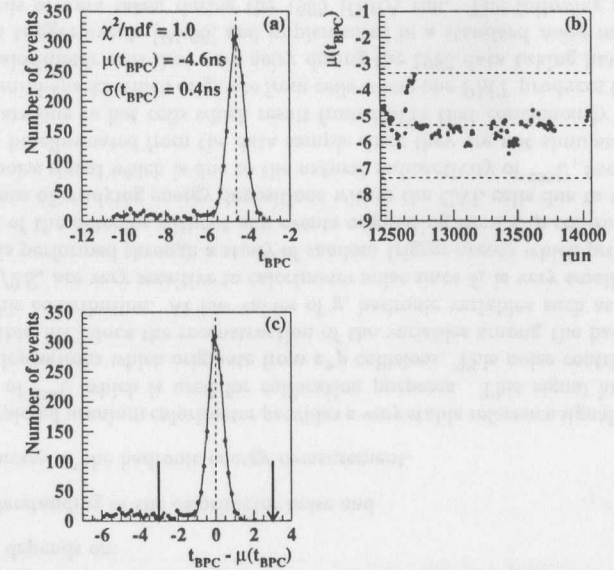


Figure 10.1: BPC timing distribution with an overlaid Gaussian fit (a). Variation of the mean-reconstructed time for one particular run as a function of the respective run number (b). Reconstructed BPC time for one particular run subtracted by the respective mean-reconstructed time (c). The vertical arrows indicate the off-line requirement on the BPC time (Equation 10.1).

applying all other selection cuts. For all data samples the BPC timing is required to be within 3 ns of the time for the  $e^+p$  collision

$$|t_{BPC} - \langle t_{BPC}^{run} \rangle| < 3 \text{ ns} \quad (10.1)$$

as denoted by the vertical arrows in Figure 10.1 (c).

##### 1b. BPC energy cut:

The BPC energy reconstruction has been presented in detail in section 8.5. The trigger efficiency of the cuts imposed at the GFLT slot 52 has been determined in section 9.2. The GFLT timing cut is 100% efficient for energies above 2 GeV measured in the BPC. The energy cut at the GFLT was found to be fully efficient for energies above 7 GeV. The chosen off-line BPC energy cut of

$$E_{BPC} > 7 \text{ GeV}, \quad (10.2)$$

ensures a 100% trigger efficiency. It represents a compromise between keeping the off-line BPC energy cut as low as possible to have access to low values in  $x$  and at the same time reducing the amount of background events which are expected to increase towards small energies of the scattered positron reconstructed in the BPC.

##### 1c. BPC fiducial volume cut:

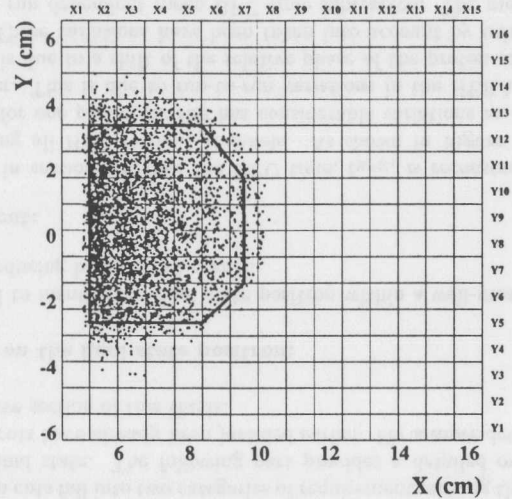


Figure 10.2: BPC fiducial volume cut showing the front face of the BPC North module as seen from the interaction point.

Figure 10.2 shows the BPC reconstructed  $Y$  position as a function of the reconstructed  $X$  position (Section 8.3) where all selection cuts have been applied except for the final fiducial volume cuts. The trapezoidal shaped fiducial volume is denoted by the solid line in Figure 10.2. The upper and lower edges, as well as the right edge of the fiducial volume, are determined by the shape of the beam pipe window whose shape can be inferred from the projection onto the front face of the BPC. The left edge is determined by the requirement to restrict the position bias to stay within 0.05 cm and to limit the amount of transverse energy leakage (Chapter 8). The final fiducial volume cuts are as follows:

$$\begin{aligned} & [((X > 8.37) \wedge (X < 9.97)) \wedge \\ & (Y < ((8.37 + 3.38) - X)) \wedge (Y > ((-8.37 - 2.62) + X))] \vee \\ & [(X > 5.17) \wedge (X < 8.37) \wedge (Y < 3.38) \wedge (Y > -2.62)] \end{aligned} \quad (10.3)$$

The effect of changing the fiducial volume cuts on the physics result will be taken into account in the determination of systematic uncertainties (Section 11.5).

#### 1d. BPC shower width cut:

The reconstruction of the shower width has been discussed in detail in section 8.4.3. The cut on the shower width of

$$\sigma = \sqrt{\frac{\sigma_x^2 + \sigma_y^2}{2}} < 0.7 \text{ cm} \quad (10.4)$$

provides a means of rejecting events of pre-showered positrons or hadrons which have a larger reconstructed shower width compared to well-measured positrons. Particles resulting in a MIP-like energy deposition such as muons and hadrons or pre-showered positrons, which have lost a large fraction of their initial energy before reaching the BPC, are mostly rejected by

the BPC energy cut. As can be seen from Figure 8.24 (c) using a KP sample, the imposed cut on the reconstructed shower width  $\sigma$  is fairly loose in order to attain a high positron identification efficiency. The dominant contribution of final state particles measured in the BPC of photoproduction background events is due to photons which cannot be rejected by the above shower width cut. Relaxing the shower width cut does therefore not lead to an unacceptable increase in the fraction of background events. This has been verified with a sample of generated photoproduction background events and LUMIE-tagged events (Section 10.4.2).

The efficiency of the shower width cut has been studied in detail in section 9.4 which showed that the shower width cut is 100% efficient in both data and MC above 12 GeV. It falls down to 98% at 7 GeV in case of MC. The uncertainty in the choice of the shower width cut and a possible discrepancy in the efficiency of the shower width cut in data and MC below 12 GeV has been taken into account in the evaluation of systematic errors (Section 11.5).

All requirements on the final state positron for the BPC  $F_2$  analysis as well as for the calibration and in-situ alignment samples are summarized in the appendix B.1 to B.4.

#### 2. Requirements on the hadronic final state:

The measurement of the proton structure  $F_2$  using the BPC is intended to be a purely inclusive measurement which follows from an identification of the final state positron by measuring its energy and angle to reconstruct the event kinematics. However, it is not possible to rely only on requirements on the final state positron. The purpose of cuts on the hadronic final state for the BPC  $F_2$  analysis is to reject background events, to reduce QED radiative corrections and to control event migrations at low  $y$  due to the poor  $y_e$  resolution (Electron method). The influence of these cuts on the acceptance has been discussed in section 9.5. Furthermore, one relies on the hadronic final state for the identification of an exclusive  $\rho^0$  sample and for the isolation of a KP sample. The reconstruction of various hadronic quantities to be discussed in the following depends on:

- the understanding of the calorimeter noise and
- the accuracy of the hadronic energy measurement.

The ZEUS depleted uranium calorimeter provides a very stable reference signal from the natural radioactivity of  $^{238}\text{U}$  which is used for calibration purposes. This signal has to be isolated from energy depositions which originate from  $e^+p$  collisions. This noise contribution has to be simulated within MC since the reconstruction of the variables among the hadronic final state suffer from this contribution. At low values of  $y$ , hadronic variables such as  $\delta_h = (E - P_z)_h$  and  $y_{JB} = \delta_h/2E_e$  are very sensitive to calorimeter noise since  $\delta_h$  is very small. The CAL noise contribution is performed through a study of random trigger events which provide information on the status of the detector without any events originating from  $e^+p$  collisions and therefore provide a means of studying energy depositions within the CAL cells due to noise.

Besides this noise signal which is due to the natural radioactivity of  $^{238}\text{U}$ , two other sources of noise have to be eliminated from the data sample since they are not simulated in MC. These noise signals are due to hot cells which result from PMTs that continuously produce a signal and so called mini-sparks which originate from cells where one PMT produces frequently a large signal. The calorimeter cells that were noisy during the 1995 data taking have been identified using random trigger events [Wa96] and implemented in a standard noise routine to be used for the analysis of data taken during the 1995 HERA run. The following requirements are implemented to remove the mentioned sources of noise:

- standard noise suppression cuts:  $< 80$  MeV (EMC),  $< 120$  MeV (HAC) for isolated cells
- relative imbalance  $> 0.7$  for isolated cells with an energy of  $< 0.7$  GeV
- explicit removal of noisy cells in data

The hadronic energy measurement of the main calorimeter has a significant impact on the reconstruction of kinematic variables among the hadronic final state. Its accuracy has been studied in detail in [Vr96].

The influence of the noise suppression cuts and the uncertainty in the hadronic energy measurement on the physics result has been taken into account in the evaluation of systematic errors (Section 11.5).

### 2a. Cut on $y_{JB}$ using the CAL:

The reconstruction of the kinematic variable  $y$  using the Jacquet-Blondel method has been discussed in detail in section 2.4:

$$y_{JB} = \frac{(E - P_Z)_h}{2E_e} = \frac{\delta_h}{2E_e} \quad (10.5)$$

$y_{JB}$  provides at low  $y$  a much more accurate determination of the kinematical variable  $y$  than the estimate of  $y$  using the Electron method. The chosen cut of  $y_{JB} > 0.06$  for the BPC  $F_2$  analysis represents a compromise between controlling event migration at low  $y$  and not cutting into the  $y_e$  distribution of the lowest  $y_e$  bins. The impact of changing the cut on  $y_{JB}$  on the physics result has been taken into account in the evaluation of systematic errors.

As discussed in detail in section 8.5.3, a cut of  $y_{JB} < 0.04$  is used for the relative as well as for the absolute energy scale calibration. The influence on changing the  $y_{JB}$  cut on the determination of the absolute energy scale has been used to estimate the systematic uncertainties of the absolute energy scale calibration.

### 2b. Cut on the total energy $E_{TOT}$ using the CAL:

A cut on the total energy  $E_{TOT}$  has been performed at the Second Level Trigger (Section 7.1) and is being replaced off-line by a cut on  $E_{TOT}$ :

$$E_{TOT} > 3.1 \text{ GeV} \quad (10.6)$$

A cut of  $y_{JB} > 0.06$  implies that  $(E - P_Z) > 3.3$  GeV. The  $y_{JB}$  cut already removes a significant fraction of events with  $E_{TOT} \leq 3.1$  GeV in particular events for which the hadronic final state is reconstructed in the forward direction. The cut of  $y_{JB} > 0.06$  implies a minimum total energy,  $E_{TOT}$ , of 1.65 GeV. As will be shown in the next section, the cut on the total energy  $E_{TOT}$  has therefore only a minor effect compared to the preceding cut on  $y_{JB}$  of  $y_{JB} > 0.06$ . It has been verified by using events from the GSLT DIS3 pass-through trigger (Section 7.1) that an off-line cut of  $E_{TOT} > 3.1$  GeV rejects all events which have been discarded by the GSLT cut on  $E_{TOT}$ .

### 2c. Cut on the total $(E - P_Z)$ using the CAL:

The main characteristics of the cut on the total  $(E - P_Z)$  can be seen from the following comparison of  $(E - P_Z)$  in DIS events and  $(E - P_Z)$  in photoproduction events.

$\Rightarrow$  DIS events:

Using four-momentum conservation among the initial and final state in  $e^+p$  scattering one obtains:

$$E = E_e + E_P = E'_e + E_{rem} + \sum_i E_i^h \quad (10.7)$$

$$P_Z \simeq -E_e + E_P = E'_e \cos \theta'_e + E_{rem} + \sum_i E_i^h \cos \theta_i^h \quad (10.8)$$

$E_{rem}$  refers to the energy of the proton remnant which is lost in the forward beamhole since the ZEUS detector is not fully hermetic (Section 4.2).  $(P_Z)_{rem}$  is approximately given by  $E_{rem}$ . The sum extends over all ZEUS calorimeter cells.

Subtracting both equations from each other results in:

$$\delta_{meas}^{DIS} = \sum_i E_i^h (1 - \cos \theta_i^h) + E'_e (1 - \cos \theta'_e) = 2E_e \quad (10.9)$$

Conservation of energy and momentum yields that the total  $(E - P_Z)$  peaks at two times the energy of the positron beam energy. This ignores possible particles losses in the backward beamhole.

For events with a radiated photon in the initial state, a significant fraction of the total  $(E - P_Z)$  can be lost in the backward beam hole by the radiated photon. In this case,  $\delta_{meas}^{DIS}$  decreases by two times the energy of the radiated photon  $E_\gamma^{ISR}$ , i.e.  $\delta_{ISR}^{DIS} = 2(E_e - E_\gamma^{ISR})$ . A cut on  $\delta$  of  $> 35$  GeV is equivalent to a cut on  $E_\gamma < 10$  GeV. This provides a way to reduce the amount of ISR events with a hard photon in the initial state and therefore the amount of radiative corrections as mentioned in section 9.6.

$\Rightarrow$  Photoproduction events:

In this case,  $\cos \theta'_e = -1$ . Equations (10.7) and (10.8) yield:

$$\delta_{meas}^{PHP} = \sum_i E_i^h (1 - \cos \theta_i^h) = 2(E_e - E'_e) = 2E_\gamma^{PHP} \quad (10.10)$$

$E_\gamma^{PHP}$  refers to the energy of the real photon in photoproduction. The photoproduction cross section decreases with increasing values of  $2E_\gamma^{PHP}$ , thus most of the photoproduction background events are removed by imposing a lower cut on  $\delta_{meas}$ . A cut on  $\delta_{meas}$  of

$$35 < \delta_{meas} < 60 \text{ GeV} \quad (10.11)$$

is used to reject various types of background events such as:

- Photoproduction events, which are characterized by small values in the  $\delta_{meas}$  distribution. The remaining photoproduction background will be subtracted statistically (Section 10.4.2).
- Initial state radiation events, with a hard radiated photon in the initial state above 10 GeV which is lost in the backward beamhole, are removed which considerably reduces the amount of radiative corrections in particular at high  $y$ .
- Proton beam gas events with the event vertex inside the main detector which lead to energy depositions in the forward direction are characterized by relatively small values in  $\delta_{meas}$ .

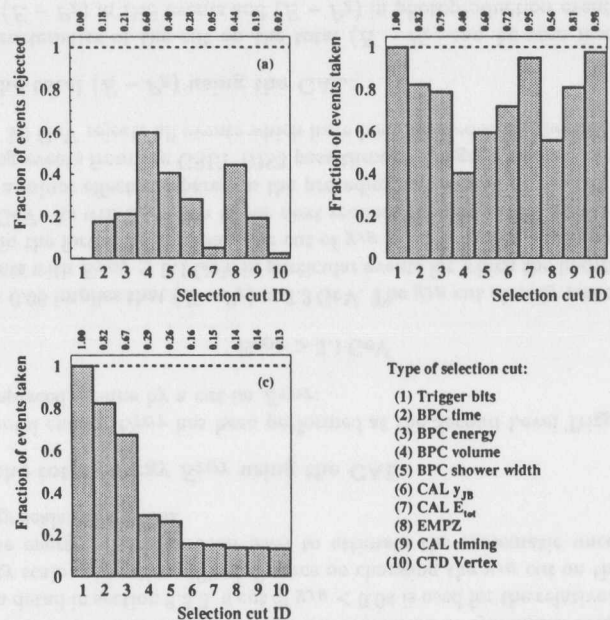


Figure 10.3: Fraction of rejected (a) and taken (b) events. Fraction of remaining events after the different stages of the selection cuts (c).

- Proton beam gas events upstream of the main detector, which could lead to considerable energy depositions in the RCAL and BPC above 60 GeV for  $\delta_{meas}$ . This cut provides another way to reject this type of background events besides timing requirements.
- Pre-showered positrons, which have lost energy in dead-material on the way to the BPC and which have passed the requirements on the BPC fiducial volume and the BPC shower width cut. This type of event is characterized by small values in  $\delta_{meas}$ .

#### 2d. Cut on the CAL timing information:

Timing requirements among the main calorimeter are used to reject additional background events such as positron/proton beam gas events which would yield a proper timing for the BPC but not for the main calorimeter.

#### 2e. Cut on the reconstructed $Z$ vertex using the CTD:

A cut on the  $Z$  vertex distribution (Section 9.3) provides another means to reject non  $e^+p$  background events such as positron and/or proton beam gas events which are characterized by a uniform  $Z$  vertex distribution contrary to the case of  $e^+p$  events with a Gaussian shaped

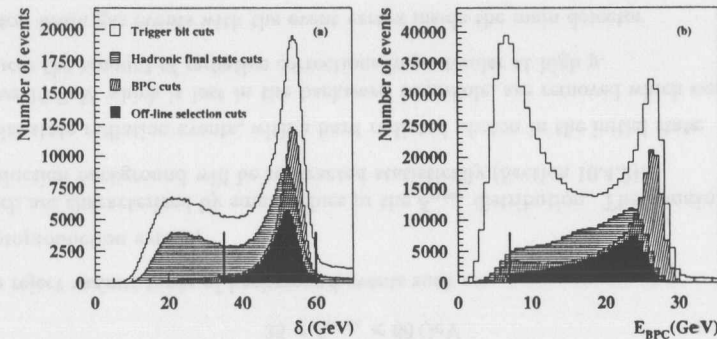


Figure 10.4: Effect of selection cuts on the  $\delta$  (a) and  $E_{BPC}$  (b) distributions.

$Z$  vertex distribution centered around the nominal interaction vertex. If the event vertex is well reconstructed within the CTD by requiring two reconstructed tracks, the  $Z$  position of the event vertex is required to be within

$$-40 \text{ cm} < Z_{VTX} < 100 \text{ cm} \quad (10.12)$$

Including the satellite peak in the  $Z$  vertex distribution minimizes the error on the total luminosity since the luminosity is measured over all  $Z$ -vertex positions, i.e. including events from  $e^+p$  collisions among the proton satellite bunch. The cuts on the  $Z$  vertex distribution have been varied to investigate the effect on the physics result (Section 11.5).

A summary of all selection cuts on the hadronic final state used for various data samples throughout the analysis can be found in the appendix B1-B4. For the following sections, off-line selection cuts are meant to be those for the BPC  $F_2$  analysis unless stated otherwise.

## 10.3 Effect of selection cuts

Figure 10.3 presents the fraction of events which have been rejected (a) and which have passed (b) the individual selection cuts, respectively among the final state positron and the hadronic final state. The fraction of remaining events after the different stages of the selection cuts are displayed in Figure 10.3 (c). The number of events in each bin in Figure 10.3 has been normalized with respect to the number of events passing the trigger bit selection for the BPC  $F_2$  analysis, i.e. GFLT SLOT 52 & TLT DIS 17.

After applying all off-line selection cuts 102803 events remain in the final sample prior to the background subtraction of photoproduction and positron/proton beam gas background events. The effect of the selection cuts on the final state positron and the hadronic final state on the  $\delta$  distribution (a) and the BPC energy spectrum (b) is shown in Figure 10.4.

Figure 10.5 shows the  $Q^2 - x$  distribution of events which have been rejected by a particular selection cut. The BPC energy cut (Figure 10.5 (a)) removes events at very high values of  $y$  as expected from Figure 2.6. Events rejected by the fiducial volume cut (Figure 10.5 (b)) populate mainly the region of very low values in  $Q^2$ . The shower width cut (Figure 10.5 (c)) removes predominately events at high values of  $y$ . The effect of the  $\delta$  cut is displayed in Figure 10.5

(d) which shows that this cut removes events at very large values of  $y$  which correspond to a significant fraction to photoproduction background events.

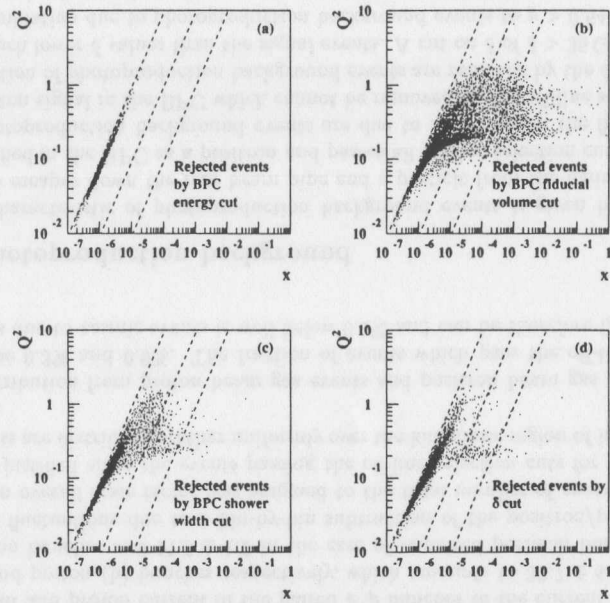


Figure 10.5: Population of events rejected by various off-line selection cuts: BPC energy cut (a), BPC fiducial volume cut (b), BPC shower width cut (c) and  $\delta$  cut (d).

## 10.4 Background subtraction

After applying all off-line selection cuts, the main sources of remaining background events are due to photoproduction and non- $e^+p$  background events. These types of background events have to be subtracted statistically.

A search has been performed for events with a positron candidate of higher  $Q^2$  found in the main calorimeter passing all off-line selection cuts which could be due to particles from the hadronic final state faking a positron signal in the BPC, elastic QED Compton events with one of the electromagnetic objects found in the BPC and the other one found in the main calorimeter or due to ISR/FSR events. This type of background has been estimated to be below 0.1%. Based on a MC study, none of these events are associated with a hadronic object measured in the BPC (Section 9.4). Elastic QED Compton events with the electromagnetic objects measured in both BPC modules are rejected by the cut on the total energy in the main calorimeter of  $E_{TOT} > 3.1 \text{ GeV}$ .

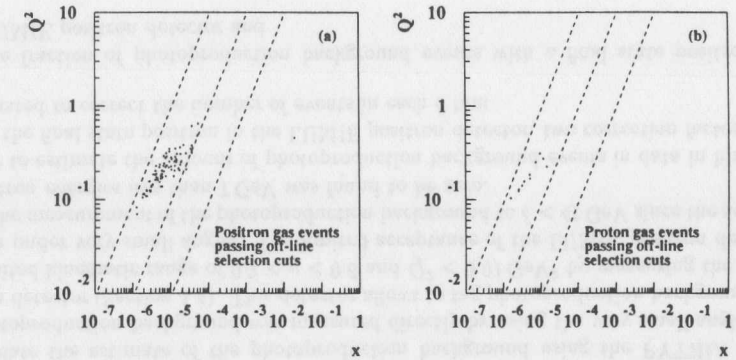


Figure 10.6: Positron and proton gas events passing off-line selection cuts.

### 10.4.1 Non- $e^+p$ background

The principle sources of non- $e^+p$  background events are due to:

- Positron/proton interactions with the residual beam gas and the beam pipe wall:  
Proton beam gas interactions occurring upstream are removed by timing requirements for events which deposit energy in the RCAL only. These cuts cannot be used to remove proton beam gas interactions which deposit energy in the FCAL since the debris reach the FCAL in time with the proton beam. Positron beam gas interactions can be removed for those events which deposit energy in the FCAL. They cannot be removed if no energy is deposited in the FCAL but only in the RCAL since the interaction products reach the RCAL in time with the positron beam.
- Synchrotron radiation:  
As discussed in section 5.6, this type of non- $e^+p$  background is completely negligible since the energy of synchrotron radiation photons peaks at very small energies (keV-range) which will therefore be absorbed in the first tungsten layers and will fail the BPC energy cut of 7 GeV.
- Off-momentum positrons:  
These type of non- $e^+p$  background events occur due to positrons which have lost part of their energy due to bremsstrahlung which are then being bent by the HERA interaction lattice into the BPC and occur in time with the positron beam and are therefore able to pass the off-line selection cuts.

All beam related non- $e^+p$  background events can be estimated by using unpaired proton and positron bunches<sup>1</sup>. 6 proton-pilot and 15 positron-pilot bunches were used for the HERA run in 1995 (Section 3.2). These types of bunches are distinguished from the colliding bunches by their respective bunch crossing number.

<sup>1</sup>The determination of proton beam induced non- $e^+p$  background events using proton-pilot bunches allows only a very rough estimate for the case of  $e^+p$  bunches, since the phase space of the proton beam for proton-pilot bunches is different from those of  $e^+p$  bunches.

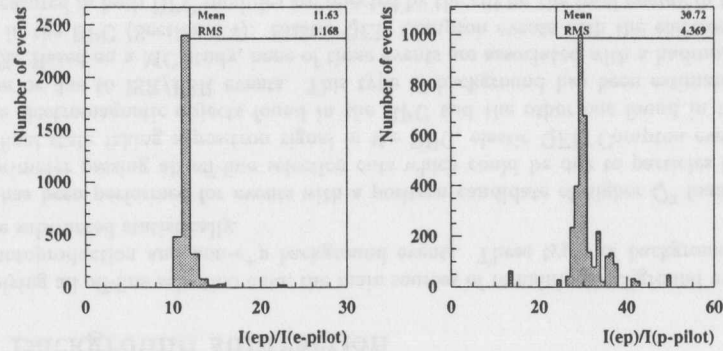


Figure 10.7: Luminosity weighted current ratios for positron-pilot and proton-pilot bunches.

Figure 10.6 shows the  $Q^2 - x$  distribution of events passing the off-line selection cuts for positron (a) and proton (b) beam gas events. Each event passing the off-line selection cuts is assigned a luminosity weighted ratio of the current in  $e^+p$  bunches to the current of positron-pilot and proton-pilot bunches, respectively. Figure 10.7 shows the ratio of the luminosity weighted positron current and proton current in the paired  $e^+p$  bunches to the current in the unpaired positron (a) and proton (b) bunches respectively, which amounts to  $30.7 \pm 4.4$  in the case of unpaired proton bunches and  $11.6 \pm 1.2$  in the case of unpaired positron bunches. To avoid any statistical fluctuations due to a bin-by-bin subtraction of the positron/proton beam gas background, an overall scale factor was assigned to the total number of events in data. This assumption is justified since the events passing the off-line selection cuts for positron/proton beam gas events are distributed rather uniformly over the kinematic region of interest as shown in Figure 10.6.

The total contribution from proton beam gas events and positron beam gas events has been estimated to be 0.3% and 0.9%. The fraction of events which pass the off-line selection for empty bunches due to cosmic events is well below 0.1% and can be therefore ignored.

#### 10.4.2 Photoproduction background

The general characteristic of photoproduction background events is given by the scattered positron which escapes down the rear beam pipe and a particle from the hadronic final state, which is identified in the BPC as a positron and passes all off-line selection cuts. A significant fraction of photoproduction background events are due to  $\pi^0$  decays in the final state which result in a photon signal in the BPC which cannot be removed by the off-line selection cuts. A significant fraction of photoproduction background events are removed by the  $\delta$  cut since those events have much lower  $\delta$  values than the signal events. A cut on  $\delta$  of  $\delta > 35$  GeV restricts the possible contamination due to photoproduction background events to  $y > 0.64$ .

Photoproduction background events were generated using the PYTHIA program [Be87a] (Section 6.5) using an ALLM cross section parameterization [Ab90]. A sample of 60000 events were generated with a  $y$  cut of  $y > 0.5$  which corresponds to a total cross section of  $1.5 \mu\text{b}$ . Taking into account a fiducial volume cut at the generator level, this yields a cross section of  $101 \text{ nb}$  which gives rise to a luminosity of  $592 \text{ nb}^{-1}$  which is approximately one third of the

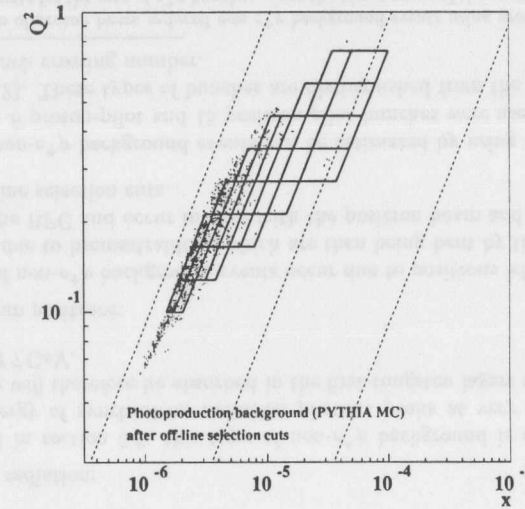


Figure 10.8:  $Q^2 - x$  distribution of photoproduction background events (PYTHIA MC) after off-line selection cuts.

integrated luminosity used for the BPC  $F_2$  analysis ( $\mathcal{L}_{DATA} = 1.65 \text{ pb}^{-1}$ ). Each event from the photoproduction MC sample which passed the off-line selection cuts was assigned a weight as the ratio of the luminosity of the photoproduction MC sample to the integrated luminosity in data:

$$w = \frac{(N_{PYTHIA}/\sigma_{PYTHIA})}{\mathcal{L}_{DATA}} = \frac{\mathcal{L}_{PYTHIA}}{\mathcal{L}_{DATA}} = 2.83 \quad (10.13)$$

This weight factor was then used to perform a bin-by-bin subtraction of the photoproduction background for MC events being subtracted in a particular bin (Section 11.2).

Figure 10.8 shows in the  $Q^2 - x$  plane all events from the photoproduction MC sample which passed the off-line selection cuts. The fractional contribution of the photoproduction estimate amounts to at most 10% for the highest  $y$  bins. It can be completely ignored for  $y < 0.4$

To validate the estimate of the photoproduction background using the PYTHIA program, the photoproduction background was measured directly by using the very small angle LUMIE positron detector (Section 4.4). This detector allows to tag photoproduction background events in a limited kinematic range of  $0.2 < y < 0.6$  and  $Q^2 < 0.01 \text{ GeV}^2$  by measuring the scattered positron under very small angles. The limited acceptance of the LUMIE positron detector restricts the measurement of the photoproduction background to  $\delta < 41 \text{ GeV}$  since the acceptance for positron energies less than  $7 \text{ GeV}$  was found to be zero.

In order to estimate the amount of photoproduction background events in data in bins of  $\delta$  by tagging the final state positron in the LUMIE positron detector, two correction factors have to be evaluated to correct the number of events in each  $\delta$  bin:

- the fraction of photoproduction background events with a final state positron in the LUMIE positron detector and
- the acceptance of the LUMIE positron detector.

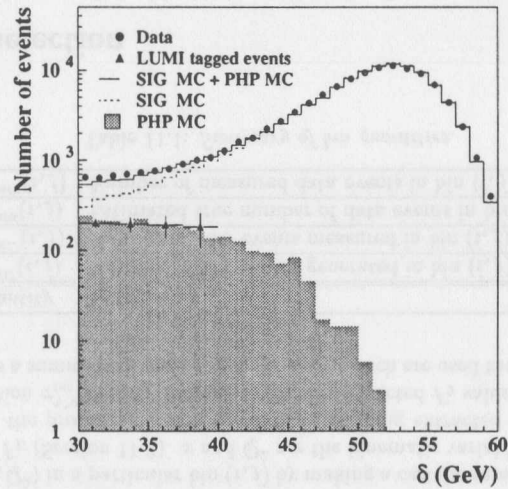


Figure 10.9:  $\delta$  distribution for data (solid circles), signal simulation (dashed line), photoproduction simulation (shaded region) and the sum of the signal and photoproduction simulations (solid line). The measured background from LUMIE-tagged events is shown as the triangular points.

These factors have been estimated from a photoproduction MC sample. Bremsstrahlung overlay events are rejected by requiring that  $\delta + 2E_{\text{LUMIE}}$  to be less than 65 GeV since those events for a BPC signal event have typically much larger values for  $\delta + 2E_{\text{LUMIE}}$ .

Figure 10.9 shows the  $\delta$  distribution for data (solid circles), signal simulation (dashed line), photoproduction simulation (shaded region) and the sum of the signal and photoproduction simulations (solid line). The latter sum and the  $\delta$  distribution for data are in good agreement. The measured background from LUMIE-tagged events is shown as the triangular points. The simulated photoproduction background and the measured LUMIE-tagged events are in good agreement. The uncertainty on the determination of the photoproduction background has been estimated to be 30% which will be used in section 11.5 for the determination of systematic errors.

## Chapter 11

### Extraction of $F_2$ and $\sigma_{tot}^{\gamma^*p}$

#### 11.1 Introduction

The following chapter is devoted to provide a detailed discussion of the extraction of the proton structure function  $F_2(x, Q^2)$  and the total  $\gamma^*p$  cross-section  $\sigma_{tot}^{\gamma^*p}$  at low  $Q^2$  and very low  $x$ .  $F_2(x, Q^2)$  and  $\sigma_{tot}^{\gamma^*p}$  were extracted for  $0.11 \leq Q^2 \leq 0.65 \text{ GeV}^2$  and  $1.7 \cdot 10^{-6} \leq x \leq 6.0 \cdot 10^{-5}$  using the ZEUS detector with the Beam Pipe Calorimeter (BPC) (Chapter 5). This analysis is based on  $1.65 \text{ pb}^{-1}$  of data which were taken during the 1995 HERA run.

The proton structure function  $F_2(x, Q^2)$  is extracted by subdividing the kinematic plane into  $y$ - $Q^2$  bins (Section 2.2.2). The following section will discuss in detail the resolution of kinematic variables and the impact on the binning of kinematic variables. Section 11.3 will present the determination of the proton structure function  $F_2$  and the total  $\gamma^*p$  cross-section  $\sigma_{tot}^{\gamma^*p}$ . This includes a discussion on the treatment of the longitudinal structure function  $F_L$  (Section 2.2.2), a description of the unfolding procedure used to obtain an estimation of the true distribution of kinematic variables from the corresponding measured distributions along with a comparison of various distributions between data and MC in section 11.4. The evaluation of systematic uncertainties will be discussed in detail in section 11.5. The final results on the proton structure function  $F_2(x, Q^2)$  and the total  $\gamma^*p$  cross-section  $\sigma_{tot}^{\gamma^*p}$  are presented in section 11.6.

The reconstruction of kinematic variables was performed using the energy and angle of the scattered positron, i.e. the Electron method (Section 2.4). The energy and impact position are measured with the BPC (Chapter 8) and the event vertex position with the CTD (Section 4.3). Various efficiencies and systematic effects such as the BPC trigger efficiency, the determination of the event vertex using the CTD, the BPC positron identification, the dependence of the acceptance on the underlying physics process due to various requirements among the hadronic final state and the understanding of radiative corrections have been presented in chapter 9. On-line and off-line selection cuts to extract a clean sample of well-measured positrons in the BPC were outlined in the preceding chapter together with a discussion of remaining background events after applying all final selection cuts.

The proton structure function  $F_2(x, Q^2)$  is obtained from the double differential cross-section ( $d^2\sigma/dy dQ^2$ ) integrated over a certain region in the kinematic plane, known as a bin. The double differential cross-section for inclusive neutral current  $e^+p$  scattering which includes radiative corrections is given as follows (Section 2.2.2):

$$\left( \frac{d^2\sigma}{dy dQ^2} \right) = \frac{2\pi\alpha^2 Y_+}{yQ^4} \left( F_2 - \frac{y^2}{Y_+} F_L \right) \cdot [1 + \delta_r(y, Q^2)] \quad (11.1)$$

where  $\delta_r(y, Q^2)$  is the electroweak radiative correction factor (Section 6.4). This cross-section,

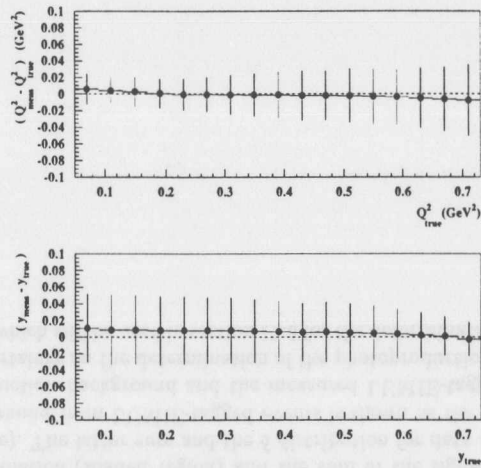


Figure 11.1: Resolution and bias for the kinematic variables  $y$  and  $Q^2$  as a function of the respective true variables from MC events. The term ‘true’ denotes the true variables at the hadronic vertex. ‘meas’ refers to the respective measured variables.

integrated over the bin  $(i, j)$ , is determined from the estimated true event distribution  $N^{data}(i, j)$  and the luminosity  $\mathcal{L}^{data}$ :

$$\int \int_{bin(i,j)} \left( \frac{d^2\sigma}{dydQ^2} \right) dydQ^2 = \frac{N^{data}(i,j)}{\mathcal{L}^{data}} \quad (11.2)$$

The indices  $i$  and  $j$  denote a particular  $y-Q^2$  bin. This then allows to extract the proton structure function  $F_2(x, Q^2)$  in a particular bin  $(i, j)$  by making a certain ansatz for the longitudinal structure function  $F_L$  (Section 11.3).  $x$  and  $Q^2$  are the kinematic variables for a particular bin  $(i, j)$  at which the the proton structure function  $F_2$  is being extracted (Section 11.3.1). The total  $\gamma^*p$  cross-section  $\sigma_{tot}^{\gamma^*p}$  is then obtained from the extracted  $F_2$  values using equation 2.37. Table 11.1 provides a summary of various bin variables which are used throughout the following discussion.

Quantity	Definition
$N^{MC}(i, j)$	Number of MC events generated in bin $(i, j)$
$M^{MC}(i, j)$	Number of MC events measured in bin $(i, j)$
$N^{data}(i, j)$	Estimated true number of data events in bin $(i, j)$
$M^{data}(i, j)$	Number of measured data events in bin $(i, j)$

Table 11.1: Summary of bin quantities.

## 11.2 Bin selection

The choice of the binning of the kinematic variables for the extraction of the proton structure function  $F_2$  represents a compromise between various requirements and experimental con-

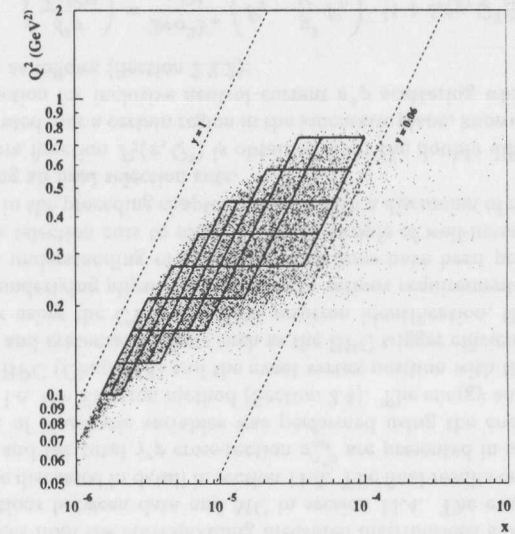


Figure 11.2: Selected  $y-Q^2$  bins in the  $x-Q^2$  plane. A sub-sample of reconstructed events is overlaid.

straints.

The examination of the behavior of the proton structure function  $F_2$  in the transition region between deep-inelastic scattering (DIS) and photoproduction (Section 2.3.5 and 5.3) makes a measurement of the proton structure function  $F_2$  over as many bins as possible in the kinematic plane at low  $Q^2$  desirable. However, the size of each bin should be large enough to limit statistical fluctuations as well as correlations and systematic effects between bins due to the finite resolution of the kinematic variables. The geometric acceptance of the BPC together with various selection cuts such as the  $y_{JB}$  cut of  $y_{JB} > 0.06$ , the BPC energy cut of  $E_{BPC} > 7$  GeV and the fiducial volume cut restrict the accessible kinematic region and therefore the region over which the proton structure function  $F_2$  can be extracted.

Figure 11.1 shows the systematic shift and resolution of  $y$  and  $Q^2$  as a function of the respective true kinematic variable using the MC sample which was discussed in detail in section 6.5. The size of the error bars denotes the RMS resolution. The size of the systematic shift is typically smaller than the resolution for a particular bin and is mainly due to events with a photon radiated in the initial state (Section 9.6).

Figure 11.2 represents the chosen  $y-Q^2$  bins in the  $Q^2-x$  kinematic plane including an overlaid sub-sample of reconstructed events passing all final selection cuts (Section 10.2). The analysis has been performed using  $y-Q^2$  bins, which make efficient use of the available phase space taking into account the cut on  $y_{JB}$  as well as the lower electron energy cut which corresponds to an upper  $y$  cut.

Figures 11.3 and 11.4 show for each bin the fractional resolution function in  $Q^2$  and  $y$ , respectively.

The migration in the  $Q^2-x$  plane is shown in Figure 11.5 for the chosen  $y-Q^2$  bins. The base of the arrow is at the average generated  $y$  and  $Q^2$  for a particular bin, whereas the head of each

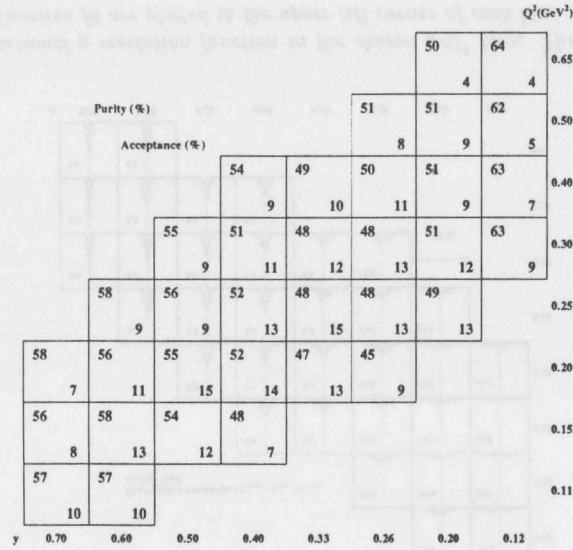


Figure 11.6: Selected  $y$ - $Q^2$  bins. The respective bin quality factors purity and acceptance are shown for each bin.

$$a(i, j) = \frac{N_{acc}^{MC}(i, j)}{N^{MC}(i, j)} \quad (11.6)$$

where  $M_{in}^{MC}(i, j)$  denotes the number of events generated and reconstructed in a bin  $(i, j)$  with respect to the measured kinematic variables.  $N_{acc}^{MC}(i, j)$  is the generated number of events with respect to the true kinematic variables passing all final selection cuts.

The bin quality factors have been determined using the MC sample as discussed in detail in section 6.5. This places stringent requirements on the accuracy of the MC simulation (Section 11.4). The acceptance factors quantify the effect of the limited BPC detector acceptance and the final selection cuts with respect to the total number of generated events  $N^{MC}(i, j)$  in a bin  $(i, j)$ . The purity  $p(i, j)$  measures the amount of event migration from surrounding bins. Bins have been selected whose purity is above 45%. The acceptance in each bin  $(i, j)$  is required to be above 4%. All selected bins are shown in Figure 11.6 along with their respective purity and acceptance values. The purity values are typically 50%. The acceptance varies between 4% and 15%. The latter corresponds to the maximum geometric acceptance. As expected, a maximum acceptance is achieved for the central bins whereas the edge bins have a significant lower acceptance due to the limited azimuthal angle acceptance of the BPC.

## 11.3 Determination of $F_2$ and $\sigma_{tot}^{\gamma^*p}$

### 11.3.1 Introduction

The proton structure function  $F_2$  has been introduced in the description of the  $e^+p \rightarrow e^+X$  double-differential cross-section ( $d^2\sigma/dy dQ^2$ ). ( $d^2\sigma/dy dQ^2$ ) can be formulated in terms of the

structure functions  $F_2$  and  $F_L$  or equivalently in terms of the total transversal and longitudinal cross-sections  $\sigma_T$  and  $\sigma_L$  (Section 2.2.2):

$$\left(\frac{d^2\sigma}{dy dQ^2}\right) = \frac{2\pi\alpha^2 Y_+}{yQ^4} (F_2 - \frac{y^2}{Y_+} F_L) \cdot [1 + \delta_r] = \frac{2\pi\alpha^2 Y_+}{yQ^4} (F_2)_{eff} \cdot [1 + \delta_r] \quad (11.7)$$

$$= \Gamma \cdot (\sigma_T + \epsilon\sigma_L) \cdot [1 + \delta_r] = \Gamma \cdot (\sigma_{tot}^{\gamma^*p})_{eff} \cdot [1 + \delta_r] \quad (11.8)$$

where  $Y_+ = 1 + (1-y)^2$ , the flux factor  $\Gamma = \alpha(1 + (1-y)^2)/(2\pi Q^2 y)$  and the photon polarization  $\epsilon = 2(1-y)/(1 + (1-y)^2)$ .

The double-differential cross-section ( $d^2\sigma/dy dQ^2$ ) is determined over a bin of size  $(\Delta y, \Delta Q^2)$  from the estimated true event distribution  $N^{data}(i, j)$  and the luminosity  $\mathcal{L}^{data}$  in the kinematic plane as discussed in the preceding sections:

$$\sigma_{\square}(i, j) = \iint_{bin(i, j)} \left(\frac{d^2\sigma}{dy dQ^2}\right) dy dQ^2 = \frac{N^{data}(i, j)}{\mathcal{L}^{data}} \quad (11.9)$$

Using an iterative procedure to reweight the MC input structure function to ensure that the  $y$  and  $Q^2$  dependence in MC match those in data (Section 11.3.3), the effective proton structure function  $(F_2)_{eff}$  or equivalently the effective cross-section  $(\sigma_{tot}^{\gamma^*p})_{eff}$  in data and MC can be related to the respective event distributions:

$$\frac{\int \int_{bin(i, j)} \left(\frac{d^2\sigma}{dy dQ^2}\right)^{data} dy dQ^2}{\int \int_{bin(i, j)} \left(\frac{d^2\sigma}{dy dQ^2}\right)^{MC} dy dQ^2} = \frac{N^{data}(i, j)/\mathcal{L}^{data}}{N^{MC}(i, j)/\mathcal{L}^{MC}} = \quad (11.10)$$

$$= \frac{(F_2)_{eff}^{data}(y, Q^2) \left[\frac{2\pi\alpha^2 Y_+}{yQ^4}\right] [1 + \delta_r^{data}(y, Q^2)]}{(F_2)_{eff}^{MC}(y, Q^2) \left[\frac{2\pi\alpha^2 Y_+}{yQ^4}\right] [1 + \delta_r^{MC}(y, Q^2)]} \quad (11.11)$$

$$= \frac{(\sigma_{tot}^{\gamma^*p})_{eff}^{data}(y, Q^2) \Gamma [1 + \delta_r^{data}(y, Q^2)]}{(\sigma_{tot}^{\gamma^*p})_{eff}^{MC}(y, Q^2) \Gamma [1 + \delta_r^{MC}(y, Q^2)]} \quad (11.12)$$

Assuming that the MC simulation provides a correct description of the radiative corrections in data (Section 9.6), the last equation can be simplified to obtain  $(F_2)_{eff}^{data}(y, Q^2) [(\sigma_{tot}^{\gamma^*p})_{eff}^{data}]$  as follows:

$$(F_2)_{eff}^{data} [(\sigma_{tot}^{\gamma^*p})_{eff}^{data}] (y, Q^2) = \frac{N^{data}(i, j)/\mathcal{L}^{data}}{N^{MC}(i, j)/\mathcal{L}^{MC}} (F_2)_{eff}^{MC} [(\sigma_{tot}^{\gamma^*p})_{eff}^{MC}] (y, Q^2) \quad (11.13)$$

where  $y$  and  $Q^2$  are the kinematic variables for each bin  $(i, j)$  at which  $(F_2)_{eff}^{data}(y, Q^2) [(\sigma_{tot}^{\gamma^*p})_{eff}^{data}]$  is being determined which are chosen to be the centers of gravity (COG) of the true MC  $Q^2$  and  $y$  distributions for a particular  $y - Q^2$  bin.

In order to obtain the proton structure function  $F_2$  from the extracted values of  $(F_2)_{eff} = F_2 - (y^2/Y_+)F_L$ , the contribution of the longitudinal structure function  $F_L$  has to be separated. The proton structure function  $F_2$  is obtained as follows:

$$F_2^{data} = (F_2)_{eff}^{data} [1 + \delta_L^{data}(y, Q^2)] \quad (11.14)$$

where  $\delta_L = \sigma_{L}^{E_L=0}(i, j)/\sigma_{L}^{E_L \neq 0}(i, j) - 1$ . The factor  $\delta_L^{MC}(y, Q^2)$  is zero, since the contribution from  $F_L$  has not been included in the generation of the used MC sample (Section 6.5). In

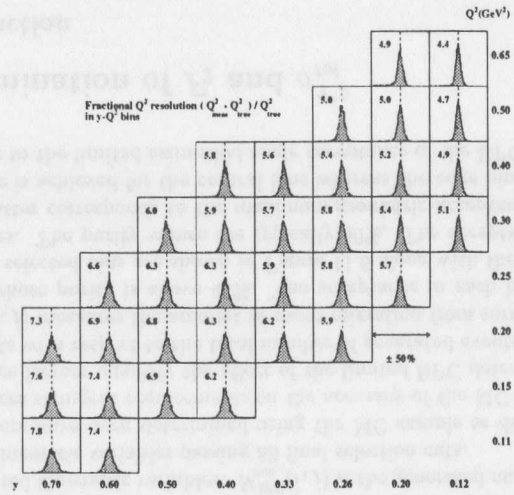


Figure 11.3: Fractional  $Q^2$  resolution function in the chosen  $y$ - $Q^2$  bins. The resolution values (in %) from a Gaussian fit are plotted in the upper left corner of each bin.

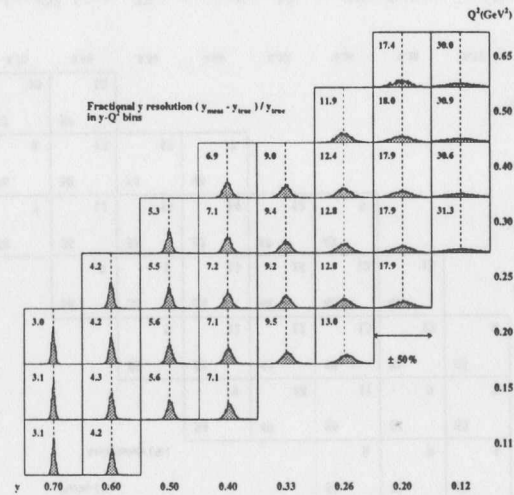


Figure 11.4: Fractional  $y$  resolution function in the chosen  $y$ - $Q^2$  bins. The resolution values (in %) from a Gaussian fit are plotted in the upper left corner of each bin.

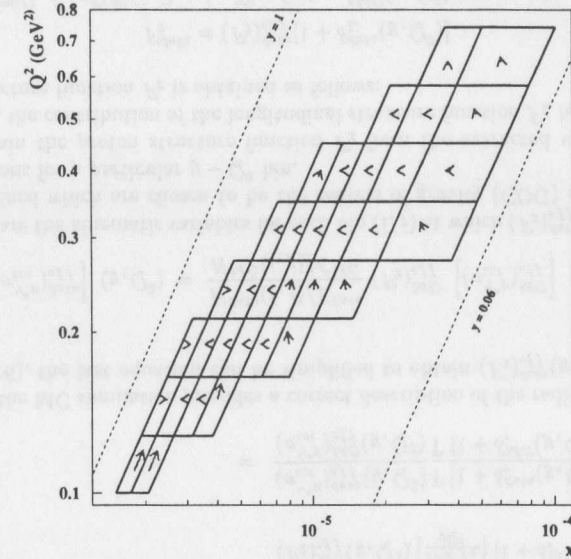


Figure 11.5: Migration of the kinematic variables  $y$  and  $Q^2$  in the  $x$ - $Q^2$  plane (See text for further details).

arrow denotes the average reconstructed  $y$  and  $Q^2$ . Only events which pass all final selection cuts (Section 10.2) were included.

The bin width  $\Delta y$  and  $\Delta Q^2$  of each bin were chosen to be larger than the corresponding resolutions  $\sigma_y$  and  $\sigma_{Q^2}$  in each bin, i.e.:

$$\Delta y > \sigma_y \quad (11.3)$$

$$\Delta Q^2 > \sigma_{Q^2} \quad (11.4)$$

The lowest bin boundary in  $Q^2$  is chosen to be at  $0.1 \text{ GeV}^2$ . The lowest  $Q^2$  bin has a width of approximately  $2.5\sigma_{Q^2}$ . A constant bin width in  $\ln Q^2$  was chosen for higher  $Q^2$  bins to accommodate the rapidly falling event statistics due to the  $1/Q^4$  dependence of the double-differential cross-section. The chosen  $Q^2$  bin sizes yield an approximately constant number of events in each  $Q^2$  interval. The  $Q^2$  bin boundaries are at  $0.10, 0.13, 0.17, 0.21, 0.27, 0.35, 0.45, 0.58$  and  $0.74 \text{ GeV}^2$ . The lowest bin boundary in  $y$  is chosen to be at  $0.08$ . The size of the lowest  $y$  bin is chosen to be  $2\sigma_y$ . For  $y$  values above  $0.37$ , bins of approximately constant width are used to take into account the decrease in the number of events due to the  $1/y$  dependence of the double-differential cross-section. The bin boundaries in  $y$  are  $0.08, 0.16, 0.23, 0.30, 0.37, 0.45, 0.54, 0.64$  and  $0.74$ .

The quality of each bin can be quantified using the bin quality factors *purity*  $p(i, j)$  and *acceptance*  $a(i, j)$ :

$$p(i, j) = \frac{M_{in}^{MC}(i, j)}{M^{MC}(i, j)} \quad (11.5)$$

this case,  $F_2^{MC} = (F_2)_{eff}^{MC}$ . The treatment of the longitudinal structure function  $F_L$  in data is subject of the next section.

To quote the extracted values for  $F_2(y, Q^2)$  at any other point within a particular  $y - Q^2$  bin, a bin centering correction is applied using an explicit parameterization of the extracted values of  $F_2(y, Q^2)$  (Section 11.3.3). For the following discussion, the kinematic variables are taken to be those at which the final values of  $F_2(y, Q^2)$  are being quoted.

The uncertainty in the radiative corrections will be taken into account in the evaluation of systematic uncertainties.

The ratio between the unfolded event distribution  $N^{data}(i, j)$  and the number of generated events with a true  $y$  and  $Q^2$  in the bin  $(i, j)$  for the MC simulation,  $N^{MC}(i, j)$ , will be determined through a bin-by-bin unfolding procedure which will be discussed in detail in section 11.3.3.

The total  $\gamma^*p$  cross-section  $\sigma_{tot}^{\gamma^*p}$  is determined from the extracted  $F_2$  values according to (Section 2.2.2):

$$\sigma_{tot}^{\gamma^*p}(W^2, Q^2) = \frac{4\pi^2\alpha}{Q^2(1-x)} \frac{Q^2 + 4m_p^2x^2}{Q^2} \cdot F_2(y, Q^2) \quad (11.15)$$

where  $W \simeq \sqrt{sy}$ .

### 11.3.2 Treatment of the longitudinal structure function $F_L$

Using the definition for  $R$  of  $R = F_L/(F_2 - F_L)$ , equation 11.7 can be written in the following form:

$$\left( \frac{d^2\sigma}{dydQ^2} \right) = \frac{2\pi\alpha^2Y_+}{yQ^4} \left[ F_2 \left( 1 - \frac{y^2}{Y_+} \frac{R}{1+R} \right) \right] \cdot [1 + \delta_r(y, Q^2)] \quad (11.16)$$

The following discussion will be restricted to  $R$ , since the proposed procedure to extract the proton structure function  $F_2$  provides explicit values for  $R$ .

The extracted  $F_2$  values are then obtained as follows:

$$F_2^{data} = (F_2)_{eff}^{data} [1 + \delta_R^{data}(y, Q^2)] \quad (11.17)$$

where  $\delta_R = \sigma_{\Delta}^{R=0}(i, j) / \sigma_{\Delta}^{R \neq 0}(i, j) - 1$ .

The longitudinal structure function  $F_L$  or equivalently the value of  $R$  has so far not been measured in the HERA kinematic region. One therefore relies on a model description for  $F_L$  in order to extract the proton structure function  $F_2$ . A perturbative QCD ansatz for  $F_L$  was used for the  $F_2$  measurement at HERA for  $Q^2 \geq 1.5 \text{ GeV}^2$  [Ai96, De96a]. The measured kinematic region in  $Q^2$  ( $0.11 \leq Q^2 \leq 0.65 \text{ GeV}^2$ ) presented in this thesis concerns the transition region between non-perturbative and perturbative QCD. Since perturbative QCD is expected to lose its validity towards the photoproduction limit (Chapter 12), a non-perturbative QCD based description for  $R$  has been chosen to extract the proton structure function  $F_2$  and the total  $\gamma^*p$  cross-section  $\sigma_{tot}^{\gamma^*p}$ .

In the first approach, an attempt is made according to [Sa72] to separate the contribution of the total transversal ( $\sigma_T$ ) and longitudinal ( $\sigma_L$ ) cross-sections from the extracted values of  $(\sigma_{tot}^{\gamma^*p})_{eff} = \sigma_T + \epsilon\sigma_L$  using a GVDM parameterization of  $\sigma_T$  and  $\sigma_L$ . This then allows to obtain a value for  $R$  constrained by the data itself. The latter approach will be discussed in detail in chapter 12. The extracted values of  $R$  are referred to as  $R_{GVDM}$ .

A pure model description is used for the second approach. Badelek, Kwicinski and Stasto [Ba97b] suggested for the low- $x$ -low- $Q^2$  region a model for  $R$  based on the photon-gluon fusion process suitably extrapolated to the region of low  $Q^2$ . It includes the required limit of  $F_L \sim Q^4$

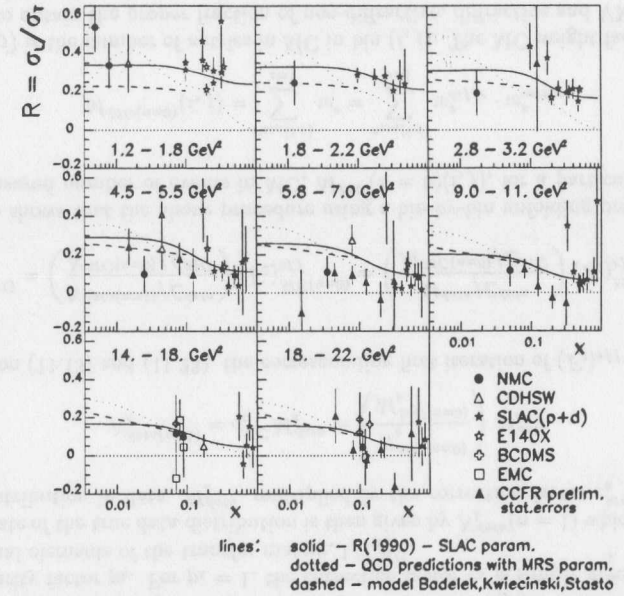


Figure 11.7: Measurement of  $R$  for different bins in  $Q^2$  from various fixed target experiments in comparison to a SLAC  $R$ -parameterization (solid line), a QCD prediction (dotted line) and the predicted  $R$  values by the BKS-models (dashed line) [Ba97a].

as  $Q^2 \rightarrow 0$  (Section 2.3.1). The prediction for  $R$  is in broad agreement with measurements of  $R$  from fixed target experiments as can be seen from Figure 11.7. In the low- $x$ -low- $Q^2$  region,  $R_{BKS}$  is found to be only weakly dependent on  $x$ .

The contribution of  $R$  to the double differential cross-section and therefore to  $(F_2)_{eff}$  increases for  $y \rightarrow 1$ . Assuming  $R$  to be zero decreases the extracted  $F_2$  values compared to the case of  $R_{BKS}$  ( $R_{GVDM}$ ) by at most 3% (2%) for the highest  $y$  bins used in this analysis (Section 11.2). Both values of  $R$  will be used in section 11.6 for the presentation of the final results on  $F_2$  and  $\sigma_{tot}^{\gamma^*p}$ .

### 11.3.3 Unfolding procedure

The measured number of events  $M^{data}(i, j)$  differs from the estimated true number of events  $N^{data}(i, j)$  due to smearing and efficiency effects as well as the limited detector acceptance. Smearing effects arise from the finite detector resolution, the choice of reconstruction method as well as the presence of radiative corrections whereas efficiency effects are due to on-line and off-line selection cuts as well as detector effects. The goal of the *unfolding procedure* is to extract an estimate of the true distribution in  $y$  and  $Q^2$ , from the corresponding measured distribution, i.e. to extract  $N^{data}(i, j)$  from  $M^{data}(i, j)$ .

In mathematical terms, the  $n$ -dimensional measured distribution  $m(x_1, \dots, x_n)$  is related to the

$n$ -dimensional true distribution  $n(y_1, \dots, y_n)$  through the transfer function  $f$ :

$$m(x_1, \dots, x_n) = \int \dots \int f(x_1, \dots, x_n; y_1, \dots, y_n) n(y_1, \dots, y_n) dy_1, \dots, dy_n \quad (11.18)$$

where the integration is performed over the whole  $x_1, \dots, x_n$  phase space. Knowing the transfer function allows to estimate the true distribution from the measured distribution. The transfer function  $f(x_1, \dots, x_n; y_1, \dots, y_n)$  is obtained by means of MC techniques which requires that a MC simulation takes into account various distortions which lead to the difference between the measured and the true distribution. The above equation can be formulated for data as well as for MC. The estimated true data distribution  $n(y_1, \dots, y_n)$  is then evaluated from the measured data distribution  $m(x_1, \dots, x_n)$  and the transfer function  $f(x_1, \dots, x_n; y_1, \dots, y_n)$ , which has been determined through MC studies.

In our case of a two dimensional unfolding problem with two discrete variables, i.e. the measured ( $M_k^{MC}$   $k = (i, j)$ ) and the true ( $N_k^{MC}$   $k = (i, j)$ ) number of events for a bin  $k = (i, j)$  denoting a particular  $y - Q^2$  bin, equation 11.18 simplifies as follows:

$$M_k^{MC} = \sum_{l=1}^n T_{kl}^{MC} N_l^{MC} \quad (11.19)$$

where  $n$  is the number of bins covering the whole  $y - Q^2$  phase space. The transfer function is now given by a  $n \times n$  dimensional matrix, the *transfer matrix*, and  $M_k^{MC}$  and  $N_l^{MC}$  are both  $n$ -dimensional vectors which refer to the measured and true number of events in each bin  $k$  and  $l$ , respectively.  $T_{kl}^{MC}$  describes the probability that an event which originated from bin  $l = (i', j')$  is reconstructed in bin  $k = (i, j)$ .

Several approaches have been taken in the past to determine the transfer matrix  $T_{kl}^{MC}$ . A rather straightforward solution of the above matrix equation is to determine the inverse of the transfer matrix  $T_{kl}^{MC}$  to obtain the true data distribution  $N_k^{data}$  as follows (*Matrix inversion method*):

$$N^{data} = (T^{MC})^{-1} M^{data} \quad (11.20)$$

It requires the transfer matrix  $T^{MC}$  to be non-singular otherwise one encounters unavoidable inversion problems. The results obtained with this method are strongly unstable and will therefore not be considered any further [Ag94].

A detailed discussion on the *Bayes unfolding method* [Ag94] and the *Matrix unfolding method* can be found in [Qa96].

The unfolding method used in this thesis is known as the *Bin-by-bin unfolding method* which has been used for several measurements of the proton structure function  $F_2$  at ZEUS [De96a].

A comparison between different unfolding methods will be given at the end of this section. The following part is devoted to a discussion of the bin-by-bin unfolding method.

If one considers only the net migration effect as the ratio of the number of reconstructed events in bin  $k$ ,  $M_k^{MC}$ , to the number of events generated in the same bin,  $N_k^{MC}$ , and therefore ignores any correlation between bins,  $M_k^{MC}$  in equation 11.19 can be formulated as follows:

$$M_k^{MC} = \sum_{l=1}^n T_{kl}^{MC} N_l^{MC} = m_k^{MC} N_k^{MC} \quad (11.21)$$

where  $m_k^{MC}$  denotes the *migration factor* as determined from a MC simulation. Solving the above equation for  $m_k^{MC}$  yields:

$$m_k^{MC} = T_{kk}^{MC} + \frac{1}{N_k^{MC}} \sum_{l=1, l \neq k}^n T_{kl}^{MC} N_l^{MC} = \frac{1}{c_k^{MC}} \quad (11.22)$$

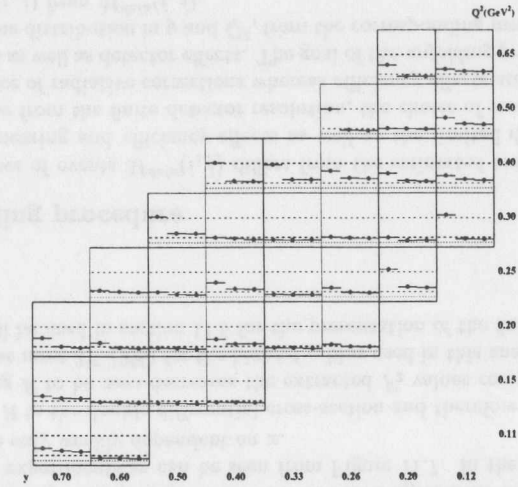


Figure 11.8:  $\chi_{bin}^2$  as a function of the number of iterations for all selected  $y - Q^2$  bins. The dotted line refers to the case of  $\chi_{bin}^2 = 0$  whereas the dashed lines indicate the case of  $\chi_{bin}^2 = 1$  and  $\chi_{bin}^2 = 5$ .

with the *correction factor*  $c_k^{MC}$ . The contribution from off-diagonal elements decreases the larger the purity factor  $p_k$ . For  $p_k = 1$ , the correction factor  $c_k$  is simply given by the inverse of the diagonal elements of the transfer matrix,  $1/T_{kk}^{MC}$ .

A first estimate of the true data distribution is then given by  $N_k^{data}(n=1)$  which is equal to the measured distribution in data,  $M_k^{data}$ , multiplied by the correction factor  $c_k^{MC}$  as determined from MC:

$$N_k^{data(n=1)} = c_k^{MC} M_k^{data} = \left( \frac{N_k^{MC(n=0)}}{M_k^{MC(n=0)}} \right) M_k^{data} \quad (11.23)$$

Using equation (11.13) and (11.23), the corresponding first iteration of  $(F_2)_{eff}$  is then given as follows:

$$(F_2)_{eff}^{data(n=1)} = \left( \frac{N^{data(n=1)}/\mathcal{L}^{data}}{N^{MC(n=0)}/\mathcal{L}^{MC}} \right) (F_2)_{eff}^{MC(n=0)} = \left( \frac{M^{data}/\mathcal{L}^{data}}{M^{MC(n=0)}/\mathcal{L}^{MC}} \right) (F_2)_{eff}^{MC(n=0)} \quad (11.24)$$

The last step shows that the above procedure using a bin-by-bin unfolding procedure requires only the measured number of events in MC,  $M^{MC}(n=0)(i, j)$ , for a particular bin which is given by:

$$M^{MC(n=0)}(i, j) = \sum_{s=1}^{n_{bin}(i, j)} w^s = \sum_{s=1}^{n_{bin}(i, j)} w_{diff}^s \cdot w_{vertex}^s \quad (11.25)$$

where  $n_{bin}(i, j)$  is the number of entries in MC in bin  $(i, j)$ . The MC weight factors  $w_{diff}^s$  and  $w_{vertex}^s$  used to obtain the proper fraction of non-diffractive, diffractive and VM events as well as the re-weighting of the  $Z$  vertex distribution were discussed in detail in sections 9.5 and 9.3, respectively. The weight factors  $w^s$  are normalized to one.

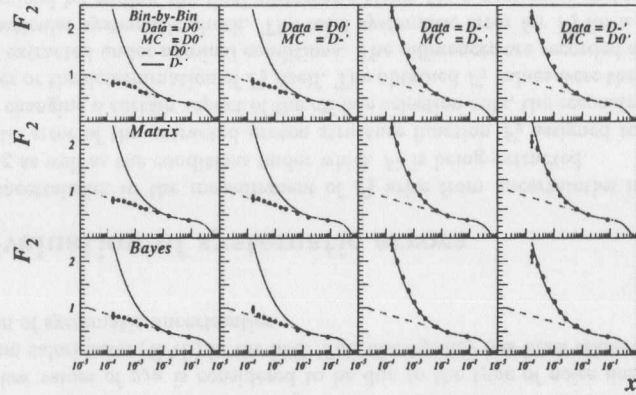


Figure 11.9: Comparison between different unfolding methods [Qa96].

For the above procedure to work it is required that the MC simulation correctly describes the data distributions very well in all phase space regions from which the measured events originate and that migration effects among bins are small, i.e. the purity is large (Section 11.2). This is achieved by iteratively reweighting each MC event to the structure function  $(F_2)_{eff}^{data(n)}$  obtained from the  $n$ th iteration. The result of this iteration,  $(F_2)_{eff}^{data(n+1)}$ , is then used for a next iteration:

$$M^{MC(n)}(i, j) = \sum_{s=1}^{n_{bin}(i, j)} w_{diff}^s \cdot w_{vertex}^s \cdot \left( \frac{(F_2)_{eff}^{data(n)}(y, Q^2)}{(F_2)_{eff}^{MC(n=0)}(y, Q^2)} \right)^s \quad (11.26)$$

where  $n \geq 1$ . The iteration is continued until a stable result is reached. The relative fraction of diffractive and VM events are kept fixed in this procedure.  $y$  and  $Q^2$  refer to the true kinematic variables in MC.

The measured  $(F_2)_{eff}^{data(n)}$  ( $n \geq 1$ ) values are fitted by a smooth function to provide a parameterization for the iterative reweighting procedure. The CKMT  $F_2$  parameterization (Section 2.3.4) has been used to fit the measured  $(F_2)_{eff}^{data(n)}$  results which yields a satisfactory description of the measured  $(F_2)_{eff}^{data(n)}$  values. As an alternative  $F_2$  parameterization, a simplified ansatz of the ALLM  $F_2$  parameterization (Section 2.3.4) ignoring the Reggeon term has been used as well. The difference of the final result on  $(F_2)_{eff}^{data(n)}$  using either the CKMT or the simplified ALLM  $F_2$  parameterization is less than 0.5%.

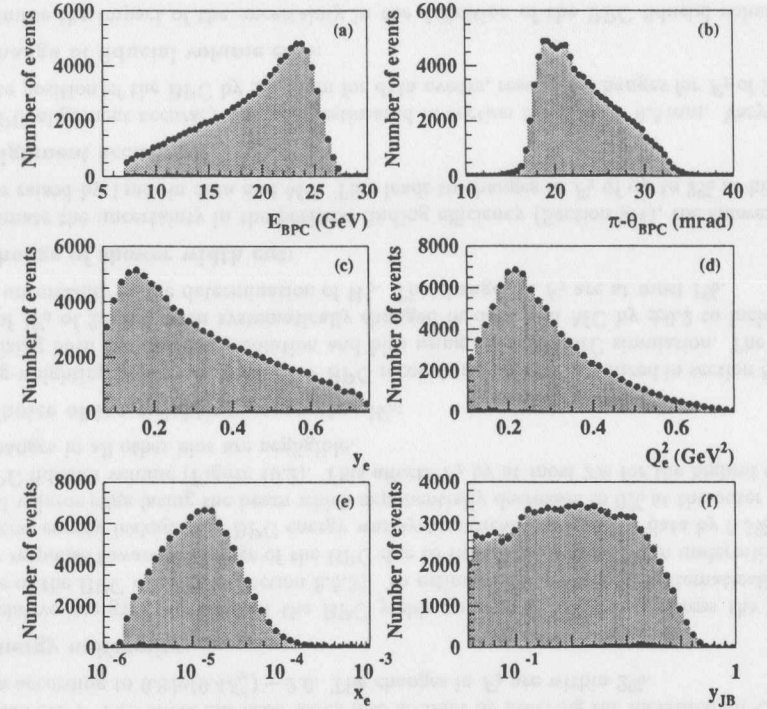
Three iterations are required to yield a result on  $(F_2)_{eff}^{data(n)}$  such that changes between subsequent iterations are less than 0.5% in all bins.

Figure 11.8 shows for each selected  $y$ - $Q^2$  bin the individual  $\chi_{bin}^2$  value

$$\chi_{bin}^2 = \frac{[M^{data}(i, j)/\mathcal{L}^{data} - M^{MC(n)}(i, j)/\mathcal{L}^{MC}]^2}{\sigma_{M^{data}(i, j)}^2 + \sigma_{M^{MC(n)}(i, j)}^2} \quad (11.27)$$

as a function of the number of iteration. The individual  $\chi_{bin}^2$  values for all  $y$ - $Q^2$  bins rapidly converge.

The above bin-by-bin unfolding procedure does not permit the determination of the covariance matrix. The statistical error on the obtained  $(F_2)_{eff}$  result,  $\delta(F_2)_{eff}/(F_2)_{eff}$ , has been therefore

Figure 11.10: Comparison of various measured variables between data and MC: BPC energy (a), BPC angle (b),  $y_e$  (c),  $Q_e^2$  (d),  $x_e$  (e) and  $y_{JB}$  (f). Data are shown as solid circles, photoproduction simulation as black histograms and the sum of the signal and photoproduction simulations as shaded histograms.

estimated from the statistical uncertainties of the data and MC samples assuming a statistical independence of the two samples and ignoring any correlation between bins:

$$\begin{aligned} \frac{\delta(F_2)_{eff}}{(F_2)_{eff}} &= \sqrt{\frac{1}{M^{data}} + \frac{1}{M_{eff}^{MC}}} \\ &= \sqrt{\frac{1}{M^{data}} + \frac{\sum_{s=1}^{n_{bin}} (w^s)^2}{(\sum_{s=1}^{n_{bin}} w^s)^2}} \end{aligned} \quad (11.28)$$

where  $w^s$  are the MC event weight factors. The small contribution of background events in data have been ignored.

Figure 11.9 shows for  $Q^2 = 10 \text{ GeV}^2$  a comparison between the bin-by-bin unfolding method, the matrix unfolding method and the Bayes unfolding method. Two statistically independent samples have been used with one being considered as the 'data' sample and the other one as the

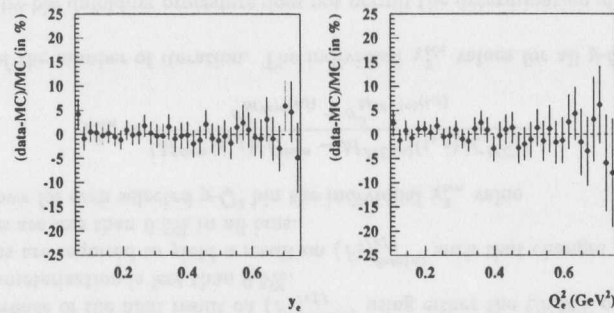


Figure 11.11: Percent deviation of data and MC distributions for the kinematic variables  $y_e$  and  $Q_e^2$ .

'MC' sample. Four combinations of the two structure function parameterizations MRSAD0' and MRSD-' have been used either as the underlying structure function in 'data' to be extracted or in 'MC'. For all three unfolding methods good agreement is found between the input structure and the extracted values for  $F_2$  even if the underlying structure function in 'data' and 'MC' are quite different. The differences are within statistical uncertainties.

## 11.4 Comparison of Data and MC

The MC sample was reweighted on an event-by-event basis to the final extracted proton structure function  $F_2$  as shown in Figure 11.10 for the measured quantities  $E_{BPC}$ ,  $\theta_{BPC}$  and  $y_{JB}$  as well as for the kinematic variables  $x_e$ ,  $y_e$  and  $Q_e^2$  in comparison to the respective data distributions. The contributions from photoproduction background are shown as the black histograms. It has been added to the signal MC sample for comparison to the respective variables in data. In all six cases, the data and MC distributions are in good agreement. Figure 11.11 shows the percent deviation of the  $y_e$  and  $Q_e^2$  distribution between data and MC which clearly underlines that both distributions for data and MC agree well within statistical uncertainties. The discrepancy at low values of  $y_{JB}$  is considered to be due to the type of noise description of the ZEUS uranium calorimeter (CAL) in the MC. This discrepancy has been taken into account in the evaluation of systematic uncertainties.

## 11.5 Evaluation of systematic errors

Systematic uncertainties in the measurement of  $F_2$  arise from uncertainties in the detector understanding as well as the conditions under which  $F_2$  is being extracted.

The systematic error of the extracted proton structure function  $F_2$  assigned to each bin was estimated by changing a certain aspect of the off-line selection cuts, the reconstruction of kinematic variables or the determination of  $F_2$  itself. The obtained  $F_2$  values were then compared to the  $F_2$  values extracted under nominal conditions. The differences are recorded as a systematic error for a particular systematic check. The total systematic error for  $F_2$  for a particular bin is then determined by adding the final systematic errors for a particular systematic check in

quadrature.

A comprehensive list of systematic checks was performed which covers various systematic uncertainties related to the BPC, the main ZEUS detector and the MC simulation. The following part will discuss in detail all systematic checks which have been performed.

### 1. Systematic errors related to the BPC

The BPC-related systematic checks concern in particular, the uncertainty of the BPC absolute energy scale (Section 8.5.3), the effect of a possible non-linear response of the BPC (Section 8.5.4), the impact of the energy uniformity (Section 8.5.3), the uncertainty in the choice of the parameter  $W_0$  which enters the BPC position reconstruction (Section 8.3.3), the effect of changing the shower width cut (Section 9.4), the uncertainty in the BPC alignment (Section 8.3.4) and the effect of changing the fiducial volume cuts (Section 10.2).

#### 1a. Energy scale:

The uncertainty of the BPC energy scale has been estimated in section 8.5.3 to be 0.5%. The energy scale of the BPC has been therefore systematically changed by  $\pm 0.5\%$  for data events only. This affects  $F_2$  by at most 3%.

#### 1b. Non-linearity:

An upper-limit for a non-linear behavior of the BPC due to radiation damage has been estimated in section 8.5.4. This effect has been taken into account by lowering the measured BPC energy in data according to  $0.8 \ln(0.4E_e') - 2.0$ . The changes in  $F_2$  are within 2%.

#### 1c. Energy uniformity:

The relative energy calibration of the BPC yields an energy uniformity across the fiducial volume of the BPC of  $\pm 0.5\%$  (Section 8.5.3). To estimate the effect of a systematically lower energy response towards the edge of the BPC due to radiation damage or an underestimate of transverse energy leakage, the BPC energy was systematically lowered in data by 0.5% at the fiducial volume edge facing the beam which exponentially decreases to 0% at the outer edge of the BPC fiducial volume (Figure 10.2). This affects  $F_2$  by at most 2% for the highest  $\theta_e'$  bins. The changes in all other bins are negligible.

#### 1d. Choice of log-weighting parameter $W_0$ :

The log-weighting parameter  $W_0$  for the BPC reconstruction was optimized in section 8.3.3 by minimizing both the position resolution and bias using an EGS4 MC simulation. The chosen value of  $W_0$  of 2.8 has been systematically changed in data and MC by  $\pm 0.2$  to include the actual uncertainty in the determination of  $W_0$ . The changes in  $F_2$  are at most 1%.

#### 1e. Change of shower width cut:

To estimate the uncertainty in the positron finding efficiency (Section 9.4), the shower width cut was raised by 1 mm in data and MC. This leads to changes in  $F_2$  of up to 2% at high  $y_e$ .

#### 1f. Alignment accuracy:

The BPC alignment accuracy has been estimated in section 8.3.4 to be 0.5 mm. Varying the absolute position of the BPC by  $\pm 0.5$  mm for data events, results in changes for  $F_2$  of 2 – 5%.

#### 1g. Change of fiducial volume cuts:

To estimate the impact of the uncertainty in the definition of the BPC fiducial volume, the fiducial volume boundaries were systematically varied by  $\pm 0.5$  cm in data and MC. The changes in  $F_2$  are well within 1%.

## 2. Systematic errors related to the main ZEUS detector

The systematic errors related to the main ZEUS detector include the uncertainty of the energy scale of the main calorimeter, the accuracy of the MC simulation of the noise of the ZEUS uranium calorimeter, the impact of changing the  $y_{JB}$  and  $\delta$  cuts as well as the use of a tighter cut on the reconstructed  $Z$  vertex position.

### 2a. Energy scale of the main calorimeter

The uncertainty of the energy scale of the main calorimeter of approximately 3% influences reconstruction of the hadronic variables  $\delta_h$  and  $y_{JB}$  (Section 10.2). The energy measured in the main calorimeter was systematically varied by  $\pm 3\%$  for data events prior to the determination of  $\delta_h$  and  $y_{JB}$ . The effects on  $F_2$  are negligible for the medium  $y$  bins. It affects  $F_2$  by 3% at high  $y$  and 4% at low  $y$  due to the impact on the reconstruction of  $\delta$  and  $y_{JB}$ .

### 2b. Treatment of noise in the main calorimeter due to the uranium radioactivity

The noise suppression cuts (Section 10.2) were systematically varied from the nominal values of 80 MeV and 120 MeV for the EMC and HAC cells of the main calorimeter to 60 MeV and 100 MeV and 100 MeV and 140 MeV in MC to check the accuracy of the noise simulation in MC. The changes in  $F_2$  are negligible for most of the bins. Bins at low  $y$  exhibit a systematic change in  $F_2$  of up to 4% due to the changes introduced in the reconstruction of  $y_{JB}$ .

### 2c. Change of $y_{JB}$ cut

The effect on changing the  $y_{JB}$  cut of  $y_{JB} > 0.06$  due to a possible mismatch in the  $y_{JB}$  resolution between data and MC and the simulation of the hadronic final state, as well as the noise description of the ZEUS uranium calorimeter, has been taken into account by changing the cut on  $y_{JB}$  of  $\pm 0.01$  for both data and MC events. This leads to changes in  $F_2$  at low  $y$  of up to 4%. The changes in the mid to high  $y$  bins are negligible.

### 2d. Change of $\delta$ cut

The impact of changing the cut on  $\delta$  of  $\delta > 35$  GeV to account for the photoproduction background contamination, a possible mismatch in the  $\delta$  resolution between data and MC and the simulation of the hadronic final state has been included in the evaluation of the systematic errors by changing the  $\delta$  cut by  $\pm 2$  GeV for both data and MC events. The changes in  $F_2$  increase towards high  $y$  to at most 3%.

### 2e. Change cuts on $Z$ vertex position

The range of the cut on the  $Z$  vertex position has been changed to  $-40 - 50$  cm in data and MC in order to estimate the uncertainty on the satellite luminosity and acceptance. This leads to changes in  $F_2$  of at most 2%.

## 3. Systematic errors related to the MC event simulation

Systematic uncertainties related to the MC event simulation are due to the amount of photoproduction background, the fraction of diffractive and VM events, the description of the hadronic final state, the fraction of events with no  $Z$  vertex information and the simulation of radiative corrections.

### 3a. Amount of photoproduction background events

The uncertainty in the amount of photoproduction background events in the final data sample was estimated to be  $\pm 30\%$  (Section 10.4.2). This has been included in the evaluation of systematic errors by lowering and raising the photoproduction event weight by  $\pm 30\%$ . This leads to changes in  $F_2$  in the highest  $y$  bins of up to 5%.

### 3b. Fraction of diffractive and VM events:

The fraction of diffractive events was determined in section 9.5. The uncertainty on the amount of diffractive events was estimated to be  $\pm 25\%$ . The fraction of non-diffractive, diffractive and VM events were therefore changed accordingly. This leads to changes in  $F_2$  of up to 4% at low and high  $y$ , since diffractive events for the same  $y$  values typically have lower values in  $\delta$  and  $y_{JB}$  compared to non-diffractive events.

### 3c. Description of hadronic final state:

The uncertainty in the description of the hadronic final state was estimated by comparing the results from various MC simulation programs. HERWIG [Ma92] was used to investigate the acceptance for diffractive events, while PYTHIA [Be87a] and EPSOFT [Ka95] have been used for non-diffractive events with respect to the cuts on  $y_{JB}$  and  $\delta$ . An error of 2% on  $F_2$  has been assigned for  $y$  less than 0.4, rising linearly to 5% at  $y = 0.74$ .

### 3d. Fraction of events with no $Z$ vertex information

The fraction of MC events with no  $Z$  vertex information has been reweighted in MC to match those in data (Section 9.3). As a systematic check, the fraction of MC events whose  $Z$  vertex information was ignored was changed by  $\pm 50\%$  to investigate the impact on the reconstructed  $F_2$  values. The effect on  $F_2$  is negligible in all chosen bins.

### 3e. Simulation of radiative corrections

The uncertainty in the amount of radiative corrections of 10 – 15% was estimated in section 9.6 to be approximately 25%. This leads to changes of 3 – 5% on  $F_2$ .

## 4. Final systematic error

The final systematic error assigned to each systematic check is taken to be the average of the positive and negative deviations with respect to a particular systematic check. This results in symmetric errors around the mean reconstructed  $F_2$  values. This approach is motivated by the fact that most of the systematic checks yield symmetric changes around the nominal extracted  $F_2$  values. Any deviation from that are due to statistical fluctuations. This is not the case for the BPC non-linearity check as well as the BPC positron identification check. Both systematic checks result in changes in  $F_2$  which are well within 2%. The contribution to the total systematic error is therefore small.

The total systematic error for a particular  $y-Q^2$  bin is determined by adding the final systematic errors for each systematic check in quadrature.

Those systematic checks which have been included in the evaluation of the total systematic errors for each  $y-Q^2$  bin are shown in Figures 11.12 and Figure 11.13. These plots display the systematic error contribution as a function of  $y$  and as a function of the respective systematic check ID, respectively. The lower two plots in Figure 11.12 represent the variation of the

statistical errors and the total systematic errors as a function of  $y$ . The statistical errors are well within 5% for all bins. The total systematic errors are within 5% to 10%. The total systematic errors are around 6% for moderate  $y$  bins and are dominated by the BPC calibration, the BPC position alignment and uncertainties in the radiative corrections. At low  $y$ , the total systematic error is dominated by the uncertainties in the description of the hadronic final state and the energy scale of the main calorimeter which leads to systematic uncertainties of up to 8%. At high  $y$ , the contributions from the photoproduction background as well as the description of the hadronic final state resulted in errors as high as 10%.

The uncertainties in the luminosity measurement and the trigger efficiency (Section 9.2) leads to a normalization error of 2.4%.

## 11.6 Presentation of final results on $F_2$ and $\sigma_{tot}^{\gamma^*p}$

The final values for  $F_2$  and  $\sigma_{tot}^{\gamma^*p}$  have been determined using the  $y - Q^2$  bins as discussed in detail in section 11.2. The mean values for  $F_2$  and  $\sigma_{tot}^{\gamma^*p}$ , including their statistical uncertainties, have been then evaluated using an iterative bin-by-bin unfolding procedure. The estimation of systematic uncertainties has been presented in the last section.

The final values for  $F_2$  assuming  $R = R_{BKS}$  together with their statistical and systematic errors are shown in Table 11.2. Values of  $R$  obtained from a GVDM-ansatz are shown for comparison. As discussed in section 11.3.2, assuming  $R$  to be zero decreases the extracted  $F_2$  values compared to the case of  $R_{BKS}$  ( $R_{GVDM}$ ) by at most 3% (2%) for the highest  $y$  bins used in this analysis.

Figure 11.14 shows the results on  $F_2$  as determined in this thesis labeled as *BPC 1995* (solid dots). The value of  $R$  has been taken from the BKS model, as discussed in section 11.3.2. Results from an independent  $F_2$  analysis (ZEUS BPC 1995) using the BPC at ZEUS are shown as well based on the same  $y-Q^2$  bins as the ones presented in section 11.2 [Br97]. This analysis is based on the same data sample. However, the complete position and energy reconstruction has been performed completely independently using in both cases a somewhat different approach as the one presented in this thesis. Both results of  $F_2$  shown as a function of  $x$  are in good agreement for all of the eight  $Q^2$  bins. Also shown in Figure 11.14 are data from the E665 [Ad96b] experiment at similar  $Q^2$  values but much larger  $x$  values. Recent low  $Q^2$  data from H1 (H1 SVTX 1995) [Ad97] are shown as well. At the bottom of Figure 11.14, the  $F_2$  values for  $Q^2 = 1.5, 3.0$  and  $6.5 \text{ GeV}^2$  are shown, taken from H1 and ZEUS publications and from E665 to illustrate the rapid rise of  $F_2$  with decreasing  $x$ . The theoretical predictions of the soft pomeron model DL [Do94] and the perturbative QCD model GRV94 [Gl94], as discussed in detail in section 2.3.4, are overlaid. Results from the ALLM parameterization [Ab97] are shown as well which included the recent low  $Q^2$  results from H1 (H1 SVTX 1995) and ZEUS (ZEUS BPC 1995) in their parameter fit.

Figure 11.15 shows the total  $\gamma^*p$  cross-section  $\sigma_{tot}^{\gamma^*p}$  as a function of  $W^2$  as extracted from the  $F_2$  measurement with  $R$  given by the BKS model. The cross-section results as determined in this thesis are labeled as *BPC 1995* (solid dots). The total cross-section for real  $\gamma p$  scattering is shown as well. The theoretical predictions of the soft pomeron model DL and the perturbative QCD model GRV94 as discussed in detail in section 2.3.4 are overlaid including the ALLM cross-section parameterization.

A comparison of these results to various low- $x$ -low- $Q^2$  models (Section 2.3.4) along with a phenomenological analysis and a QCD analysis will be presented in the next chapter.

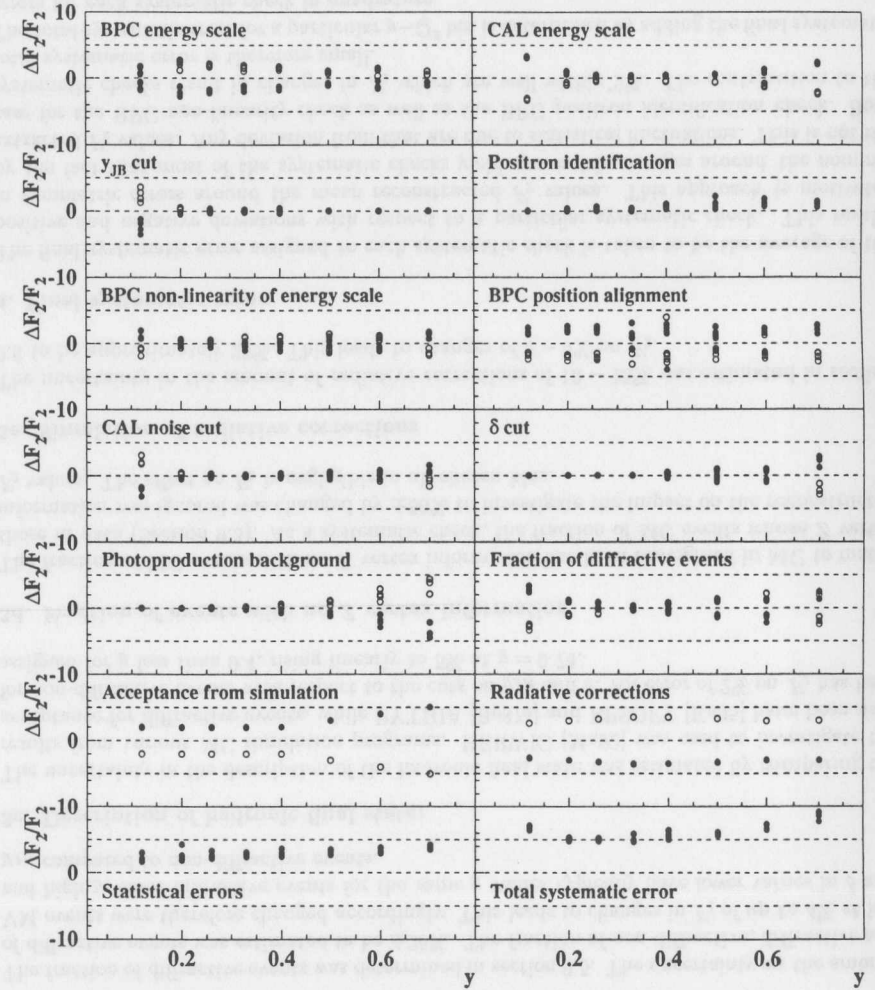


Figure 11.12: Individual systematic errors,  $\Delta F_2/F_2$  (in %), as a function of  $y$  which have been taken into account in the evaluation of the total systematic error. Solid circles refer to positive changes whereas the open circles denote the case of negative changes for a particular systematic check. The statistical errors and the total systematic errors for each  $y-Q^2$  bin are shown on the bottom as a function of  $y$ .

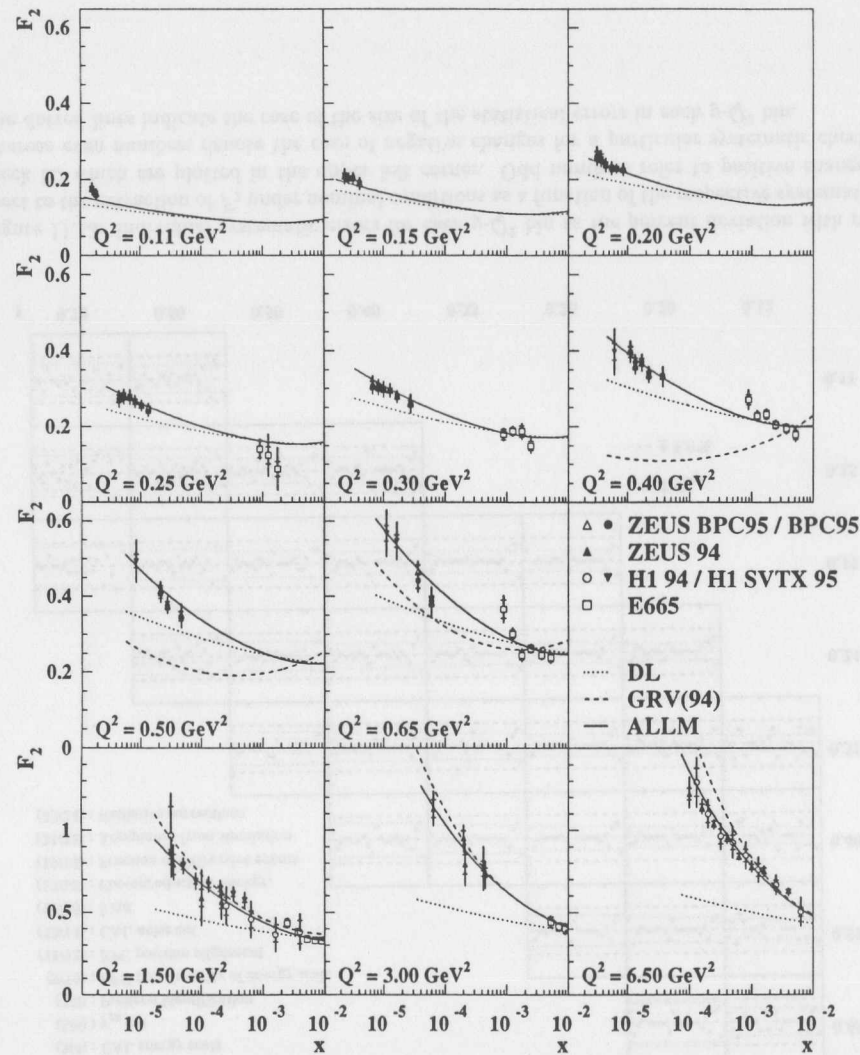


Figure 11.14:  $F_2(x, Q^2)$  as a function of  $x$  for different  $Q^2$  values. The data from this analysis, BPC 95, are shown as solid dots, with E665, H1 and previous ZEUS points shown as open squares, open circles and solid triangles, respectively. Results from an independent BPC  $F_2$  analysis are shown as open triangles (ZEUS BPC 1995) [Br97]. New points from H1 [Ad97] at low  $Q^2$  are shown as solid inverted triangles (the point at  $Q^2 = 0.35$  GeV $^2$  is displayed in the 0.4 GeV $^2$  bin). Curves from the models of DL and GRV and the ALLM parameterization are overlaid.

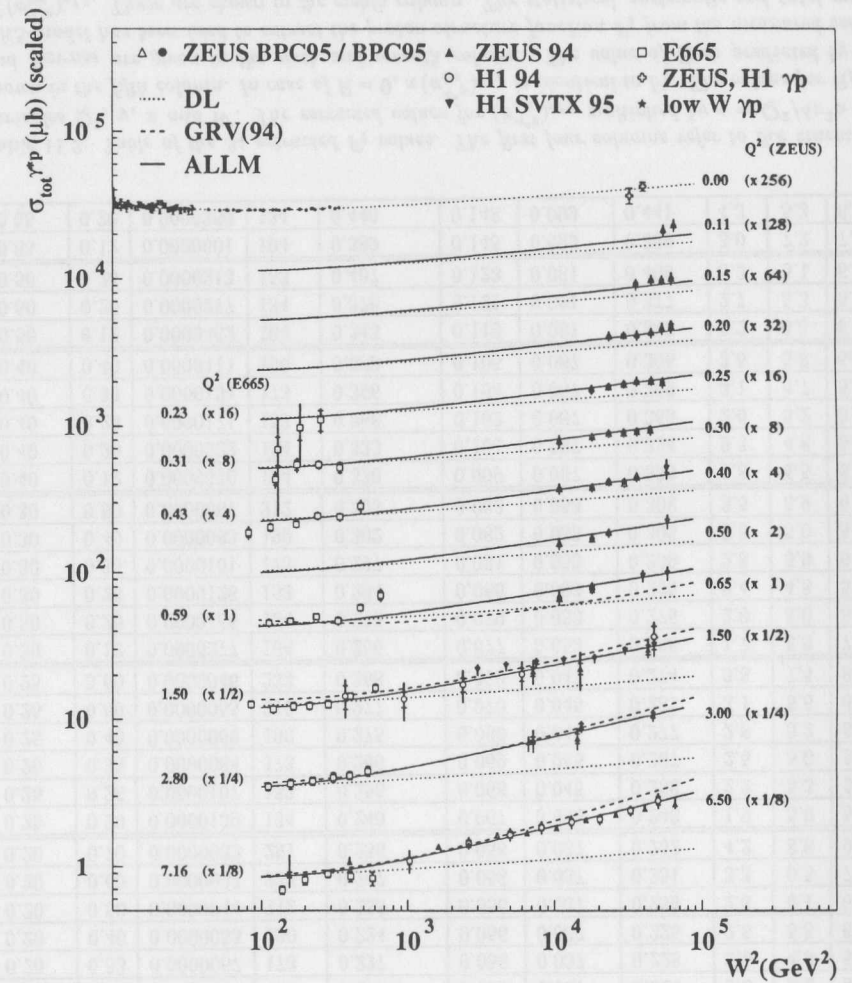


Figure 11.15: The total virtual photon-proton cross-section  $\sigma_{tot}^{\gamma^*p}$  as a function of  $W^2$ . The data from this analysis (BPC 95), previous 1994 ZEUS analyses, H1, and E665 are shown. Results from an independent BPC  $F_2$  analysis are shown as open triangles (ZEUS BPC 1995) [Br97]. The total cross-section for real photon-proton scattering from ZEUS, H1 and photoproduction experiments at low  $W$  are also shown. The predictions of DL and GRV and the ALLM parameterization (at the ZEUS  $Q^2$  values) are indicated by the dotted, dashed and solid curves, respectively.

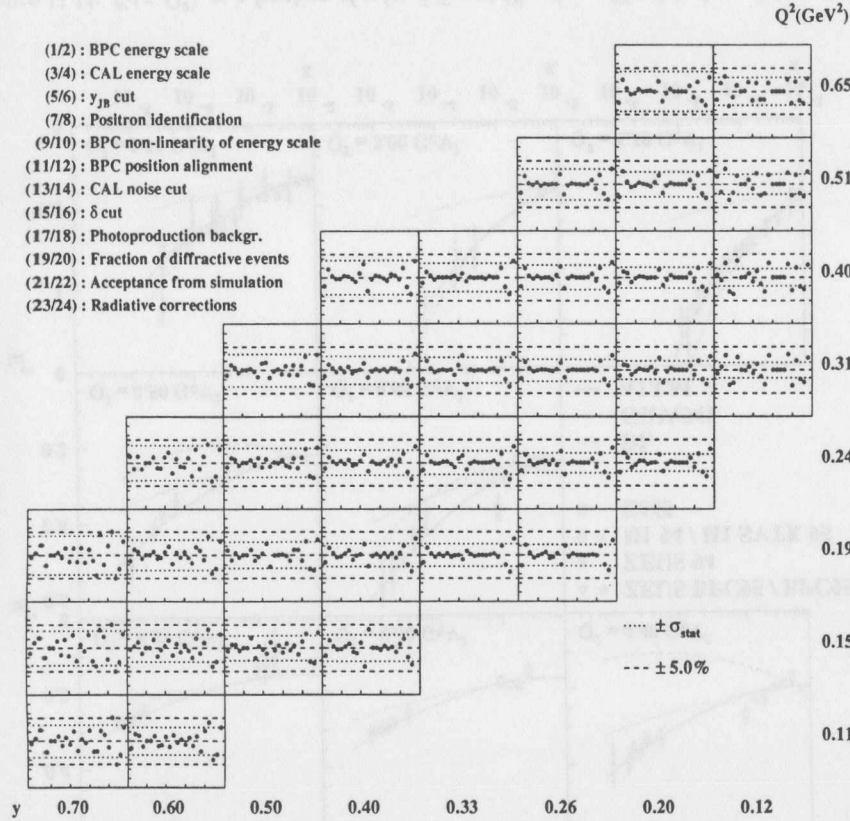


Figure 11.13: Individual systematic errors for each  $y$ - $Q^2$  bin as the percent deviation with respect to the extraction of  $F_2$  under nominal conditions as a function of the respective systematic check ID which are plotted in the upper left corner. Odd numbers refer to positive changes whereas even numbers denote the case of negative changes for a particular systematic check. The dotted lines indicate the case of the size of the statistical errors in each  $y$ - $Q^2$  bin.

$Q^2$ (GeV <sup>2</sup> )	$y$	$x$	$W$ (GeV)	$\kappa (\sigma_{tot}^{\gamma^*p})_{eff}$	$R_{BKs}$	$R_{GVDM}$	$F_2$ ( $R_{BKs}$ )	$\delta_{stat}$ (%)	$\delta_{sys}$ (%)	$\delta_{tot}$ (%)
0.11	0.60	0.0000020	233	0.157	0.031	0.022	0.158	2.9	6.7	7.3
0.11	0.70	0.0000017	251	0.171	0.031	0.022	0.173	3.5	7.8	8.5
0.15	0.40	0.0000042	190	0.191	0.042	0.029	0.192	2.9	6.5	7.1
0.15	0.50	0.0000033	212	0.200	0.042	0.029	0.202	2.8	6.0	6.6
0.15	0.60	0.0000028	233	0.199	0.042	0.029	0.202	3.0	6.7	7.3
0.15	0.70	0.0000024	251	0.204	0.042	0.029	0.208	3.7	9.2	9.9
0.20	0.26	0.0000085	153	0.223	0.055	0.037	0.224	2.2	5.2	5.7
0.20	0.33	0.0000067	173	0.227	0.056	0.037	0.228	2.5	4.8	5.4
0.20	0.40	0.0000055	190	0.224	0.056	0.037	0.225	2.5	5.5	6.1
0.20	0.50	0.0000044	212	0.233	0.056	0.037	0.235	2.8	6.1	6.7
0.20	0.60	0.0000037	233	0.247	0.056	0.037	0.251	3.3	6.5	7.2
0.20	0.70	0.0000032	251	0.256	0.056	0.037	0.262	4.2	8.6	9.6
0.25	0.20	0.0000139	134	0.240	0.067	0.045	0.240	1.9	5.0	5.3
0.25	0.26	0.0000107	153	0.255	0.068	0.045	0.256	2.2	5.3	5.7
0.25	0.33	0.0000084	173	0.266	0.069	0.045	0.267	2.5	5.0	5.6
0.25	0.40	0.0000069	190	0.275	0.069	0.045	0.277	2.8	5.2	5.9
0.25	0.50	0.0000055	212	0.277	0.070	0.045	0.281	3.1	5.6	6.4
0.25	0.60	0.0000046	233	0.268	0.070	0.045	0.274	3.8	7.4	8.3
0.30	0.12	0.0000277	104	0.256	0.077	0.053	0.256	1.7	6.9	7.1
0.30	0.20	0.0000166	134	0.276	0.079	0.053	0.276	2.0	5.0	5.4
0.30	0.26	0.0000128	153	0.294	0.080	0.053	0.295	2.4	4.8	5.3
0.30	0.33	0.0000101	173	0.297	0.081	0.053	0.299	2.8	5.9	6.5
0.30	0.40	0.0000083	190	0.302	0.082	0.053	0.305	3.0	5.0	5.9
0.30	0.50	0.0000067	212	0.303	0.083	0.053	0.308	3.5	5.9	6.9
0.40	0.12	0.0000370	104	0.330	0.099	0.067	0.330	1.8	6.5	6.7
0.40	0.20	0.0000222	134	0.333	0.101	0.067	0.334	2.3	4.8	5.3
0.40	0.26	0.0000171	153	0.368	0.102	0.067	0.369	2.6	5.2	5.8
0.40	0.33	0.0000134	173	0.366	0.104	0.067	0.369	3.1	4.7	5.6
0.40	0.40	0.0000111	190	0.392	0.105	0.067	0.396	3.6	5.8	6.9
0.50	0.12	0.0000462	104	0.343	0.119	0.081	0.343	2.2	6.5	6.8
0.50	0.20	0.0000277	134	0.376	0.121	0.081	0.377	2.7	5.3	5.9
0.50	0.26	0.0000213	153	0.407	0.123	0.081	0.409	3.3	5.1	6.1
0.65	0.12	0.0000601	104	0.389	0.145	0.099	0.389	3.0	7.2	7.8
0.65	0.20	0.0000360	134	0.440	0.148	0.099	0.441	4.3	5.3	6.8

Table 11.2: Table of the 34 extracted  $F_2$  values. The first four columns refer to the kinematic variables  $Q^2$ ,  $y$ ,  $x$  and  $W$ . The extracted values for  $(\sigma_{tot}^{\gamma^*p})_{eff}$  multiplied by  $\kappa = Q^2/4\pi^2\alpha$  are shown in the fifth column. In case of  $R = 0$ ,  $\kappa (\sigma_{tot}^{\gamma^*p})_{eff}$  is identical to  $F_2$ . The values for  $R_{BKs}$  and  $R_{GVDM}$  are given in the sixth and seventh column. The value of  $R$  as predicted by the BKs-model has been used to extract the proton structure function  $F_2$  from the measured values of  $(\sigma_{tot}^{\gamma^*p})_{eff}$ . These are shown in the eighth column. The statistical, systematic and total errors (in %) for each bin are shown in the last three columns.

## Chapter 12

### Results

#### 12.1 Introduction

The investigation of the transition region between non-perturbative and perturbative QCD (pQCD) by measuring the proton structure function  $F_2$  in inelastic neutral current scattering,  $e^+p \rightarrow e^+X$ , at low  $Q^2$ , is the main physics motivation of this thesis (Section 2.3.5).

Results on measurements of the proton structure function  $F_2$  from the two HERA experiments H1 and ZEUS [Ai96, De96a] revealed that the kinematic region of  $Q^2 \geq 1.5 \text{ GeV}^2$  exhibits a strong rise of  $F_2$  with decreasing  $x$  or equivalently of the total virtual photon-proton ( $\gamma^*p$ ) cross-section  $\sigma_{tot}^{\gamma^*p}$  (Equation 2.37) with increasing  $W^2$ . pQCD allows to describe the rapid rise of  $F_2$  with decreasing  $x$  down to  $Q^2 = 1.5 \text{ GeV}^2$ . In contrast to  $\sigma_{tot}^{\gamma^*p}$ , the total cross-section for real photon-proton ( $\gamma p$ ) scattering  $\sigma_{tot}^{\gamma p}$  shows only a modest rise with  $W^2$ . This behavior can be well described within the framework of non-perturbative QCD such as Regge theory (Section 2.3.3), which predicts a power law behavior for the total hadron-hadron cross-sections at large energies.

The results of the measurement of  $F_2$  for  $0.11 \leq Q^2 \leq 0.65 \text{ GeV}^2$ , as obtained in this thesis, will be used together with other data sets (Figure 12.1) to investigate in detail the behavior of  $F_2(x, Q^2)$  and  $\sigma_{tot}^{\gamma^*p}(W^2, Q^2)$  in the transition region of non-perturbative and perturbative QCD at low  $Q^2$ .

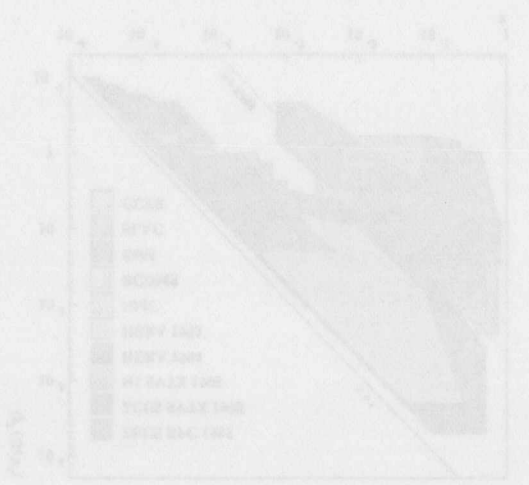
The next section will present the behavior of  $F_2$  as a function of  $x$  and  $Q^2$ , as well as the behavior of  $\sigma_{tot}^{\gamma^*p}$  as a function of  $W^2$  and  $Q^2$  in comparison to various models which have been discussed in detail in section 2.3.4.

The transition from a ‘soft’ to a ‘hard’ behavior of  $F_2$  and  $\sigma_{tot}^{\gamma^*p}$  will be quantified by employing several model descriptions within the framework of non-perturbative and perturbative QCD to the observed behavior of  $F_2$  and  $\sigma_{tot}^{\gamma^*p}$  to establish their reliability and region of applicability including possible physical interpretations of  $F_2$  and  $\sigma_{tot}^{\gamma^*p}$  within the transition region.

A first ansatz within the framework of the generalized vector dominance model (GVDM) (Section 2.3.2) will be used according to [Sa72], to extrapolate the  $Q^2$  dependence of the measured values of  $(\sigma_{tot}^{\gamma^*p})_{eff} = \sigma_T^{\gamma^*p} + \epsilon \sigma_L^{\gamma^*p}$  (Section 11.6) to the total  $\gamma p$  cross-section. The GVDM prediction for  $R = \sigma_L^{\gamma^*p} / \sigma_T^{\gamma^*p}$  will be presented as well. A simple Regge motivated ansatz for  $F_2$  is used according to [Do94] to investigate the range of validity of a simple soft pomeron behavior. These studies will be presented in section 12.3.

Results of a QCD-analysis (Section 12.4) will be used to examine the reliability and stability of pQCD calculations at low  $Q^2$ .

Section 12.5 summarizes the current status of the measurement of the proton structure function  $F_2$  at low  $Q^2$  and the current understanding of the transition from ‘soft’ to ‘hard’ physics.



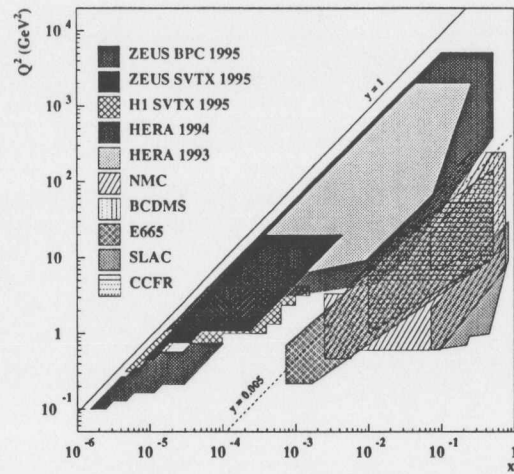


Figure 12.1: Kinematic coverage in the  $Q^2 - x$  plane for various fixed-target experiments and the HERA collider experiments H1 and ZEUS as of 1995. The data sets of ZEUS BPC 1995, ZEUS SVTX 1995 and H1 SVTX 1995 allowed a significant increase of the kinematic coverage at low  $Q^2$  and low  $x$  compared to the results on the measurement of  $F_2$  from H1 and ZEUS as of 1994 (HERA 1994) (See Figure 2.4).

## 12.2 Dependence of $F_2$ and $\sigma_{tot}^{\gamma^*p}$ on $x$ , $W^2$ and $Q^2$

### (a) $x$ and $W^2$ dependence

Figure 12.3 and 12.4, at the end of this section, show results on  $F_2$  and  $\sigma_{tot}^{\gamma^*p}$  as a function of  $x$  and  $W^2$  respectively, for different  $Q^2$  values. The results on  $F_2$  and  $\sigma_{tot}^{\gamma^*p}$ , as determined in this thesis (BPC 1995), are displayed as solid dots. Preliminary results from the 1995 ZEUS shifted vertex run (ZEUS SVTX 95 Prel.) [Su97] are shown as solid squares whereas the recent low  $Q^2$  data from H1 (H1 SVTX 1995) [Ad97] are shown as inverted solid triangles. The ZEUS 1994  $F_2$  results are shown as open triangles [De96b]. Also shown are data from the E665 [Ad96b] experiment at similar  $Q^2$  values, but much larger  $x$  values (open circles). The  $x$  and  $W^2$  dependence with respect to  $F_2$  and  $\sigma_{tot}^{\gamma^*p}$  of the individual data sets, show a satisfactory agreement within errors.

The data exhibit a smooth transition from a steeper rise of  $F_2$  in  $x$  and  $\sigma_{tot}^{\gamma^*p}$  in  $W^2$  respectively, observed at the higher  $Q^2$  bins, to a modest rise when approaching the photoproduction limit towards low values of  $x$ .

### (b) $Q^2$ dependence

Figure 12.5 and 12.6, at the end of this section, show results on  $F_2$  and  $\sigma_{tot}^{\gamma^*p}$  as a function of  $Q^2$  for fixed values of  $x$  and  $W^2$ , respectively. The results on  $F_2$  and  $\sigma_{tot}^{\gamma^*p}$  as determined in this thesis (BPC 1995), are displayed as solid dots. Preliminary results from the 1995 ZEUS shifted vertex run (ZEUS SVTX 95 Prel.) [Su97] are shown as solid squares whereas the recent low  $Q^2$  data from H1 (H1 SVTX 1995) [Ad97] are shown as inverted solid triangles. The 1994 ZEUS

$F_2$  results are shown as open triangles which allowed to reach  $Q^2$  values as large as 5000 GeV<sup>2</sup> [De96b]. The  $Q^2$  dependence with respect to  $F_2$  and  $\sigma_{tot}^{\gamma^*p}$  of the individual data sets, shows as well a satisfactory agreement within errors.

The dependence of  $\sigma_{tot}^{\gamma^*p}$  on  $Q^2$  for fixed values of  $W$  ( $104 \leq W \leq 251$  GeV) shows three distinct kinematic regions:

- $Q^2 \lesssim 0.1$  GeV<sup>2</sup> ('photoproduction region'),  
with an almost flat behavior of  $\sigma_{tot}^{\gamma^*p}$  as a function of the logarithm in  $Q^2$  with  $\sigma_{tot}^{\gamma^*p} \rightarrow \sigma_{tot}^{\gamma p}$ .
- $0.1 \lesssim Q^2 \lesssim 1.0$  GeV<sup>2</sup>,  
with a characteristic change of  $\sigma_{tot}^{\gamma^*p}$  as a function of the logarithm in  $Q^2$  from the photoproduction to the deep-inelastic scattering region ('transition region').
- $Q^2 \gtrsim 1.0$  GeV<sup>2</sup>,  
with a steady decrease of  $\sigma_{tot}^{\gamma^*p}$  as a function of the logarithm in  $Q^2$  ('deep-inelastic scattering region').

It can be clearly seen that the BPC  $F_2$  data cover the 'transition region'. A GVDM-ansatz will be used to extrapolate the BPC ( $\sigma_{tot}^{\gamma^*p})_{eff} = \sigma_T^{\gamma^*p} + \epsilon\sigma_L^{\gamma^*p}$  results to the photoproduction limit, i.e.  $Q^2 = 0$ .

As can be seen from Figure 12.5,  $F_2$  exhibits, for fixed values of  $x$  with  $x \geq 0.0001$ , an almost linear increase with the logarithm of  $Q^2$  indicating the violation of scaling as expected from pQCD (Section 2.2.4). The scaling violation is expected to increase at low  $x$  values and to decrease towards larger values of  $x$ . This behavior can be clearly inferred from Figure 12.5. For  $x$  bins of  $0.0000120 < x < 0.0000630$  with  $F_2$  data points around  $Q^2 = 1.0$  GeV<sup>2</sup>, a change in the slope of  $F_2$  as a function  $Q^2$  is noticeable indicating the region where non-perturbative effects become dominant.

### (c) Comparison to low- $x$ -low- $Q^2$ models

The following section will discuss in detail, various low- $x$ -low- $Q^2$  models in comparison to results on  $F_2$  and  $\sigma_{tot}^{\gamma^*p}$  as a function of  $x$  and  $Q^2$  based on the data sets discussed above (Figures 12.3, 12.4, 12.5 and 12.6)

The emphasis will be placed on the  $x$  and  $Q^2$  dependence in the transition region, as well as on the approach of the photoproduction and deep-inelastic scattering region. The models presented have been discussed in detail in section 2.3.4.

#### 1. Donnachie, Landshoff - DL:

The parameters of the DL model have not been fitted to the data sets used for the comparison.  $F_2$ -DL is systematically lower than the data, as shown in Figure 12.3 and 12.4 for  $Q^2 \geq 0.11$  GeV<sup>2</sup>. However, the DL model for the total photoproduction cross-section (Figure 12.4) successfully describes the  $W^2$  dependence of the total photoproduction cross-section measurements from the low  $W$  data [Ca78] and those obtained by the two HERA experiments H1 and ZEUS [Ai95, De94]. The fact that it undershoots the BPC  $F_2$  results already at the lowest  $Q^2$  values indicates that there seems to be a discrepancy in the BPC  $F_2$  results and the photoproduction measurements at HERA. This will be discussed in the next section when extrapolating from the BPC  $\sigma_T^{\gamma^*p} + \epsilon\sigma_L^{\gamma^*p}$  results to the total photoproduction cross-section. The  $F_2$  data for  $Q^2 < 1$  GeV<sup>2</sup> favor a constant slope in  $W^2$  but with a value somewhat larger

than the one implemented in the DL model based on a soft Pomeron ansatz with an intercept of 1.0808. It will be shown in the next section that a DL ansatz fitted to the  $F_2$  data allows to describe the  $F_2$  behavior well for  $Q^2 < 1 \text{ GeV}^2$  which shows that a simple soft Pomeron ansatz, as implemented in the DL model, allows to describe the behavior of  $F_2$  up to approximately  $1 \text{ GeV}^2$ .

The slope of  $F_2$  as a function of  $Q^2$  is reasonably well reflected by the DL model for the four lowest  $x$  bins, as shown in Figure 12.5, taking into account the mentioned discrepancy in the normalization between data and the DL model. It cannot reproduce the beginning of the steeper rise of  $F_2$  in  $Q^2$  at around  $Q^2 \approx 1 \text{ GeV}^2$  when pQCD effects become important.

## 2. Capella, Kaidalov, Merino, Tran-Thanh-Van - CKMT:

The CKMT model, which did not include the data sets used for the comparison in the parameter fit, provides a description of  $F_2$  with a  $Q^2$  dependent Pomeron intercept which interpolates between the effective soft pomeron and the effective hard pomeron. It is almost equal to the description of  $F_2$  as given by the DL model for the four lowest  $Q^2$  bins, as shown in Figure 12.3. Due to the  $Q^2$  dependent Pomeron intercept, the slope of the CKMT  $F_2$  parameterization starts to deviate for  $Q^2 \gtrsim 0.3 \text{ GeV}^2$  from the slope as given by the DL model. However, it cannot account for the rapid rise of  $F_2$  in  $x$  at larger values of  $Q^2$ . It allows to provide a successful description of the total photoproduction cross-section (Figure 12.4), but undershoots in the same way as the DL model the BPC  $F_2$  results. The CKMT parameterization has been used as the re-weighting function for the determination of  $F_2$  in this thesis (Section 11.3). It allows to provide a reasonable description of  $F_2$  up to approximately  $2 - 3 \text{ GeV}^2$  in  $Q^2$ .

## 3. Badelek, Kwicinski - BK:

$F_2$  is represented as the sum of a vector meson part and a partonic part based on the GVDM model. The expression for  $\sigma_{tot}^{\gamma^*p}$  is given as follows:

$$\sigma_{tot}^{\gamma^*p} = \frac{4\pi^2\alpha}{Q^2} \left[ \frac{Q^2}{4\pi} \sum_{\rho^0, \omega, \phi} \left( \frac{m_V^4 \sigma_V(W^2)}{\gamma_V^2(Q^2 + m_V^2)^2} \right) + \left( \frac{Q^2}{Q^2 + Q_0^2} \right) F_2^{AS}(\bar{x}, Q^2 + Q_0^2) \right] \quad (12.1)$$

where  $\bar{x} = (Q^2 + Q_0^2)/(s + Q^2 - m_p^2 + Q_0^2)$ .  $Q_0^2$  is chosen to be  $1.2 \text{ GeV}^2$ , i.e. only the three lightest vector mesons  $\rho$ ,  $\omega$  and  $\phi$  are taken into account (Section 2.3.4). The asymptotic structure function  $F_2^{AS}$  has been taken from GRV(94). The BK prediction provides a reasonable description of the  $x$  and  $Q^2$  dependence for  $Q^2 > 1 \text{ GeV}^2$  (Figure 12.3 and Figure 12.5). It however starts to overshoot the measured  $F_2$  results for  $Q^2 < 1 \text{ GeV}^2$ .

The BK model, by construction, predicts a vector meson as well as a partonic contribution at any  $Q^2$  value as can be seen from equation 12.1. At  $Q^2 = 0$ , the BK model yields a partonic contribution to the total photoproduction cross-section of about 10 – 15% which gives rise to the fact that the BK model starts to overshoot the  $F_2$  measurements for  $Q^2 < 1 \text{ GeV}^2$  and in particular the measured total photoproduction cross-section [Ba97a]. The authors remark that improvements of the model have to be made by reducing the partonic contribution rather than changing the VDM contribution.

## 4. Glück, Reya, Vogt - GRV:

The GRV pQCD model rests on the assumption of a valence like quark and gluon distribution at a very low starting scale of  $Q_0^2 = 0.34 \text{ GeV}^2$ . Those are then evolved using a next-to-leading

(NLO) DGLAP evolution. The rise of  $F_2$  at low  $x$  is generated dynamically, since all starting distributions are assumed to be valence like.

As can be seen from Figure 12.3 and 12.4, the GRV(94) prediction reproduces the rapid rise of  $F_2$  for  $Q^2 \gtrsim 1 \text{ GeV}^2$ , but tends to lie somewhat above the data. GRV is not expected to work close to the starting scale. The value of  $F_2$  as given by the GRV model, amounts to approximately 50% of the measured  $F_2$  values at  $Q^2 = 0.50 \text{ GeV}^2$ , rising to about 80% at  $Q^2 = 0.65 \text{ GeV}^2$ .

Figure 12.5 displays the predicted  $Q^2$  dependence for  $F_2$  in bins of  $x$ . In all bins, GRV(94) predicts a slope in  $F_2$  as a function of  $Q^2$ , i.e. the size of scaling violations, which is significantly larger than the one seen in the data. This will be discussed in more detail in section 12.4.

Although GRV(94) provides a reasonable description of the  $x$  dependence of the  $F_2$  results, the choice of the very low starting scale of  $Q_0^2 = 0.34 \text{ GeV}^2$  is subject of some debate, since  $\alpha_s$  is on the order of 0.5. The reliability of pQCD calculations at such a low starting scale will be discussed in section 12.4.

## 5. Adel, Barreiro, Ynduráin - ABY:

The ABY parameterization including a recent update [Ba97c], used low  $Q^2$   $F_2$  results from H1 and ZEUS [Ba97c] in the parameter fit. It gives a good description of the  $x$  and  $Q^2$  dependence at low  $x$  ( $x < 10^{-2}$ ) (Figures 12.3, 12.4, 12.5 and 12.6). A recent parameterization of the total photoproduction cross-section provides a good description of the measured photoproduction cross-section at low and high  $W$  values [Ba97c].

## 6. Schildknecht, Spiesberger, - ScSp:

The virtual-photon proton cross-section and thus  $F_2$  is expressed in terms of  $\sigma_T^{\gamma^*p}$  and  $\sigma_L^{\gamma^*p}$  which are described in the framework of the GVDM model using a logarithmic rise of the spectral weight function in  $W^2$  (Section 2.3.2), i.e.  $\rho_T(W^2, m^2) = N \ln(W^2/am^2)/m^4$ . The so-obtained expression for  $F_2$  is then fitted to the HERA data from the H1 and ZEUS experiments over the full  $Q^2$  range from the photoproduction region to  $Q^2 = 350 \text{ GeV}^2$  and energies  $W$  from  $W \simeq 60 \text{ GeV}$  to  $W \simeq 245 \text{ GeV}$ , i.e.  $x \lesssim 0.05$ . This GVDM ansatz provides a reasonable description of the  $W^2$  and  $Q^2$  dependence at high values of  $W$  including the measured photoproduction cross-sections at HERA (Figures 12.3, 12.4 and 12.6). The present ansatz does not permit to describe the low  $W$  region which requires a refinement of the proposed GVDM ansatz [Sc97b].

## 7. Abramowicz, Levin, Levy, Maor - ALLM:

An update of the ALLM parameterization [Ab97] which included the ZEUS BPC and the H1 shifted vertex  $F_2$  results from the 1995 HERA run in the parameter fit, provides a good description of the  $W^2$  and  $Q^2$  dependence of  $\sigma_{tot}^{\gamma^*p}$  over the whole  $(x, Q^2)$  kinematic region including the photoproduction region down to  $W^2 = 3 \text{ GeV}^2$ , as can be seen from Figures 11.14, 11.15 and 12.6. The ALLM approach thus provides a parameterization to describe the data on  $\sigma_{tot}^{\gamma^*p}$  in the whole kinematic region.

### (d) Bjorken plot

Figure 12.2 shows  $Q^2 \sigma_{tot}^{\gamma^*p} \propto F_2$  as a function of  $Q^2$  in bins of  $W^2$  for all fixed-target and HERA data from inelastic lepton-nucleon scattering including the one presented in this thesis. Such a presentation has been suggested by Bjorken [Bj96] in order to investigate tendencies towards a BFKL dynamics.

This can be qualitatively understood by comparing the following DGLAP and BFKL approximations for  $F_2$  (Section 2.2.4):

$$F_2^{DGLAP}(x, Q^2) \sim \ln Q^2 \cdot x^{-\lambda^{DGLAP}} \quad (12.2)$$

$$F_2^{BFKL}(x, Q^2) \sim (Q^2)^{0.5} \cdot x^{-\lambda^{BFKL}} \quad (12.3)$$

For fixed values of  $W^2$ , the above expressions yield the following behavior:

$$F_2^{DGLAP}(W^2 \text{ fixed}, Q^2) \sim \ln Q^2 \cdot (Q^2)^{-\lambda^{DGLAP}} \quad (12.4)$$

$$F_2^{BFKL}(W^2 \text{ fixed}, Q^2) \sim (Q^2)^{0.5-\lambda^{BFKL}} \quad (12.5)$$

The different  $Q^2$  dependence would give rise to a different shape of  $F_2$  as a function of  $Q^2$  for fixed values of  $W^2$ . It would be curved concave downwards in case of DGLAP whereas for BFKL,  $F_2$  would show only a little dependence with  $Q^2$ .

As can be seen from Figure 12.2, the  $F_2$  data in bins of  $W^2$  are clearly curved concave downwards. Thus, no tendencies for a BFKL dynamics is visible in the presently available data. The product of  $Q^2$  times the measured photoproduction cross-section by ZEUS is shown as the dashed line. It has been suggested that differences in the DGLAP and the BFKL evolution equations could show up in exclusive measurements [Mu90, Kw94].

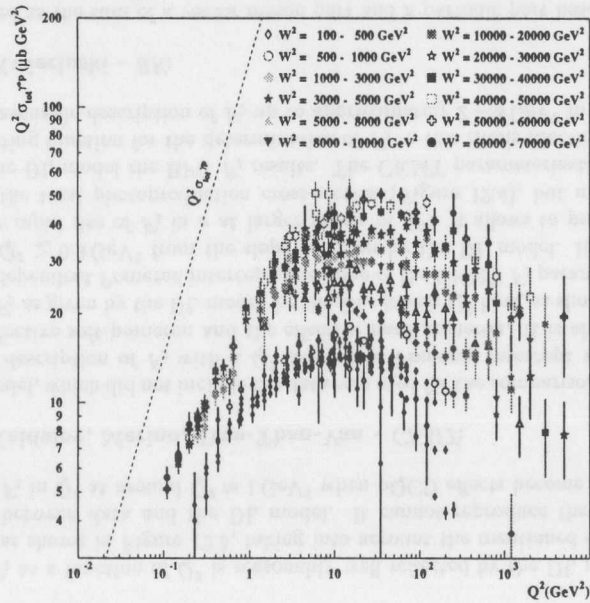


Figure 12.2: Bjorken plot of  $Q^2 \sigma_{tot}^{\gamma p}$  as a function of  $Q^2$  in bins of  $W^2$ . The dashed line refers to the total photoproduction cross-section limit.

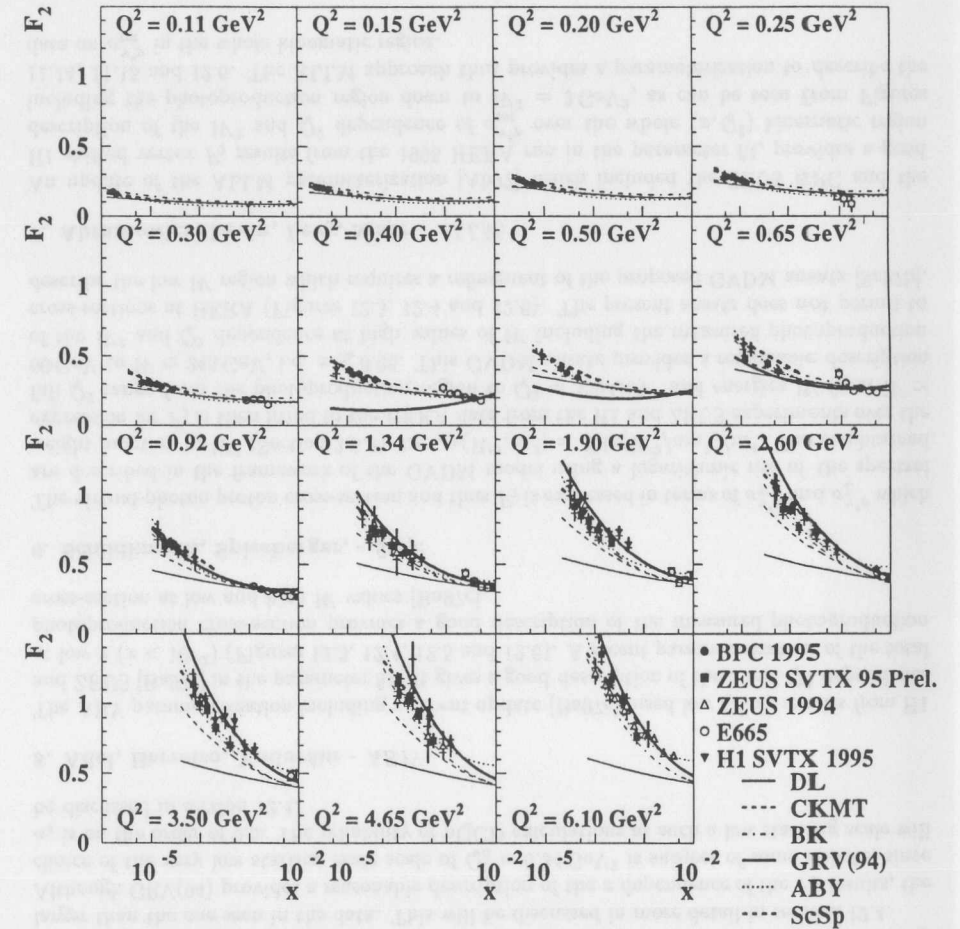


Figure 12.3:  $F_2$  as a function of  $x$  for different  $Q^2$  values. Curves from the models of DL, CKMT, BK, GRV(94), ABY and ScSp are overlaid. The eight lowest  $Q^2$  bins can be seen more clearly in Figure 11.14. This presentation has been chosen to display the change from a steep rise of  $F_2$  in  $x$  at high  $Q^2$  to a modest rise at low  $Q^2$ .

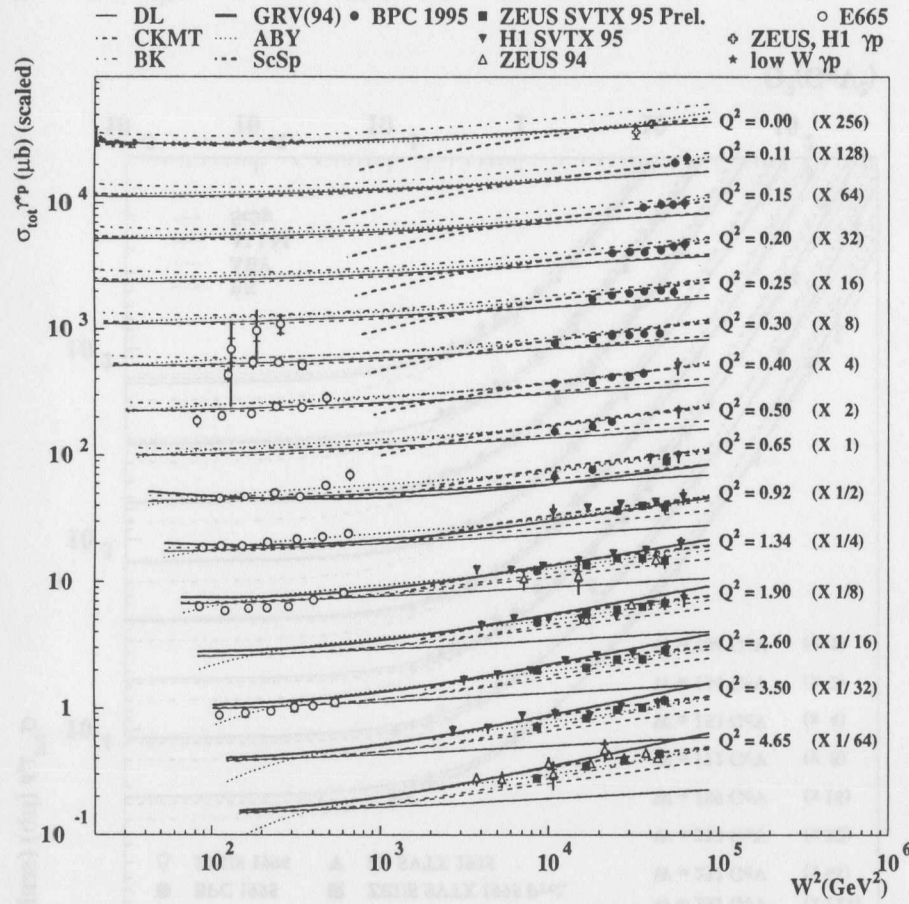


Figure 12.4: The total virtual-photon proton cross-section  $\sigma_{tot}^{\gamma^*p}$  as a function of  $W^2$  for different  $Q^2$  values. Curves from the models of DL, CKMT, BK, GRV(94), ABY and ScSp are overlaid.

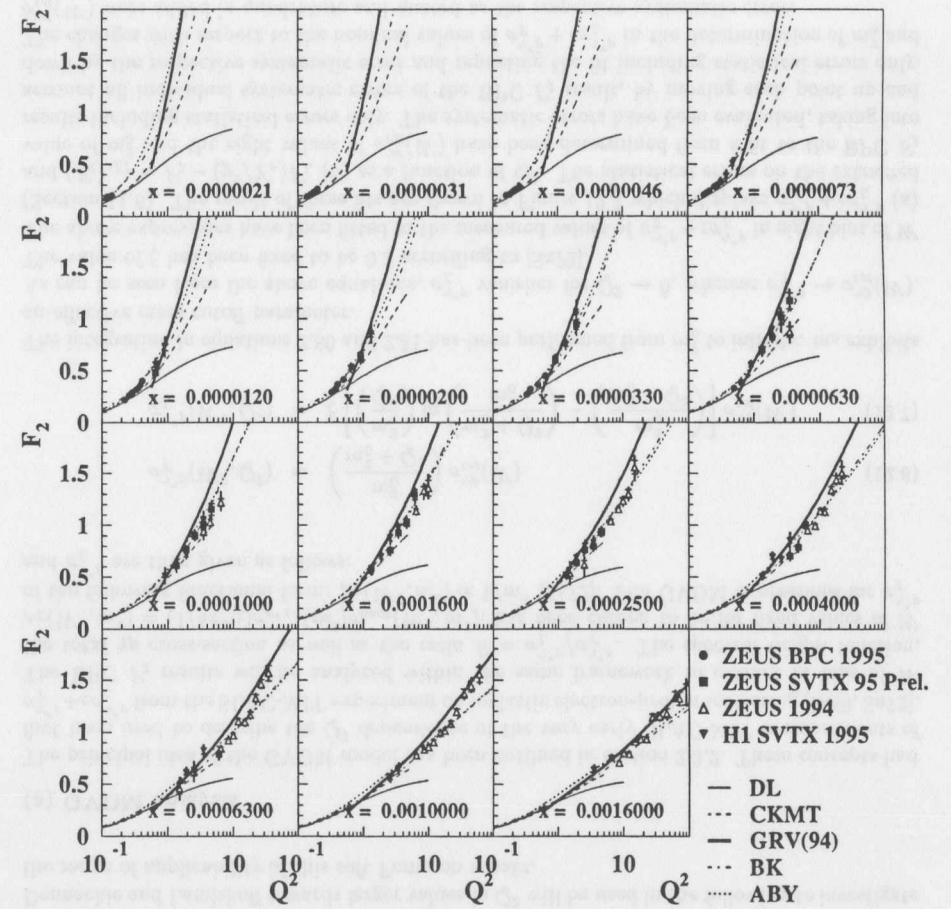


Figure 12.5:  $F_2$  as a function of  $Q^2$  for different  $x$  values. Curves from the models of DL, CKMT, GRV(94), BK and ABY are overlaid.

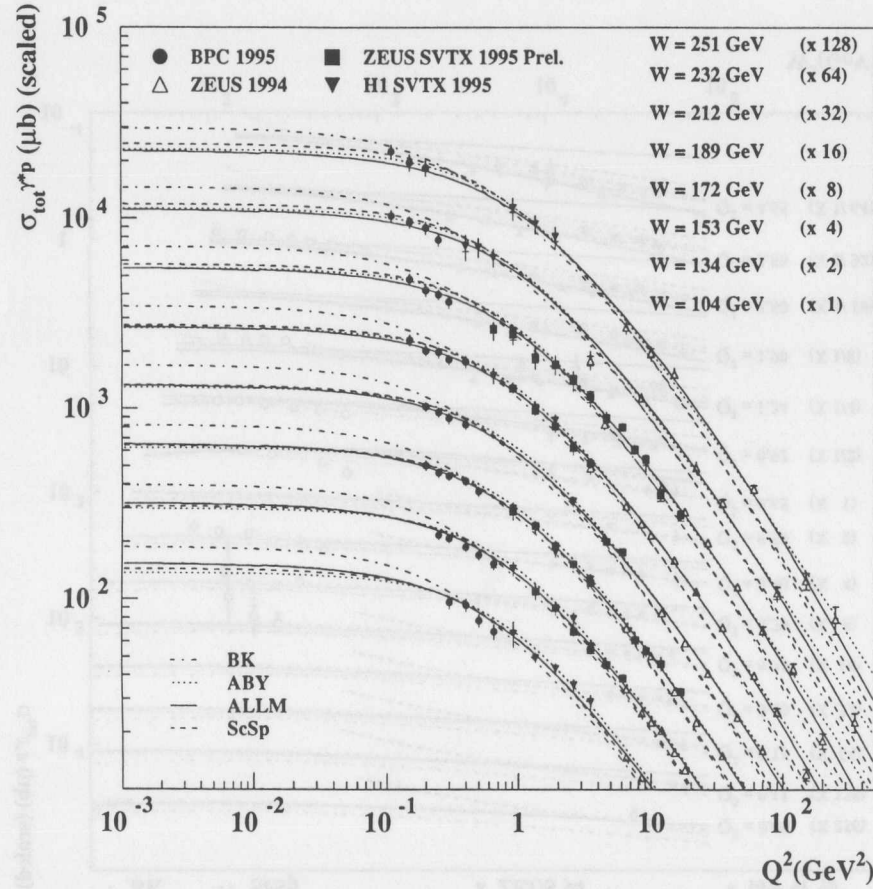


Figure 12.6:  $\sigma_{tot}^{\gamma^*p}$  as a function of  $Q^2$  for different  $W$  values. Curves from the models of BK, ABY, ALLM and ScSp are overlaid.

## 12.3 Phenomenological analysis

The vector meson dominance (VDM) model and its extension to the generalized vector dominance model (GVDM) as well as Regge theory have been discussed in detail in section 2.3 as two non-perturbative concepts which are used in a variety of phenomenological models. A GVDM prediction for the  $Q^2$  dependence of  $\sigma_T^{\gamma^*p}$  and  $\sigma_L^{\gamma^*p}$  will be used in the following section to describe the  $Q^2$  dependence of the BPC results on  $\sigma_T^{\gamma^*p} + \epsilon\sigma_L^{\gamma^*p}$ . Regge theory predicts a power law behavior of the total photoproduction cross-section. The extension of this concept by Donnachie and Landshoff towards larger values in  $Q^2$  will be used in the following to investigate the range of applicability of this soft Pomeron ansatz.

### (a) GVDM analysis

The principal idea of the GVDM model has been outlined in section 2.3.2. These concepts had first been used to describe the  $Q^2$  dependence of the very early SLAC-MIT measurements of  $\sigma_T^{\gamma^*p} + \epsilon\sigma_L^{\gamma^*p}$  from the SLAC-MIT experiment on inelastic electron-proton scattering [Bl69, Sa72]. The BPC  $F_2$  results will be analyzed within the same framework to extract in bins of  $W$  the total  $\gamma p$  cross-section as well as the ratio  $R = \sigma_L^{\gamma^*p}/\sigma_T^{\gamma^*p}$ . The spectral weight function,  $\rho_T(W^2, m^2) = (1/4\pi^2\alpha)\sigma_{e^+e^-}(m^2)\sigma_{\text{hadr}}(W^2, m^2)$ , has been chosen to be for fixed values of  $W$  of the following functional form:  $\rho_T(W^2, m^2) \propto 1/m^4$  [Sa72]. The GVDM expressions for  $\sigma_T^{\gamma^*p}$  and  $\sigma_L^{\gamma^*p}$  are then given as follows:

$$\sigma_T^{\gamma^*p}(W^2, Q^2) = \left( \frac{m_0^2}{m_0^2 + Q^2} \right) \sigma_{tot}^{\gamma p}(W) \quad (12.6)$$

$$\sigma_L^{\gamma^*p}(W^2, Q^2) = \xi \left[ \left( \frac{m_0^2}{Q^2} \right) \ln \left( \frac{m_0^2 + Q^2}{m_0^2} \right) - \left( \frac{m_0^2}{m_0^2 + Q^2} \right) \right] \sigma_{tot}^{\gamma p}(W) \quad (12.7)$$

The integration in equations 2.80 and 2.81 has been performed from  $m_0^2$  to infinity.  $m_0$  exhibits an effective mass cutoff parameter.

As can be seen from the above equations,  $\sigma_L^{\gamma^*p}$  vanishes for  $Q^2 \rightarrow 0$ , whereas  $\sigma_T^{\gamma^*p} \rightarrow \sigma_{tot}^{\gamma p}(W)$ . The value of  $\xi$  has been fixed to be 0.2 according to [Sa72].

The above expressions have been fitted to the measured values of  $\sigma_T^{\gamma^*p} + \epsilon\sigma_L^{\gamma^*p}$  in eight bins of  $W$  (Section 11.6). The result of these fits are shown in Figure 12.7 which displays  $\sigma_T^{\gamma^*p} + \epsilon\sigma_L^{\gamma^*p}$  (a) and  $(F_2)_{eff} = F_2 - (y^2/Y_+)F_L$  (b) as a function of  $Q^2$ . The statistical errors on the extracted value of  $m_0^2$  and the eight values of  $\sigma_{tot}^{\gamma p}(W)$  have been determined from a fit to the BPC  $F_2$  results including statistical errors only. The systematic errors have been evaluated, taking into account all individual systematic errors of the BPC  $F_2$  result, by moving each point up and down by the respective systematic error and repeating the fit including statistical errors only. The changes with respect to the nominal values of  $\sigma_T^{\gamma^*p} + \epsilon\sigma_L^{\gamma^*p}$  in the determination of  $m_0^2$  and  $\sigma_{tot}^{\gamma p}(W)$  were added in quadrature and quoted as the respective systematic error.

The value for  $m_0^2$  has been determined to be:  $m_0^2 = 0.475 \pm 0.038$  (stat)  $\pm 0.066$  (sys). The results for each extracted total  $\gamma p$  cross-section are shown in Table 12.1 with the  $W$  values,  $\epsilon$  and the cross-section values together with their statistical and systematic uncertainties. It has been found that the choice  $\xi = 0.2$  yields a minimal  $\chi^2$ . To account for the effect of a change in  $\xi$  on the extracted  $\sigma_{tot}^{\gamma p}(W)$  values,  $\xi$  has been varied by  $\pm 0.2$  with respect to  $\xi = 0.2$ . The changes in the total  $\gamma p$  cross-section are indicated in the last column which are less than the statistical uncertainties.

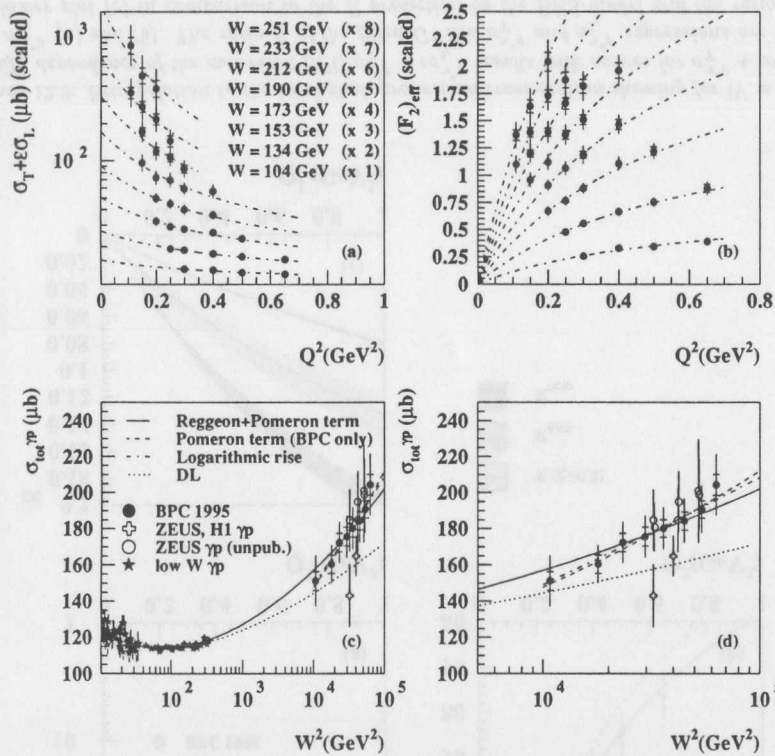


Figure 12.7: Extrapolation to the total photoproduction cross-section using the BPC  $\sigma_T^{\gamma^*p} + \epsilon\sigma_L^{\gamma^*p}$  results:  $\sigma_T^{\gamma^*p} + \epsilon\sigma_L^{\gamma^*p}$  (a) and  $(F_2)_{eff} = F_2 - (y^2/Y_+)F_L$  (b) as a function of  $Q^2$ . The respective GVDM-expression is overlaid (dashed-dotted curve). The extrapolated values for  $\sigma_{tot}^{\gamma p}(W)$  are shown in (c) and (d) (solid dots) together with published measurements of the total photoproduction cross-section from H1 and ZEUS (open crosses) and unpublished ZEUS results (open circles). Various fitted curves are overlaid for comparison.

$W$ (GeV)	$\epsilon$	$\sigma_{tot}^{\gamma p} \pm \text{stat} \pm \text{sys}$ ( $\mu\text{b}$ )	$\Delta\sigma_{tot}^{\gamma p}(\xi = 0.0)$ ( $\mu\text{b}$ )	$\Delta\sigma_{tot}^{\gamma p}(\xi = 0.4)$ ( $\mu\text{b}$ )
104	0.99	$151.2 \pm 5.2 \pm 13.2$	-2.2	+2.1
134	0.98	$160.9 \pm 5.0 \pm 9.2$	-2.6	+2.6
153	0.96	$172.6 \pm 5.0 \pm 10.2$	-3.0	+3.0
173	0.92	$175.8 \pm 5.1 \pm 10.3$	-3.3	+3.4
190	0.88	$180.4 \pm 4.9 \pm 10.5$	-3.5	+3.8
212	0.80	$184.5 \pm 5.0 \pm 11.0$	-4.1	+4.6
233	0.69	$190.9 \pm 4.8 \pm 12.2$	-4.4	+5.1
251	0.55	$204.5 \pm 5.8 \pm 16.0$	-5.1	+6.2

Table 12.1: Results on the extrapolation of the BPC results of  $\sigma_T + \epsilon\sigma_L$  to  $Q^2 = 0$ .

Figure 12.8 (a) shows for one  $W$  bin ( $W = 134$  GeV) the measured values of  $\sigma_T^{\gamma^*p} + \epsilon\sigma_L^{\gamma^*p}$  ( $\epsilon = 0.98$ ) together with the fitted curves for  $\sigma_T^{\gamma^*p}$ ,  $\sigma_L^{\gamma^*p}$  and  $\sigma_T^{\gamma^*p} + \epsilon\sigma_L^{\gamma^*p}$ . Figure 12.8 (b) indicates that the above GVDM ansatz provides a good description of the observed  $Q^2$  dependence ( $\chi^2/ndf = 34/(34 - 9) = 1.3$ ).

Figure 12.8 (c) shows the ratio  $R$  of the fitted  $\sigma_T^{\gamma^*p}$  and  $\sigma_L^{\gamma^*p}$  expressions, taking into account the total error of  $m_0^2$  as denoted by the error band. The plotted values for  $\xi = 0.2$  are shown in comparison to the  $R$  prediction by the BKS-model and the ratio  $R$  based on the recent GVDM-ansatz of Schildknecht and Spiesberger (ScSp).

Using the simple GVDM inspired ansatz for  $\sigma_T^{\gamma^*p}$  (Equation 12.6) and  $\sigma_L^{\gamma^*p}$  (Equation 12.7) allows to successfully describe the  $Q^2$  dependence of the measured values of  $\sigma_T + \epsilon\sigma_L$  as obtained in this thesis. This then allows to extract the total  $\gamma p$  cross-section as well as the ratio  $R = \sigma_L^{\gamma^*p}/\sigma_T^{\gamma^*p}$  using a particular GVDM-ansatz.

### (b) Regge analysis

Figure 12.7 (c) shows a fit to low  $W$  data [Ca78], the BPC extrapolated total  $\gamma p$  cross-sections and the published measurement of the total photoproduction cross-section at HERA [Ai95, De94] using a Regge motivated description as the sum of a Reggeon and a Pomeron contribution (Section 2.3.3):

$$\sigma_{tot}^{\gamma p}(W) = A_R(W^2)^{\alpha_R-1} + A_P(W^2)^{\alpha_P-1} \quad (12.8)$$

This fit yields the following result:

$$\begin{aligned} \alpha_R &= 0.663 \pm 0.022(\text{stat}) \pm 0.044(\text{sys}) \\ A_R &= 127.7 \mu\text{b} \pm 1.5 \mu\text{b}(\text{stat}) \pm 9.7 \mu\text{b}(\text{sys}) \\ \alpha_P &= 1.118 \pm 0.006(\text{stat}) \pm 0.024(\text{sys}) \\ A_P &= 50.1 \mu\text{b} \pm 2.9 \mu\text{b}(\text{stat}) \pm 9.4 \mu\text{b}(\text{sys}) \end{aligned} \quad (12.9)$$

The extrapolated total  $\gamma p$  cross-sections using the BPC  $F_2$  results are based on a common value for  $m_0^2$ , as discussed in the preceding section. The statistical errors on the extrapolated total  $\gamma p$  cross-sections are therefore correlated. This correlation has been ignored for the above Regge inspired fit.

Ignoring the Reggeon contribution, which is less than 5% for  $W^2 > 10000$  GeV<sup>2</sup> based on the above expression, the fit to the extrapolated total  $\gamma p$  cross-sections using only the BPC  $F_2$

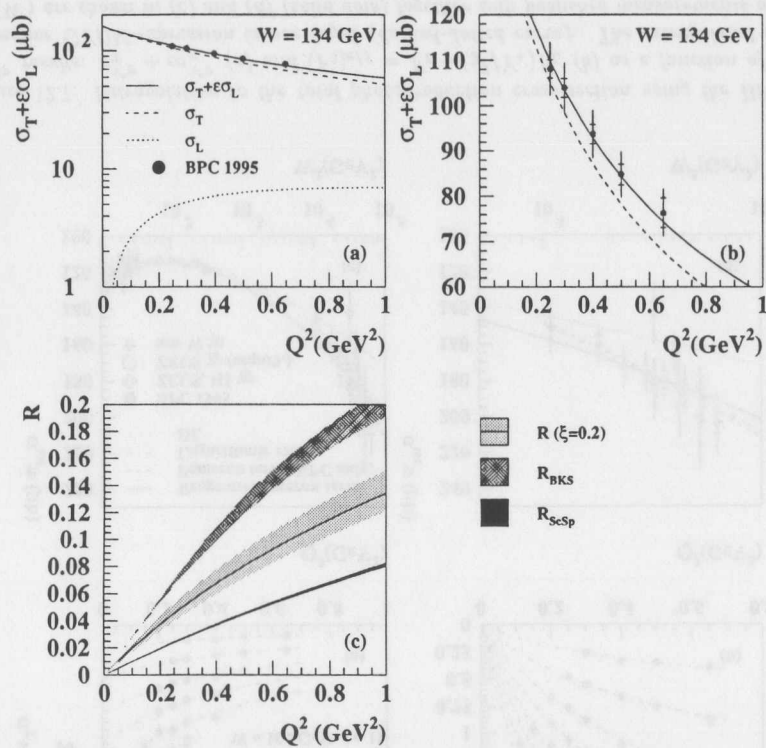


Figure 12.8: Extrapolation to the total photoproduction cross-section showing for  $W = 134$  GeV the  $Q^2$  dependence of the measured BPC  $\sigma_T^{\gamma p} + \epsilon\sigma_L^{\gamma p}$  results with curves for  $\sigma_T^{\gamma p} + \epsilon\sigma_L^{\gamma p}$ ,  $\sigma_T^{\gamma p}$  and  $\sigma_L^{\gamma p}$  (a) and (b). The ratio  $R$  of the fitted GVDM  $\sigma_T^{\gamma p}$  and  $\sigma_L^{\gamma p}$  expressions are shown in the lower plot (c) in comparison to the  $R$  prediction by the BKS-model and the ratio  $R$  based on the recent GVDM-ansatz of Schildknecht and Spiesberger (ScSp).

measurements, including the Pomeron term only, yields the following result:

$$\begin{aligned}\alpha_P &= 1.157 \pm 0.019 (\text{stat}) \pm 0.040 (\text{sys}) \\ A_P &= 34.8 \mu\text{b} \pm 7.0 \mu\text{b} (\text{stat}) \pm 14.7 \mu\text{b} (\text{sys})\end{aligned}\quad (12.10)$$

A fit to the extrapolated total  $\gamma p$  cross-sections using the BPC  $F_2$  results based on a logarithmic rise in  $W^2$  with  $\sigma_{tot}^{\gamma p} = A \ln^\gamma W^2$  yields the following result:

$$\begin{aligned}\gamma &= 1.500 \pm 0.324 (\text{stat}) \pm 0.107 (\text{sys}) \\ A &= 5.340 \mu\text{b} \pm 0.054 \mu\text{b} (\text{stat}) \pm 1.470 \mu\text{b} (\text{sys})\end{aligned}\quad (12.11)$$

Figure 12.7 (d) shows the BPC extrapolated total  $\gamma p$  cross-sections together with measured total  $\gamma p$  cross-sections at HERA in comparison to the DL description of the total  $\gamma p$  cross-section, the above two Regge inspired fits and the fit assuming a logarithmic rise of  $\sigma_{tot}^{\gamma p}$  in  $W^2$ . The  $W^2$  dependence of the extracted values of  $\sigma_{tot}^{\gamma p}$  using the BPC  $F_2$  results can be equally well described by a logarithmic rise,  $\sigma_{tot}^{\gamma p} \propto \ln^\gamma W^2$ , and a Regge-type power law behavior,  $\sigma_{tot}^{\gamma p} \propto (W^2)^{\alpha_P - 1}$ .

The value for the Pomeron intercept of  $\alpha_P = 1.118 \pm 0.006 (\text{stat}) \pm 0.024 (\text{sys})$  was obtained in this analysis. A DL-type analysis performed by Cudell et al. [Cu96] resulted in a Pomeron intercept of  $\alpha_P = 1.096^{+0.012}_{-0.009}$ . Both fitting results yield a Pomeron intercept which is higher than the one given by DL of 1.0808. The latter case provides a good description of the measured total  $\gamma p$  cross-sections at HERA. Those measured cross-sections are below the ones extrapolated from the BPC  $F_2$  results. Unpublished results on a measurement of the total  $\gamma p$  cross-section at ZEUS [Ma95, Sa96] lie slightly above the extrapolated values using the BPC  $F_2$  results as shown in Figure 12.7 (d). This discrepancy can only be resolved with a measurement of the total  $\gamma p$  cross-section at HERA with higher precision compared to the ones performed in the past.

The above Regge ansatz, as the sum of a Reggeon and Pomeron contribution, can be extended towards larger values of  $Q^2$  to investigate the contribution of non-perturbative mechanisms at larger values in  $Q^2$  similar to the DL model presented in [Do94]. The measured  $\sigma_{tot}^{\gamma p}$  cross-section values are fitted to the following functional form:

$$\sigma_{tot}^{\gamma p}(W^2, Q^2) = \left( \frac{M_R^2}{M_R^2 + Q^2} \right) A_R (W^2)^{\alpha_R - 1} + \left( \frac{M_P^2}{M_P^2 + Q^2} \right) A_P (W^2)^{\alpha_P - 1} \quad (12.12)$$

The parameters for  $A_R$  and  $\alpha_R$  as well as  $A_P$  and  $\alpha_P$ , are fixed to the ones extracted from the fit to low  $W$ , the extrapolated total  $\gamma p$  cross-section values and published measurements of the total photoproduction cross-section at HERA. The effective Reggeon and Pomeron masses  $M_R$  and  $M_P$  are constrained by the fit and are determined to be:  $M_R^2 = 0.144 \text{ GeV}^2$  and  $M_P^2 = 0.511 \text{ GeV}^2$ . The result of this fit is shown in Figure 12.9. Only  $Q^2$  bins with  $Q^2 \leq 0.65 \text{ GeV}^2$  are included in the fit which yield  $\chi^2/ndf = 38/(34 - 2) = 1.2$ . Including higher  $Q^2$  bins worsen the quality of the fit. This Regge fit, dominated by the contribution from a soft Pomeron mechanism, provides a good description of the BPC  $F_2$  results. It cannot account for the steeper rise in  $F_2$  as a function of  $x$  for  $Q^2 \geq 0.92 \text{ GeV}^2$ . The behavior of  $F_2$  as a function of  $x$  at low values of  $x$  is therefore consistent with the exchange of a soft Pomeron for  $Q^2 \leq 0.65 \text{ GeV}^2$ .

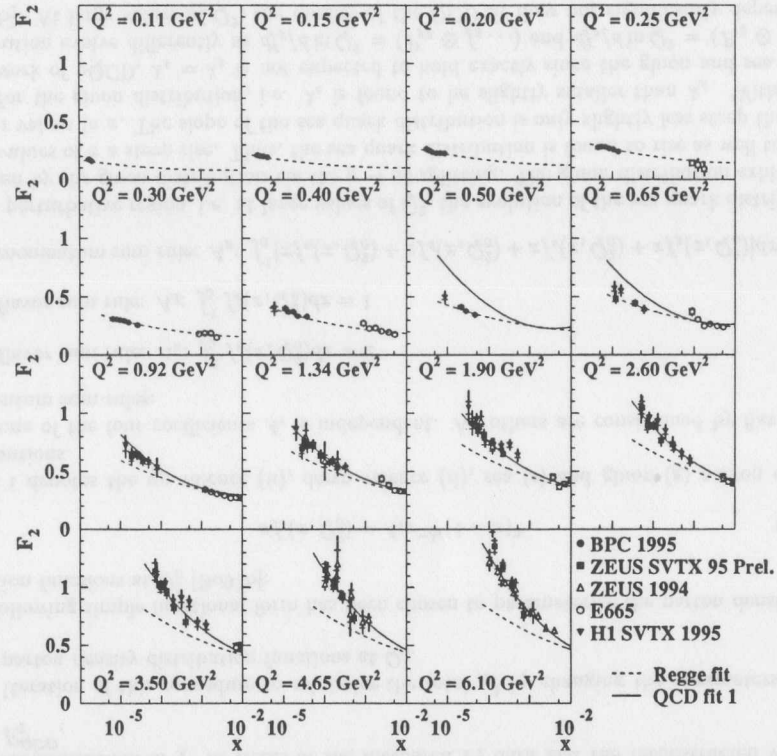


Figure 12.9: Comparison of a Regge-fit (Equation 12.12) and a QCD fit (QCD fit 1 with  $Q_0^2 = Q_{\min}^2 = 1.0 \text{ GeV}^2$ ; see section 12.4 for further details.) to  $F_2$  as function of  $x$  for different  $Q^2$  values.

In the low  $x$  region or equivalently at large values of  $W^2$  keeping  $Q^2$  fixed, the Pomeron term in equation 12.12 is the dominant contribution to  $\sigma_{tot}^{\gamma^*p}$ . This implies that  $F_2$  behaves like  $F_2 \propto x^{-\lambda}$  with  $\lambda = \alpha_P - 1$ , independent of  $Q^2$ . To investigate the applicability of this picture as a function of  $Q^2$ , fits of the form  $F_2 = C \cdot x^{-\lambda_{eff}}$  have been made to the  $F_2$  results of the BPC 1995 data, the preliminary results of the ZEUS SVTX 95 analysis and the ZEUS 94 data. For the high  $x$  region,  $F_2$  has been constrained by the E665 data [Ad96b]. These fits have been performed over 27  $Q^2$  bins between  $0.15 \text{ GeV}^2$  and  $45 \text{ GeV}^2$ , which thus cover the transition region from a ‘soft’ to a ‘hard’ behavior of  $F_2$ . For each  $Q^2$  bin, a minimum of four data points is required. For each data point included in the fit, it is required that  $x < 10^{-2}$  such that Reggeon contributions are small. The slope in  $F_2$ ,  $d \ln F_2 / d \ln x$ , is thus equivalent to  $\lambda_{eff}$ .

The statistical errors on  $\lambda_{eff}$  for each  $Q^2$  bin have been determined by fitting the above expression to each of the 24  $Q^2$  bins including statistical errors of the used data sets only. The systematic uncertainties on  $\lambda_{eff}$  have been estimated assuming that systematic checks per-

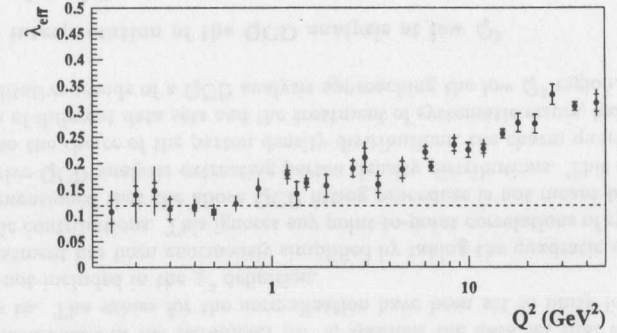


Figure 12.10:  $\lambda_{eff}$  ( $F_2 \propto x^{-\lambda_{eff}}$ ) as a function of  $Q^2$ . The dashed line refers to a determination of the soft Pomeron intercept (Equation 12.9).

formed for each of the four data sets to be independent. For one particular data set, the  $F_2$  points for each  $Q^2$  bin were moved up and down by the respective systematic error and the fit was repeated including statistical errors only, keeping the respective other data sets fixed. The changes, with respect to the nominal values of  $F_2$  in the determination of  $\lambda_{eff}$ , were added in quadrature and quoted as the respective systematic error for each extracted  $\lambda_{eff}$  value.

Figure 12.10 shows the slope of  $F_2$ ,  $\lambda_{eff} = d \ln F_2 / d \ln x$ , as a function of  $Q^2$ . The slope of  $F_2$  is found to be constant up to the highest  $Q^2$  values of the BPC  $F_2$  data set. The dashed line refers to a determination of the soft Pomeron intercept (Equation 12.9). For  $Q^2 < 1 \text{ GeV}^2$ , the results on  $F_2$  exhibit a rise in  $F_2$  which is equivalent to that of a soft Pomeron in the photoproduction case. For  $Q^2 \gtrsim 1 \text{ GeV}^2$ ,  $\lambda_{eff}$  gradually increases with  $Q^2$  indicating a ‘hard’ behavior of  $F_2$  and  $\sigma_{tot}^{\gamma^*p}$  and therefore the onset of pQCD.

## 12.4 QCD analysis at low $Q^2$

### Introduction

The following section is devoted to a QCD analysis of the proton structure function  $F_2$  at low values of  $Q^2$  based on an evolution of parton density distributions using the QCD DGLAP evolution equations in next-to-leading order (NLO) in the  $\overline{\text{MS}}$  scheme (Section 2.2.4). The main emphasis of this study is placed on qualitative features of a QCD analysis at low values of  $Q^2$  investigating various dependencies of the quality of the performed QCD fit, the  $x$  and  $Q^2$  dependence of  $F_2^{QCD}$ , the impact of the shape of the parton density distributions, the influence of the factorization and renormalization scales and the difference between a LO and NLO QCD evolution. It is the intention of these studies to provide qualitative arguments on the validity of pQCD calculations at low values of  $Q^2$ . The data sets used for the QCD fits to be presented are based on: BPC 1995, ZEUS SVTX 1995 Prel., ZEUS 1994, H1 SVTX 1995 and E665 (Figure 12.1).

### Technical details of the QCD analysis

The DGLAP evolution equations [A177, Gr72] have been discussed in section 2.2.4. The QCD analysis to be presented is based on the QCDNUM program [Bo97c] which allows to perform a NLO DGLAP evolution. It permits to evaluate the  $Q^2$  evolution of the gluon, singlet and non-singlet distributions, the  $Q^2$  evolution of  $\alpha_s$ , the calculation of  $F_2$ ,  $F_L$  and  $xF_3$  and the heavy quark contributions to  $F_2$  and  $F_L$ . These calculations can be carried out in LO and NLO. The QCDNUM program in connection with the function minimization package MINUIT [MI97], proceeds through the following steps:

1. Specification of a set of parton density distribution functions as a function of  $x$  at the starting scale  $Q_0^2$ .
2. Evaluation for each parton density distribution function the respective value at the starting scale  $Q_0^2$  on a user defined grid in  $x$  using a certain set of initial parameters.
3. Numerical solution of the DGLAP evolution equations and calculation of the resulting parton density distribution functions on a user defined grid in  $x$  and  $Q^2$ .
4. Reconstruction of  $F_2^{QCD}$  from the parton density distribution functions.
5. Determination of  $\chi^2$  in terms of the measured  $F_2$  data and the reconstructed value of  $F_2^{QCD}$ .
6. Iteration of this procedure to minimize the total  $\chi^2$  by changing the parameters of the parton density distribution functions at  $Q_0^2$ .

The following simple functional form has been chosen to parameterize the parton density distribution functions at  $Q_0^2$  [Bo97b]:

$$xf_i(x, Q_0^2) = A_i x^{-\lambda_i} (1-x)^{n_i} \quad (12.13)$$

where  $i$  denotes the up valence (u), down valence (d), sea (s) and gluon (g) parton density distributions.

Only one of the four coefficients  $A_i$  is independent. All others are constrained by flavor and momentum sum rules:

- flavor sum rule:  $A_u: \int_0^1 f_u(x, Q_0^2) dx = 2$
- flavor sum rule:  $A_d: \int_0^1 f_d(x, Q_0^2) dx = 1$
- momentum sum rule:  $A_g: \int_0^1 [xf_u(x, Q_0^2) + xf_d(x, Q_0^2) + xf_s(x, Q_0^2) + xf_g(x, Q_0^2)] dx = 1$

In the perturbative region, i.e. at large values of  $Q^2$ , the evolution of the sea quark distribution is driven by the gluon distribution via the  $g \rightarrow q\bar{q}$  splitting. The gluon distribution exhibits at small values of  $x$  a steep rise. Thus, the sea quark distribution is found to rise as well towards smaller values in  $x$ . The slope of the sea quark distribution is only slightly less steep than the slope for the gluon distribution, i.e.  $\lambda_s$  is found to be slightly smaller than  $\lambda_g$ . Within the framework of pQCD,  $\lambda_s = \lambda_g$  is not expected to hold exactly since the gluon and sea quark distribution evolve differently as  $df_g/d\ln Q^2 = (P_{gg} \otimes f_g \dots)$  and  $df_s/d\ln Q^2 = (P_{sg} \otimes f_g \dots)$  [Ma96b]. At large values of  $Q^2$ , the quality of the QCD fit does not significantly depend on, if  $\lambda_s$  is set equal to  $\lambda_g$  or if both parameters are left free. The latter case yields values on  $\lambda_s$ ,

which are slightly smaller than  $\lambda_g$ . The assumption on  $\lambda_s$  and  $\lambda_g$ ,  $\lambda_s = \lambda_g$ , is a well justified simplification at high  $Q^2$ .

In order to study the small  $x$  behavior of the sea quark and gluon distributions at low  $Q^2$ , QCD fits have been performed by allowing  $\lambda_s$  and  $\lambda_g$  to be different. It will be shown in the following section that the relation of the low  $x$  behavior of the gluon and sea quark distribution at high  $Q^2$  is no longer valid when approaching the region of small values in  $Q^2$ . It provides one indication besides others that expectation from QCD fits at high  $Q^2$ , start to lose their validity when approaching the low  $Q^2$  region.

The proton charge density distribution is written as follows:

$$q^{ep}(x, Q^2) = \sum_i e_i^2 [q_i(x, Q^2) + \bar{q}_i(x, Q^2)] = \langle e^2 \rangle \Sigma(x, Q^2) + q_{NS}^{ep}(x, Q^2) \quad (12.14)$$

where  $e_i$  is the quark charge of flavor  $i$  in units of the electron charge,  $\langle e^2 \rangle = (1/n_f) \sum e_i^2$  is the average of the square of quark charges.  $n_f$  is the number of flavors. The distribution  $q_{NS}^{ep}(x, Q^2)$  is a pure  $q^+$ -type non-singlet distribution and is given as follows:  $q_{NS}^{ep}(x, Q^2) = \sum_{i=1}^{n_f} e_i^2 q_i^+(x, Q^2)$ .

The QCD evolution to be presented here has been performed in the light flavor scheme such that the three lightest quark flavors  $u$ ,  $d$  and  $s$  as well as the charm quark  $c$ , are evolved in  $Q^2$  [Bo97c].

The strong coupling constant has been taken to be the world average value of  $\alpha_s$  at the mass of the  $Z_0$  boson:  $\alpha_s(M_Z) = 0.118$  [Ba96b].

The contribution of higher twist terms has been shown to be only important at large values of  $x$  [Vi92]. The following QCD fit has been simplified by taking into account only  $F_2$  measurements for which  $W^2 > 10 \text{ GeV}^2$ . The contribution from higher twist terms has been therefore ignored. The data sets included in the QCD fit are the HERA data from BPC 1995, ZEUS 1994, ZEUS SVTX 1995 Prel., H1 SVTX 1995 and data from the fixed-target experiment of E665. The  $\chi^2$ , minimized in the QCD fitting procedure, has been defined as follows:

$$\chi^2 = \sum_{i=1}^{N_p} \left( \frac{F_2^{data}(x_i, Q_i^2) - f(s_i) F_2^{QCD}(x_i, Q_i^2)}{\sigma_i^{data}} \right)^2 + \sum_{j=1}^{N_s} \left( \frac{1 - f(j)}{\sigma_j^{norm}} \right)^2 \quad (12.15)$$

$N_p$  is the number of data points,  $F_2^{data}(x_i, Q_i^2)$  and  $F_2^{QCD}(x_i, Q_i^2)$  are the values for  $F_2$  from data and the QCD fit at a particular data point  $(x_i, Q_i^2)$  and  $\sigma_i^{data}$  are the errors on  $F_2^{data}(x_i, Q_i^2)$ .  $f(j)$  is the normalization and  $\sigma_j^{norm}$  is the uncertainty on the normalization of the  $N_s$  data sets taken into account in the parameter fit.  $s_i$  specifies the data set that a particular data point belongs to. The values for the normalization have been set to unity for simplicity and are therefore not included in the  $\chi^2$  definition.

The error treatment has been enormously simplified by taking the quadratic sum of statistical and systematic contributions. This ignores any point-to-point correlations of systematic errors. It should be mentioned that the above QCD fitting procedure is not meant to perform a precise quantitative QCD analysis extracting parton density distributions. This simple approach with respect to the choice of the parton density distributions, the charm quark treatment, the normalization of different data sets and the treatment of systematic errors, has been chosen to show the qualitative trends of a QCD analysis approaching the low  $Q^2$  region.

### Results and interpretation of the QCD analysis at low $Q^2$

The intention of the following section is to provide qualitative arguments on the validity of pQCD calculations at low values of  $Q^2$ . Those are based on a variety of detailed studies

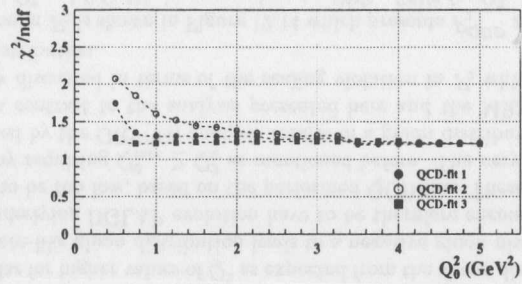


Figure 12.11:  $\chi^2$  per degree of freedom of QCD fits at low  $Q^2$ .

taking into account several aspects of the DGLAP QCD evolution. These studies include the dependence on the starting scale  $Q_0^2$ , on the lower  $Q^2$  cut,  $Q_{min}^2$ , with respect to the data sets to be included in the QCD fit, an investigation of the shape of the gluon and sea quark distribution and the impact of a LO or NLO QCD evolution as well as the impact of a change in the renormalization and factorization scale on  $F_2$  and  $F_2^c$ . The emphasis will be placed on characteristic changes of the latter aspects when reaching the low  $Q^2$  region.

Previous QCD analyses, such as those performed by the MRS group, have shown that a QCD fit with a starting scale,  $Q_0^2$ , of 4.5 GeV<sup>2</sup> provides a good description of  $F_2$  data. The general strategy of the following QCD analysis is based on several QCD fits with a starting scale of 5.0 GeV<sup>2</sup> which is steadily reduced in steps of 0.25 GeV<sup>2</sup> down to 0.5 GeV<sup>2</sup>. The lower cut on  $Q^2$ ,  $Q_{min}^2$ , with respect to the data sets to be included in the QCD fit, has been required for each QCD fit to be larger or equal to the respective starting scale, i.e.,  $Q_{min}^2 \geq Q_0^2$ . This procedure avoids the problem of backward evolution in cases of  $Q_{min}^2 < Q_0^2$  which has been found to be an extremely unstable procedure at low  $Q^2$  contrary to the case for QCD fits performed at high  $Q^2$  [Bo97b]. It has been found that a backward evolution at low  $Q^2$  could deteriorate the chosen input distribution resulting in unphysical parton density distributions. This will be discussed in the following in connection with the gluon distribution. The following QCD fits have been performed:

1. NLO:  $Q_0^2 = Q_{min}^2 = 0.5 \dots 5.0$  GeV<sup>2</sup> in steps of 0.25 GeV<sup>2</sup> and  $\lambda_s \neq \lambda_g$
2. NLO:  $Q_0^2 = Q_{min}^2 = 0.5 \dots 5.0$  GeV<sup>2</sup> in steps of 0.25 GeV<sup>2</sup> and  $\lambda_s = \lambda_g$
3. NLO:  $Q_{min}^2 = 5.0$  GeV<sup>2</sup> with  $Q_0^2 = 0.5 \dots 5.0$  GeV<sup>2</sup> in steps of 0.25 GeV<sup>2</sup> and  $\lambda_s \neq \lambda_g$
4. LO:  $Q_0^2 = Q_{min}^2 = 0.5 \dots 5.0$  GeV<sup>2</sup> in steps of 0.25 GeV<sup>2</sup> and  $\lambda_s \neq \lambda_g$

The third QCD fit has been carried out to investigate the impact of excluding low  $Q^2$  data from the QCD fit on the quality of the fit as well as on the shape of the extracted gluon and sea quark distribution in comparison to the first QCD fit.

Figure 12.11 shows the  $\chi^2$  per degree of freedom ( $ndf$ ) as a function of the starting scale  $Q_0^2$  for the first, second and third QCD fit. For the first and the third case,  $\chi^2/ndf$  rises for  $Q_0^2 < 1$  GeV<sup>2</sup>. Excluding low  $Q^2$  data for the third QCD fit leads to a somewhat better fit and the rise for  $Q_0^2 < 1$  GeV<sup>2</sup> occurs to be less steep compared to the first QCD fit. In case of the second QCD fit, i.e. in case of  $\lambda_s = \lambda_g$ , the rise in  $\chi^2/ndf$  as a function of  $Q_0^2$  occurs already at around 3 GeV<sup>2</sup>. This would imply that, based on the quality of the fit, the case of  $\lambda_s \neq \lambda_g$

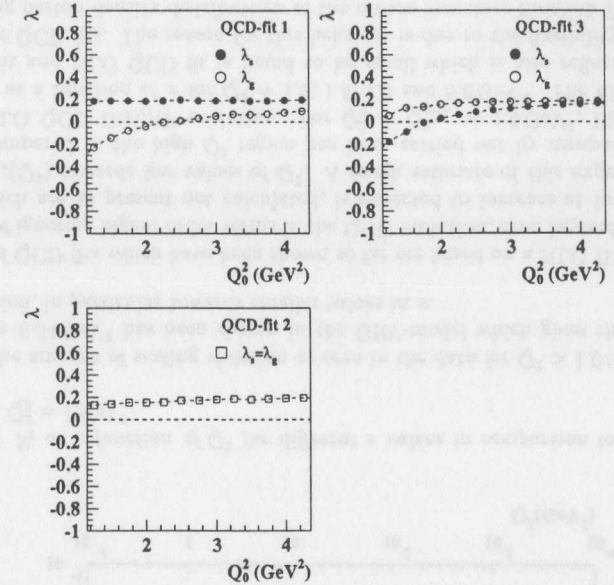


Figure 12.12: Exponents of the gluon ( $\lambda_g$ ) and sea ( $\lambda_s$ ) distribution as a function of  $Q_0^2$  for several QCD fits at low  $Q^2$  (See text for further details).

is in favor compared to the case of  $\lambda_s = \lambda_g$ , to describe the  $F_2$  data down to low values in  $Q^2$ . Such a behavior is not expected for QCD fits at high  $Q^2$  as mentioned in the previous section. Figure 12.9 shows  $F_2$  as a function of  $x$  in bins of  $Q^2$ . The result from the first QCD fit for  $Q_{min}^2 = Q_0^2 = 1.0$  GeV<sup>2</sup> is overlaid. It shows that such a QCD fit allows to provide a good description of  $F_2$  data down to around 1.0 GeV<sup>2</sup> as already seen from the respective  $\chi^2/ndf$  of the fit.

The above three cases of the performed QCD fits will be now compared with respect to the shape of the extracted gluon and sea quark distribution in terms of the values of  $\lambda_g$  and  $\lambda_s$  as a function of the respective starting scale  $Q_0^2$ . It has been discussed in the last section that in the framework of pQCD,  $\lambda_g$  is slightly larger than  $\lambda_s$ , that is the sea quark distribution is driven by the gluon distribution which has been found to be valid for QCD fits performed at high values of  $Q^2$ . It will be shown that this is no longer the case when reaching the low  $Q^2$  region.

Figure 12.12 displays for the first three QCD fits, the values of  $\lambda_s$  and  $\lambda_g$  as a function of  $Q_0^2$ . For the first QCD fit, the sea quark distribution remains singular, i.e.  $\lambda_s > 0$ , down to the lowest value of  $Q_0^2$  whereas the gluon distribution becomes less and less singular and turns into a valence-like gluon distribution, i.e.  $\lambda_g < 0$ , at around 2.5 GeV<sup>2</sup>. This behavior is not seen for the third QCD fit which includes  $F_2$  data only above 5.0 GeV<sup>2</sup>.  $\lambda_g$  is found to be always larger than  $\lambda_s$ , similar to QCD fits performed at high  $Q^2$ . This is in contrast to the first QCD fit which includes low  $Q^2$  data. In case of the second QCD fit, the condition  $\lambda_s = \lambda_g$  forces both distribution to be singular. The quality of the fit for the first QCD fit ( $\lambda_s \neq \lambda_g$ ) compared to

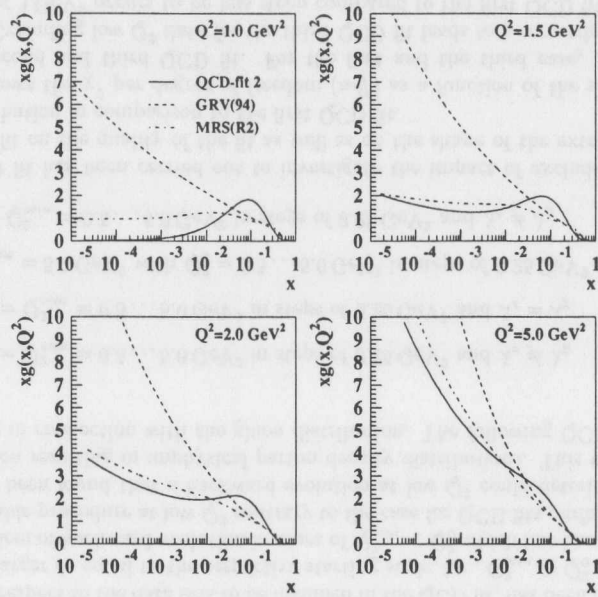


Figure 12.13: Gluon distribution functions as a function of  $x$  for different  $Q^2$  values.

the second QCD fit ( $\lambda_s = \lambda_p$ ) therefore implies that the  $F_2$  data favor the case of a valence-like gluon distribution in connection with a singular sea quark distribution if a QCD fit is performed including  $F_2$  data down to low values in  $Q^2$ . This is not expected from QCD fits at high  $Q^2$  and shows that well established pQCD results at high  $Q^2$  lose their validity at low  $Q^2$ . It indicates the beginning of a soft behavior in the  $F_2$  data included in the QCD fit [Ma97]. This behavior has been also found by [Ma96b] when performing QCD fits at a scale of  $Q_0^2 = 1 \text{ GeV}^2$  including low  $Q^2$  data down to  $1.5 \text{ GeV}^2$ .

The extracted gluon distribution is shown for the first QCD fit in Figure 12.13 as a function of  $x$  for four bins in  $Q^2$ . The gluon distributions from the GRV(94) and the MRS(R2) analyses are overlaid for comparison. It shows that the gluon distribution is valence-like for  $Q^2 = 1.0 \text{ GeV}^2$  and becomes singular for higher values of  $Q^2$  as expected from the above discussion. A backward evolution of a valence-like gluon distribution leads to a negative gluon distribution. Numerical problems of the underlying DGLAP evolution have to be therefore encountered if the starting scale  $Q_0^2$  is chosen to be too low, based on the performed QCD-fits. These problems have been therefore avoided by requiring  $Q_{\text{min}}^2 \geq Q_0^2$  as mentioned before. The very low starting scale of  $Q_0^2 = 0.34 \text{ GeV}^2$  used by the GRV(94) analysis results in a gluon distribution which is singular at  $Q^2 = 1 \text{ GeV}^2$  in contrast to the analysis presented here and the MRS(R2) analysis. This feature will be now discussed in terms of the scaling violation in  $F_2$  which increases with the respective gluon distribution.

The scaling violation in  $F_2$  is shown in Figure 12.14 which presents  $F_2^{QCD}$  as a function of  $Q^2$  for fixed values of  $x$  for  $Q_0^2 = 1.0 \text{ GeV}^2$ , in comparison to  $F_2^{\text{data}}$ .  $F_2^{\text{data}}$  for  $Q^2 < 1.0 \text{ GeV}^2$  are shown as well. Those have not been included in the performed QCD fit.  $F_2^{QCD}$  for  $Q_0^2 = 1.0 \text{ GeV}^2$  can

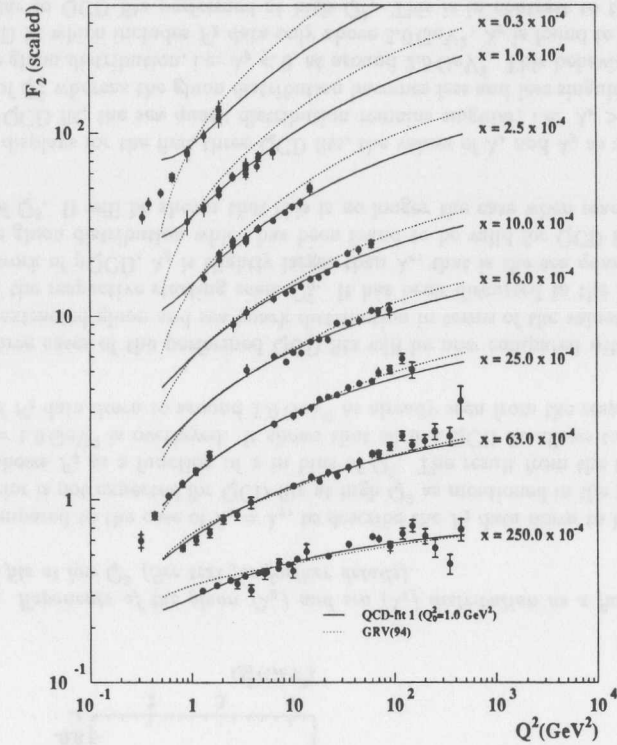


Figure 12.14:  $F_2$  as a function of  $Q^2$  for different  $x$  values in comparison to GRV(94) and a QCD-fit with  $Q_0^2 = 1 \text{ GeV}^2$ .

account for the amount of scaling violation as seen in the data for  $Q^2 > 1.0 \text{ GeV}^2$ . A starting scale of  $Q_0^2 = 0.34 \text{ GeV}^2$  has been chosen in the GRV-model which gives rise to a too large scaling violation, in particular towards smaller values in  $x$ .

The results of QCD fits which have been shown so far are based on a NLO DGLAP evolution. The impact of ignoring higher order terms in the QCD evolution, even beyond a NLO DGLAP evolution which are at present not calculated, is expected to increase at low  $Q^2$  due to the increase of  $\alpha_s(Q^2)$  towards low values of  $Q^2$ . A rough estimate of this expected uncertainty at low  $Q^2$  compared to the high  $Q^2$  region has been carried out by comparing results from a LO and NLO QCD DGLAP evolution. For  $Q_0^2 = Q_{\text{min}}^2 = 1.0 \text{ GeV}^2$ , Figure 12.15 (top) shows  $F_2^{QCD}$  as a function of  $x$  for  $Q^2 = 1.0, 1.5, 2.0$  and  $5.0 \text{ GeV}^2$ . The difference between a LO QCD fit and NLO QCD fit is found to be small which is also reflected by the  $\chi^2$  of the respective QCD fits. The reason for this behavior is due to the flexibility in the choice of the underlying parton density distributions of the proton structure function  $F_2$  at the starting scale  $Q_0^2$  which thus hides the effect of ignoring higher order terms in the DGLAP evolution. The gluon distribution is shown as well in Figure 12.15 (bottom). Large differences are found

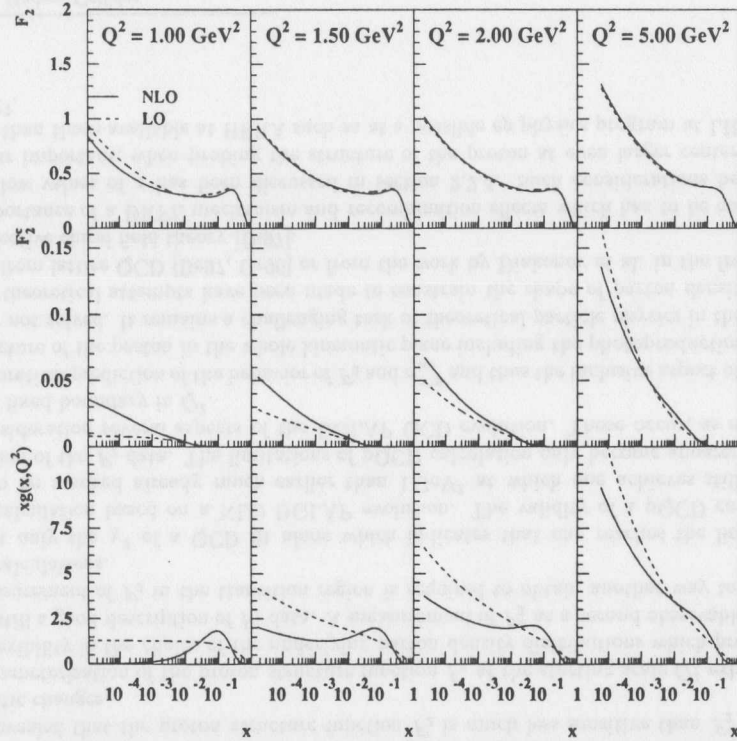


Figure 12.15: Comparison of  $F_2$  and  $F_2^\gamma$  in LO and NLO QCD evolution as a function of  $x$  for different  $Q^2$  values.

between a LO QCD fit and NLO QCD fit. However, the gluon distribution is not a directly measurable quantity. To examine the impact of higher order terms in the DGLAP evolution, the measurement of a second observable besides  $F_2$  is required. Candidates for such a measurement are the longitudinal structure function  $F_L$  and the structure function  $F_2^\gamma$ .  $F_2^\gamma$  can be calculated up to NLO using the QCDNUM program which has been therefore chosen for a comparison between a LO QCD fit and a NLO QCD fit. These results are shown in Figure 12.15 (middle). It is clearly visible that the difference between a LO QCD fit and a NLO QCD fit in case of  $F_2^\gamma$  increases towards low values of  $Q^2$ . It exhibits a difference of approximately 20% at  $2 \text{ GeV}^2$  which rises up to 50% at  $1 \text{ GeV}^2$ .

The sensitivity to the choice of the renormalization and factorization scale provides another useful check on the impact of ignoring higher order terms in the QCD evolution. Similar to the above comparison of a LO QCD fit and a NLO QCD fit, it was found that  $F_2$  exhibits essentially no change, whereas the structure function  $F_2^\gamma$  as a second observable shows as well drastic changes when varying the renormalization and factorization scale. Those differences increase towards smaller values in  $Q^2$ .

To conclude, the parameterization of the proton structure function  $F_2$  at the starting scale  $Q_0^2$ , exhibits too much flexibility in the choice of the underlying parton density distributions which thus hides the effect of ignoring higher order terms in the DGLAP evolution. A measurement of  $F_2^\gamma$  as a second observable besides the measurement of  $F_2$  in the transition region is required to validate pQCD calculations based on a NLO DGLAP evolution at low values of  $Q^2$ . A summary of these qualitative studies on the validity of pQCD calculations at low values of  $Q^2$  will be made in the next section.

## 12.5 Summary

It was the aim of this chapter to provide a detailed discussion on the behavior of  $F_2$  and  $\sigma_{tot}^{\gamma^*p}$  in the transition region between non-perturbative and perturbative QCD (pQCD) at low  $Q^2$  by investigating

- the  $x$ ,  $W^2$  and  $Q^2$  dependence of  $F_2$  and  $\sigma_{tot}^{\gamma^*p}$ ,
- the description of  $F_2$  and  $\sigma_{tot}^{\gamma^*p}$  in terms of theoretical models and
- the applicability of several model descriptions of the observed behavior of  $F_2$  and  $\sigma_{tot}^{\gamma^*p}$  within the framework of non-perturbative and perturbative QCD.

The slope in  $F_2$ ,  $d \ln F_2 / d \ln x$ , is found to be flat for  $Q^2 \lesssim 1 \text{ GeV}^2$  indicating a ‘soft’ behavior in  $F_2$  and  $\sigma_{tot}^{\gamma^*p}$ . The value of the slope is consistent with that of a soft Pomeron behavior based on a Regge-type fit to extrapolated values of the total  $\gamma p$  cross-section from a GVDM-ansatz using the BPC  $F_2$  data as obtained in this thesis. For  $Q^2 \gtrsim 1 \text{ GeV}^2$ , the slope in  $F_2$  begins to deviate from a ‘soft’ behavior and indicates the beginning of a ‘hard’ behavior in  $F_2$  and thus the onset of pQCD. The qualitative features of the ‘soft’ dominated region can be well accounted for by a Regge-type model such as DL, whereas the ‘hard’ dominated region can be represented by a pQCD model such as GRV(94). Within the current statistical and systematic errors of  $d \ln F_2 / d \ln x$ , the transition from non-perturbative to perturbative QCD at low  $Q^2$  appears to be smooth.

Several low- $x$ -low- $Q^2$  models have been compared to results on  $F_2$  and  $\sigma_{tot}^{\gamma^*p}$ . So far, none of the presented theoretical models allows to predict the behavior of  $F_2$  and  $\sigma_{tot}^{\gamma^*p}$  over the whole  $(x, Q^2)$  kinematic region, including the photoproduction limit. A recent update of the ALLM parameterization, taking into account the BPC  $F_2$  results and the H1 shifted vertex  $F_2$  results from the 1995 HERA run, allows to describe the data on  $\sigma_{tot}^{\gamma^*p}$  in the whole kinematic region. The transition region has been investigated in detail using well-established theoretical models such as the GVDM model and a Regge ansatz in the ‘soft’ dominated kinematic region and pQCD calculations based on a NLO DGLAP evolution in the ‘hard’ dominated kinematic region.

It has been shown that the  $Q^2$  dependence of the BPC  $F_2$  data can be well described using a GVDM-ansatz using explicit expressions for  $\sigma_T^{\gamma^*p}$  and  $\sigma_L^{\gamma^*p}$ . In the limit  $Q^2 \rightarrow 0$ , the result of a fit of these expressions to the measured values of  $\sigma_T^{\gamma^*p} + \epsilon \sigma_L^{\gamma^*p}$  allowed to extract the total  $\gamma p$  cross-section  $\sigma_{tot}^{\gamma^*p}$  in eight bins of  $W$ . The results on the parameters within  $\sigma_T^{\gamma^*p}$  and  $\sigma_L^{\gamma^*p}$  allowed to determine a model dependent estimate of  $R = \sigma_L^{\gamma^*p} / \sigma_T^{\gamma^*p}$ . The  $W^2$  dependence of the extracted values of  $\sigma_{tot}^{\gamma^*p}$  can be equally well described by a Regge-type power law behavior,  $\sigma_{tot}^{\gamma^*p} \propto (W^2)^{\alpha_P - 1}$  with  $\alpha_P = 1.157 \pm 0.019$  (stat)  $\pm 0.040$  (sys), and a logarithmic rise,  $\sigma_{tot}^{\gamma^*p} \propto \ln^\gamma W^2$  with  $\gamma = 1.500 \pm 0.324$  (stat)  $\pm 0.107$  (sys). Extending a Regge-type fit towards larger

values of  $Q^2$  according to [Do94] shows that the region of  $Q^2 \lesssim 1\text{GeV}^2$  can be well accounted for by a soft Pomeron behavior as expected from the dependence of  $d \ln F_2 / d \ln x$  as a function of  $Q^2$ .

A QCD analysis based on several QCD fits to  $F_2$  data using a NLO DGLAP evolution clearly revealed that pQCD calculations start to lose their validity when approaching the region of low values of  $Q^2$  taking into consideration several aspects of the DGLAP QCD evolution.

Including  $F_2$  data down to approximately  $1\text{GeV}^2$  showed that the  $\chi^2$  per degree of freedom rises rapidly as a function of  $Q_0^2$  for  $Q_0^2 < 1\text{GeV}^2$  in case of  $\lambda_s \neq \lambda_g$ , whereas for  $\lambda_s = \lambda_g$  the rise of  $\chi^2/ndf$  as a function of  $Q_0^2$  occurs already at around  $3\text{GeV}^2$ . Based on the quality of the fit, the  $F_2$  data seem to favor  $\lambda_g < \lambda_s$ . This behavior is in contrast to what one would expect from QCD fits using a NLO DGLAP evolution at high  $Q^2$  that the gluon distribution drives the sea quark distribution. It thus indicates a drastic change in the shape of parton density distributions when approaching the 'soft' region.

Numerical problems of the underlying DGLAP evolution have to be encountered if the starting scale  $Q_0^2$  is chosen too low.

The impact of ignoring higher order terms in the QCD evolution is expected to increase at low  $Q^2$  due to the increase of  $\alpha_s(Q^2)$  towards low values of  $Q^2$ . A rough estimate of this expected uncertainty at low  $Q^2$  compared to the high  $Q^2$  region has been carried out by comparing results from a LO and NLO QCD DGLAP evolution. A comparison between a LO and NLO QCD fit as well as a comparison between different choices of the renormalization and factorization scales revealed that the proton structure function  $F_2$  is much less sensitive than  $F_2^c$  to these systematic changes.

The parameterization of the proton structure function  $F_2$  at the starting scale  $Q_0^2$  exhibits too much flexibility in the choice of the underlying parton density distributions which provides at low  $Q^2$  still a good description of  $F_2$  data. A measurement of  $F_2^c$  as a second observable besides the measurement of  $F_2$  in the transition region is required to obtain another way to validate pQCD calculations.

It is not only the  $\chi^2$  of a QCD fit alone which indicates that one reaches the limits of a pQCD calculation based on a NLO DGLAP evolution. The validity of a pQCD calculation seems to be reached already much earlier than  $1\text{GeV}^2$  at which one achieves still a good description of the  $F_2$  data. The limitations of pQCD calculation only become apparent taking into consideration several aspects of the DGLAP QCD evolution. Those occur, as expected, not at a fixed boundary in  $Q^2$ .

The theoretical prediction of the behavior of  $F_2$  and  $\sigma_{tot}^{\gamma^*p}$  and thus the inclusive aspect of probing the structure of the proton in the whole kinematic plane including the photoproduction region, is by far not solved. It remains a challenging task of theoretical particle physics in the future. Various theoretical attempts have been made to constrain the shape of parton density distributions from lattice QCD [Be97, Gr96] or from the work by Diakonov et al. in the framework of an effective chiral field theory [Di97].

The importance of a BKFL mechanism and recombination effects which has to be considered at very low values of  $x$  has been discussed in section 2.2.4. Such considerations become in particular important, when probing the structure of the proton at even larger center-of-mass energies than those available at HERA such as at a possible  $ep$  physics program at LHC<sup>1</sup> or at the NLC<sup>2</sup>.

<sup>1</sup>Large Hadron Collider.

<sup>2</sup>Next Linear Collider.

## Chapter 13

### Summary and conclusions

The main physics motivation of this thesis has been the investigation of the transition region of non-perturbative to perturbative QCD (pQCD) in inelastic neutral current scattering,  $e^+p \rightarrow e^+X$ , at HERA by measuring the proton structure function  $F_2$  at low  $Q^2$ .

In order to study the transition from the photoproduction to the deep-inelastic scattering region, the kinematic coverage of the ZEUS detector was substantially extended in 1995 with the installation of two Beam Pipe Calorimeter (BPC) modules located on two sides of the beam at approximately 3 m from the interaction point in the outgoing positron direction.

In the first part of this thesis, the main emphasis was placed on the design, construction and operation of the BPC. The design had to incorporate various requirements to achieve a precise measurement of the energy and impact position of the scattered positron to reconstruct the event kinematics based on the Electron method. To limit systematic shifts on  $y$  and  $Q^2$  for  $y > 0.1$  and  $Q^2 > 0.1\text{GeV}^2$  to be less than 5%, the energy scale has to be determined at the level of 0.5% and the angle measurement with a precision of at least 0.3 mrad which requires the intrinsic position bias and the detector alignment to be well below 1 mm. This places stringent requirements on the energy and position reconstruction as well as the detector alignment. The design of the BPC as a segmented tungsten-scintillator sampling calorimeter with alternating 8 mm wide scintillator fingers, permits an energy resolution of  $17\%/\sqrt{E}$  and a position resolution of less than 1 mm. The performance of the BPC has been examined within a test-beam experiment at the DESY II test-beam facility for electron energies between 2 and 6 GeV which confirmed the specified requirements on the energy and position resolution. A stand-alone detector simulation of the BPC within EGS4 was written and used for the development of energy and position reconstruction algorithms.

The installation of the BPC within the existing ZEUS detector as a new component required, besides the implementation of a fast readout and trigger system to incorporate the 96 ns HERA bunch structure, a radiation monitoring system using active and passive radiation monitors since the BPC modules are installed very close to the HERA beams. During the 1995 HERA run, an accumulated dose of approximately 12 kGy had been observed at the closest distance of the BPC of approximately 4.3 cm to the beam. The effect of this radiation on the scintillator material had been examined using the results from <sup>60</sup>Co scans and scans of individual scintillator fingers using a <sup>106</sup>Ru source after the 1995 HERA run. The results of these scans had been incorporated in an EGS4 MC simulation to determine the effect on the energy linearity which was found to be less than 1% above the off-line positron energy cut of 7 GeV.

The position reconstruction has been carried out by logarithmically weighting the lateral energy depositions. This allowed to achieve a better position resolution as well as a smaller intrinsic position bias compared to a linear weighting. This method has also been used to reconstruct

the shower width through the second moment of the lateral shower distribution. A cut on the shower width was used as part of the positron identification. The absolute position of the BPC has been determined using elastic QED Compton events, besides an optical survey. A comparison between both results allowed to establish the required alignment accuracy of the BPC to be 0.5 mm. The relative and absolute energy scale calibration have been performed using  $e^+p$  kinematic peak events, taking into account possible degradations due to radiation damage. It has been shown that an energy uniformity of 0.5% can be achieved across the fiducial volume. The accuracy of the energy scale has been cross-checked using elastic  $\rho^0$  events. This allowed to establish an accuracy of the absolute energy scale of 0.5%.

The ZEUS BPC allowed a first measurement of the proton structure function  $F_2(x, Q^2)$  and the total  $\gamma^*p$  cross-section  $\sigma_{tot}^{\gamma^*p}$  for  $0.11 \leq Q^2 \leq 0.65 \text{ GeV}^2$  and  $1.7 \cdot 10^{-6} \leq x \leq 6.0 \cdot 10^{-5}$  which corresponds to a range in the  $\gamma^*p$  center-of-mass energy of  $104 \leq W \leq 251 \text{ GeV}$ . This analysis is based on  $1.65 \text{ pb}^{-1}$  of data which were taken during the 1995 HERA run. The statistical errors are well within 5% for all extracted  $F_2$  values. The total systematic errors are within 5% to 10%.

The behavior of  $F_2$  as a function of  $x$  for  $0.11 \leq Q^2 \leq 0.65 \text{ GeV}^2$  exhibits a slower rise in  $x$  compared to measurements of  $F_2$  at larger values of  $Q^2$ . This behavior can be well accounted for by a soft Pomeron. The transition from a 'soft' to a 'hard' dominated behavior appears to be smooth within errors. A recent update of the ALLM parameterization allows to describe the data on  $\sigma_{tot}^{\gamma^*p}$  in the whole kinematic region. None of the existing theoretical models allow to predict the behavior of  $F_2$  and  $\sigma_{tot}^{\gamma^*p}$  over the whole  $(x, Q^2)$  kinematic region, including the photoproduction limit.

The generalized vector dominance model (GVDM) has been used to extrapolate from the  $Q^2$  dependence of the measured values of  $\sigma_T^{\gamma^*p} + \epsilon\sigma_L^{\gamma^*p}$  to the total  $\gamma p$  cross-section. The GVDM expressions for  $\sigma_T^{\gamma^*p}$  and  $\sigma_L^{\gamma^*p}$  provide a good description of the measured values of  $\sigma_T^{\gamma^*p} + \epsilon\sigma_L^{\gamma^*p}$ . A model dependent estimate of  $R$  has been obtained from the fitted expressions of  $\sigma_T^{\gamma^*p}$  and  $\sigma_L^{\gamma^*p}$ . The  $W^2$  dependence of the extracted values of  $\sigma_{tot}^{\gamma^*p}$  can be equally well described by a logarithmic rise,  $\sigma_{tot}^{\gamma^*p} \propto \ln^\gamma W^2$  ( $\gamma = 1.500 \pm 0.324$  (stat)  $\pm 0.107$  (sys)), and a Regge-type power law behavior,  $\sigma_{tot}^{\gamma^*p} \propto (W^2)^{\alpha_P - 1}$  ( $\alpha_P = 1.157 \pm 0.019$  (stat)  $\pm 0.040$  (sys)).

A QCD analysis based on several QCD fits to  $F_2$  data using a NLO DGLAP evolution clearly revealed that pQCD calculations start to lose their validity when approaching the region of low values of  $Q^2$  taking into consideration several aspects of the DGLAP QCD evolution. Including  $F_2$  data down to  $1 \text{ GeV}^2$  showed that the  $\chi^2$  per degree of freedom rises rapidly as a function of  $Q_0^2$  for  $Q_0^2 \lesssim 1 \text{ GeV}^2$ . Numerical problems of the underlying DGLAP evolution are encountered if the starting scale  $Q_0^2$  is chosen to be too low. The size of scaling violations as predicted by the GRV(94) model with  $Q_0^2 = 0.34 \text{ GeV}^2$  are too large compared to those seen in the data. Expectations from QCD fits at high  $Q^2$  on the shape of the sea and gluon distribution are no longer valid when approaching the small  $Q^2$  region below approximately  $5 \text{ GeV}^2$ . The impact of including higher order terms in the QCD evolution, which is expected to increase at low  $Q^2$ , has been carried out by comparing results from a LO and NLO QCD DGLAP evolution. A comparison between a LO and NLO QCD fit as well as a comparison between different choices of the renormalization and factorization scales revealed that the proton structure function  $F_2$  is much less sensitive than  $F_2^z$  to these systematic changes. The parameterization of the proton structure function  $F_2$  at the starting scale  $Q_0^2$ , exhibits too much flexibility in the choice of the underlying parton density distributions which provides at low  $Q^2$  still a good description of  $F_2$  data. A measurement of  $F_2^z$  as a second observable besides the measurement of  $F_2$  in the transition region is required to obtain another way to validate pQCD calculations.

## Appendix A

### Drawings and pictures on the design and construction of the BPC

#### A.1 Beam pipe

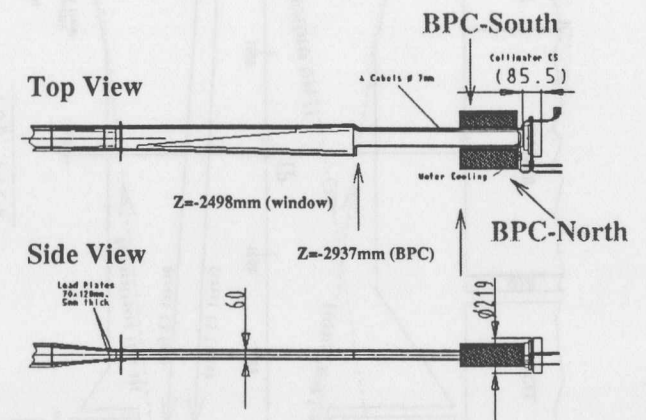


Figure A.1: Top and side view of the beam pipe (new in 1995) indicating the location of the BPC North and South module.

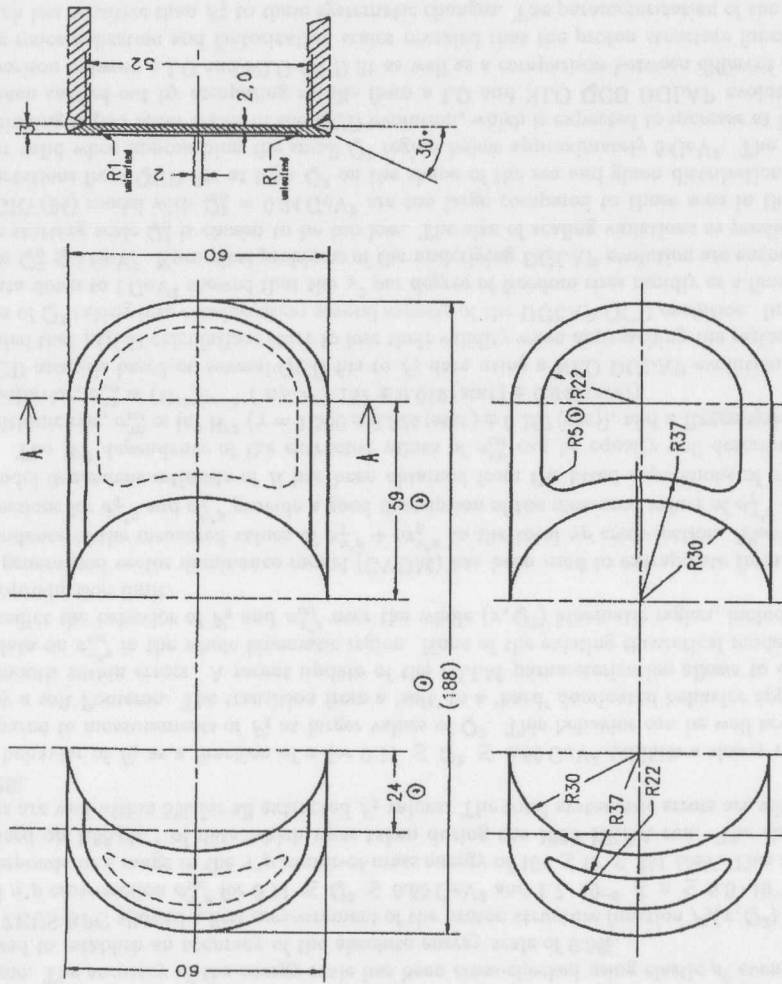


Figure A.2: Front view of the ZEUS beam pipe exit window at  $Z = -2498$  mm as seen from the interaction point. The center of HERA points upwards. All dimensions are in mm.

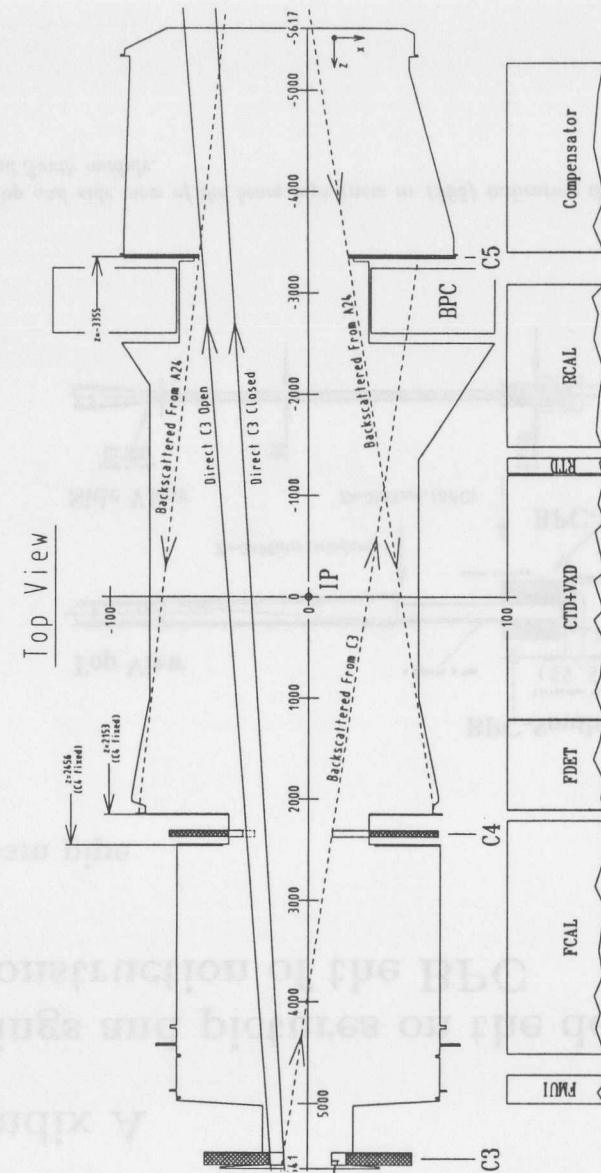


Figure A.3: Top view of the ZEUS interaction region indicating the direction of direct and backscattered synchrotron radiation and the location of the collimators C3-C5, the interaction point (IP) and several ZEUS detector components such as the BPC. All dimensions are in mm.

## A.2 Top and side view of the BPC

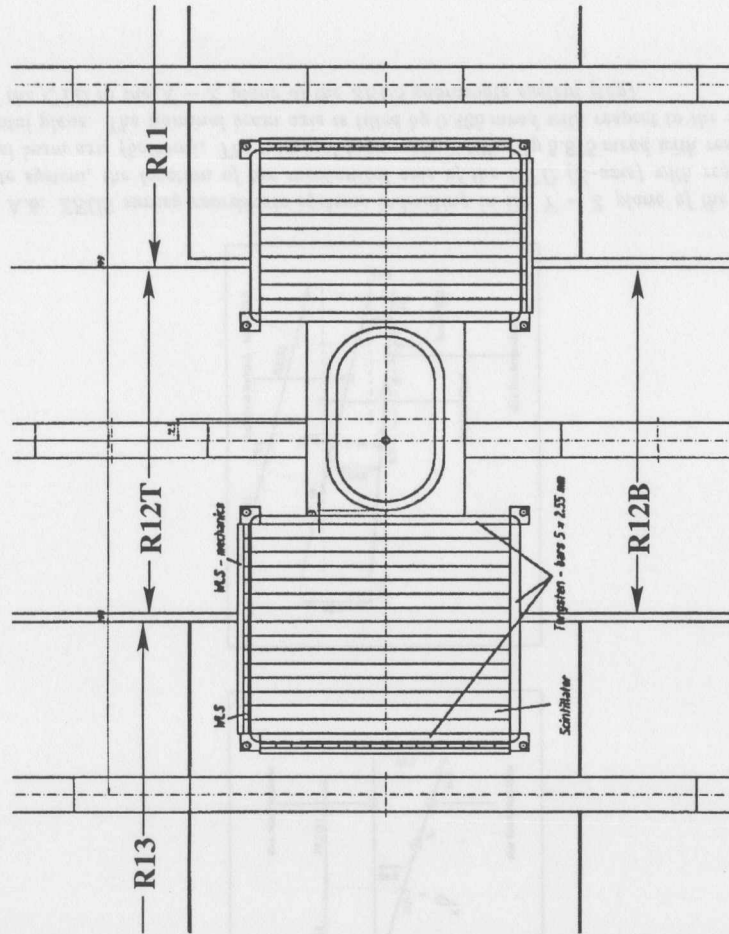


Figure A.4: Front view of the BPC modules and the location of the beam pipe and the surrounding RCAL modules (X - Y view).

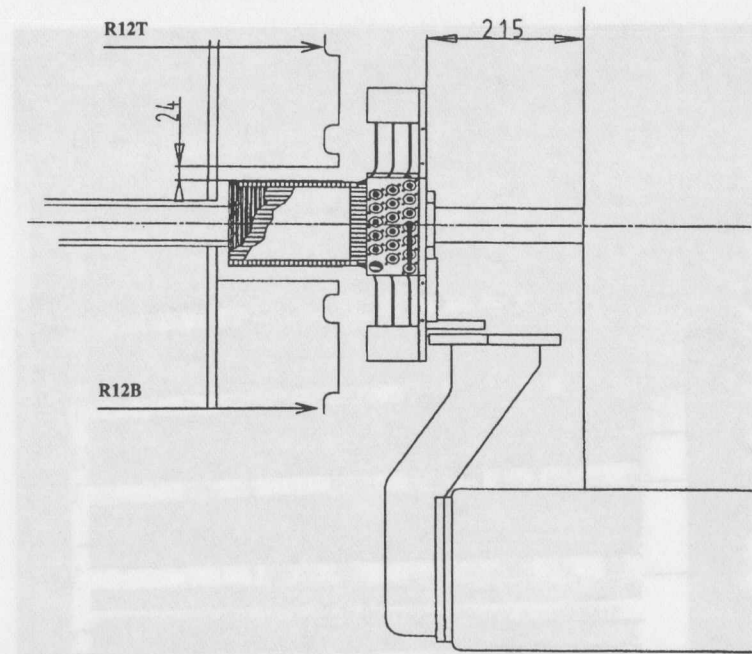


Figure A.5: Side view of the BPC with the location of the RCAL modules R12B and R12T and the compensator magnet (Y - Z view). All dimensions are in mm.

## A.3 ZEUS survey coordinate systems

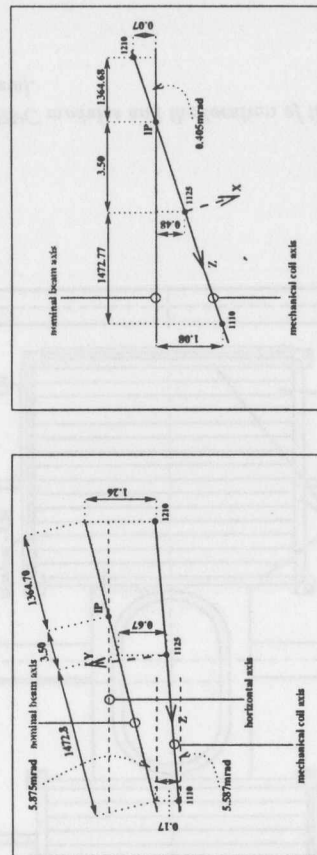


Figure A.6: *ZEUS* survey coordinate systems indicating in the  $Y - Z$  plane of the *ZEUS* coordinate system, the location of the mechanical axis of the CTD ( $Z$ -axis) with respect to the nominal beam axis (bottom). The nominal beam axis is tilted by 5.875 mrad with respect to the horizontal plane. The nominal beam axis is tilted by 0.405 mrad with respect to the mechanical axis of the CTD in the  $X - Z$  plane of the *ZEUS* coordinate system (top).

## A.4 Pictures of various BPC components

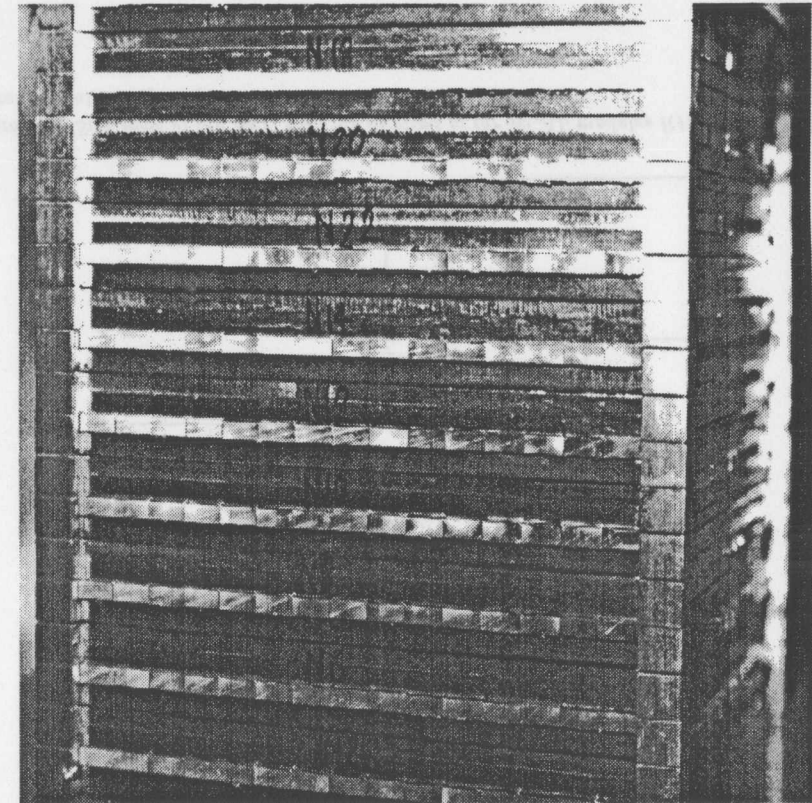


Figure A.7: Side view of the BPC North calorimeter stack showing for several scintillator layers the respective ends of each scintillator finger towards the wavelength shifters.

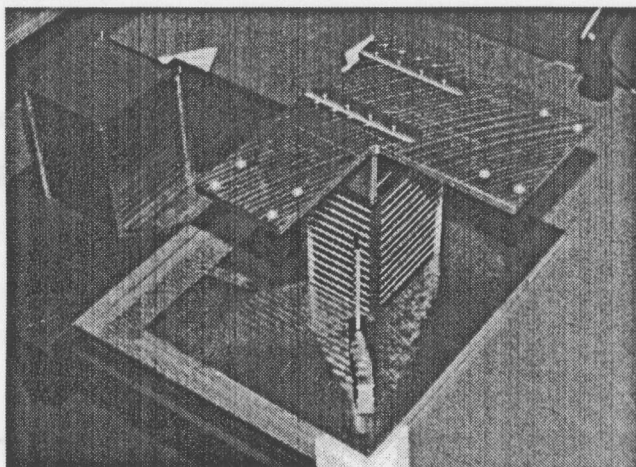


Figure A.8: Stacking of individual tungsten-scintillator layers with the aluminum support structure on top.

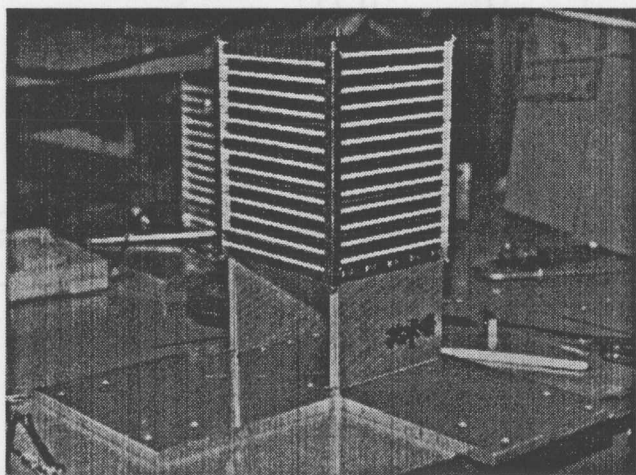


Figure A.9: Completed stack of individual tungsten-scintillator layers on top of the aluminum support structure.



Figure A.10: View of the assembled BPC North module.

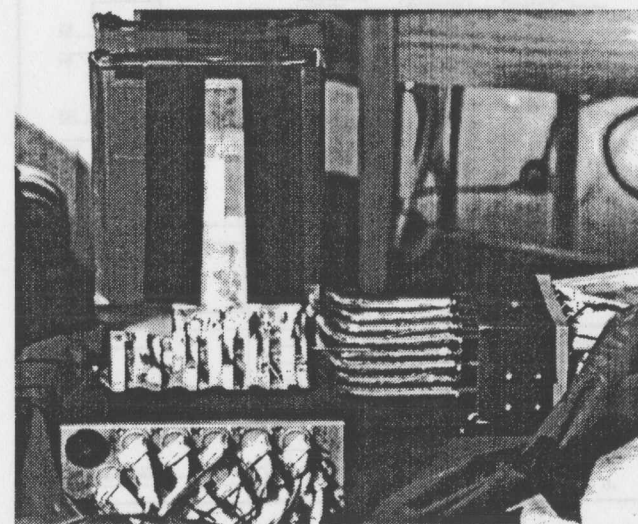


Figure A.11: View of the assembled BPC North module.

### A.5 BPC readout system

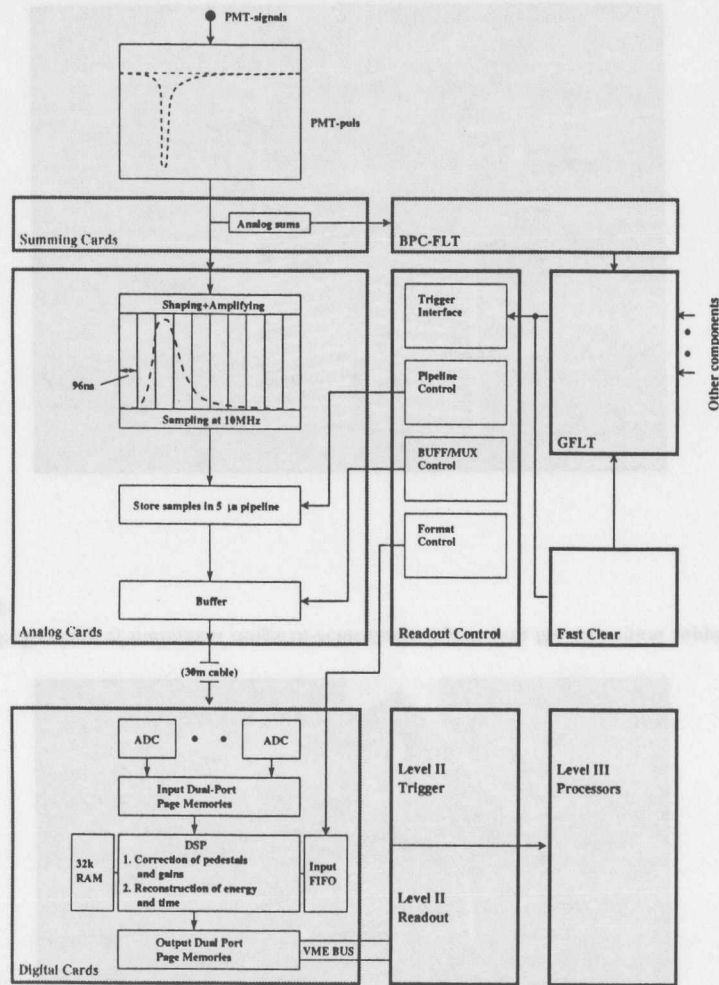


Figure A.12: Schematic diagram of the BPC trigger and readout system.

### A.6 BPC First-Level Trigger

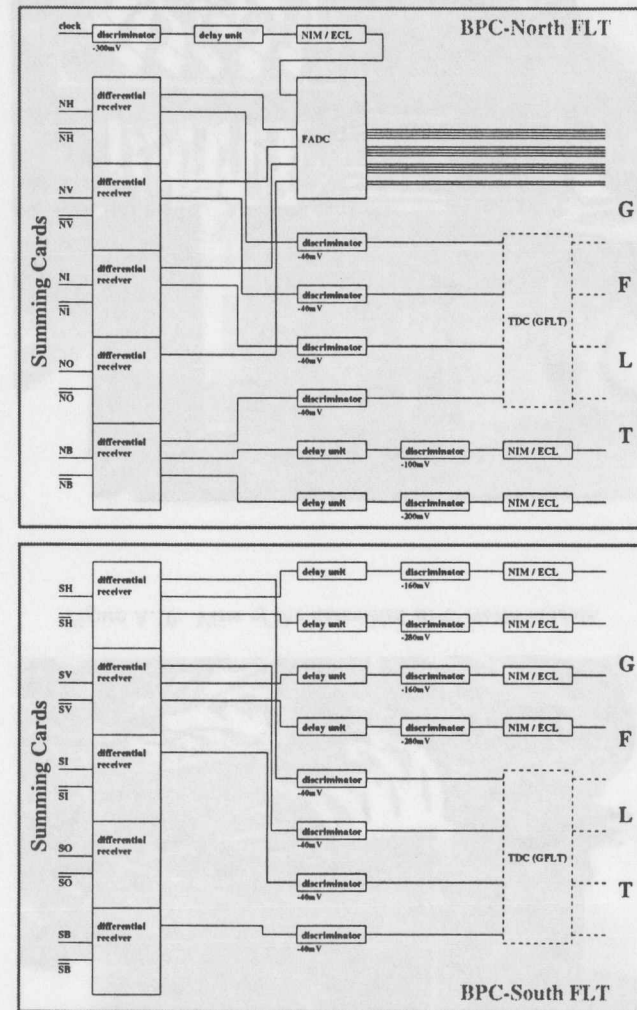


Figure A.13: Schematic diagram of the BPC FLT (See section 5.6 for further details).

## A.7 Location of various BPC readout components

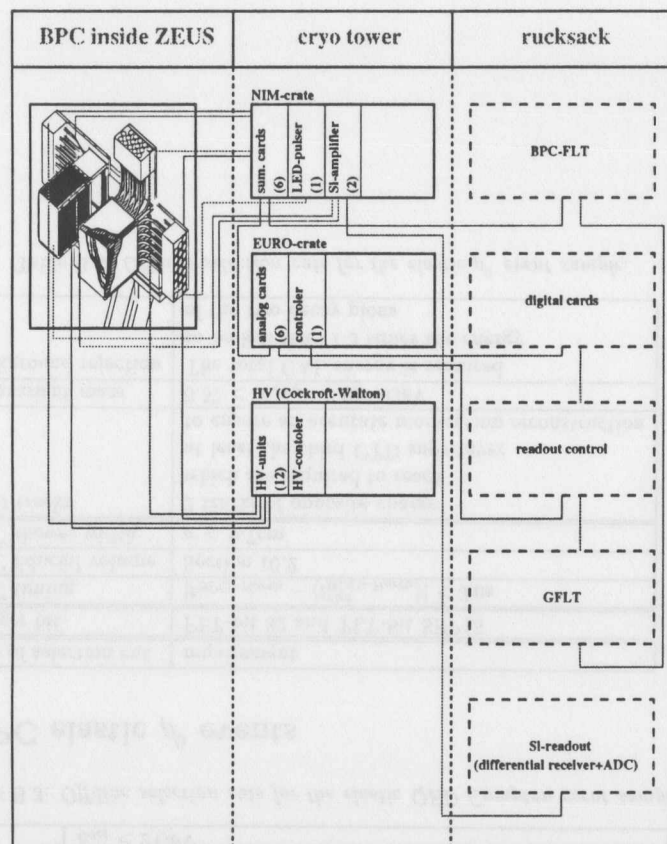


Figure A.14: Location of various BPC readout components

## Appendix B

## Summary of off-line selection cuts

B.1 BPC  $F_2$  analysis

type of selection cut	requirement
Trigger bit	FLT-bit 52 and TLT-bit DIS17
BPC timing	$ t_{BPC} - \langle t_{BPC}^{run} \rangle  < 3 \text{ ns}$
BPC energy	$E_{BPC-North} > 7 \text{ GeV}$
BPC fiducial volume	Section 10.2
BPC shower width	$\sigma < 0.7 \text{ cm}$
CAL $y_{JB}$	$y_{JB} > 0.06$
CAL $E_{tot}$	$E_{tot} > 3.1 \text{ GeV}$
EMPZ	$35 < EMPZ < 60 \text{ GeV}$
CAL timing	Section 10.2
CTD vertex	Section 10.2

Table B.1: Off-line selection cuts for the BPC  $F_2$  sample.

## B.2 BPC kinematic peak events

type of selection cut	requirement
Trigger bit	FLT-bit 52 and TLT-bit DIS18
BPC timing	$ t_{BPC} - \langle t_{BPC}^{run} \rangle  < 3 \text{ ns}$
BPC fiducial volume	Section 10.2
BPC shower width	$\sigma < 0.7 \text{ cm}$
CAL $y_{JB}$	$y_{JB} < 0.04$
EMPZ	$EMPZ > 35 \text{ GeV}$
CAL timing	Section 10.2
CTD vertex	Section 10.2

Table B.2: Off-line selection cuts for the kinematic peak event sample.

### B.3 BPC elastic QED Compton events

type of selection cut	requirement
Trigger bit	FLT-bit 31 and TLT-bit DIS19
BPC timing	$ t_{\text{BPC-North}} - \langle t_{\text{BPC-North}}^{\text{un}} \rangle  < 3 \text{ ns}$ and $ t_{\text{BPC-South}} - \langle t_{\text{BPC-South}}^{\text{un}} \rangle  < 3 \text{ ns}$
BPC energy 1	$E_{\text{BPC-North}} > 12 \text{ GeV}$ and $E_{\text{BPC-South}} > 6 \text{ GeV}$
BPC energy 2	$ E_{\text{BPC-North}} + E_{\text{BPC-South}} - 27.5  < 5 \text{ GeV}$
BPC fiducial volume	BPC North and South (Section 10.2)
BPC shower width	BPC North and South (Section 10.2)
CAL $E_{\text{tot}}$	$E_{\text{tot}} < 2 \text{ GeV}$

Table B.3: Off-line selection cuts for the elastic QED Compton event sample.

### B.4 BPC elastic $\rho^0$ events

type of selection cut	requirement
Trigger bit	FLT-bit 32 and TLT-bit SPP15
BPC timing	$ t_{\text{BPC-North}} - \langle t_{\text{BPC-North}}^{\text{un}} \rangle  < 3 \text{ ns}$
BPC fiducial volume	Section 10.2
BPC shower width	$\sigma < 0.7 \text{ cm}$
CTD tracks	2 tracks of opposite charge which are required to reach at least the third CTD superlayer to ensure an accurate momentum reconstruction
$\rho^0$ invariant mass	$0.57 < m_{\tau^+\tau^-} < 0.97 \text{ GeV}$
Background rejection	The total CAL energy is required to be less than 1.5 times the energy of the two decay pions

Table B.4: Off-line selection cuts for the elastic  $\rho^0$  event sample.

## Bibliography

- [Ab83] CDHS Collaboration, H. Abramowicz et al., *Z. Phys. C* **17** (1983) 283.
- [Ab90] H. Abramowicz et al., *Phys. Lett. B* **269** (1991) 465.
- [Ab95] H. Abramowicz et al., *DESY 95-047* (1995).
- [Ab96] H. Abramowicz et al., in *Proceedings of the Workshop on Future Physics at HERA*, edited by G. Ingelman et al. (Hamburg, Germany, 1995).
- [Ab97] H. Abramowicz and A. Levy, *DESY 97-251* (1997).
- [Ad96a] K. Adel, et al., *FTUAM 96-39* (1996).
- [Ad96b] M. Adams et al., *Phys. Rev. D* **54** (1996) 3006.
- [Ad97] H1 Collaboration, C. Adloff et al., *Nucl. Phys. B* **497** (1997) 3.
- [Ag94] G. D'Agostini, *DESY 94-099* (1994).
- [Ai95] H1 Collaboration, S. Aid et al., *Z. Phys. C* **69** (1995) 27.
- [Ai96] H1 Collaboration, S. Aid et al., *Nucl. Phys. B* **470** (1996) 3.
- [Ak77] G.A. Akopjanov et al., *Nucl. Instr. and Meth.* **140** (1977) 441.
- [Ak95] A. Akhundov et al., *DESY 95-185* (1995).
- [Al77] G. Altarelli and G. Parisi, *Nucl. Phys. B* **126** (1977) 298.
- [Am81] U. Amaldi, *Phys. Scripta*, Vol. **23** (1981) 409.
- [An83] B. Anderson et al., *Phys. Rev.* **97** (1983) 31.
- [An89] B. Anderson et al., *Z. Phys. C* **43** (1989) 625.
- [An91] A. Andresen et al., *Nucl. Instr. and Meth. A* **309** (1991) 101.
- [An92] J. Andruskow et al., *DESY 92-066* (1992).
- [Ar95] ARMCO EISEN GmbH, *Technical information*, (Köln, Germany, 1990).
- [As94a] A.J. Askew et al., *Phys. Rev. D* **49** (1994) 4402.
- [As94b] A.J. Askew et al., *Phys. Lett. B* **325** (1994) 212.
- [Aw92] T.C. Awes et al., *Nucl. Instr. and Meth.* **311** (1992) 130.
- [Ba64] V.E. Barnes, *Phys. Rev. Lett.* **12** (1964) 204.
- [Ba68] W. Bartel et al., *Phys. Lett. B* **28** (1968) 148.
- [Ba78] Y. Balitzki and L.N. Lipatov, *Phys. Rev. Lett.* **28** (1978) 822;  
E.A. Kuraev et al., *Phys. Rev. Lett.* **44** (1976) 443;  
E.A. Kuraev et al., *Phys. Rev. Lett.* **45** (1977) 199.
- [Ba90] B. Badelek and J. Kwiecinski, *Phys. Lett. B* **295** (1992) 263.
- [Ba92a] T.H. Bauer et al., *Rev. Mod. Phys.* **50** (1978) 261.
- [Ba92b] I. Baur, diploma thesis., Univ. of Hamburg (1992).
- [Ba95a] L.A.T. Bauerdick et al., *DESY-95-296* (1995).
- [Ba95b] L.A.T. Bauerdick et al., in *Proceedings of the Workshop on Future Physics at HERA*, edited by G. Ingelman et al. (Hamburg, Germany, 1995).
- [Ba96a] B. Badelek et al., *DTP-96-16* (1996).
- [Ba96b] Particle Data Group, R.M. Barnett et al., *Phys. Rev. D* **54** (1996) 1.
- [Ba97a] B. Badelek, private communications.
- [Ba97b] B. Badelek, *Z. Phys. C* **74** (1997) 297.
- [Ba97c] F. Barreiro, private communications.
- [Be34] H. Bethe and W. Heitler, *Proc. Roy. Soc. A* **146** (1934) 83.
- [Be87a] M. Bergtsson and T. Sjöstrand, *Comp. Phys. Comm.* **46** (1987) 43.
- [Be87b] M. Bergtsson and T. Sjöstrand, *Comp. Phys. Comm.* **43** (1987) 367.
- [Be88] M. Bengtsson and T. Sjöstrand, *Z. Phys. C* **37** (1988) 465.
- [Be91] S. Bentvelsen et al., in *Proceedings of the Workshop on Physics at HERA*, edited by W. Buchmüller and G. Ingelman (Hamburg, Germany, 1991).
- [Be92] U. Behrens et al., *Nucl. Instr. and Meth. A* **323** (1992) 611.
- [Be93] B. Bernstein et al., *Nucl. Instr. and Meth. A* **336** (1993) 23.
- [Be97] C. Best et al., in *Proceedings of the Workshop on Deep Inelastic Scattering and QCD (DIS 97)*, edited by J. Repond (AIP, Chicago, 1997).
- [Bi94] A.F. Bielajew et al., *SLAC-PUB-6499* (1994);  
R. L. Ford and W. R. Nelson, *SLAC-PUB-210* (1978);  
W. R. Nelson et al., *SLAC-PUB-265* (1985).
- [Bj67] J.D. Bjorken, *Phys. Rev.* **163** (1967) 1767.
- [Bj69a] J.D. Bjorken, *Phys. Rev.* **179** (1969) 1547.
- [Bj69b] J.D. Bjorken and E.A. Paschos, *Phys. Rev.* **185** (1969) 1975.

- [Bj96] J.D. Bjorken, *SLAC-PUB-7096* (1996).
- [Bl69] E.D. Bloom et al., *Phys. Rev. Lett.* **23** (1969) 930.
- [Bl91] J. Blümlein, in *Proceedings of the Workshop on Physics at HERA*, edited by W. Buchmüller and G. Ingelman (Hamburg, Germany, 1991).
- [Bl93] J. Blümlein et al., *DESY 93-097* (1993).
- [Bo96a] I. Bohnet and B. Surrow, *ZEUS-note* (in preparation) (1998).
- [Bo97a] I. Bohnet, 'Investigations of the optical components of the ZEUS calorimeter components', Ph.D. thesis, Univ. of Hamburg, in preparation.
- [Bo97b] M. Botje, private communications.
- [Bo97c] M. Botje, *ZEUS-note 97-066* (1997).
- [Br89] R. Brun et al., *GEANTS, CERN DD/EE/81-1* (1989).
- [Br96a] R. Brun et al., *PAW Physics Analysis Workstation*, CERN (1997).
- [Br96b] R. Brun et al., *HBOOK Reference Manual*, CERN (1997).
- [Br97] ZEUS Collaboration, J. Breitweg et al., *Phys. Lett. B* **407** (1997) 434.
- [Bu77] L. Bugge, *Nucl. Instr. and Meth.* **145** (1977) 267.
- [CMS94] CMS Collaboration, Technical proposal, *CERN/LHCC 94-38* (1994).
- [Ca69] C.G. Callan and D. Gross, *Phys. Rev. Lett.* **22** (1969) 156.
- [Ca78] D.O. Caldwell et al., *Phys. Rev. Lett.* **40** (1978) 1222.
- [Ca90] S. Catani, et al., *Phys. Lett. B* **234** (1990) 339;  
S. Catani, et al., *Nucl. Phys. B* **336** (1990) 18.
- [Ca93] A. Caldwell et al., *Nucl. Instr. and Meth. A* **321** (1992) 356.
- [Ca94] A. Capella et al., *Phys. Lett. B* **337** (1994) 358.
- [Ca96] A. Caldwell et al., *ZEUS-note 96-044* (1996).
- [Cl86] F. Close, M. Marten and C. Sutton, *The Particle Explosion*, (Oxford University Press Inc., New York, 1986).
- [Co70] R.D.B. Collins, *An Introduction into Regge Theory and High Energy Physics*, (Cambridge University Press, Cambridge, 1977).
- [Co92] A. Courau and P. Kessler, *Phys. Rev. D* **46** (1992) 117.
- [Cu96] J. Cudell et al., *BROWN-HET-1060* (1997).
- [DESY94] DESY, *Annual report* (1994)

- [Da96] A. Dannemann, 'Untersuchung zur Strahlenresistenz polymerer Materialien für den Einsatz in Experimenten der Hochenergiephysik', Ph.D. thesis., Univ. of Hamburg (1996).
- [De91] M. Derrick et al., *Nucl. Instr. and Meth. A* **309** (1991) 77.
- [De94] ZEUS Collaboration, M. Derrick et al., *Z. Phys. C* **63** (1994) 391.
- [De96a] ZEUS Collaboration, M. Derrick et al., *Z. Phys. C* **69** (1996) 607.
- [De96b] ZEUS Collaboration, M. Derrick et al., *Z. Phys. C* **72** (1996) 399.
- [De96c] ZEUS Collaboration, M. Derrick et al., *Z. Phys. C* **73** (1996) 73.
- [Di97] D.I. Diakonov et al., *Phys. Rev. D* **56** (1997) 4069.
- [Do92] A. Donnachie and P.V. Landshoff, *Phys. Lett. B* **296** (1992) 227.
- [Do94] A. Donnachie and P.V. Landshoff, *Z. Phys. C* **61** (1994) 139.
- [Dr64] S.D. Drell and J.D. Walecka, *Amn. Phys. (N.Y.)* **28** (1964) 18.
- [Fa82] C.W. Fabjan and T. Ludlam, *Ann. Rev. Nucl. Part. Sci.* **32** (1982) 335.
- [Fa85] C.W. Fabjan, in *Techniques and Concepts in High Energy Physics*, edited by T. Ferbel, (Addison-Wesley, New York, 1985).
- [Fe69] R.P. Feynman, *Phys. Rev. Lett.* **23** (1969) 1415.
- [Fe88] G. Ferri et al., *Nucl. Instr. and Meth. A* **273** (1988) 123.
- [Fo74] D.J. Fox et al., *Phys. Rev. Lett.* **33** (1975) 898.
- [Fo93] B. Foster et al., *Nucl. Instr. and Meth. A* **338** (1993) 254.
- [Fr61] M. Froissart, *Phys. Rev.* **123** (1961) 1053.
- [Fr73] H. Fritzsche et al., *Phys. Lett. B* **47** (1973) 365.
- [Fr96] A. Frey, 'Messung der Protonstrukturfunktion  $F_2(x, Q^2)$  in radiativer  $ep$ -Streuung mit dem ZEUS-Detektor', Ph.D. thesis., Univ. of Bonn (1996).
- [Fu82] W. Furmanski and R. Petronzio, *Phys. Lett. B* **97** (1980) 437.
- [Ge53] M. Gell-Mann, *Phys. Rev.* **92** (1953) 553.
- [Ge62] M. Gell-Mann, *Phys. Rev.* **125** (1962) 1067.
- [Ge64a] M. Gell-Mann, *Phys. Lett.* **8** (1964) 214.
- [Ge64b] M. Gell-Mann and Y. Ne'eman, *The Eightfold Way*, (W.A. Benjamin Inc., New York 1964).
- [Ge94] Gebex AG, *Technical information*, (Uster, Switzerland, 1994).
- [Gi72] F.J. Gilman, *Phys. Rev.* **129** (1968) 1365.

- [Gl94] M. Glück et al., *Z. Phys. C* **48** (1990) 471;  
M. Glück et al., *Z. Phys. C* **53** (1992) 127;  
M. Glück et al., *Z. Phys. C* **67** (1995) 433.
- [Go81] H. Gordon et al., *Phys. Scripta*, Vol. **23** (1981) 564.
- [Go96] M. Gospic and H. Groenstege, *ZEUS-note 96-006* (1996);  
M. Gospic and H. Groenstege, *ZEUS-note 96-007* (1996).
- [Gr64] O.W. Greenberg, *Phys. Rev. Lett.* **13** (1964) 598.
- [Gr72] V.N. Gribov and L.N. Lipatov, *Sov. J. Nucl. Phys.* **15** (1972) 438;  
L.N. Lipatov, *Sov. J. Nucl. Phys.* **20** (1975) 96;  
Y.L. Dokshitzer, *Sov. Phys. JETP*. **46** (1977) 641.
- [Gr73] D.J. Gross and F. Wilczek, *Phys. Rev. D* **8** (1973) 3633.
- [Gr81] V.N. Gribov et al., *Nucl. Phys. B* **188** (1981) 555.
- [Gr89] M.G. Green, *RNBNC 89-01* (1989).
- [Gr94] G. Gratta et al., *Ann. Rev. Nucl. Part. Sci.* **14** (1994) 453.
- [Gr96] T. DeGrand, in *Proceedings of the XXIV SLAC Summer Institute*,  
edited by J. Chan et al. (Stanford, USA, 1996).
- [Gu80] G. Gurci et al. *Nucl. Phys. B* **175** (1980) 27.
- [HB94] HERA-B Collaboration, *Technical Design Report*, DESY-PRC 95/01 (1995).
- [HE93] HERMES Collaboration, *Technical Design Report* (1993).
- [Ha63] L.N. Hand, *Phys. Lett. B* **129** (1963) 1834.
- [Ha84] F. Halzen and A.D. Martin, *Quarks and Leptons*,  
(John Wiley Sons Inc., New York, 1984).
- [Ha94] Hamamatsu, *Technical information*, (Tokyo, Japan, 1994).
- [He44] W. Heisenberg, *Physikalische Prinzipien der Quantentheorie*,  
(S. Hirzel Verlag, Stuttgart, 1958).
- [Ho53] R. Hofstadter et al., *Phys. Rev.* **91** (1953) 422.
- [Ho55] R. Hofstadter and R.W. McAllister, *Phys. Rev.* **98** (1955) 217.
- [Ho57] R. Hofstadter, *Ann. Rev. Nucl. Part. Sci.* **7** (1957) 458.
- [Ho93] ZEUS Collaboration, *The ZEUS Detector*, Status Report 1993,  
edited by U. Holm, (1993).
- [Ho96] M. Lomperski, private communications.
- [Ho97] B. Holzer, private communications.
- [In87] G. Ingelman and R. Rückl, *Phys. Lett.* **201** (1988) 369.

- [In96] G. Ingelman et al., *DESY 96-057* (1996).
- [Io69] B.L. Ioffe, *Phys. Lett. B* **30** (1969) 123.
- [Ja79] F. Jacquet and A. Blondel, in *Proceedings of the study of an ep facility for Europe*,  
edited by U. Amaldi, (Hamburg, Germany, 1979).
- [Jo99] P.K. Job et al., *Nucl. Instr. and Meth. A* **271** (1988) 442.
- [Ka83] T. Kamon et al., *Nucl. Instr. and Meth.* **213** (1983) 261.
- [Ka95] M. Kasprzak, *ZEUS-note 95-161* (1995).
- [Kö95] U. Kötz, *ZEUS-note 95-161* (1995).
- [Kö97] U. Kötz, private communications.
- [Kw91] A. Kwiatkowski et al., in *Proceedings of the Workshop on Physics at HERA*,  
edited by W. Buchmüller and G. Ingelman (Hamburg, Germany, 1991).
- [Kw94] J. Kwiecinski et al., *Phys. Rev. D* **50** (1994) 217.
- [Kw97] J. Kwiecinski et al., in *Proceedings of the Workshop on Deep Inelastic Scattering  
and QCD (DIS 97)*, edited by J. Repond (AIP, Chicago, 1997).
- [Le87] W.R. Leo, *Techniques for Nuclear and Particle Physics Experiments*,  
(Springer, New York, 1987).
- [Le97] A. Levy, *DESY 97-019* (1997).
- [Lo75] E. Longo and I. Sestelli, *Nucl. Instr. and Meth. A* **128** (1975) 283.
- [Lö92] L. Lönnblad, *Z. Phys. C* **65** (1995) 285;  
L. Lönnblad, *Comp. Phys. Comm.* **71** (1992) 15.
- [Lo96] E. Lohrmann et al., *ZEUS-note 96-089* (1996).
- [Lo96] M. Loewe, 'Measurement of Positron-Proton Scattering at  $Q^2 = 0.25 \text{ GeV}^2$ ',  
Ph.D. thesis., Univ. of Hamburg (1996), *DESY F35D-96-03* (1996).
- [Ma92] G. Marchesini, *Comp. Phys. Comm.* **67** (1992) 465.
- [Ma94] A. D. Martin et al., *Phys. Rev. D* **50** (1994) 6734;  
A. D. Martin et al., *Phys. Lett. B* **354** (1995) 155.
- [Ma95] J. Mainusch, 'Measurement of the total photon-proton cross-section  
at HERA energies', Ph.D. thesis., Univ. of Hamburg (1995), *DESY F35D-95-14*  
(1995).
- [Ma96a] S. Mattingly, private communications.
- [Ma96b] A.D. Martin et al., *DTP-96-44* (1996).
- [Ma97] A.D. Martin, private communications.
- [Me95] N. Meyners, private communications.

- [MI97] R. Brun et al., *MINUIT Reference Manual*, CERN (1997).
- [Mo29] N.F. Mott, *Proc. Roy. Soc.* **124** (1929) 425.
- [Mo69] L. Mo and Y. Tsai, *Rev. Mod. Phys.* **41** (1969) 205.
- [Mo94] B. Mouëllic, *CERN-PPE/94-194* (1994).
- [Mo96] T. Monteiro, private communications.
- [Mo97a] T. Monteiro in *Proceedings of the Workshop on Deep Inelastic Scattering and QCD (DIS 97)*, edited by J. Repond (AIP, Chicago, 1997).
- [Mo97b] T. Monteiro, 'Exclusive electroproduction of  $\rho^0$  mesons for  $0.25 < Q^2 < 0.85 \text{ GeV}^2$  at HERA', Ph.D. thesis., Univ. of Hamburg, in preparation.
- [Mu90] A.H. Mueller, *Nucl. Phys. B (Proc. Suppl.)* **18 C** (1990) 125.
- [Ne61] Y. Ne'eman, *Nucl. Phys.* **26** (1961) 222.
- [Pa68] W. Panofski, in *Proceedings of the International Conference in High Energy Physics*, (Vienna, Austria, 1968).
- [Pi93] K. Piotrkowski, *DESY F35D-93-06* (1993).
- [Pi96] K. Piotrkowski, private communications.
- [Pl94] Metallwerk Plansee GmbH, *Technical information*, (Lechbruck, Austria, 1994).
- [Pr93] K. Prytz, *Phys. Lett. B* **311** (1993) 286.
- [Qa96] A. Quadt, 'Measurement and QCD analysis of the Proton Structure Function  $F_2$  from the 1994 HERA Data using the ZEUS Detector', Ph.D. thesis., Univ. of Oxford (1996).
- [Ri94] S. Ritz, private communications.
- [Ro50] M.N. Rosenbluth, *Phys. Rev.* **79** (1950) 615.
- [Ro61] B. Rossi, *High Energy Particles*, (Prentice-Hall Inc., New York, 1961).
- [Ro96] M. Rohde, private communications.
- [Ru11] E. Rutherford, *Phil. Mag.* **211** (1911) 669.
- [Sa60] J.J. Sakurai, *Ann. Phys.* **11** (1960) 1.
- [Sa72] J.J. Sakurai and D. Schildknecht, *Phys. Lett. B* **40** (1972) 121.
- [Sa96] C. Sampson, 'Measurement of the total photoproduction cross-section', Ph.D. thesis., Univ. of Toronto (1996).
- [Sc81] W. Schmidt-Parzefall, *Physic. Scripta Vol.* **23** (1981) 425.
- [Sc97a] D. Schildknecht and H. Spiesberger, *BI-TP 97/25* (1997).

- [Sc97b] D. Schildknecht, private communications.
- [Sm89] W.H. Smith et al., *ZEUS-note 89-084* (1989).
- [Sp92] H. Spiesberger et al., in *Proceedings of the Workshop on Physics at HERA*, edited by W. Buchmüller and G. Ingelman (Hamburg, Germany, 1991).
- [St95] G. Sterman et al., *Rev. Mod. Phys.* **67** (1995) 157.
- [Su97] B. Surrow in *Proceedings of the Workshop on Deep Inelastic Scattering and QCD (DIS 97)*, edited by J. Repond (AIP, Chicago, 1997).
- [Te64] A.A. Sokolov and I.N. Ternov, *Soviet Physics Doklady No.12* (1964) 1203.
- [Ti96] J. Tickner, private communications.
- [Ti97] J. Tickner, 'Proton Structure Functions at low  $Q^2$ ', Ph.D. thesis., Univ. of Oxford (1997).
- [Ui92] H. Uijterwaal, 'The Global Second Level Trigger for ZEUS', Ph.D. thesis., Univ. of Amsterdam (1992).
- [Vr96] Marcel Vreeswijk, 'Measurement of the Structure Function  $F_2$  and the Gluon Density of the Proton', Ph.D. thesis., Univ. of Amsterdam (1996).
- [Vi92] M. Virchaux and A. Milsztajn, *Phys. Lett. B* **274** (1992) 221.
- [Wa96] S.M. Wang, *ZEUS-note 96-121* (1996).
- [We73] S. Weinberg, *Phys. Rev. Lett.* **31** (1973) 494.
- [We92] J. Wear, private communications.
- [We96] E. Weiss, private communications.
- [Wi82] B. Wiik and G. Voss, *Ann. Rev. Nucl. Part. Sci.* **32** (1982) 335.
- [Wi87] R. Wigmans, *Nucl. Instr. and Meth. A* **259** (1987) 389.
- [Wi96] F. Willeke, private communications.
- [Wu84] S.L. Wu, *Phys. Rep.* **107** (1984) 1.
- [Yo92] C. Youngman, *DESY 92-150A* (1992).
- [Zw64] G. Zweig, *CERN-8192/TH 401* (1964);  
G. Zweig, *CERN-8419/TH 402* (1964).

## Acknowledgements

The opportunity I was given to work on my Ph.D. within the ZEUS collaboration at DESY enriched my life tremendously. Working amongst an international collaboration within the high energy physics community was both challenging and rewarding.

First of all, I want to thank all of the members of the ZEUS collaboration who's spirit and teamwork contributed to the success of this thesis.

Of utmost importance my gratitude is extended to Professors Robert Klanner and Erich Lohrmann, each giving me outstanding guidance and advice each step along the way. The professional manner in which my thesis draft was read is something to be commended. The fact that I always felt comfortable when I needed questions answered showed me that our relationship was based on respect and trust. This enabled me to gain confidence in my work as well as in my personal growth. In a very personal way I would like to thank Dr. Gerhard Söhngen. He gave me the chance to start working for ZEUS during my undergraduate education at Würzburg, thus inspiring me to continue my work with the ZEUS collaboration. All of them were always very considerate to me and my family.

The work performed within the BPC group in particular by U. Fricke, D. Keira, T. Monteiro, J. Tickner, and Q. Zhu was very much appreciated. They deserve due credit for their exhaustive amount of work.

Dr. Frank Chlebana taught me a very efficient manner in which to do my physics analysis. I am very grateful to him for guiding me through the first steps of the  $F_2$  analysis.

The BPC project would not have been possible and would not have gone as smoothly without the help of so many technicians and engineers such as J. Hausschildt, K. Löffler, E. Weiss, A. Maniatis and H. Schult.

It was truly a wonderful experience having met many people at DESY from whom I learned an invaluable amount of information from, in particular during the preparation of the thesis draft. They include: H. Abramowicz, C. Amelung, L.A.T. Bauerdick, F. Barreiro, I. Bohnet, M. Botje, A. Caldwell, A. Dannemann, A. deRoeck, R. Devenish, T. Doyle, C. Foudas, T. Haas, D. Haidt, U. Holm, G. Iacobucci, M. Inuzuka, K. Johnson, M. Kasemann, U. Kötz, F. Lehner, E. Levin, A. Levy, L. Lindemann, B. Mellado, A. Meyer, N. Pavel, A. Pellegrino, K. Piotrkowski, A. Prinias, A. Quadt, S. Ritz, M. Roco, M. Rohde, F. Sciulli, U. Schneekloth, K. Tokushuku, D. Westphal, K. Wick, G. Wolf and W. Zeuner.

A special thanks is extended to Dr. W. Zeuner, Dr. A. Quadt and Dr. J. Tickner for reading the whole thesis draft.

I would like to thank the DESY directorate for their continuous support which made it possible for me to profit from the educational experiences I had in Ljubljana, BNL, SLAC, Chicago, Stony Brook and Durham.

Of course this thesis was only able to blossom because of the love and care given by both my family and my wife's family. I want to thank them for helping to motivate me to achieve my goal.

I want to thank my lovely wife Suzanne for giving me support and encouragement, for being patient and for creating a warm and loving home environment. Finally, I want to thank our 'bundle of joy' Carl who brings a whole new dimension to the term 'high energy'. Suzanne's and Carl's unique sense of humor added laughter to my days - they have truly made the last few years the happiest years of my life.

# Annual Report

The following table shows the results of the various projects undertaken during the year. The figures are in thousands of dollars.

Project	1987-88	1986-87
Project A	120	110
Project B	80	75
Project C	150	140
Project D	90	85
Project E	110	105
Project F	130	125
Project G	100	95
Project H	140	135
Project I	160	155
Project J	180	175
Project K	190	185
Project L	200	195
Project M	210	205
Project N	220	215
Project O	230	225
Project P	240	235
Project Q	250	245
Project R	260	255
Project S	270	265
Project T	280	275
Project U	290	285
Project V	300	295
Project W	310	305
Project X	320	315
Project Y	330	325
Project Z	340	335
Project AA	350	345
Project AB	360	355
Project AC	370	365
Project AD	380	375
Project AE	390	385
Project AF	400	395
Project AG	410	405
Project AH	420	415
Project AI	430	425
Project AJ	440	435
Project AK	450	445
Project AL	460	455
Project AM	470	465
Project AN	480	475
Project AO	490	485
Project AP	500	495
Project AQ	510	505
Project AR	520	515
Project AS	530	525
Project AT	540	535
Project AU	550	545
Project AV	560	555
Project AW	570	565
Project AX	580	575
Project AY	590	585
Project AZ	600	595
Project BA	610	605
Project BB	620	615
Project BC	630	625
Project BD	640	635
Project BE	650	645
Project BF	660	655
Project BG	670	665
Project BH	680	675
Project BI	690	685
Project BJ	700	695
Project BK	710	705
Project BL	720	715
Project BM	730	725
Project BN	740	735
Project BO	750	745
Project BP	760	755
Project BQ	770	765
Project BR	780	775
Project BS	790	785
Project BT	800	795
Project BU	810	805
Project BV	820	815
Project BV	830	825
Project BV	840	835
Project BV	850	845
Project BV	860	855
Project BV	870	865
Project BV	880	875
Project BV	890	885
Project BV	900	895
Project BV	910	905
Project BV	920	915
Project BV	930	925
Project BV	940	935
Project BV	950	945
Project BV	960	955
Project BV	970	965
Project BV	980	975
Project BV	990	985
Project BV	1000	995

The following table shows the results of the various projects undertaken during the year. The figures are in thousands of dollars.

Project A: 120, Project B: 80, Project C: 150, Project D: 90, Project E: 110, Project F: 130, Project G: 100, Project H: 140, Project I: 160, Project J: 180, Project K: 190, Project L: 200, Project M: 210, Project N: 220, Project O: 230, Project P: 240, Project Q: 250, Project R: 260, Project S: 270, Project T: 280, Project U: 290, Project V: 300, Project W: 310, Project X: 320, Project Y: 330, Project Z: 340, Project AA: 350, Project AB: 360, Project AC: 370, Project AD: 380, Project AE: 390, Project AF: 400, Project AG: 410, Project AH: 420, Project AI: 430, Project AJ: 440, Project AK: 450, Project AL: 460, Project AM: 470, Project AN: 480, Project AO: 490, Project AP: 500, Project AQ: 510, Project AR: 520, Project AS: 530, Project AT: 540, Project AU: 550, Project AV: 560, Project AV: 570, Project AV: 580, Project AV: 590, Project AV: 600, Project AV: 610, Project AV: 620, Project AV: 630, Project AV: 640, Project AV: 650, Project AV: 660, Project AV: 670, Project AV: 680, Project AV: 690, Project AV: 700, Project AV: 710, Project AV: 720, Project AV: 730, Project AV: 740, Project AV: 750, Project AV: 760, Project AV: 770, Project AV: 780, Project AV: 790, Project AV: 800, Project AV: 810, Project AV: 820, Project AV: 830, Project AV: 840, Project AV: 850, Project AV: 860, Project AV: 870, Project AV: 880, Project AV: 890, Project AV: 900, Project AV: 910, Project AV: 920, Project AV: 930, Project AV: 940, Project AV: 950, Project AV: 960, Project AV: 970, Project AV: 980, Project AV: 990, Project AV: 1000.